

Integrated Design Optimization of Electrically-Driven Vapor Compression Cycle Systems for Aircraft

Powered by High-Speed Centrifugal Compressors

Giuffré, A.

DOI

[10.4233/uuid:b4f6a4a4-2e48-4bbe-9093-3f1368282f63](https://doi.org/10.4233/uuid:b4f6a4a4-2e48-4bbe-9093-3f1368282f63)

Publication date

2023

Document Version

Final published version

Citation (APA)

Giuffré, A. (2023). *Integrated Design Optimization of Electrically-Driven Vapor Compression Cycle Systems for Aircraft: Powered by High-Speed Centrifugal Compressors*. [Dissertation (TU Delft), Delft University of Technology]. <https://doi.org/10.4233/uuid:b4f6a4a4-2e48-4bbe-9093-3f1368282f63>

Important note

To cite this publication, please use the final published version (if applicable). Please check the document version above.

Copyright

Other than for strictly personal use, it is not permitted to download, forward or distribute the text or part of it, without the consent of the author(s) and/or copyright holder(s), unless the work is under an open content license such as Creative Commons.

Takedown policy

Please contact us and provide details if you believe this document breaches copyrights. We will remove access to the work immediately and investigate your claim.

INTEGRATED DESIGN OPTIMIZATION OF ELECTRICALLY-DRIVEN VAPOR COMPRESSION CYCLE SYSTEMS FOR AIRCRAFT

POWERED BY HIGH-SPEED CENTRIFUGAL COMPRESSORS

Dissertation

for the purpose of obtaining the degree of doctor
at Delft University of Technology,
by the authority of the Rector Magnificus prof. dr. ir. T.H.J.J. van der Hagen,
chair of the Board for Doctorates,
to be defended publicly on
Thursday 18 January 2024 at 10:00 o'clock

by

Andrea GIUFFRÉ

Master of Science in Mechanical Engineering,
Politecnico di Milano, Italy
born in Carate Brianza, Italy

This dissertation has been approved by the promotor.

Composition of the doctoral committee:

Rector Magnificus,	Chairperson
Prof. dr. ir. P. Colonna di Paliano,	Delft University of Technology, <i>promotor</i>
Dr. ir. M. Pini,	Delft University of Technology, <i>copromotor</i>

Independent members:

Prof. dr. K. Hooman	Delft University of Technology
Prof. dr. ir. J. Seume	Leibniz University Hannover, Germany
Prof. dr. P. Gaetani	Politecnico di Milano, Italy
Dr. ir. W. Casas	Airbus, Germany
Prof. dr. ir. S. Hickel	Delft University of Technology, <i>reserve member</i>

Other members:

Dr. C. M. De Servi	Delft University of Technology
--------------------	--------------------------------

The research presented in this dissertation has been performed at the Flight Performance and Propulsion Section, Department of Flow Physics and Technology, Faculty of Aerospace Engineering. This work is part of the research project "Novel Electrically-Driven Environmental Control Systems for Aircraft" (NEDEFA), funded by the Dutch Technology Foundation TTW, Applied Science Division of NWO, the Technology Program of the Ministry of Economic Affairs, and by Aeronamic B.V. (Grant No. 17091).



AERONAMIC

Printed by Ridderprint B.V.

Cover illustration and design by M. Perego

Copyright © 2023 by A. Giuffré

An electronic version of this dissertation is available at
<http://repository.tudelft.nl/>.

*Dedicated to V.
May your spirit be as free as the wind
and your dreams as boundless as the sky.*

CONTENTS

Summary	ix
Samenvatting	xi
1 Introduction	1
1.1 Aircraft Environmental Control Systems	2
1.2 High-Speed Centrifugal Compressors	8
1.3 Motivation	10
1.4 Original Contributions	12
1.5 Outline	13
2 Design Guidelines for High-Speed Centrifugal Compressors	17
2.1 Introduction	18
2.2 Objective	20
2.3 Conceptual Design based on Scaling Principles	21
2.3.1 Loss Modeling	23
2.3.2 Off-Design Performance	27
2.3.3 Validation	29
2.4 Design Maps for Single-Stage Compressors	32
2.4.1 Influence of the Working Fluid	32
2.4.2 Influence of Size	35
2.5 Case Study	36
2.5.1 Conceptual Design Optimization	37
2.5.2 Performance Investigation based on CFD	39
2.6 Conclusions.	41
3 Design of the Twin-Stage Centrifugal Compressor for the IRIS Test Rig	49
3.1 Introduction	50
3.2 Methodology	51
3.2.1 Scaling Analysis for Twin-Stage Compressors	51
3.2.2 Extension of the Compressor Design Model	54
3.3 Fluid Dynamic Design of the IRIS Compressor	58
3.3.1 Conceptual Design Optimization	58
3.3.2 3D Blade Design	60
3.3.3 Preliminary Structural Assessment.	62
3.4 Fluid Dynamic Performance Analysis	65
3.4.1 Hybrid Computational Method	65
3.4.2 Results	68
3.5 Conclusions.	71

4	Dynamic Thermal Model of Pressurized Aircraft Fuselage	75
4.1	Introduction	76
4.2	Methodology	78
4.2.1	System Model	78
4.2.2	Model of External Environment	84
4.2.3	Model of Composite Structures	85
4.2.4	Model of Transparent Surfaces	87
4.2.5	Fuselage Model	88
4.3	Validation	92
4.4	Applications	94
4.4.1	ECS Operating Envelope	94
4.4.2	Pull-Down Operating Point	96
4.5	Conclusions.	99
5	Integrated Design Optimization of ECS for Next-Generation Aircraft	105
5.1	Introduction	106
5.2	Methodology	108
5.2.1	System Model	108
5.2.2	Model of Air Intakes	110
5.2.3	Air-to-Air Heat Exchanger Model.	113
5.2.4	Air-to-Refrigerant Heat Exchanger Model	116
5.2.5	Centrifugal Compressor Model	119
5.2.6	Integrated Design Optimization	122
5.3	Results	125
5.3.1	Air Cycle Machine	129
5.3.2	Vapor Compression Cycle System	132
5.4	Conclusions.	138
6	Data-Driven Compressor Modeling for ECS Design Optimization	147
6.1	Introduction	148
6.2	Data-Driven Compressor Model	149
6.3	Integrated Design Optimization.	154
6.4	Results	159
6.5	Conclusions.	166
7	Conclusion	173
7.1	Limitations and Recommendations.	175
7.2	Outlook	176
A	Solar Radiation	179
A.1	Clear-Sky Solar Radiation	179
A.2	Solar Radiation on a Receiving Surface	181
B	Airbus A320 Technical Specifications	187
C	Software	193
	About the Author	195

List of Publications

197

SUMMARY

In 2022 the aviation sector accounted for 1.9% of global greenhouse gas emissions, 2.5% of global CO₂ emissions, and 3.5% of effective radiative forcing. To reach the long-term target of net zero emissions, revolutionary aircraft designs, featuring electrified or hydrogen-powered propulsion systems, are needed. At the same time, the electrification of the non-propulsive aircraft subsystems is necessary to comply with the requirements of emissions abatement in the short and medium time horizon.

Among the auxiliary subsystems, the Environmental Control System (ECS) is the largest consumer of non-propulsive power, accounting for up to 3-5% of the total fuel burn. The replacement of the conventional Air Cycle Machine (ACM) with an electrically-powered ECS based on the Vapor Compression Cycle (VCC) system could enable: i) a substantial decrease in fuel consumption; ii) a finer regulation of the relative humidity in the air distribution system, leading to improved air quality in the cabin and flight deck; iii) a reduction in maintenance costs and an increase in system reliability, due to the removal of the maintenance-intensive bleed system. However, the adoption of VCC systems in the aerospace sector has been historically very limited, due to safety concerns regarding the ozone depleting potential, toxicity and flammability of the working fluids used as refrigerants, as well as because of a lack of research specifically targeting airborne applications.

This dissertation documents research work performed as part of the NEDEFA project, which entails the investigation of VCC-based ECS architectures powered by oil-free high-speed centrifugal compressors. The first objective is to advance of the state-of-the-art regarding high-speed compressors operating with gas bearings, i.e., the key technological enablers of airborne VCC systems. The second target is to develop of a methodology for the integrated design of aircraft ECS, namely, a design philosophy in which the system and the main components are optimized simultaneously.

The main outcomes of this work are the development of a preliminary design model for high-speed compressors, extensively validated with experimental data and computational fluid dynamics simulations, and the implementation of an integrated design framework for aircraft ECS, embedding a multi-point and multi-objective optimization strategy. The compressor model has been applied to derive design guidelines for single-stage and twin-stage machines operating with arbitrary working fluids, as well as to perform the fluid dynamic design optimization of the compressor that will be installed in the IRIS (Inverse organic Rankine Integrated System) test rig of the Propulsion and Power Laboratory. Furthermore, the integrated design method has been used to size and compare the performance of two alternative ECS configurations for a single-aisle, short-haul aircraft resembling the configuration of an Airbus A320, i.e., a bleedless ACM and an electrically-driven VCC. The results reveal that the optimal VCC system could be both more efficient and lighter than the corresponding ACM architecture, leading to potential fuel savings in the order of 20% for the prescribed application.

SAMENVATTING

In 2022 was de luchtvaartsector verantwoordelijk voor 1,9% van de mondiale uitstoot van broeikasgassen, 2,5% van de CO₂-uitstoot en 3,5% van de effectieve stralingsforcering. Om de langetermijndoelstelling van het elimineren van alle uitstoot te bereiken zijn revolutionaire vliegtuigontwerpen, aangedreven doormiddel van elektriciteit of waterstof. Tegelijkertijd is de elektrificatie van de subsystemen voor niet-voortstuwingsvliegtuigen noodzakelijk om te voldoen aan de eisen omtrend emissiereductie op de korte en middellange termijn.

Van de aanvullende subsystemen gebruikt het Environmental Control System (ECS) de meeste energie naast de voortstuwing; 3-5% van het totale brandstofverbruik van het vliegtuig. Het vervangen van het Air Cycle Machine (ACM) systeem door een elektrisch aangedreven ECS gebaseerd op het Vapor Compression Cycle (VCC) systeem brengt de volgende voordelen omtrend duurzaamheid en prestaties: i) een substantiële verlaging van het brandstofverbruik; ii) een fijnere regeling van de relatieve vochtigheid in het luchtverdeelsysteem, leidend tot een betere luchtkwaliteit in de cabine en cockpit; iii) een verlaging van de onderhoudskosten en een verhoging van de systeembetrouwbaarheid, als gevolg van het verwijderen van het onderhoudsintensieve systeem wat lucht van de motoren naar de ACM brengt. De toepassing van VCC-systemen in de lucht- en ruimtevaartsector is historisch zeldzaam vanwege veiligheidsproblemen met betrekking tot het mogelijk aantasten van de ozonlaag, de toxiciteit en de ontvlambaarheid van de drijfstoffen die als koelmiddelen worden gebruikt, en vanwege een gebrek aan onderzoek dat specifiek gericht is op toepassingen in de luchtvaart.

Dit proefschrift documenteert onderzoekswerk dat is uitgevoerd als onderdeel van het NEDEFA-project, dat het onderzoek omvat van op VCC gebaseerde ECS systemen aangedreven door olievrije, hogesnelheidscentrifugaalcompressoren. Het eerste doel is het voortzetten van de techniek op het gebied van hogesnelheidscompressoren die werken met gaslagers, welke cruciaal zijn voor de toepassing van VCC-systemen in de lucht. Het tweede doel is het ontwikkelen van een ontwerpmethode voor VCC-ECS systemen in de luchtvaart, waarbij het systeem en de hoofdcomponenten gelijktijdig worden geoptimaliseerd.

Dit werk presenteert twee belangrijke resultaten: de ontwikkeling van een voorlopig ontwerpmodel voor hogesnelheidscompressoren, uitgebreid gevalideerd met experimentele gegevens en computersimulaties, en de implementatie van een ontwerp werkwijze voor vliegtuig-ECS, waarin een multi-point en multi-point-optimalizatie strategieën zijn geïmplementeerd. Het compressormodel werd gebruikt om drijfstof-agnostische ontwerprijlijnen te bepalen voor eentrap- en tweetrapsmachines, en om de vloeistofdynamische ontwerpoptimalisatie uit te voeren van de compressor die zal worden geïnstalleerd in de IRIS (Inverse Organic Rankine Integrated System) testopstelling van het Propulsion and Power Laboratory. Daarnaast werd de methode gepresenteerd in dit werk toegepast in het ontwerp van twee ECS-systeem variaties. De prestaties van deze systemen werden

vergeleken in de toepassing van een korte-afstands-, enkel-gangpad-vliegtuig, verwand aan de Airbus A320 met een elektrisch aangedreven VCC en zonder de verbinding tussen de motoren en ACM. De resultaten laten zien dat het optimale VCC-systeem zowel efficiënter als lichter zou kunnen zijn dan de overeenkomstige, huidige ACM-architectuur, wat zou kunnen leiden tot potentiële brandstofbesparingen in de orde van 20% voor de voorgeschreven toepassing.

1

INTRODUCTION

*Science knows no country because knowledge belongs to humanity,
and is the torch which illuminates the world.*

Louis Pasteur

1.1. AIRCRAFT ENVIRONMENTAL CONTROL SYSTEMS

IF no immediate actions are taken, the climate crisis will produce catastrophic changes in natural ecosystems resulting in irreparable effects on human civilization [1]. The solution or mitigation of this problem demands a complex set of behavioral transformations, concerted actions, global and continental policies, national implementations, and new or improved technologies [2]. Among the different sectors contributing to global emissions, in 2022 aviation accounted for: 1.9% of global greenhouse gas emissions, 2.5% of global CO₂ emissions, and 3.5% of effective radiative forcing [3]. Aircraft fuel efficiency increased by 2.4% per year between 2000 and 2010, and by 1.9% from 2010 to 2019, indicating that incremental improvements are becoming increasingly challenging. Meanwhile, passenger demand grew at a rate higher than 5% per year from 2000 to 2019 [4], implying that annual improvements in fuel efficiency are currently insufficient to comply with the goals set by the Advisory Council for Aeronautics Research in Europe (ACARE) in the Flightpath 2050 [5]. These targets include a 75% reduction in CO₂ emissions per passenger kilometer, a 90% reduction in nitrogen oxide (NO_x) emissions, and a 65% reduction in noise emissions during flight. The historical evolution of CO₂ emissions from aviation prior to the COVID-19 pandemic is displayed in Fig. 1.1. The forecasts about the impact of aviation on climatic change are exacerbated by considering that a large portion of the global population still has no access to or cannot afford to fly. As reported in [6], high-income countries that host about 16% of the global population are responsible for 51% of the total number of flights per year. Therefore, if the disparity in the accessibility to flight transportation is gradually reduced, air traffic and emissions are expected to surge in the following decades.

From a technological standpoint, revolutionary aircraft designs, featuring new airframe configurations, and electrified or hydrogen-powered propulsion systems, are needed to reach the long-term target of net zero emissions. At the same time, further improvements to engines and aerodynamics, as well as mild hybridization strategies, involving the electrification of the non-propulsive aircraft subsystems, must be implemented to comply with the requirements of emissions abatement in the short and medium time horizon. To this purpose, in the last decade, a large number of resources have been invested in R&D programs for the development of new technologies for the More Electric Aircraft (MEA) [7]. Among the auxiliary subsystems, the Environmental Control System (ECS) is the largest consumer of non-propulsive power, accounting for up to 3-5% of the total fuel burn [8]. The ECS is responsible for providing dry, sterile, and dust-free conditioned air to the airplane cabin at the proper temperature, flow rate, and pressure, to satisfy the safety and comfort requirements, as well as to ensure adequate avionics cooling [9]. In addition, the ECS must be lightweight, accessible for quick inspection and servicing, highly reliable, tolerant to a wide range of environmental conditions, able to withstand aircraft vibratory and maneuver loads, and must feature redundancy to guarantee emergency operation in case of failures during flight [10]. Despite its sizeable impact on aircraft fuel efficiency and its pivotal role in the context of flight safety, the technological innovations in the ECS architecture have been very limited since the 1960s [11]. The research work documented in this dissertation aims to bridge this knowledge gap by investigating Novel Electrically-Driven ECS configurations For next-generation Aircraft (NEDEFA). This study has been performed as part of the NEDEFA project, which entails a long-standing collaboration between Delft University of Technology and numerous industrial and academic

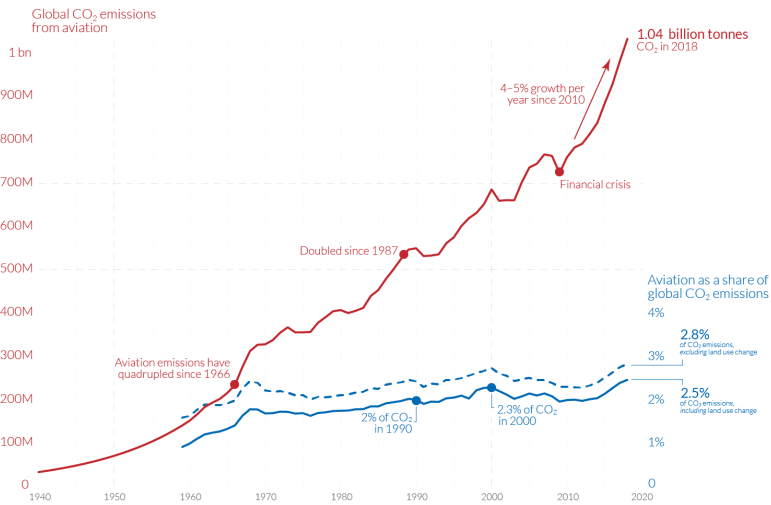


Figure 1.1: Historical evolution of global CO₂ emissions from aviation prior to the COVID-19 pandemic [12]. The emissions include passenger air travel, freight, and military operations.

partners, including, but not limited to, Aeronamic BV and Airbus.

In the conventional ECS configuration, i.e., that of the so-called Air Cycle Machine (ACM), cabin air conditioning is achieved by means of an inverse Brayton cycle using ram air as a coolant. During flight or taxiing, the ACM is powered by a stream of pressurized air bled from the compressor stages of the main engines. When the aircraft is on the ground and the engines are switched off, the ACM is driven by the Auxiliary Power Unit (APU). However, conventional pneumatic systems extract from the engines more power than is needed in most operating conditions, causing excess energy to be wasted. To overcome this issue and reduce the fuel consumption of the ECS, the Boeing 787 has been equipped with a bleedless ECS, driven by an electrical motor. This solution eliminates the extraction of pneumatic power generated by the engines and enables a reduction of specific fuel consumption in the range of 1-2% at cruise conditions [13]. In addition to fuel savings, the adoption of an electrically-powered ECS allows a finer regulation of the relative humidity in the air distribution system, leading to improved air quality in the cabin and flight deck, and is expected to reduce maintenance costs and increase system reliability, due to the removal of the maintenance-intensive bleed system.

A simplified process flow diagram of an ECS based on the bleedless three-wheel bootstrap ACM configuration is shown in Fig. 1.2. Following the cabin air stream, displayed in black, the thermodynamic cycle can be described as follows. At first, fresh air is collected in the intake, which partially recovers the available dynamic head during flight. Then, the fresh air is pressurized by the Cabin Air Compressor (CAC) and is cooled in the primary heat exchanger, i.e., an air-to-air plate-fin heat exchanger. Next, the air is further compressed by the ACM compressor and is cooled in the secondary heat exchanger, which features the same topology as the primary heat exchanger. If the aircraft is flying, the water content in the fresh air is negligible, thus the air stream at the outlet of the secondary

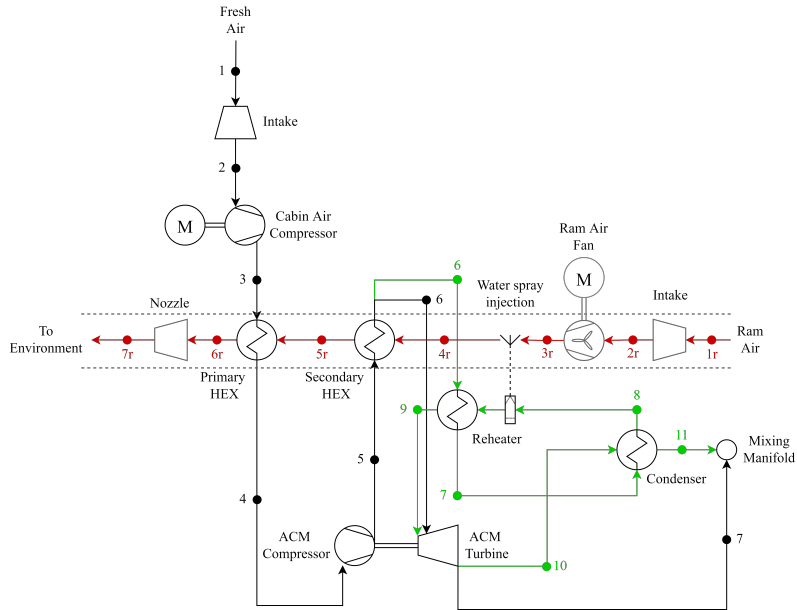


Figure 1.2: Simplified process flow diagram of an ECS based on the bleedless three-wheel bootstrap air cycle machine architecture. The cabin air stream and ram air stream are displayed in black and red, respectively. The high-pressure dehumidification loop is highlighted in green. The dashed black line refers to water spray injection at ground conditions.

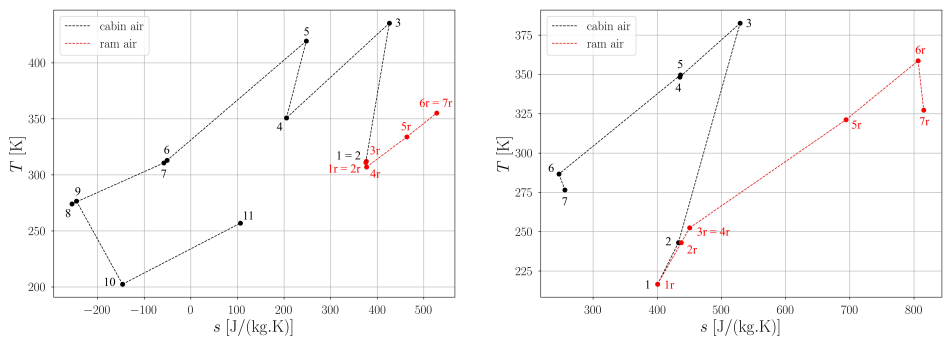


Figure 1.3: Thermodynamic diagram of an exemplary bleedless three-wheel bootstrap air cycle machine sized for an Airbus A320, operating on the ground (left) and in cruise conditions (right).

heat exchanger can be directly expanded in the ACM turbine and delivered to the mixing manifold, which is connected to the air distribution system. Conversely, during ground operation in a humid environment, the fresh air must be dehumidified before entering the mixing manifold. The dehumidification can be accomplished with two alternative solutions called the *low-pressure* or the *high-pressure water separation system*. In the low-

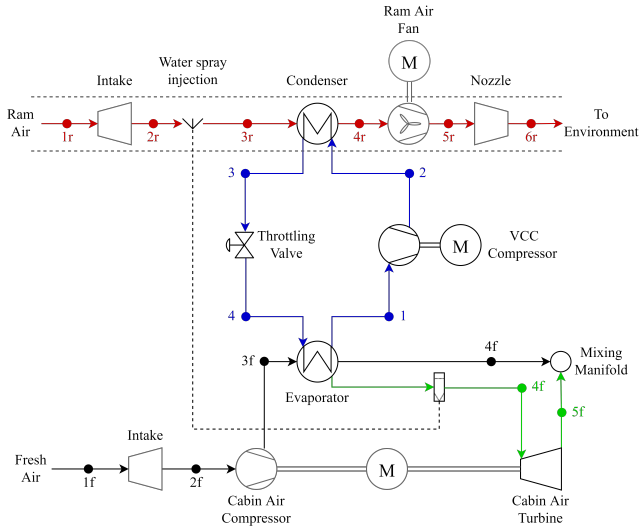


Figure 1.4: Simplified process flow diagram of an ECS based on the electrically-driven vapor compression cycle architecture. The cabin air stream, the ram air stream, and the refrigerant loop are displayed in black, red, and blue, respectively. The high-pressure dehumidification loop is highlighted in green. The dashed black line refers to water spray injection at ground conditions.

pressure system, water droplets are mechanically separated at the outlet of the ACM turbine by means of a swirl generator. Although this layout features fewer components and lower weight than the high-pressure system, it is not widely adopted, as it requires more frequent maintenance and it can lead to icing issues in the ACM turbine. In the high-pressure water separation loop, highlighted in green in Fig. 1.2, the water content in the fresh air is condensed and removed before entering the ACM turbine, thus avoiding the risk of icing. On the ram air side, the airflow is collected in the intake, is heated in the primary and secondary heat exchangers, and is discharged to the environment by means of a nozzle. During ground operations, the condensed water collected in the high-pressure water separation system is sprayed in the ram air stream after the intake, to increase its heat capacity. Moreover, when the aircraft is stationary, an axial fan is used to draw the air in the ram air duct and to overcome the pressure drops throughout the heat exchangers. To facilitate the reader's understanding, the thermodynamic diagram of an exemplary bleedless three-wheel bootstrap ACM sized for an Airbus A320 is displayed in Fig. 1.3 for both ground and flight operations.

A further reduction in the ECS power consumption can arguably be achieved by replacing the traditional ACM with an electrically-driven Vapor Compression Cycle (VCC) system, i.e., an inverse organic Rankine cycle system. The operating principle and the main components of an airborne VCC system are the same of heat pumps and industrial refrigeration systems. In recent years, the production and installation of domestic heat pumps have grown exponentially in developed countries, due to their superior thermodynamic performance over their fossil fuel-based counterpart. According to a recent study

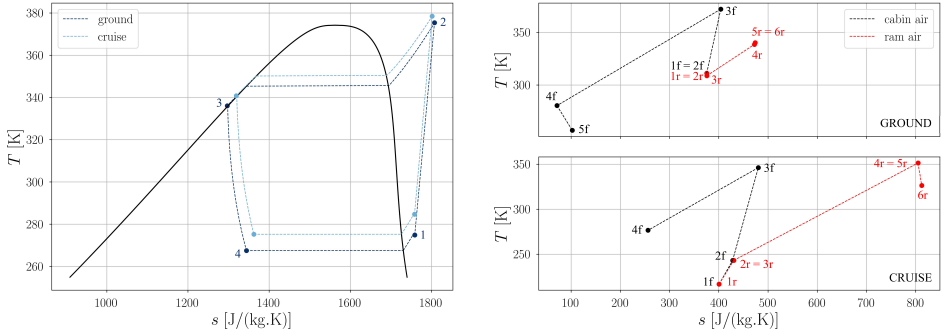


Figure 1.5: Thermodynamic diagram of an exemplary electrically-driven vapor compression cycle system sized for an Airbus A320, operating on the ground and in cruise conditions.

by the International Energy Agency [14], heat pumps currently available on the market are three to five times more energy efficient than natural gas boilers. Similarly, an ECS based on the VCC system features an efficiency value that is remarkably higher than the one associated with the traditional ACM. However, the adoption of this technology in the aerospace sector has been historically very limited, due to safety concerns regarding the toxicity and flammability of the working fluids used as refrigerants, as well as because of a lack of research specifically targeting airborne applications. An example of a single-pressure level VCC system for aircraft ECS is illustrated in Fig. 1.4. In the same fashion as for the bleedless ACM, the fresh air is first collected in the intake and then pressurized by the cabin air compressor. When the aircraft is flying and the dehumidification loop is bypassed, the CAC has only to provide the pressure ratio required for cabin pressurization, thus reducing the electric power demand as compared to the ACM layout. Next, the fresh air is cooled in the evaporator and is delivered to the mixing manifold. During ground operations, the fresh air stream is cooled in two steps. First, the fresh air is cooled in the evaporator down to the dew point¹, then the water content is progressively condensed and removed. Then, the dehumidified fresh air is expanded in a turbine and is finally delivered to the mixing manifold. In this scenario, the CAC has to provide a pressure ratio sufficient to allow for the expansion in the cabin air turbine and to simultaneously meet the temperature and pressure set points specified at the inlet of the mixing manifold. The simplest layout of the refrigerant loop consists of two compact heat exchangers, a compressor driven by an electric motor, and a throttling valve. The pressure ratio provided by the refrigerant compressor increases with the temperature lift, i.e., the difference between the condensation and the evaporation temperatures. In turn, if the temperature difference between the thermal energy source and the thermal energy sink is high, it is necessary to adopt a multi-stage compressor to meet the required pressure ratio. In this case, it is possible to adopt a more advanced VCC configuration featuring multiple pressure levels. Such system layout features a higher Coefficient of Performance (COP), defined as the evaporator heat duty divided by the power absorbed by the refrigerant compressor, at

¹Saturation temperature of water at its partial pressure in moist air

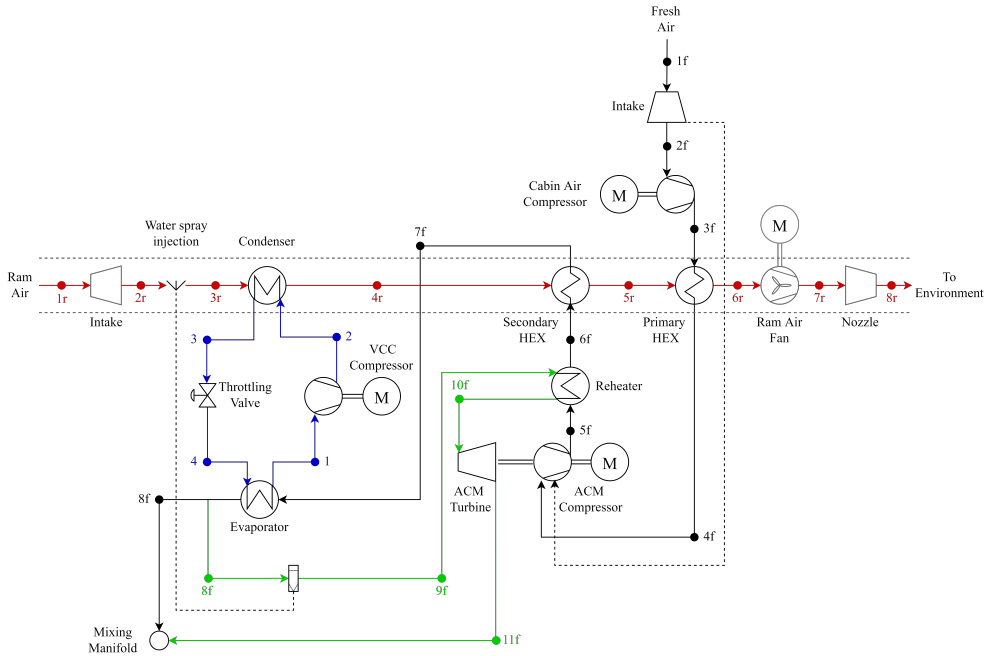


Figure 1.6: Simplified process flow diagram of an ECS featuring a hybrid air cycle machine-vapor compression cycle architecture. The cabin air stream, the ram air stream, and the refrigerant loop are displayed in black, red, and blue, respectively. The high-pressure dehumidification loop is highlighted in green. The dashed black lines refer to the water spray injection and the bypass fresh air stream used at ground conditions.

the expense of higher complexity, thus possibly weight and volume, and a higher number of components. On the ram air side, the thermodynamic processes are the same as the ones occurring in the bleedless ACM system, whereby the primary and secondary heat exchangers are replaced by the condenser. For the sake of clarity, Fig. 1.5 shows the thermodynamic diagram of an exemplary single-pressure level VCC system sized for an Airbus A320, operating both at ground and cruise conditions.

An alternative strategy aimed at reducing the fuel consumption of the ECS consists in combining the ACM and the VCC system in a hybrid architecture. This concept has been investigated by the DLR [8], and the technology is under development in the framework of an on-going collaboration between Airbus and Liebherr [15]. The simplified process flow diagram of one of the hybrid ACM-VCC configurations under scrutiny is displayed in Fig. 1.6. In this layout, adapted from [8], the heat load is split between the ACM and the VCC system as follows. During ground operation, cabin pressurization is not required, thus the CAC and the primary heat exchanger are bypassed by the fresh air stream. As a result, cabin air conditioning is achieved by means of the secondary heat exchanger and the evaporator of the VCC system. When the aircraft is flying, the fresh air stream is cooled by the primary and secondary heat exchangers of the bleedless ACM, and by the evaporator of the VCC system, while the ACM turbine is bypassed. In this way, neither the heat exchangers of the ACM nor the refrigerant loop need to be oversized to guarantee proper

operation in the extreme operating points of the ECS. As a result, the complexity and the number of components characterizing the VCC system can be minimized by adopting a single-pressure level inverse organic Rankine cycle.

1.2. HIGH-SPEED CENTRIFUGAL COMPRESSORS

Centrifugal compressors belong to a class of pressure-producing devices known as turbo-compressors. As in other turbomachines, the energy needed to pressurize the fluid is transferred by means of the dynamic interaction between a rotating component, i.e., the impeller, and a continuous flow of working fluid [16]. However, as opposed to axial compressors, centrifugal compressors feature an axial inlet and a fully radial discharge. Moreover, they generally deliver a higher pressure ratio per stage and are characterized by a lower flow capacity than their axial counterpart. Upon the industrial revolution at the end of the 19th century, centrifugal compressors have been progressively adopted in the metallurgical, chemical, and petrochemical sectors, as well as in the gas and pipeline industry. During the first half of the 20th century, Whittle and von Ohain independently developed the world's first jet engines. Both pioneers resorted to centrifugal compressor technology. Nowadays, the civil aviation sector is dominated by axial compressors. However, centrifugal compressors still find widespread application in aviation whenever higher power density is needed, i.e., small aircraft engines, helicopter engines, and APUs for all types of aircraft [17]. The recent advancements in the field of high-speed permanent magnet electric motors [18] have triggered the development of miniature high-speed centrifugal compressors. The possible applications of this technology include heat pumps [19], mini gas turbines [20], cryogenic coolers based on the inverse Brayton cycle [21], fuel cell air management systems and electrical supercharging [22]. Schiffmann et al. recently demonstrated the technical feasibility of an efficient small-scale centrifugal compressor for domestic heat pump applications [19], [23]. Conversely, the adoption of this technology for airborne applications is still limited to research projects and technology development programs by OEMs, such as Liebherr.

In the framework of the NEDEFA project, a new experimental facility has been designed and commissioned at the Propulsion and Power Laboratory of Delft University of Technology. The objective is to study the performance and operational advantages deriving from the adoption of a VCC system powered by a high-speed centrifugal compressor for next-generation ECS. The process flow diagram of the test rig, named IRIS (Inverse organic Rankine Integrated System), is shown in Fig. 1.7. The experimental facility consists of a two-pressure levels refrigeration cycle operating with refrigerant R1233zd(E), sized to comply with the load requirements of the ECS of a large passenger helicopter, i.e., 19 passengers and 2 pilots. The VCC system layout features an intercooler at the intermediate pressure level to increase the subcooling degree of the refrigerant stream at the inlet of the evaporator, thus the available latent heat of evaporation, and ultimately the COP. Moreover, the test rig entails a heat exchanger test bed, designed to characterize the performance of different condenser configurations. The test section is equipped with pressure transducers and temperature rakes to measure the pressure drop across the condenser and record the temperature profiles at the inlet and outlet sections. In the commissioning phase, the prescribed condenser topology consists of a bundle of flat tubes with an internal microchannel structure, and louver fins on the external surface. The temperature

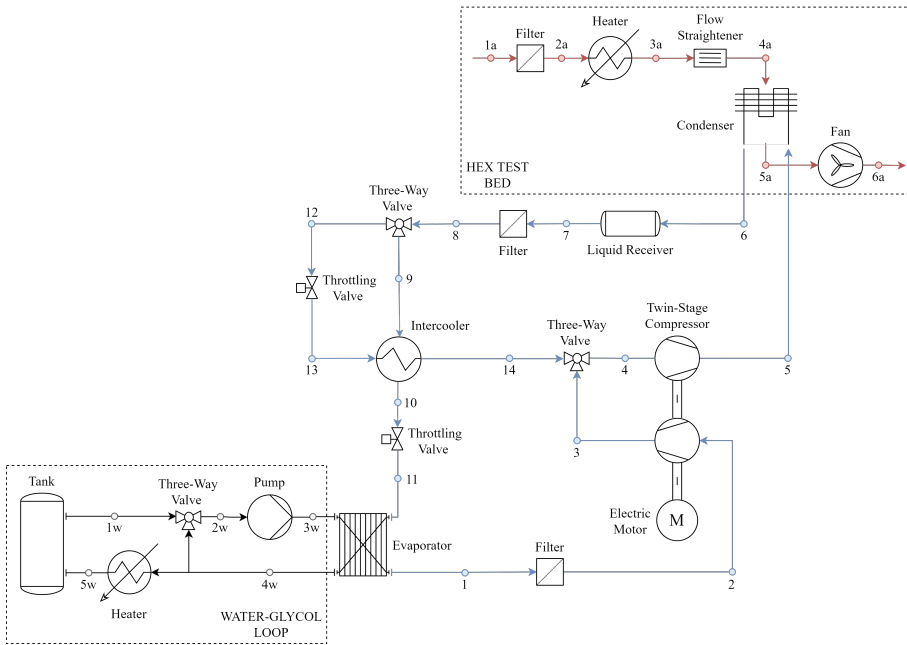


Figure 1.7: Process flow diagram of the IRIS test rig. The air stream, the refrigerant stream, and the water-glycol loop are displayed in red, blue, and black respectively.

of the incoming air is controlled by an electric heater and can be varied between 20 and 50°C, to reproduce different environmental conditions. The evaporator features a plate heat exchanger topology, to comply with space limitations and simplify the system layout. A water-glycol loop, an electric heater, and an electrically-actuated three-way valve are used to tightly control the temperature of the heat source.

At the core of the IRIS test rig there is a high-speed twin-stage centrifugal compressor, featuring two compressor wheels mounted back-to-back on the same shaft, and running on foil bearings, lubricated by the refrigerant vapor. A multi-stage configuration of the compressor is mandatory given the high pressure ratio needed to attain the prescribed maximum temperature lift, which is of the order of 60°C in extreme hot weather conditions. Moreover, the adoption of a back-to-back impeller configuration is dictated by the necessity to minimize the axial thrust acting on the foil bearings. The compressor is equipped with pressure and temperature sensors at the inlet and outlet sections, as well as with a Coriolis flow meter, to accurately measure the mass flow rate and evaluate the compressor operating envelope. The main drivers for the use of high-speed centrifugal compressors in place of standard volumetric machines for airborne VCC systems are: i) the potential for reaching higher compressor efficiency, thus higher COP; ii) the overall volume and weight reduction; iii) the absence of lubricant oil in the circuit, due to the adoption of foil bearings [24]. To showcase the downsizing capabilities offered by this technology, a qualitative comparison between the size of a centrifugal compressor prototype realized by the industrial partner Aeronamic BV and an equivalent volumetric machine is displayed

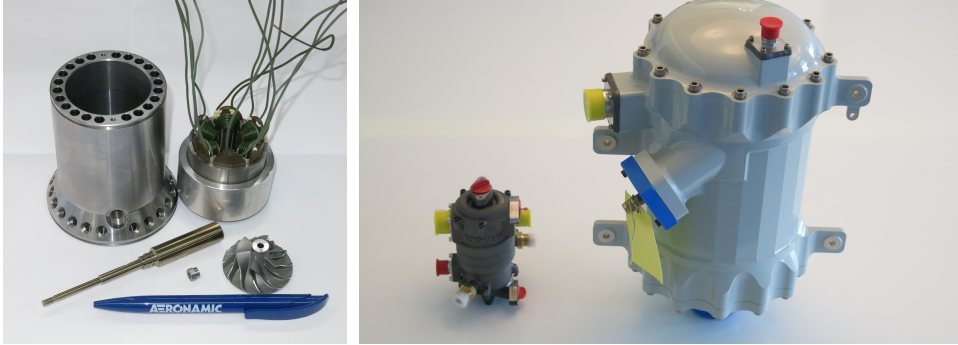


Figure 1.8: Compressor prototype operating with refrigerant R134a developed by Aeronamic BV. The figure on the right displays a size comparison between the prototype and a volumetric machine of equivalent power rating.

in Fig. 1.8.

The operating envelope of the VCC system is limited by the choke and stall margins of the compressor, and the COP is directly proportional to the efficiency of the turbomachine, as shown in Fig. 1.9. Moreover, once the temperature levels of the VCC system are fixed, the use of a more efficient compressor leads to a reduction of the condenser heat load, as displayed on the right chart of Fig. 1.9. In turn, this allows the design of a more compact and lightweight condenser unit. As a result, the requirements for the optimal design of high-speed centrifugal compressors are high efficiency, wide operating range, and high power density. Furthermore, the design must comply with strict constraints on the minimum impeller dimensions for manufacturability, the maximum allowable rotational speed for structural integrity and compatibility with the electric motor, and the maximum tolerable axial thrust, to enable the use of gas bearings. Moreover, the design of a twin-stage compressor involves additional consideration regarding the split of the pressure ratio among the two stages, the balance of axial thrust, the cooling of the bearings, and that of the electric motor. Finally, the selection of the optimal compressor design variables is influenced by the choice of the working fluid, which, in turn, is dictated by the design requirements of the heat pump system [25]. As a result, an ad hoc strategy based on novel design guidelines is needed to tackle the optimal design of these unconventional turbomachines.

1.3. MOTIVATION

The performance of the ECS is strongly affected by that of its components, i.e., heat exchangers and turbomachines [26], which in turn is strongly interdependent. Therefore, the optimal design of the system can be arguably achieved only by resorting to an integrated design approach, i.e., a framework in which the design of the system and the main components is optimized simultaneously. This is enabled by the continuous improvement of computational power and by the latest developments in modeling science, as documented in this dissertation. However, this aspect is often overlooked and the ECS is commonly designed adopting a top-down approach. In this case, the conceptual design of the system is tackled first, and the design of the main components is performed at a

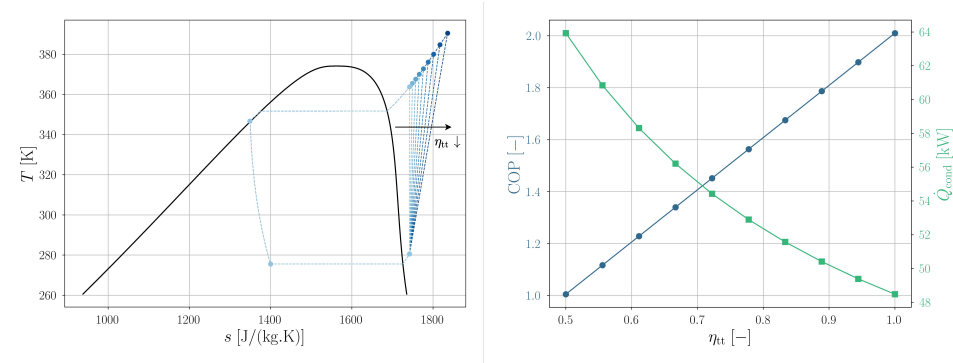


Figure 1.9: Influence of the compressor efficiency on the performance of an exemplary single-pressure level VCC system. The pressure ratio and the refrigerant mass flow rate are set to $\beta_{tt} = 8$ and $\dot{m} = 0.35$ kg/s, whereas the evaporation and condensation temperatures are equal to $T_{eva} = 275.6$ K and $T_{cond} = 351.8$ K, respectively.

later stage, without any coupling between the two design steps. The consequence thereof is the attainment of a sub-optimal design. In addition to the design philosophy, multiple trade-offs must be accounted for when comparing the performance of different ECS architectures. For this purpose, it is necessary to identify and evaluate the metrics that have the highest influence on the reduction of aircraft fuel consumption, the ultimate objective. For an electrically-driven ECS, these are the total electric power consumption, the weight of the system, and the drag penalty associated with the presence of the intakes and the pressure drop in the ram air duct. Furthermore, the ECS is characterized by a broad operating envelope, ranging from cruise operation to extreme operating points, such as ground operation on a very hot and humid day, and flight operation in the presence of a faulty ECS pack. As a result, the design of a novel ECS configuration implies the solution of a multi-objective, multi-point optimal design problem.

A pioneering application of the integrated design method for the optimization of a simplified ECS configuration is documented in [27]. Following this work, numerous attempts have been made to apply the integrated design approach to more complex and more realistic ECS configurations. In [28], the authors performed a multi-objective optimization of a two-wheel bootstrap ACM, including the design of the two offset strip fin heat exchangers. The objectives selected for the optimization were the minimization of the volume of the heat exchangers, and the minimization of the total entropy generation at cruise conditions. The study has been subsequently extended to include a thermo-economic analysis, as documented in [29]. More recently, an unconventional ECS architecture, featuring a hybrid ACM-VCC system, has been targeted for a multi-objective optimization [30]. In this work, the ECS has been simulated under three different operating conditions, and the Specific Fuel Consumption (SFC) has been computed as a weighted average of the values obtained in the three scenarios. In [31], the authors performed a multi-objective optimization of a three-wheel bootstrap ACM, including the high-pressure water separation loop. The objectives of the optimization were the minimization of the entropy generation rate and of the Number of Transfer Units (NTU).

All the aforementioned studies have targeted conventional or hybrid ACM configura-

tions, focusing the modeling effort on the heat exchangers. However, in a VCC system featuring a high-speed centrifugal compressor operating with gas bearings, the most critical component of the system is arguably the compressor. In light of the above, the scope of the research documented in this dissertation is twofold.

- The advancement of the state-of-the-art regarding high-speed centrifugal compressors, with emphasis on the development of new guidelines for the optimal preliminary design of single and twin-stage machines, and their application to the fluid dynamic design of the compressor for the IRIS test rig.
- The development of an automated integrated design framework for aircraft ECS, suitable for both ACM, VCC-based, and hybrid configurations, embedding a multi-point and multi-objective optimization strategy.

The design methods described in this dissertation are intended to support aircraft manufacturers in the early stage of development of novel electrically-driven ECS for next-generation aircraft. However, the potential impact of this work is not limited to the aviation sector. According to [32], heat is the largest energy end-use, accounting for 50% of the global energy consumption in 2018 and contributing to 40% of global CO₂ emissions. In that year, about 50% of the total heat produced was used for industrial processes, another 46% was consumed in buildings for space and water heating, while the remainder was used in agriculture, essentially for greenhouse heating. Heating in buildings requires relatively low temperature levels - 30°C for floor space heating and 60°C for tap water - therefore making heat pumps a valuable alternative to the burning of fossil fuels in domestic heaters. Moreover, as reported in [33], high-temperature heat pumps - inverse Rankine cycle systems featuring heat sink temperatures above 100°C - are suitable for waste heat recovery in various industrial processes such as drying, sterilization, evaporation, paper-making, or food preparation. In this context, the design methodologies developed and documented in this work can be applied to enhance the energy efficiency of heat pumps and to further promote their adoption in the industrial and residential sectors. In addition to the mitigation of the climate crisis, the widespread adoption of heat pumps could play a central role in addressing the energy security issue, reducing the European Union's reliance on the Russian natural gas supply.

1.4. ORIGINAL CONTRIBUTIONS

The original contributions documented in this dissertation can be summarized as follows:

- A methodology for the preliminary design optimization of single-stage and twin-stage centrifugal compressors has been conceptualized, developed, implemented and validated against experimental data available in the scientific literature. The method can be used to design centrifugal compressors operating with arbitrary working fluids in ideal and non-ideal thermodynamic states. The novel design tool has been used to tackle the preliminary design of the twin-stage compressor to be installed in the IRIS test rig. The method is coded in Python and is part of *TurboSim*, i.e., an in-house software suite for the conceptual design of unconventional turbomachinery, developed and maintained by the Propulsion and Power group of Delft University of Technology.

- A dynamic thermal model of the pressurized compartments of passenger aircraft has been developed and implemented using the Modelica acausal modeling language. The model has been validated against proprietary data provided by Airbus, one of the industrial partners in the project, and will be released open-source upon publication of the fourth chapter of this dissertation.
- A novel integrated framework for the design optimization of aircraft ECS has been created by coupling the system models developed in Modelica with the Turbosim compressor module. The multi-point and multi-objective optimization of the ECS is tackled by combining the capabilities of open-source optimization packages available in Python with in-house implementations tailored to the prescribed application.
- A data-driven model for the design of high-speed centrifugal compressors has been created by leveraging the open-source TensorFlow package. The dataset has been generated by means of the validated TurboSim compressor module. The data-driven model has been coupled to the optimization framework for aircraft ECS in order to reduce its computational cost and improve its robustness.

1.5. OUTLINE

This dissertation contains material presented at international conferences or published in peer-reviewed international journals. It is structured in seven chapters and the content of the following chapters is summarized below.

Chapter 2 documents the development and validation of a conceptual design tool tailored to high-speed centrifugal compressors. The compressor model has been used to derive new design guidelines for single-stage centrifugal compressors, with emphasis on the impact of the machine size and the working fluid on the efficiency, operating range, and magnitude of axial thrust acting on the gas bearings. To corroborate the validity of the proposed design guidelines, the multi-objective optimization of a compressor stage resembling the first stage of the IRIS test rig has been performed as a design exercise.

Chapter 3 reports the extension of the conceptual design tool to address the design of twin-stage compressors, featuring two impellers mounted in back-to-back configuration on the same shaft. The design guidelines for single-stage compressors have been extended, focusing on the choice of the optimal split of pressure ratio among the two stages. In addition, the novel design method has been applied to perform the fluid dynamic design optimization of the twin-stage centrifugal compressor which will be installed in the IRIS test rig.

Chapter 4 addresses the development of a dynamic thermal model of the pressurized areas of passenger aircraft. The objective is to compute the operating envelope of the ECS, given a limited set of data related to the aircraft configuration and the flight mission. Moreover, the chapter documents the model validation against proprietary data provided by Airbus and two examples of applications.

Chapter 5 introduces a novel integrated design methodology for aircraft ECS, which includes the conceptual design of the compact heat exchangers and the centrifugal compressors within the system-level design. The proposed design framework has been applied to the multi-objective, multi-point optimization of the ECS of an Airbus A320, accounting for the minimization of the electric power consumption, weight, and drag penalty associated with the ram air. The system architectures selected for this study are the bleedless three-wheel bootstrap ACM and the electrically-driven VCC system. At the end of the chapter, the optimal design of the two ECS configurations is compared and the performance advantage deriving from the adoption of an electrically-driven VCC system is evaluated.

Chapter 6 focuses on the increased computational cost and the deteriorated convergence properties of the numerical solver encountered when tackling the integrated design optimization of a complex system, such as the ECS of a passenger aircraft. To address these issues, a data-driven surrogate model of the centrifugal compressor was developed and coupled to a modified version of the integrated design framework described in Chapter 5. The capabilities of the proposed methodology are demonstrated by performing the multi-objective optimization of an electrically-driven VCC system with and without the use of the data-driven compressor model.

Chapter 7 summarizes the main findings of this research, outlining the current limitations of the proposed methodology, and providing an outlook for future work.

BIBLIOGRAPHY

- [1] W. J. Ripple, C. Wolf, T. M. Newsome, *et al.*, “World Scientists’ Warning to Humanity: A Second Notice”, *BioScience*, vol. 67, no. 12, pp. 1026–1028, Dec. 2017, ISSN: 0006-3568. DOI: 10.1093/biosci/bix125.
- [2] M. Astolfi, M. Baresi, J. van Buijtenen, *et al.*, “Thermal Energy Harvesting - The Path to Tapping into a Large CO₂-free European Power Source”, Knowledge Center on Organic Rankine Cycle technology – KCORC, Tech. Rep., 2022.
- [3] H. Ritchie, M. Roser, and P. Rosado, “Energy”, *Our World in Data*, 2022, <https://ourworldindata.org/energy>.
- [4] “Aviation”, International Energy Agency (IEA), Tech. Rep., 2022.
- [5] “Strategic Research and Innovation Agenda”, Advisory Council for Aviation Research and Innovation in Europe (ACARE), Tech. Rep., 2017.
- [6] M. Andrew, S. Valentin, E. Thomas, *et al.*, “Roadmap to Climate Neutral Aviation in Europe”, Transport and Environment, Tech. Rep., 2022.
- [7] P. W. Wheeler, J. C. Clare, A. Trentin, and S. Bozhko, “An overview of the more electrical aircraft”, *Proceedings of the Institution of Mechanical Engineers, Part G: Journal of Aerospace Engineering*, vol. 227, no. 4, pp. 578–585, Dec. 2012, ISSN: 09544100. DOI: 10.1177/0954410012468538.
- [8] D. Bender, “Exergy-based analysis of aircraft environmental control systems and its integration into model-based design”, Ph.D. dissertation, Technische Universität Berlin, 2018. DOI: 10.14279/DEPOSITONCE-8101.
- [9] M. Dechow and C. Nurcombe, “Aircraft Environmental Control Systems”, in *Air Quality in Airplane Cabins and Similar Enclosed Spaces*, M. Hocking, Ed., Berlin, Heidelberg: Springer Berlin Heidelberg, 2005, pp. 3–24, ISBN: 978-3-540-31491-2. DOI: 10.1007/b107234.
- [10] “Aircraft”, in *ASHRAE Handbook - Heating, Ventilating, and Air-Conditioning Applications*, American Society of Heating, Refrigerating and Air-Conditioning Engineers - ASHRAE, 2019, ISBN: 978-1-947192-13-3.
- [11] A. Pollok, “Modelling and control of aircraft environmental control systems”, Ph.D. dissertation, Politecnico di Milano, 2018.
- [12] D. S. Lee, D. W. Fahey, A. Skowron, *et al.*, “The contribution of global aviation to anthropogenic climate forcing for 2000 to 2018”, *Atmospheric Environment*, vol. 244, p. 117834, Jan. 2021, ISSN: 1352-2310. DOI: 10.1016/j.atmosenv.2020.117834.
- [13] Boeing, “AERO magazine, 4th quarter”, 2007.
- [14] “The Future of Heat Pumps”, International Energy Agency (IEA), Tech. Rep., 2022.
- [15] S. A. Schmidt, J. Riedel, F. Hepcke, *et al.*, “New air systems for more electric aircraft”, in *MEA2021, More Electric Aircraft - Towards Cleaner Aviation*, Bordeaux, France, Oct. 2021.
- [16] H. Krain, “Review of centrifugal compressor’s application and development”, *Journal of Turbomachinery*, vol. 127, no. 1, pp. 25–34, Jan. 2005, ISSN: 0889504X. DOI: 10.1115/1.1791280.
- [17] D. P. Kenny, “The History and Future of the Centrifugal Compressor in Aviation Gas Turbines”, *SAE Technical Papers*, Oct. 1984, ISSN: 0148-7191. DOI: 10.4271/841635.
- [18] C. Zwyssig, J. W. Kolar, and S. D. Round, “Megaspeed drive systems: Pushing beyond 1 million r/min”, *IEEE/ASME Transactions on Mechatronics*, vol. 14, no. 5, pp. 564–574, 2009, ISSN: 10834435. DOI: 10.1109/TMECH.2008.2009310.
- [19] J. Schiffmann and D. Favrat, “Experimental investigation of a direct driven radial compressor for domestic heat pumps”, *International Journal of Refrigeration*, vol. 32, no. 8, pp. 1918–1928, Dec. 2009, ISSN: 01407007. DOI: 10.1016/j.ijrefrig.2009.07.006.

-
- [20] P. A. Pilavachi, "Mini- and micro-gas turbines for combined heat and power", *Applied Thermal Engineering*, vol. 22, no. 18, pp. 2003–2014, Dec. 2002, ISSN: 1359-4311. DOI: 10.1016/S1359-4311(02)00132-1.
- [21] M. V. Zagarola and J. A. McCormick, "High-capacity turbo-Brayton cryocoolers for space applications", *Cryogenics*, vol. 46, no. 2-3, pp. 169–175, Feb. 2006, ISSN: 0011-2275. DOI: 10.1016/J.CRYOGENICS.2005.11.018.
- [22] M. V. Casey, D. Krähenbühl, and Z. Christof, "The Design of Ultra-High-Speed Miniature Centrifugal Compressors", in *European Conference on Turbomachinery Fluid Dynamics and Thermodynamics*, 2013.
- [23] J. Schiffmann and D. Favrat, "Design, experimental investigation and multi-objective optimization of a small-scale radial compressor for heat pump applications", *Energy*, vol. 35, no. 1, pp. 436–450, Jan. 2010, ISSN: 03605442. DOI: 10.1016/j.energy.2009.10.010.
- [24] H. Heshmat, J. F. Walton, C. D. Corte, and M. Valco, "Oil-free turbocharger demonstration paves way to gas turbine engine applications", in *Proceedings of the ASME Turbo Expo*, vol. 1, American Society of Mechanical Engineers (ASME), Aug. 2000, ISBN: 9780791878545. DOI: 10.1115/2000-GT-0620.
- [25] A. Giuffré, P. Colonna, and M. Pini, "The Effect of Size and Working Fluid on the Multi-Objective Design of High-Speed Centrifugal Compressors", *International Journal of Refrigeration*, vol. 143, pp. 43–56, Nov. 2022, ISSN: 0140-7007. DOI: 10.1016/J.IJREFRIG.2022.06.023.
- [26] H. Yang and C. Yang, "Application of scaling-endoreversible thermodynamic analysis model to aircraft environmental control system-methodology development", *International Journal of Refrigeration*, vol. 112, pp. 90–99, Apr. 2020, ISSN: 0140-7007. DOI: 10.1016/J.IJREFRIG.2019.12.006.
- [27] J. V. Vargas and A. Bejan, "Integrative thermodynamic optimization of the environmental control system of an aircraft", *International Journal of Heat and Mass Transfer*, vol. 44, no. 20, pp. 3907–3917, Oct. 2001, ISSN: 0017-9310. DOI: 10.1016/S0017-9310(01)00033-3.
- [28] I. Pérez-Grande and T. J. Leo, "Optimization of a commercial aircraft environmental control system", *Applied Thermal Engineering*, vol. 22, no. 17, pp. 1885–1904, Dec. 2002. DOI: 10.1016/S1359-4311(02)00130-8.
- [29] T. J. Leo and I. Pérez-Grande, "A thermoeconomic analysis of a commercial aircraft environmental control system", *Applied Thermal Engineering*, vol. 25, no. 2-3, pp. 309–325, Feb. 2005, ISSN: 1359-4311. DOI: 10.1016/J.APPLTHERMALENG.2004.06.011.
- [30] M. Sielemann, T. Giese, B. Oehler, and M. Gräber, "Optimization of an Unconventional Environmental Control System Architecture", *SAE International Journal of Aerospace*, vol. 4, no. 2, pp. 1263–1275, Oct. 2011, ISSN: 1946-3855. DOI: 10.4271/2011-01-2691.
- [31] Z. Duan, H. Sun, C. Wu, and H. Hu, "Multi-objective optimization of the aircraft environment control system based on component-level parameter decomposition", *Energy*, vol. 245, p. 123 330, Apr. 2022, ISSN: 0360-5442. DOI: 10.1016/J.ENERGY.2022.123330.
- [32] "Renewables - Heat", International Energy Agency (IEA), Tech. Rep., 2019.
- [33] C. Arpagaus, F. Bless, M. Uhlmann, J. Schiffmann, and S. S. Bertsch, "High temperature heat pumps: Market overview, state of the art, research status, refrigerants, and application potentials", *Energy*, vol. 152, pp. 985–1010, Jun. 2018, ISSN: 0360-5442. DOI: 10.1016/J.ENERGY.2018.03.166.

2

DESIGN GUIDELINES FOR HIGH-SPEED CENTRIFUGAL COMPRESSORS

*Look up at the stars and not down at your feet.
Try to make sense of what you see, and wonder about what makes the universe exist.
Be curious.*

Stephen Hawking

Parts of this chapter have been published in:

A. Giuffre', P. Colonna, and M. Pini, "The Effect of Size and Working Fluid on the Multi-Objective Design of High-Speed Centrifugal Compressors", *International Journal of Refrigeration*, vol. 143, pp. 43-56, 2022, ISSN: 0140-7007. DOI: 10.1016/j.ijrefrig.2022.06.023.

Abstract

The impact of size and working fluid on the efficiency, operating range, and axial thrust on bearings is examined for high-speed, oil-free centrifugal compressors. First, the development and validation of a reduced-order model based on scaling principles for the design, analysis, and optimization of single-stage compressors are documented. Then, the validated compressor model is used to generate design maps for stages operating with arbitrary fluid molecules, and characterized by different sizes. The results show that compressors operating with fluids made by heavy and complex molecules provide lower efficiency over the entire design space if compared to their simple-molecule counterparts. However, compressors for complex-molecule fluids require lower rotational speed and generate lower axial thrust on the bearings, thus making them particularly suitable for small-scale applications. Furthermore, a decreasing value of the size parameter has a detrimental effect on the stage efficiency, as a result of manufacturing constraints. The results computed by the compressor model suggest that the efficiency penalty is more sensitive to variations of clearance gap than to surface finishing. Lastly, the reduced-order model has been used to perform a design exercise, i.e., the multi-objective optimization of a compressor stage resembling the first stage of the vapor compression cycle test rig being realized at the Delft University of Technology. The key characteristics of the optimal compressor design have been compared to those derived from the design maps, to corroborate their validity. The optimal design has been extensively characterized by means of CFD, providing further evidence that efficient high-speed compressors operating with organic fluids, and featuring pressure ratios up to five at off-design, are feasible.

2.1. INTRODUCTION

THE recent advancements in the field of high-speed permanent magnet electric motors [1] have triggered the development of miniature high-speed centrifugal compressors, i.e., machines featuring an impeller tip diameter as small as 20 mm, and a rotational speed as high as 200 krpm. The possible applications of this technology include heat pumps [2], mini gas turbines [3], cryogenic coolers based on the inverse Brayton cycle [4], fuel cell air management systems, and electrical supercharging [5]. Schiffmann et al. recently demonstrated the technical feasibility of an efficient small-scale centrifugal compressor for domestic heat pump applications [2], [6]. The adoption of an electrically-driven heat pump, featuring a twin-stage, high-speed centrifugal compressor, for the environmental control system (ECS) of next-generation aircraft is currently under investigation at Delft University of Technology. The main drivers for the use of high-speed centrifugal compressors in place of standard volumetric machines for airborne heat pumps are: i) the potential for reaching higher compressor efficiency, thus higher COP; ii) the overall volume and weight reduction; iii) the absence of lubricant oil in the circuit, due to the adoption of foil bearings [7].

The requirements for the optimal design of mini centrifugal compressors are high efficiency, wide operating range, and high power density. On top of that, the design must comply with strict constraints on the minimum impeller dimensions for manufacturability, the maximum allowable rotational speed, and on the maximum tolerable axial thrust, to enable the use of gas bearings. As demonstrated by Casey et al. [5], halving the impeller outlet diameter, while keeping the mass flow rate constant, i.e., shifting towards an

impeller design featuring a larger swallowing capacity

$$\phi_{t1} = \frac{\dot{m}}{\rho_{t1} U_2 D_2^2}, \quad (2.1)$$

leads to an increase in power density by a factor of eight. More compact stages entail lower material and machining costs, lower weight and inertia, and a smaller frontal area, thus a lower axial thrust. In contrast, a reduction of the impeller outlet diameter at a constant work coefficient

$$\psi = \frac{\Delta h_{tt}}{U_2^2}, \quad (2.2)$$

can lead to an increase of rotational speed up to the mechanical limits of the impeller material. Moreover, compressor downsizing comes at the expense of larger friction and clearance losses, due to the increase of relative surface roughness and relative clearance at the blade tip.

The selection of the optimal compressor design parameters is further complicated by the choice of the working fluid, which, in turn, is dictated by the design requirements of the heat pump. As an illustrative example, consider two stages providing the same total-to-total pressure ratio $\beta_{tt} = 3$, but operating with two different fluids: hydrogen and refrigerant R134a. The isentropic work performed by a compressor stage operating with an arbitrary working fluid can be expressed as

$$\Delta h_{tt,is} = \frac{a_{t1}^2}{\overline{\gamma_{Pv}} - 1} \left(\beta_{tt}^{\frac{\overline{\gamma_{Pv}} - 1}{\overline{\gamma_{Pv}}}} - 1 \right), \quad (2.3)$$

where $\overline{\gamma_{Pv}}$ is the average value of the isentropic pressure-volume exponent [8], defined as

$$\gamma_{Pv} = - \frac{v}{P} \frac{\partial P}{\partial v} \Big|_s = - \frac{v}{P} \frac{c_p}{c_v} \frac{\partial P}{\partial v} \Big|_T, \quad (2.4)$$

$$\overline{\gamma_{Pv}} = \frac{\ln \left(\frac{P_{in}}{P_{out}} \right)}{\ln \left(\frac{\rho_{in}}{\rho_{out}} \right)}. \quad (2.5)$$

In Eqn (2.5), the subscripts in and out correspond to the initial and final states of the thermodynamic transformation. In dilute gas conditions, the average value of the isentropic pressure-volume exponent resembles the one of the heat capacity ratio computed under the assumption of ideal gas, denoted by γ_∞ in Tab. 2.1. On the other hand, when operating in the dense gas region, e.g., in the proximity of the critical point, the fluid properties exhibit a departure from the ideal gas behavior, which can be detected by the deviation between the values of $\overline{\gamma_{Pv}}$ and γ_∞ . By combining Eqn. (2.4) and Eqn. (2.2), the impeller tip speed Mach number $M_{U_2} = U_2 / a_{t1}$ can be correlated to the pressure ratio of the stage as

Table 2.1: Fluid properties and total inlet conditions specified in the reduced-order model to create the design maps presented in Section 2.4.

Fluid	P_{t1} [bar]	T_{t1} [K]	$R \left[\frac{J}{kg \cdot K} \right]$	M/M_{air}	γ_∞	$\overline{\gamma_{Pv}}$
Argon	2.0	253.15	208.13	1.38	1.67	1.674
H ₂	1.2	103.15	4124.44	0.07	1.67	1.516
Air	2.5	308.15	287.05	1.00	1.40	1.402
CO ₂	1.5	283.15	188.92	1.52	1.29	1.271
R134a	0.55	243.15	81.49	3.52	1.09	1.095
R1233zd(E)	0.5	283.15	63.71	4.51	1.07	1.055

$$M_{U_2} = \sqrt{\frac{\frac{\overline{\gamma_{Pv}}^{-1}}{\beta_{tt}^{\overline{\gamma_{Pv}}} - 1}}{\psi(\overline{\gamma_{Pv}} - 1)}}. \quad (2.6)$$

Assuming that both compressor stages are designed at $\psi = 0.8$ and operate at the total inlet conditions specified in Tab. 2.1, the ratio of the peripheral speed at the impeller outlet for the two fluids reads

$$\frac{M_{U_2, H_2}}{M_{U_2, R134a}} = \frac{1.048}{1.147} = 0.91 \quad (2.7)$$

$$\frac{U_{2, H_2}}{U_{2, R134a}} = \frac{M_{U_2, H_2}}{M_{U_2, R134a}} \frac{a_{t1, H_2}}{a_{t1, R134a}} = 5.11.$$

As a consequence, the stage operating with hydrogen must be designed with a higher work coefficient, to keep the outlet peripheral speed below an acceptable threshold, at the expense of a fluid dynamic performance penalty. In this example, the two working fluids are in the dilute gas region, as testified by the values of $\overline{\gamma_{Pv}}$ and γ_∞ reported in Tab. 2.1. Therefore, the cause of the change in the impeller peripheral speed can be mostly attributed to the disparity in the molar mass of the two fluids.

2.2. OBJECTIVE

The typical procedure for the preliminary design of centrifugal compressors is described in [9]–[12]. A thorough attempt to devise design guidelines for large-scale centrifugal compressors operating with air and featuring vaned diffusers can be found in [13]. Extensive studies on similarity parameters used to characterize the off-design performance of compressors operating with non-ideal flows are documented in [14], [15]. The main implications related to the design of small-scale impellers featuring vaneless diffusers are qualitatively described in [16]. However, the aforementioned study is application-specific and, as such, it does not provide general design guidelines valid for compressors of different

scales and operating with arbitrary working fluids. The study documented here aims to bridge this knowledge gap by extending the work of Rusch and Casey [13]. The objective is to develop design maps for single-stage compressors, accounting for the influence of the fluid and the machine size on the stage efficiency, operating range, and the magnitude of the axial thrust acting on gas bearings. In particular, the influence of the fluid is related to both its molecular complexity and the thermodynamic conditions at which the compression process occurs, which may entail the flow to depart from the ideal gas behavior [17]. The applications in which the effect of flow non-ideality is relevant are arguably limited to compressors for high-temperature heat pumps and supercritical CO₂ cycles for power generation and refrigeration. Within the scope of the present work, only the influence of fluid molecular complexity is investigated. The design maps are generated by means of a reduced-order model based on scaling principles and validated with experimental data of reference compressors [6], [18]–[20], and with CFD simulation results.

Moreover, the reduced-order model is used to perform a design exercise, i.e., the multi-objective optimization of a compressor stage resembling the first stage of the heat pump test rig designed and commissioned at the Propulsion and Power Laboratory of the Delft University of Technology. The case study features a Pareto analysis, and a complete characterization of the fluid dynamic performance of the optimal design by means of CFD. To corroborate the validity of the proposed design guidelines, the key design variables selected by the optimizer, and the corresponding compressor performance metrics, are compared to the ones that can be derived from the design maps.

2.3. CONCEPTUAL DESIGN BASED ON SCALING PRINCIPLES

The main dimensions and performance metrics of a centrifugal compressor stage can be expressed as

$$\mathbf{y} = f(\phi_{t1}, \psi, \alpha_2, \beta, \overline{\gamma_{pv}}, Re, \boldsymbol{\sigma}), \quad (2.8)$$

where \mathbf{y} is a vector collecting the compressor characteristics and performance metrics. Several considerations can be drawn from Eqn. (2.8). The impeller flow angles are univocally determined by the swallowing capacity ϕ_{t1} , the work coefficient ψ_{is} , and the degree of reaction χ . Here, the degree of reaction is replaced by the absolute flow angle at the inlet of the diffuser α_2 , i.e., a parameter directly related to diffuser stability. The work provided by the impeller scales with the pressure ratio β and the thermodynamic behavior of the fluid, determined by the average value of γ_{pv} . The impact of the viscous effects is quantified by the average value of the Reynolds number within the impeller, diffuser, and volute. The vector $\boldsymbol{\sigma}$ contains basic information regarding the stage geometry, see Tab. 2.2. Few of the quantities composing $\boldsymbol{\sigma}$ are intentionally taken as dimensional parameters, because, when dealing with miniature turbomachinery, some geometrical features cannot be scaled due to limits of manufacturability. In Section 2.4.2 the effect of scale is investigated, by comparing compressor designs characterized by different dimensions, quantified by the value of the size parameter

$$SP = \frac{\dot{V}_1^{1/2}}{\Delta h_{ts}^{1/4}}, \quad (2.9)$$

Table 2.2: Specification of the compressor geometrical characteristics used in the reduced-order model, and collected in the vector σ . The values reported in the table are the ones prescribed in the reduced-order model to create the design maps presented in Section 2.4.

Description	Definition	Value
Impeller shape factor	$k = 1 - \left(\frac{R_{1,h}}{R_{1,s}}\right)^2$	0.9
Number of blades	$N_{bl} + N_{split}$	14
Diffuser radius ratio	R_3/R_2	1.5
Diffuser blade height ratio	H_3/H_2	0.85
Diffuser pinch radius ratio	R_{pinch}/R_2	1.3
Non-dimensional length	L_{ax}/R_2	0.7
Leading edge thickness	t_{le} [mm]	2-1-0.2
Trailing edge thickness	t_{te} [mm]	2-1-0.2
Impeller tip clearance	e_t [mm]	0.15
Back face clearance	e_b [mm]	0.15
Surface roughness	Ra [mm]	0.01

but featuring the same values of tip clearance and surface roughness.

The in-house reduced-order compressor model relies on the lumped parameters approach. The flow quantities and the main dimensions of the machine are evaluated at each streamwise station depicted in Fig. 2.1. The incoming flow is assumed to be axial and uniform, due to the absence of inlet guide vanes. At the impeller inlet, the flow quantities are evaluated at five different spanwise locations, to capture the free-vortex flow distribution. The relative flow angle at the impeller shroud is selected to minimize the local relative Mach number, following the methodology proposed by Rusch and Casey [13]. The effective blade count is defined as $N_{eff} = N_{bl} + 0.75N_{split}$. Splitter blades are considered in the calculations whenever the estimated throat length is smaller than a user-defined threshold, to ensure impeller manufacturability. The diffuser is assumed to be vaneless and pinched close to the inlet section, to delay rotating stall inception. The slip effect is accounted for by means of the unified model for axial, radial, and mixed-flow impellers proposed by Qiu et al. [21]. Unlike more established slip models [22]–[24], the method adopted in this work relies on the analysis of the blade loading to incorporate the effect of blade turning at the impeller discharge. As a result, the predictions of the slip factor are reliable also in presence of highly backswept blades, and in off-design conditions, as proven by the comparison with experimental data. The external volute is designed by resorting to the conservation equations, assuming no friction and no pressure gradient in the circumferential direction, as suggested in [25]. The thermo-physical fluid properties are evaluated by means of the reference thermodynamic library developed by NIST [26] and implemented in the open-source CoolProp library [27]. The axial thrust acting on gas bearings is estimated with the method reported in [28]:

$$F_{ax} = F_{in} + F_{imp} + F_s - F_{bd}, \quad (2.10)$$

where F_{in} and F_{imp} are the pressure and the impulse forces acting on impeller inlet, whereas F_s and F_{bd} refer to pressure forces acting on the shroud and the back disk, respectively.

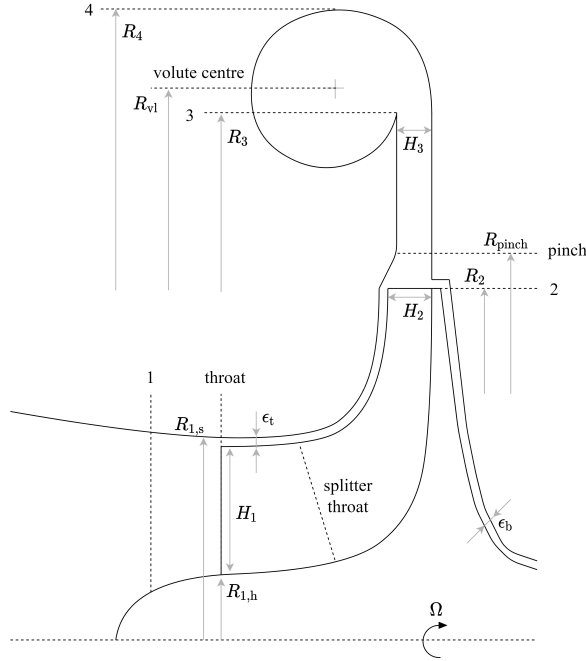


Figure 2.1: Meridional view of a centrifugal compressor stage featuring splitter blades, pinched vaneless diffuser, overhung volute, and no inlet guide vanes.

Within this model, the shaft is assumed to be of the cantilever type, and the impeller is assumed to have no radial labyrinth seals. The shaft radius is either an input from the user, or is expressed as a fraction of the impeller hub radius. The design maps presented in the following section were obtained by assuming a given fraction of the impeller hub radius, to preserve the effect of scaling.

The reduced-order model is complemented with a method for preliminary weight estimation. To compute the weight of the compressor assembly, the model is coupled to a Python library for the creation of parametric 3D CAD models [29]. Once the dimensions of the main components, i.e., impeller, shaft, vaneless diffuser, volute, and exit cone, are set, a preliminary CAD model is automatically generated. Next, the weight of each component is computed according to its volume and the prescribed material. Moreover, the weight of the electric motor is estimated based on the trends of power density for high-speed permanent magnet synchronous machines documented in [30]. The correlations implemented in the in-house model are derived by assuming optimal forced air cooling to keep the magnet temperature below the threshold of 150°C and are valid for rotor surface speeds up to 200 m/s and electrical powers as high as 1 MW.

2.3.1. LOSS MODELING

The compressor efficiency is evaluated as a function of the internal and external loss sources, expressed in terms of total enthalpy loss, namely

$$\eta_{tt} = \frac{w_{eul} - \Delta h_{t,int}}{w_{eul} + \Delta h_{t,ext}}. \quad (2.11)$$

The internal losses affect both the pressure ratio and the stage efficiency. The loss mechanisms that are not associated with the main flow are grouped in the so-called parasitic or external losses. They affect the stage efficiency, but they have no influence on the pressure ratio.

If the flow at the inlet of the impeller is supersonic, the entropy production associated with the presence of shock waves is accounted for by means of the model proposed by Denton [31], extended to non-ideal flows, i.e.,

$$\Delta s_{sw} = c_{v,1} \frac{2\overline{\gamma_{pv}}(\overline{\gamma_{pv}} - 1)}{3(\overline{\gamma_{pv}} + 1)^2} (M_{W1}^2 - 1)^3. \quad (2.12)$$

At off-design conditions, the incidence angle deviates from the estimated optimal value [9], and the associated efficiency loss is computed as [32]

$$\Delta h_{t,i} = \frac{W_1 \sin |i - i_{opt}|^2}{2}. \quad (2.13)$$

The impact of viscous friction on the impeller performance is evaluated by means of the model of Jansen [33]

$$\begin{aligned} \Delta h_{t,sf} &= 2C_f \frac{L_{hd}}{D_{hd}} \overline{W}^2 \\ \overline{W} &= \frac{V_{1,s} + V_2 + W_{1,s} + 2W_{1,h} + 3W_2}{8}, \end{aligned} \quad (2.14)$$

where the hydraulic length and diameter are expressed as

$$\begin{aligned} L_{hd} &= \frac{\pi}{8} (D_2 - (R_{1,s} + R_{1,h}) - H_2 + 2L_{ax}) \left(\frac{2}{\overline{\cos \beta_1} + \cos \beta_2} \right) \\ D_{hd} &= D_2 \left(\frac{\cos \beta_2}{\frac{N_{eff}}{\pi} + \frac{D_2 \cos \beta_2}{H_2}} + \frac{\frac{1}{2} \left(\frac{D_{1,s}}{D_2} + \frac{D_{1,h}}{D_2} \right) \overline{\cos \beta_1}}{\frac{N_{eff}}{\pi} + \left(\frac{D_{1,s} + D_{1,h}}{D_{1,s} - D_{1,h}} \right) \overline{\cos \beta_1}} \right) \\ \overline{\cos \beta_1} &= \frac{\cos \beta_{1,s} + \cos \beta_{1,h}}{2}, \end{aligned} \quad (2.15)$$

and the skin friction coefficient is computed according to the weighted average method proposed by Aungier [34]. The losses associated with diffusion in the blade passage are estimated as [35]

$$\Delta h_{t,bl} = 0.05 \cdot (D_f U_2)^2$$

$$D_f = 1 - \frac{W_2}{W_{1,s}} + \frac{0.75 \frac{|\Delta h_{tt}|}{U_2^2} \frac{W_2}{W_{1,s}}}{\frac{N_{\text{eff}}}{\pi} \left(1 - \frac{D_{1,s}}{D_2}\right) + 2 \frac{D_{1,s}}{D_2}}. \quad (2.16)$$

The total enthalpy loss due to tip clearance is calculated by means of the correlation introduced by Brasz [36]

$$\Delta h_{t,cl} = \frac{0.6 \epsilon_t |V_{\theta,2}|}{H_2 + \frac{\epsilon_t}{2}} \sqrt{\frac{4\pi |V_{\theta,2}| V_{m,1}}{\left(H_2 + \frac{\epsilon_t}{2}\right) N_{\text{eff}}} \cdot k_{cl}}$$

$$k_{cl} = \frac{R_{1,s}^2 - R_{1,h}^2}{(R_2 - R_{1,s}) \left(1 + \frac{\rho_2}{\rho_1}\right)}. \quad (2.17)$$

As will be discussed in Chapter 3, when dealing with miniature compressor stages, featuring high relative tip clearance gaps, e.g. exceeding 10%, the designer should account not only for a reduction of η_{tt} due to the detrimental effect of tip clearance but also for a decrease of β_{tt} . Such penalty is proportional to the relative tip gap and the work performed by the impeller, hence to the compression ratio. In the present work, the following empirical correction of the impeller work has been implemented in the in-house compressor model, to match the performance trends obtained with CFD

$$|\Delta h_{tt}| = |\Delta h_{tt, \text{no gap}}| \cdot \left(1 - 0.2 \frac{\epsilon_t}{H_2}\right). \quad (2.18)$$

The irreversibility associated with wake mixing at the impeller outlet is computed as [37]

$$\Delta h_{t, \text{mx}} = \frac{1}{1 + \tan^2(\alpha_2)} \left(\frac{1 - \epsilon_w - H^*}{1 - \epsilon_w}\right)^2 \frac{V_2^2}{2}, \quad (2.19)$$

where the sudden expansion coefficient H^* is fixed to one. To reproduce the efficiency decay observed in the proximity of the choking point, the wake area fraction ϵ_w is increased following a geometric progression between the selected minimum and maximum values, i.e., 0.3 and 0.65, once the mass flow rate reaches 80% of the choking point value at the prescribed rotational speed. The flow in the vaneless diffuser is modeled by integrating the system of two-dimensional differential equations derived by Stanitz [38].

$$\begin{aligned}
V_m \frac{dV_m}{dR} - \frac{V_\theta^2}{R} + C_f \frac{V^2 \cos \alpha}{H \sin \chi} + \frac{1}{\rho} \frac{dP}{dR} &= 0 \\
V_m \frac{dV_\theta}{dR} + \frac{V_m V_\theta}{R} + C_f \frac{V^2 \cos \alpha}{H \sin \chi} &= 0 \\
\frac{1}{\rho} \frac{d\rho}{dR} + \frac{1}{V_m} \frac{dV_m}{dR} + \frac{1}{H} \frac{dH}{dR} + \frac{1}{R} &= 0 \frac{dH}{dR} \\
V_m \frac{dV_m}{dR} + V_m \frac{dV_m}{dR} + V_\theta \frac{dV_\theta}{dR} &= 0
\end{aligned} \tag{2.20}$$

Within this model, the average value of the friction factor is estimated using the empirical correlation proposed by Japikse [11]

$$C_f = k_{vd} \left(\frac{1.8 \cdot 10^5}{Re} \right)^{0.2} \tag{2.21}$$

In this work, the value of $k_{vd} = 0.01$ has been selected as the one providing the best match with experimental data. The losses in the volute and in the exit cone are evaluated in terms of total pressure according to [11] and [39], respectively, yielding

$$\begin{aligned}
\Delta P_{t,vl} &= (K_m + K_\theta)(P_{t,3} - P_3) \\
K_m &= \frac{F_1}{1 + \lambda^2} \quad \text{where } \lambda = \frac{V_{\theta,3}}{V_{m,3}} \\
K_\theta &= F_2 \left(\frac{R_3}{R_{vl}} \right)^2 \frac{(\lambda - A_3/A_4)^2}{1 + \lambda^2} \quad \text{if } \frac{A_4}{A_3} \cdot \lambda > 1
\end{aligned} \tag{2.22}$$

and

$$\Delta P_{t,cn} = \rho_3 \frac{V_3^2}{2} \frac{8C_f L_{cn}}{\rho_3 + \rho_4} \tag{2.23}$$

In Eqn. (2.22) the value of both the empirical coefficients F_1 and F_2 is set to 0.8, whereas in Eqn. (2.23) the friction coefficient, C_f , is computed with the Colebrook-White correlation [40]. The efficiency penalty due to disk friction is estimated as [41]

$$\begin{aligned}
\Delta h_{t,df} &= K_f \frac{\rho_1 + \rho_2}{2} \frac{R_2^2 U_2^3}{4\dot{m}} \\
\text{if } Re_{df} = \frac{\rho_2 R_2 U_2}{\mu_2} < 3 \cdot 10^5 & \quad K_f = \frac{3.7(\epsilon_b/H_2)^{0.1}}{Re_{df}^{0.5}} \\
\text{if } Re_{df} = \frac{\rho_2 R_2 U_2}{\mu_2} \geq 3 \cdot 10^5 & \quad K_f = \frac{0.102(\epsilon_b/H_2)^{0.1}}{Re_{df}^{0.2}}.
\end{aligned} \tag{2.24}$$

The seal leakage loss is accounted for by means of the empirical model of Aungier [34]:

$$\begin{aligned}\Delta h_{t, \text{lk}} &= \frac{\dot{m}_{\text{lk}} U_{\text{lk}} U_2}{2 \dot{m}} \\ U_{\text{lk}} &= 0.816 \sqrt{\frac{2 \Delta P_{\text{lk}}}{\rho_2}} \\ \dot{m}_{\text{lk}} &= \rho_2 U_{\text{lk}} N_{\text{eff}} \epsilon_t L_{\text{hd}} \\ \Delta P_{\text{lk}} &= \frac{\dot{m} (R_2 V_{\theta, 2} - R_{1, s} V_{\theta, 1, s})}{N_{\text{eff}} L_{\text{hd}} \frac{R_{1, s} + R_2}{2} \frac{H_1 + H_2}{2}}.\end{aligned}\quad (2.25)$$

The recirculation loss is expressed as [42]

$$\Delta h_{t, \text{rc}} = 8 \cdot 10^{-5} \sinh(3.5 \cdot \alpha_2^3) (D_f U_2)^2, \quad (2.26)$$

where the diffusion factor is computed according to Eqn. (2.16).

2.3.2. OFF-DESIGN PERFORMANCE

In the following, the procedure adopted to evaluate the compressor characteristic curve along the design speedline is described. The same calculations are repeated at different rotational speeds to construct the compressor operating map. To facilitate the reader's understanding, the method is schematically illustrated in Fig. 2.2.

The choking point is estimated by progressively increasing the mass flow rate from the design point value, and evaluating the meridional Mach number at the outlet of the exducer, together with the relative Mach number at the throat section of the main blade passage. The latter is computed by solving the one-dimensional isentropic flow equations within the control volume defined by the impeller inlet and throat section, at five different spanwise locations:

$$\begin{aligned}\rho_1 W_1 \cos \beta_1 \frac{2\pi R_1}{N_{\text{bl}}} &= \rho_a W_a \left(\frac{2\pi R_1}{N_{\text{bl}}} \cos \beta_{1, \text{bl}} - t_{\text{le}} \right) \\ h_1 + \frac{W_1^2}{2} - \frac{U_1^2}{2} &= h_a + \frac{W_a^2}{2} - \frac{U_a^2}{2} \\ \rho_a &= f(h_a, s_1).\end{aligned}\quad (2.27)$$

The impeller is considered choked when either the outlet meridional Mach number is equal to one, or the throat Mach number is unitary over the entire blade span.

The minimum mass flow rate at constant rotational speed is limited by the inception of unstable operating conditions, i.e., surge or rotating stall. A conservative estimate can be obtained by assuming that surge is triggered when the slope of the speedline becomes null [43], i.e., $d\beta/d\dot{m} = 0$. Due to the complexity of the flow phenomena involved in rotating stall, an accurate prediction of its onset is only possible by resorting to time-accurate,

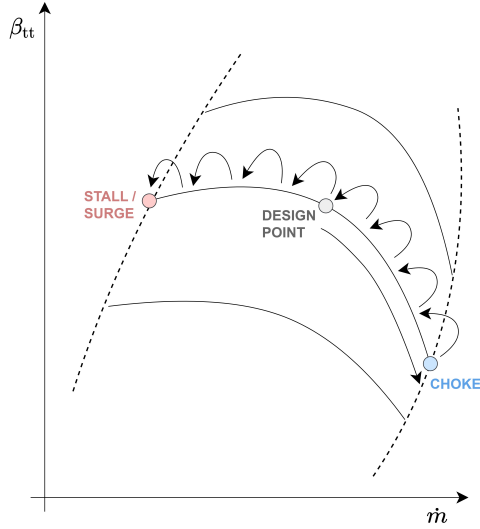


Figure 2.2: Schematic description of the procedure adopted to compute the compressor off-design performance and the operating range.

three-dimensional, full annulus CFD simulations [44]. In the reduced-order model, the inception of rotating stall is estimated using the semi-empirical correlation of Kobayashi et al. [45]

$$\alpha_{2,c} = \alpha_{2,\text{senoo}} + \left(17.02 - 74.2 \frac{H_2}{R_2} \right) \left(1 - \frac{H_3}{H_2} \right), \quad (2.28)$$

where $\alpha_{2,\text{senoo}}$ refers to the critical flow angle at the diffuser inlet computed with the model proposed by Senoo and Kinoshita [46].

Once the choking point has been estimated, the mass flow rate is progressively reduced, and the compressor performance is computed, until either the conditions of surge, i.e., $d\beta/d\dot{m} \leq 0$, rotating stall inception, i.e., $\alpha_2 > \alpha_{2,c}$, or minimum allowable efficiency, e.g., $\eta_{tt} < 50\%$, are met. The operating range at the prescribed rotational speed is then computed according to the following definition

$$OR = \frac{\dot{m}_{\text{choke}} - \min(\dot{m})}{\dot{m}_{\text{des}}}. \quad (2.29)$$

A complete overview of the compressor design workflow is displayed in Fig. 2.3. Once the design specifications, the constraints, and the design variables are provided, either as fixed values or as upper and lower bounds for optimization, the design point computation is performed. During this step, the dimensions of the main components are set, and the impeller work coefficient is adjusted to match the target compression ratio, after accounting for the detrimental effects of slip and losses. Next, the compressor off-design performance is computed for a range of rotational speeds, specified as multiplies or fractions of the design point value. If the model is used to perform a design optimization,

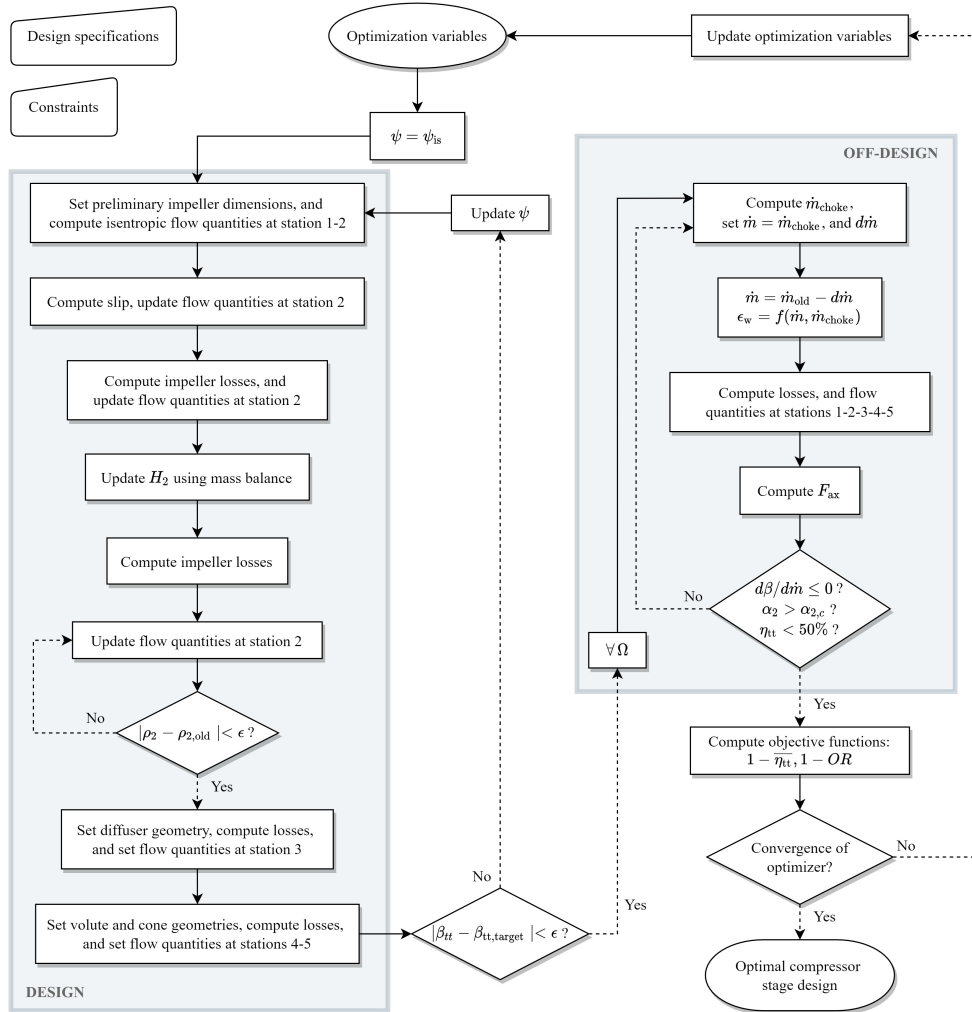


Figure 2.3: Flowchart of the reduced-order compressor model: design, off-design, and optimization. The symbol ϵ refers to the tolerance prescribed in the algorithm.

the off-design performance is computed only at the design rotational speed to reduce the computational cost.

2.3.3. VALIDATION

In order to assess the accuracy of the tool, the predictions of the compressor model have been compared with experimental data from three well-documented test cases available in the open literature, as well as with CFD simulation results. The first two test cases are the Eckardt impeller O and impeller B [18]–[20], [47], i.e., two large centrifugal compressors featuring a vaneless diffuser, and operating with air. The accuracy of the experimen-

Table 2.3: Data of the centrifugal compressors used to validate the reduced-order model.

Variable	Eckardt O	Eckardt B	EPFL	IRIS Stage 1 V1
Fluid	Air	Air	R134a	R1233zd(E)
T_{t1} [K]	288.15	288.15	283.15	283.2
P_{t1} [bar]	1.01	1.01	1.65	0.478
Ω [krpm]	10-18	10-16	150-210	80-99
$R_{1,s}$ [mm]	140	140	5.6	15.4
$R_{1,h}$ [mm]	45	96	1	3.5
R_2 [mm]	200	200	10	20.4
R_3 [mm]	338	338	16.5	31.01
H_2 [mm]	26.7	26.7	1.2	2.8
H_3 [mm]	13.6	13.6	1	2
L_{ax} [mm]	130	84.2	7.7	14.2
N_{bl}	20	20	9	7
N_{split}	0	0	9	7
$\beta_{1,bl,s}$ [deg]	-63	-60	-60	-60
$\beta_{1,bl,h}$ [deg]	-33	-45	-20.5	-17
$\beta_{2,bl}$ [deg]	0	-40	-45	-20.7
Ra [mm]	0.01	0.01	0.01	0.0032
t_{le} [mm]	2.5	2.5	0.2	0.3-0.6
t_{te} [mm]	1.25	1.25	0.2	0.3-0.6
c_t [mm]	0.372	0.372	0.15	0.25-0.3
c_b [mm]	0.372	0.372	0.2	0.2

tal data is $\pm 1\%$ for the mass flow rate, ± 3 rpm for the rotational speed, and $\pm 0.25\%$ for the pressure measured at the nominal location [20]. The third test case is a small-scale compressor designed and tested by Schiffmann and Favrat at EPFL [2]. The machine features backswept blades, a vaneless diffuser, and operates with refrigerant R134a. The uncertainty of the experimental measurements is $\pm 0.5\%$ for the mass flow rate, and ± 0.02 bar for the pressure [6]. The last case study is the first compressor stage of the IRIS test rig, obtained as an outcome of the first design iteration, which is documented in [48]. The impeller is characterized by backswept blades and operates with refrigerant R1233zd(E). The CFD simulations have been performed by means of a commercial steady-state RANS solver [49]. Further information about the numerical setup can be found in [48] and in Chapter 3. In the analysis presented here, the volute and the exit cone are not modeled, in order to closely reproduce the experimental conditions and the CFD model. The geometrical characteristics and the boundary conditions used for each test case are summarized in Tab. 2.3.

The results are illustrated in Fig. 2.4 and Fig. 2.5. The comparison has been performed over the entire range of rotational speeds for each test case. However, only the efficiency predictions for the EPFL compressor are reported in Fig. 2.5 for brevity. The outcome of the validation study is that more than 95% of the experimental data fall within the $\pm 5\%$ uncertainty bands of the calculated values, excluding the β_{tt} measurements of the EPFL compressor in the close proximity of the choking point at 210 krpm. Moreover, the semi-empirical correlation proposed by Kobayashi et al. [45] correctly captures the trend of rotating stall inception but may lead to an underestimation of the operating range for small-

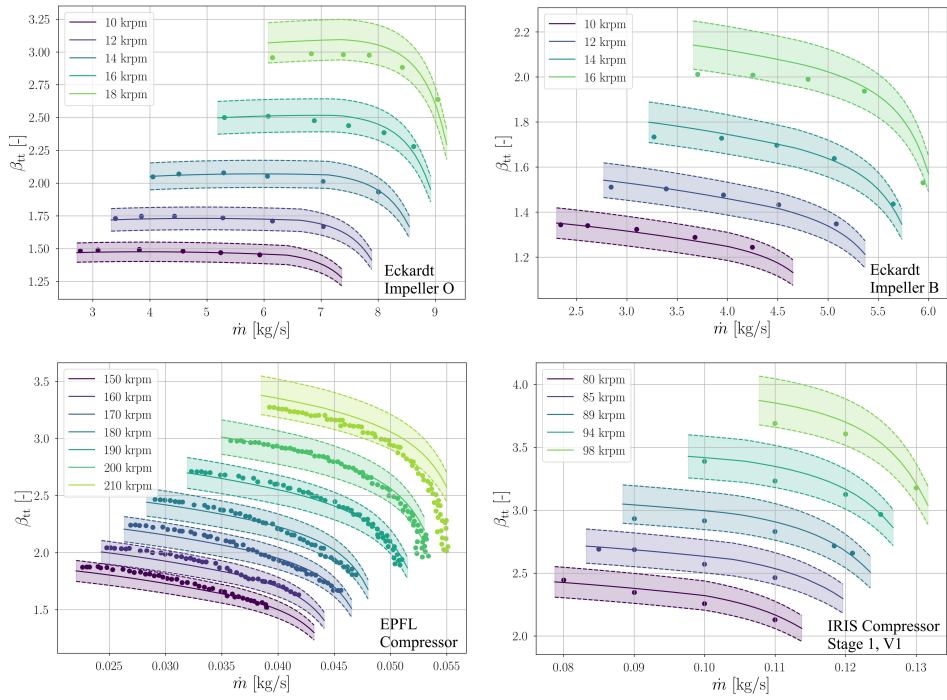


Figure 2.4: Validation of the reduced-order model. Solid lines represent compressor model predictions; dashed lines bound colored $\pm 5\%$ uncertainty bands; dots correspond to experimental data of Eckardt impellers O and B [20], [47], EPFL compressor [6], and CFD simulation results of the first stage of the IRIS compressor.

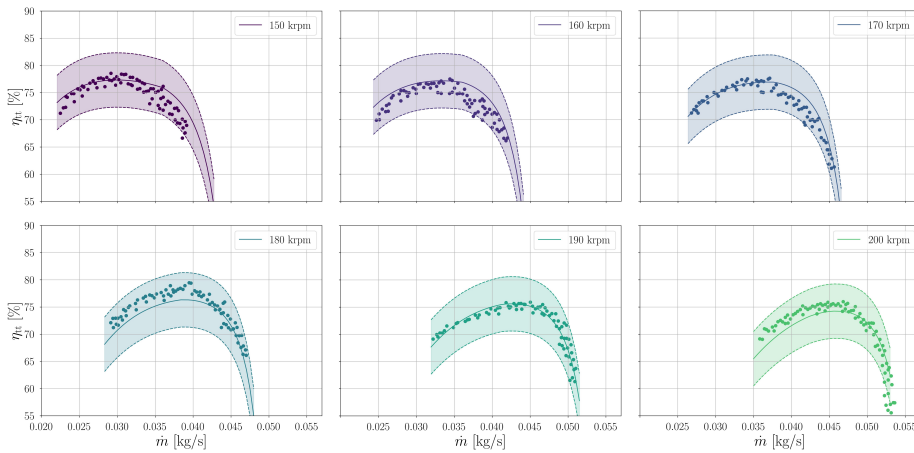


Figure 2.5: Total-to-total efficiency vs. mass flow rate for the EPFL compressor. Solid lines represent compressor model predictions; dashed lines bound colored $\pm 5\%$ uncertainty bands; dots correspond to experimental data [6].

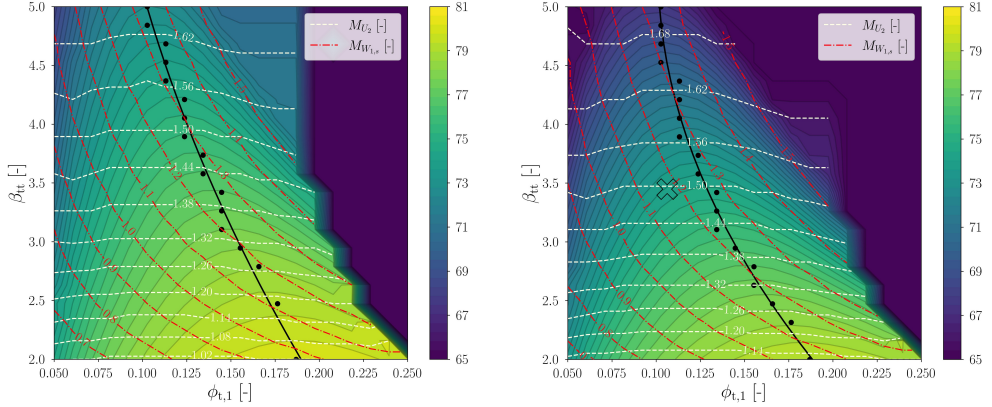


Figure 2.6: Design maps of η_{tt} , M_{U_2} , and $M_{W_{1,s}}$, computed for air and refrigerant R1233zd(E) at $\psi_{is} = 0.8$, $SP = 0.01$, $k = 0.9$, and at P_{t1} , T_{t1} specified in Tab. 2.1. The dots correspond to the values of ϕ_{t1} that maximize η_{tt} for each β_{tt} ; the solid line represents their spline interpolation of order two. The cross indicates the design point resulting from the optimization study described in Section 2.5.1.

scale compressors at large rotational speed. The predictive capabilities of the model may be improved only by resorting to additional experiments or high-fidelity, time-accurate numerical simulations. However, this is beyond the scope of the present work.

2.4. DESIGN MAPS FOR SINGLE-STAGE COMPRESSORS

The validated compressor model is used to generate design maps, namely two-dimensional contours of different performance metrics, computed as a function of ϕ_{t1} and β_{tt} , while fixing the values of the remaining independent variables of Eqn. (2.8). The prescribed ranges of ϕ_{t1} and β_{tt} are discretized with 20 sampling points, i.e., each design map presented in the following is constituted by 400 unique compressor designs.

2.4.1. INFLUENCE OF THE WORKING FLUID

The influence of the working fluid on the stage layout and performance is investigated by comparing design maps computed for compressors characterized by the same size parameter $SP = 0.01$ and isentropic work coefficient $\psi_{is} = 0.8$, but operating with different fluids. The working fluids and the corresponding total inlet conditions considered in the present study are listed in Tab. 2.1. To separately investigate the effect of the fluid molecule and of the compressor size, the values of total inlet pressure and temperature are chosen to guarantee dynamic similarity, i.e., the average Reynolds number based on the hydraulic diameter is kept nearly constant in all test cases. Moreover, the total inlet conditions are selected so that all the fluids are in the dilute gas state, i.e., $\overline{\gamma_{Pv}} \approx \gamma$. Consequently, the influence of flow non-ideality, which is outside the scope of this investigation, can be neglected. However, due to the adoption of the generalized isentropic exponent in the scaling law and in the loss models, the methodology described in this work is applicable also to compressors operating with non-ideal flows, i.e., $\overline{\gamma_{Pv}} \neq \gamma$.

The contours of stage total-to-total efficiency, tip speed Mach number, and relative

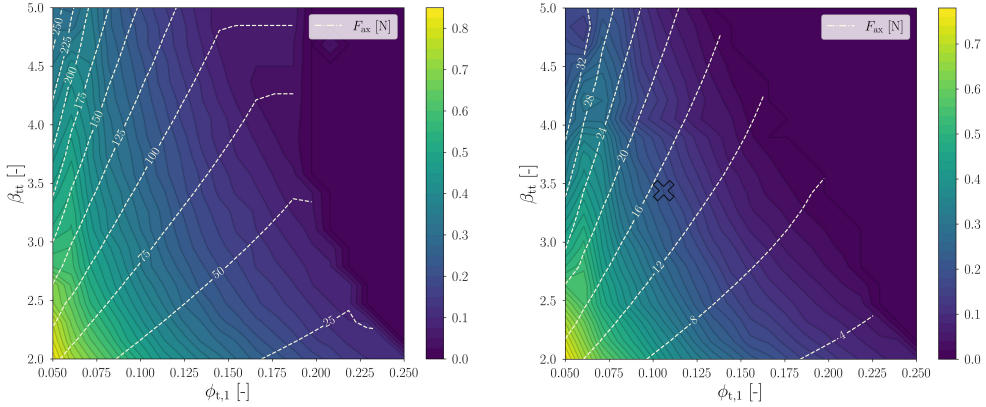


Figure 2.7: Design maps of OR , and F_{ax} , computed for air and refrigerant R1233zd(E) at $\psi_{is} = 0.8$, $SP = 0.01$, $k = 0.9$, and at P_{t1} , T_{t1} specified in Tab. 2.1. The cross indicates the design point resulting from the optimization study described in Section 2.5.1.

Mach number at the inducer shroud are illustrated in Fig. 2.6 for air and refrigerant R1233zd(E). The following considerations can be drawn by comparing the two design maps. The compressor stage operating with air features larger values of efficiency over the entire design space, and the performance gap increases when departing from the region of optimal efficiency. Moreover, the fluid molecular complexity affects the shape and the position of the locus of optimal efficiency, as illustrated by the solid black lines. The stage operating with R1233zd(E) features a moderate increment of $M_{W_{1,s}}$ and M_{U_2} over the design space, as highlighted by the dashed red and white lines, respectively. The increase of $M_{W_{1,s}}$ is caused by the lower speed of sound associated with the more complex fluid molecules, whereas the rise of M_{U_2} is due to the smaller value of $\overline{\gamma_{Pv}}$ calculated for R1233zd(E) over the compression process, as discussed in Section 2.1.

The contours of the compressor operating range, and axial thrust acting on bearings are depicted in Fig. 2.7, for the same couple of working fluids. The main outcomes can be summarized as follows. On the one hand, the stage operating with air is characterized by a wider operating range over the design space. This is mainly due to the smaller value of $M_{W_{1,s}}$ associated with the simpler fluid molecule, which leads to a larger choke margin at the design point. On the other hand, the stage operating with air features larger values of axial thrust, as compared to the ones obtained with R1233zd(E). The reason is twofold. First, the two compressor stages are characterized by comparable dimensions, but different total inlet pressure, to achieve dynamic similarity. In turn, the higher inlet pressure imposed on the stage operating with air leads to a larger axial thrust acting on the compressor's eye. Furthermore, the air compressor features a higher inlet meridional velocity, thus a larger mass flow rate, and a larger impulse force acting on the inlet.

The previous considerations can be generalized, by analyzing the trends of the stage performance metrics computed for all the working fluids listed in Tab. 2.1. As illustrated in Fig. 2.8, an increase of fluid molecular complexity, that is associated with a decrease of $\overline{\gamma_{Pv}}$, leads to a decrease of the optimal value of swallowing capacity. This effect can be attributed to the growing impact of shock losses on impeller performance at increasing

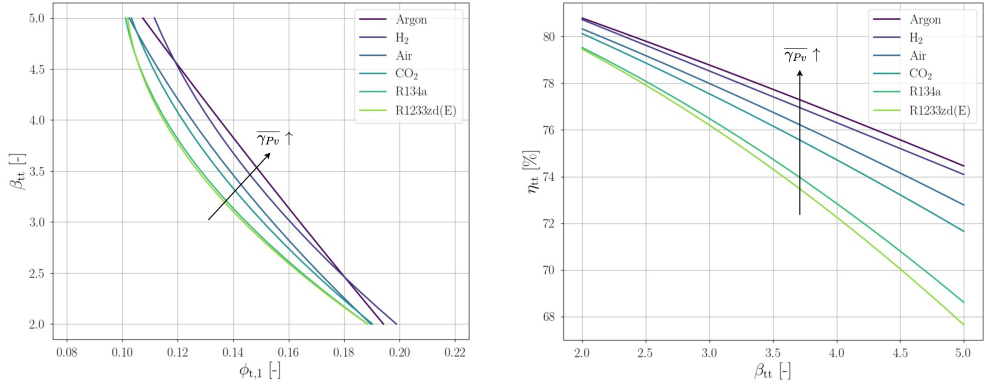


Figure 2.8: Locus of optimal efficiency for compressors operating with fluids of increasing molecular complexity. All the computations are performed with $\psi_{is} = 0.8$, $SP = 0.01$, $k = 0.9$, and at P_{t1} , T_{t1} specified in Tab. 2.1.

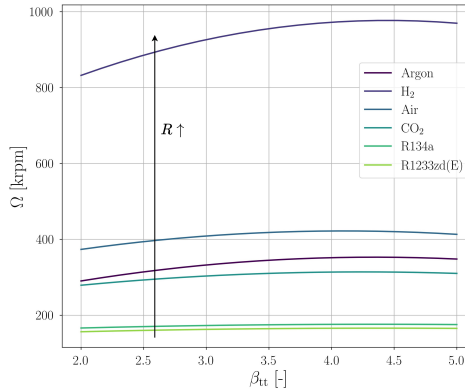


Figure 2.9: Rotational speed computed along the locus of optimal efficiency for the test cases listed in Tab. 2.1

values of $M_{W_{1,s}}$, observed in correspondence of small values of $\overline{\gamma_{Pv}}$ and large values of ϕ_{t1} . Moreover, the optimal stage efficiency is directly proportional to $\overline{\gamma_{Pv}}$ and inversely proportional to the target pressure ratio, see Fig. 2.8. The rotational speed at the design point shows an opposite trend, as displayed in Fig. 2.9. To summarize, given the compressor scale, measured by SP , and the isentropic work coefficient ψ_{is} , the stages operating with working fluids made of simple molecules, characterized by large values of $\overline{\gamma_{Pv}}$ and R , are more efficient, but their rotational speed is higher. As a consequence, Ω may exceed the maximum allowable limit for mechanical resistance, and the stage must be re-designed at a higher work coefficient, at the expense of fluid dynamic efficiency. Fluid molecules like Argon, featuring high values of isentropic exponent and relatively high molecular weight, are attractive, as they enable the design of mini compressors characterized by both high efficiency and moderate rotational speed.

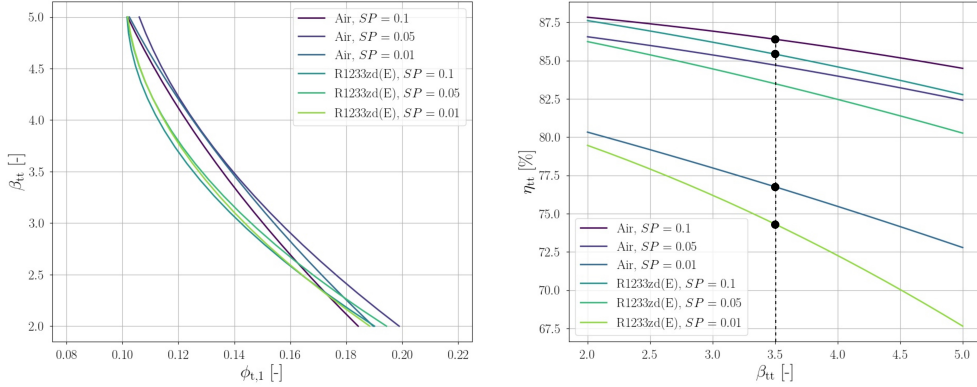


Figure 2.10: Locus of optimal efficiency for compressors characterized by different values of the size parameter. All the computations are performed at $\psi_{is} = 0.8$, $k = 0.9$, and at P_{t1} , T_{t1} specified in Tab. 2.1. The black dots correspond to the stage designs chosen for the loss breakdown analysis.

2.4.2. INFLUENCE OF SIZE

The influence of scale on compressor design is studied by comparing design maps computed for stages operating with Air and R1233zd(E), but characterized by different values of size parameter $SP = 0.1 - 0.05 - 0.01$. The total inlet conditions are kept unaltered, but the dynamic similarity condition is not valid anymore, due to the different compressor dimensions. Moreover, the magnitude of relative clearances and relative surface roughness decreases with increasing values of the size parameter, due to the relaxation of manufacturing constraints.

The stages featuring a larger size parameter are characterized by higher efficiency values over the entire design space, as shown in Fig. 2.10. However, the size parameter has only a minor influence on the locus of optimal efficiency in the $\phi_{t1} - \beta_{t1}$ plane. To gain further insights about the sources of efficiency penalty in small-scale compressors, a detailed loss breakdown analysis has been performed for stages with varying size parameter and designed at moderate pressure ratio in the neighborhood of the optimal efficiency region, i.e., $SP = 0.1 - 0.01$, $\beta_{t1} = 3.5$, $\phi_{t1} = 0.13$, see Fig. 2.11. The loss sources that are mostly affected by the change of SP are the ones associated with tip clearance, seal leakage, recirculation, and viscous friction in the impeller and the diffuser. The increase of recirculation loss at low values of size parameter is induced by the rise of the optimal α_2 computed by the reduced-order model, and thus cannot be significantly mitigated. On the contrary, the increase in clearance and leakage losses can be alleviated by reducing the relative tip gap. In the same fashion, the efficiency penalties due to viscous friction can be mitigated by reducing the relative surface roughness. Quantifying the impact of the different manufacturing constraints on stage efficiency is of paramount importance to focus efforts and resources on the areas that can enable the largest performance gain. The calculations performed with the reduced-order model show that an increase in relative tip gap of one order of magnitude leads to an efficiency penalty of $\approx 6\%$ for the stage operating with refrigerant R1233zd(E). In the same fashion, an increase of relative surface roughness of one order of magnitude produces a performance decay of the order of 3.8%.

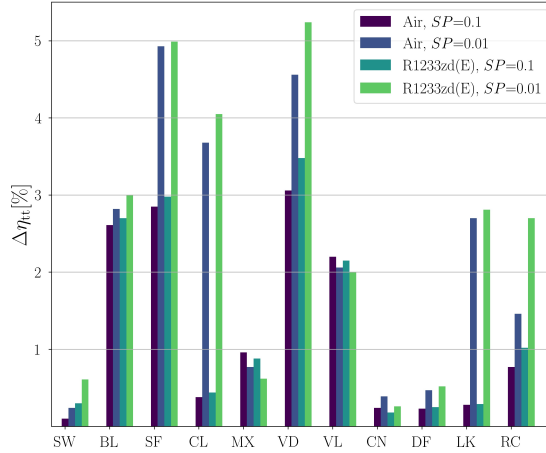


Figure 2.11: Loss breakdown for compressor stages operating with air and refrigerant R1233zd(E), featuring $\phi_{t1} = 0.13$, $\psi_{is} = 0.8$, $\beta_{tt} = 3.5$, $SP = 0.1 - 0.01$. The abbreviations displayed on the abscissa refer to the subscripts used to identify the loss components.

Similar trends are calculated for the air compressor.

To summarize, the value of swallowing capacity maximizing the stage efficiency is not remarkably influenced by the size parameter and lies between $\phi_{t1} = 0.1 - 0.15$ for stages featuring moderate to high pressure ratio. However, the stage operating range is maximum at low values of swallowing capacity, i.e., $\phi_{t1} = 0.05 - 0.07$. A similar argument can be used to prove that there is a trade-off between stage efficiency and operating range with respect to most of the design variables listed in Eqn. 2.8. Therefore, the optimal design of this kind of turbomachines can be arguably achieved only by resorting to a multi-objective optimization strategy.

2.5. CASE STUDY

In order to verify the validity of the design guidelines derived from the maps presented in Section 2.4, a design exercise was carried out, namely the multi-objective optimization of a compressor stage resembling the first stage of the IRIS test rig. The selected case study is particularly relevant, as it features small dimensions, a working fluid of moderate molecular complexity, and stringent requirements in terms of both efficiency and operating range.

In mathematical form, the multi-objective design optimization of a single-stage centrifugal compressor can be formulated as follows:

$$\begin{aligned}
\min_{\mathbf{x} \in \mathbb{R}^n} F(\mathbf{x}) &= [f_1(\mathbf{x}), \dots, f_{n_{\text{obj}}}(\mathbf{x})], \quad \text{s.t.} \\
h_k(\mathbf{x}) &= 0 \quad k = 1, \dots, n_{\text{eq}} \\
g_i(\mathbf{x}) &\leq 0 \quad i = 1, \dots, n_{\text{ineq}} \\
x_{l,j} &\leq x_j \leq x_{u,j} \quad j = 1, \dots, n
\end{aligned} \tag{2.30}$$

where \mathbf{x} is the vector of independent variables, $F(\mathbf{x})$ is the vector of the objective functions, and $h_k(\mathbf{x})$, $g_i(\mathbf{x})$ are the vectors of the equality and inequality constraints, respectively. The objective functions selected in this work are the operating range and the compressor efficiency, both evaluated at the design rotational speed. To account for multiple operating points, the compressor efficiency is computed as the weighted average of the total-to-total efficiency, evaluated over the entire design speed-line. The weights used for this calculation are inversely proportional to the distance of each operating point from the selected design point. The parameters, the optimization variables, and the inequality constraints considered in the present work are listed in Tab. 2.4. Overall, the optimization problem comprises eight design variables, two objectives, and seven inequality constraints.

2.5.1. CONCEPTUAL DESIGN OPTIMIZATION

The Pareto front is computed by means of the NSGA-II algorithm described in [50] and implemented in [51]. All the optimization variables are of floating point type, except for the number of blades, which is treated as an integer. The initial population comprises ten individuals for each design variable and is sampled according to the latin hypercube methodology along the floating point directions, and randomly along the integer axis. The population is evolved for eighty generations, applying simulated binary crossover and polynomial mutation, leading to 6400 function evaluations. As displayed in Fig. 2.12, the resulting Pareto front shows larger variability over the axis associated with compressor operating range than over the one related to stage isentropic efficiency. In turn, the optimal conceptual design has been chosen among the non-dominated solutions by prioritizing the compressor operating range over the average stage efficiency.

The main features of the optimal design are reported in Tab. 2.5, while the meridional view of the resulting impeller and diffuser is displayed in Fig. 2.12. The optimal compressor design is characterized by $\psi_{\text{is}} \approx 0.8$, $SP \approx 0.01$, and $k \approx 0.9$, thus the corresponding design point can be displayed on the maps shown in Fig. 2.6-2.7. Three main considerations can be outlined.

- As expected, the swallowing capacity of the optimal design lies in between the locus of optimal efficiency and the region of maximum operating range. The higher the prescribed pressure ratio, and the molecular complexity of the selected working fluid, the smaller the distance between the loci of maximum efficiency and operating range. This information is essential to address the trade-off between design point efficiency and operability when approaching the design of a new prototype.

Table 2.4: Setup of the multi-objective compressor design optimization.

Variable	Type	Value
β_{tt}	Parameter	3.45
\dot{m} [kg/s]	Parameter	0.114
fluid	Parameter	R1233zd(E)
P_{t1} [kPa]	Parameter	47.789
T_{t1} [K]	Parameter	278.13
ϕ_{t1}	Design variable	0.05-0.2
ψ_{is}	Design variable	0.6-1.0
α_2 [deg]	Design variable	60-75
k	Design variable	0.65-0.95
N_{b1}	Design variable	12-20
R_3/R_2	Design variable	1.3-2.0
$\frac{H_3 - H_2}{H_2(R_2/R_{pinch} - 1)}$	Design variable	0-1
$\frac{R_{pinch} - R_2}{R_3 - R_2}$	Design variable	0-1
$\min(R_{1,h})$ [mm]	Inequality constraint	3.25
$\max(R_4)$ [mm]	Inequality constraint	50
$\min(a)$ [mm]	Inequality constraint	1.0
$\min(H_2)$ [mm]	Inequality constraint	1.35
$\max(\Omega)$ [krpm]	Inequality constraint	150
$\max(F_{ax})$ [N]	Inequality constraint	50
$\max(M_3)$	Inequality constraint	0.65

- The tip speed Mach number and the relative Mach number at the inducer shroud can be accurately predicted from the design maps. The tip speed Mach number scales with the prescribed pressure ratio, whereas the relative Mach number is also a function of the swallowing capacity. In the proposed design exercise, in order to comply with the requirement of subsonic flow in the inducer, one has to select a lower swallowing capacity, thus further compromising the design point efficiency.
- The optimal design is not located on the Cordier line, i.e., the locus of optimal efficiency in the N_s - D_s chart [52], where

$$N_s = \Omega \frac{\dot{V}_1^{1/2}}{\Delta h_{ts}^{3/4}}, \quad (2.31)$$

$$D_s = D_1 \frac{\Delta h_{ts}^{1/4}}{\dot{V}_1^{1/2}}. \quad (2.32)$$

Therefore, such a design cannot be obtained by applying existing design rules.

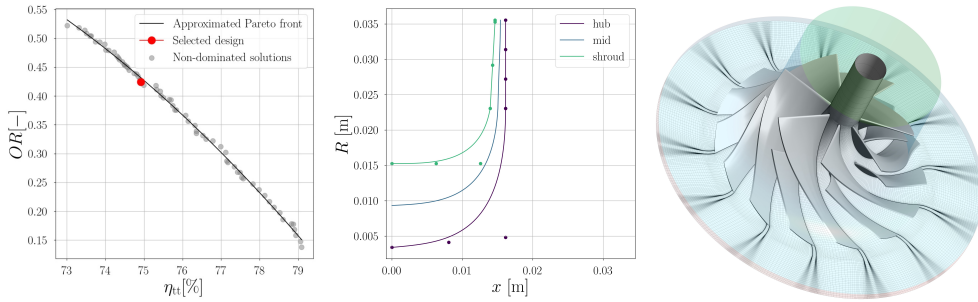


Figure 2.12: Optimal design of the first compressor stage for the IRIS test rig. From left to right: Pareto front obtained with the multi-objective optimization framework, meridional flow path of the selected design, 3D impeller geometry and computational grid. The hub and shroud curves are defined as third order Bezier curves, whose control points are displayed in the central image.

Table 2.5: Main characteristics of the compressor design selected along the Pareto front generated by the reduced-order model coupled to a gradient-free optimizer.

Variable	Value	Variable	Value
N_s	1.208	D_s	1.870
$M_{W_{1,s}}$	1.12	M_{U_2}	1.5
ϕ_{t1}	0.106	ψ_{is}	0.793
SP	0.019	k	0.95
Ω [krpm]	68-94	$\beta_{1,bl,s}$ [deg]	60
$R_{1,s}$ [mm]	15.2	$\beta_{1,bl,h}$ [deg]	16.5
$R_{1,h}$ [mm]	3.4	$\beta_{2,bl}$ [deg]	29.6
R_2 [mm]	22.8	Ra [mm]	0.032
R_3 [mm]	35.2	R_4 [mm]	49.3
H_2 [mm]	2.3	$D_{cn,out}$ [mm]	17.8
H_3 [mm]	1.6	t_s [mm]	0.3
L_{ax} [mm]	16.0	t_h [mm]	0.6
N_{bl}	7	ϵ_t [mm]	0.15
N_{split}	7	ϵ_b [mm]	0.15

2.5.2. PERFORMANCE INVESTIGATION BASED ON CFD

The three-dimensional geometry of the impeller and the diffuser are constructed from the conceptual design data of the optimal compressor design, using commercial software [53]. The shape of the main and the splitter blades are controlled by specifying the hub, mid, and shroud profiles, and by stacking them along the radial direction at the leading edge. To cope with transonic flow in the inducer, the blades are designed to be aft-loaded at the shroud, aiming to improve the choke margin and reduce the shock losses [25]. The wrap angle at each spanwise location is set to obtain 16.5° of rake angle, to enhance the structural integrity of the impeller. The blades feature constant thickness distribution in the meridional direction and linear tapering in the spanwise direction. The vaneless diffuser is characterized by a linear pinch extending through its entire length. The presence of the volute is neglected in this analysis to reduce the computational cost.

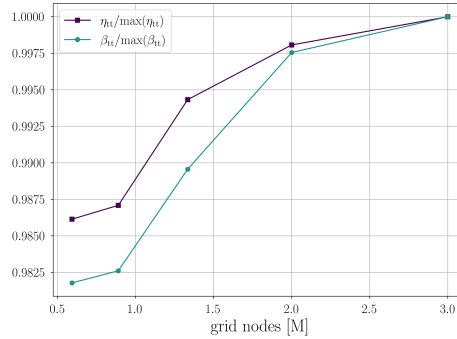


Figure 2.13: Sensitivity of total-to-total pressure ratio and internal isentropic efficiency on the number of grid nodes.

Steady-state, single passage RANS computations [49] with a mixing-plane interface are used to assess the compressor fluid dynamic performance over the entire operating range. The boundary conditions are imposed in terms of flow direction, total pressure, and total temperature at the inlet, whereas the mass flow rate is assigned at the outlet. The $\kappa - \omega$ SST turbulence model is employed together with adequate cell clustering near walls to guarantee $y^+ \leq 1$. Turbulence boundary conditions are set in terms of inlet turbulence intensity ($\kappa = 5\%$) and eddy viscosity ratio ($\mu/\mu_t = 10$), while the turbulent Prandtl number is set to $Pr_t = 1$, in accordance with what is documented in [54]. The advective and turbulent fluxes are discretized with total variation diminishing schemes [55], while a central difference scheme is adopted for discretizing the viscous fluxes. A look-up table method is employed to speed up the evaluation of the thermo-physical fluid properties. The property values are calculated using the multi-parameter equation of state model available in [26]. The vapor properties are extended up to the spinodal line to improve solver robustness in the initial phase of the calculation, without affecting the accuracy of the converged solution. After performing a sensitivity analysis, see Fig. 2.13, a grid size of approximately two million cells and a thermodynamic mesh of one million elements are set as an optimal trade-off between accuracy and computational cost.

A total of 27 RANS computations have been performed to compute the compressor operating map in a range of rotational speeds extending from 80% to 110% of the design point value, corresponding to 85.7 krpm, as shown in Fig. 2.14. The CFD calculations determined a design point pressure ratio of 3.38 and an isentropic efficiency equal to 85.93%, neglecting the effect of parasitic losses, and of the efficiency decay in the volute and the exit cone. The maximum deviation between the predictions of the reduced-order model and CFD is 6.18% and 6.86% in terms of β_{tt} and η_{tt} , respectively, whereas the average deviation measured for both performance metrics is below 5%. These results provide further evidence of the accuracy of the in-house tool and additional confidence in the trends described in Section 2.4.

Further insights about the compressor flow field at the design point can be gained by inspecting Fig. 2.15. The largest entropy generation is predicted in the shroud region of the inducer, due to the occurrence of transonic Mach number, and in the rear part of the

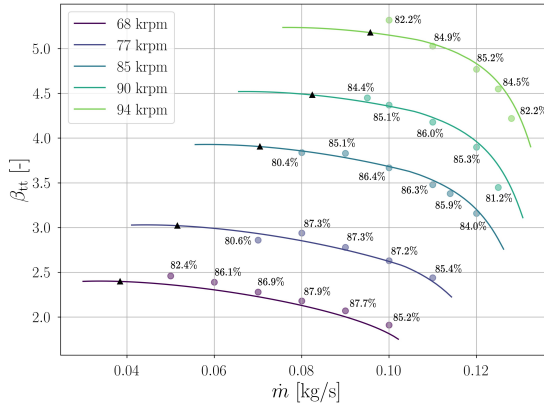


Figure 2.14: Compressor operating map. The solid lines represent the predictions of the reduced-order model; the results computed by CFD are displayed by the dots, in terms of both mass-flow averaged β_{tt} and internal η_{tt} .

blades, as a result of viscous mixing of the tip leakage vortex with the main flow. As highlighted by the streamlines, the use of aft-loaded blades at the shroud is effective in delaying the formation of the tip leakage vortex, thus reducing the efficiency penalty associated with large tip clearance, as reported in [16]. More advanced three-dimensional design strategies, supported by a CFD-based optimization framework, see [56], can be used to further refine the candidate design, enabling even higher efficiency and wider operating range.

2.6. CONCLUSIONS

The effect of size and working fluid on the efficiency, operating range, and axial thrust on bearings has been investigated for single-stage centrifugal compressors by means of a reduced-order model, validated with experimental data. Moreover, the reduced-order model has been used to perform a design exercise, i.e., the multi-objective optimization of the first compressor stage of the IRIS test rig. The key characteristics of the optimal compressor design have been compared to those derived from the design maps, to corroborate their validity. The optimal design has been extensively characterized by means of 3D steady RANS simulations. The outcomes of this study can be summarized as follows.

1. Compressor stages operating with fluids made of heavy and complex molecules exhibit lower efficiency if compared to compressors for fluids made of simpler molecules. The locus of optimal efficiency shifts towards lower values of swallowing capacity for decreasing values of $\overline{\gamma_{Pv}}$. However, compressors operating with simple-molecule fluids optimally operate with higher rotational speed. If Ω exceeds the maximum allowable threshold, the stage should be re-designed at a higher work coefficient, therefore penalizing fluid dynamic performance.
2. Fluid molecular complexity has a minor influence on the stage operating range, but it remarkably affects the axial thrust acting on the bearings. Compressor stages

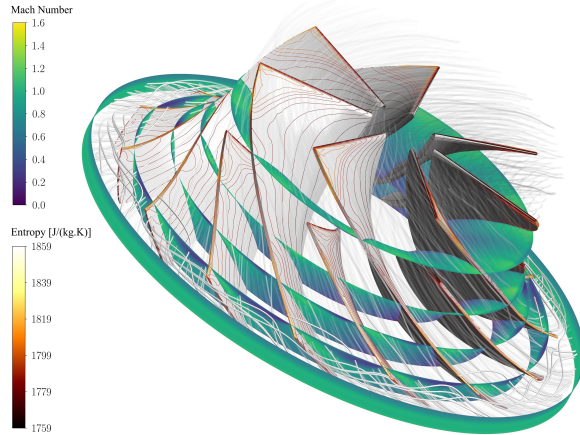


Figure 2.15: Flow field computed by means of CFD at the design point. The Mach number distribution is shown in the form of contour plots over different secondary planes. The iso-entropy lines are displayed over the blade surfaces. 3D streamlines are colored from transparent to white, according to the local value of entropy, to highlight the tip leakage vortex.

operating with complex-molecule fluids produce lower axial thrust if compared to their simple-molecule counterparts, thus making them particularly suitable for the use of oil-free gas bearings.

3. Compressors featuring a lower size parameter are characterized by lower efficiency, as a result of manufacturing constraints, leading to higher relative tip clearance and higher relative surface roughness. The efficiency penalty is more sensitive to variations of clearance gap than to surface finishing. However, the size parameter has a negligible influence on the shape and the position of the locus of optimal efficiency.
4. The optimal design obtained as an outcome of the case study complies with the guidelines that can be derived from the $\phi_{t1} - \beta_{tt}$ maps, in terms of design point efficiency, operating range, tip speed Mach number, and relative Mach number at the inducer shroud. Moreover, the optimal design can not be readily obtained by applying existing design rules, as it is not located on the Cordier line in the $N_s - D_s$ chart.
5. Steady-state RANS simulations of the flow past the optimal compressor layout predict a design point pressure ratio of $\beta_{tt} = 3.38$, an internal isentropic efficiency equal to $\eta_{is} = 85.93\%$, and an operating range of 0.49 at 85.7 krpm. These findings provide further evidence that efficient mini-compressors operating with organic fluids, and featuring pressure ratios up to five at off-design conditions, are feasible from the fluid dynamic standpoint.

METADATA

The geometry of the compressor stage obtained as a result of the multi-objective design optimization, and the full set of design maps can be downloaded at the website link¹.

¹<https://github.com/Propulsion-Power-TU-Delft/Metadata/tree/main/IRISCompressor>

NOMENCLATURE

Roman symbols

A	Surface area [m ²]
a	Sound speed [m s ⁻¹]
	Throat length [m]
c	Specific heat capacity [J kg ⁻¹ K ⁻¹]
C_f	Skin friction coefficient [-]
D	Diameter [m]
F_{ax}	Axial thrust acting on bearings [N]
H	Blade height [m]
H^*	Sudden expansion coefficient [-]
h	Specific enthalpy [J kg ⁻¹]
i	Incidence angle [deg]
k	Impeller shape factor [-]
	Empirical constant [-]
L_{ax}	Impeller axial length [m]
M	Mach number [-]
	Molar mass [kg mol ⁻¹]
\dot{m}	Mass flow rate [kg s ⁻¹]
N_{bl}	Number of main blades [-]
N_{split}	Number of splitter blades [-]
N_{eff}	Effective number of blades [-]
N_s	Specific speed [-]
OR	Operating range [-]
P	Pressure [Pa]
Pr	Prandtl number [-]
R	Radius [m]
	Specific gas constant [J kg ⁻¹ K ⁻¹]
Ra	Surface roughness [m]
Re	Reynolds number [-]
SP	Size parameter [-]
s	Specific entropy [J kg ⁻¹ K ⁻¹]
T	Temperature [K]
t	Thickness [m]
U	Peripheral speed [m s ⁻¹]
V	Absolute velocity [m s ⁻¹]
\dot{V}	Volumetric flow rate [m ³ s ⁻¹]
v	Specific volume [m ³ kg ⁻¹]
W	Relative velocity [m s ⁻¹]

Greek symbols

α	Absolute flow angle [deg]
β	Pressure ratio [-]
	Relative flow angle [deg]
γ	Heat capacity ratio [J kg ⁻¹ K ⁻¹]
γ_{Pv}	Isentropic pressure-volume exponent [J kg ⁻¹ K ⁻¹]
e_b	Back face clearance [m]
e_t	Tip clearance gap [m]
e_w	Wake area fraction [-]
η	Efficiency [-]
μ	Dynamic viscosity [Pa s ⁻¹]
ρ	Density [kg m ⁻³]
σ	Stage geometrical characteristics [-]

ϕ_{t1}	Swallowing capacity [-]
χ	Degree of reaction [-]
	Diffuser inclination [deg]
ψ	Work coefficient [-]
Ω	Rotational speed [rpm]
ω	Turbulence specific dissipation rate [s ⁻¹]
κ	Turbulence kinetic energy [J kg ⁻¹]

Subscripts

∞	Ideal gas conditions
a	Throat section
c	Critical
choke	Choking point
cn	Cone
h	Hub
hd	Hydraulic
is	Isentropic
le	Leading edge
r	Reduced
s	Specific - shroud
t	Total - turbulent
te	Trailing edge
ts	Total-to-static
tt	Total-to-total
θ	Tangential component
des	Design point
m	Meridional component
mx	Mixing
rc	Recirculation
sf	Skin friction
sw	Shock waves
i	Incidence
bl	Blade loading
cl	Clearance
vl	Volute
vd	Vaneless diffuser
df	Disk friction
lk	Leakage
1	Inducer
2	Exducer - diffuser inlet
3	Diffuser outlet - volute inlet
4	Volute outlet - cone inlet
P	Evaluated at constant pressure
v	Evaluated at constant volume

Abbreviations

CO ₂	Carbon dioxide
ECS	Environmental control system
H ₂	Hydrogen
IRIS	Inverse Rankine integrated system
R134a	Tetrafluoroethane
R1233zd(E)	Trifluoropropene

BIBLIOGRAPHY

- [1] C. Zwysig, J. W. Kolar, and S. D. Round, "Megasp speed drive systems: Pushing beyond 1 million r/min", *IEEE/ASME Transactions on Mechatronics*, vol. 14, no. 5, pp. 564–574, 2009, ISSN: 10834435. DOI: 10.1109/TMECH.2008.2009310.
- [2] J. Schiffmann and D. Favrat, "Experimental investigation of a direct driven radial compressor for domestic heat pumps", *International Journal of Refrigeration*, vol. 32, no. 8, pp. 1918–1928, Dec. 2009, ISSN: 01407007. DOI: 10.1016/j.ijrefrig.2009.07.006.
- [3] P. A. Pilavachi, "Mini- and micro-gas turbines for combined heat and power", *Applied Thermal Engineering*, vol. 22, no. 18, pp. 2003–2014, Dec. 2002, ISSN: 1359-4311. DOI: 10.1016/S1359-4311(02)00132-1.
- [4] M. V. Zagarola and J. A. McCormick, "High-capacity turbo-Brayton cryocoolers for space applications", *Cryogenics*, vol. 46, no. 2-3, pp. 169–175, Feb. 2006, ISSN: 0011-2275. DOI: 10.1016/J.CRYOGENICS.2005.11.018.
- [5] M. V. Casey, D. Krähenbühl, and Z. Christof, "The Design of Ultra-High-Speed Miniature Centrifugal Compressors", in *European Conference on Turbomachinery Fluid Dynamics and Thermodynamics*, 2013.
- [6] J. Schiffmann and D. Favrat, "Design, experimental investigation and multi-objective optimization of a small-scale radial compressor for heat pump applications", *Energy*, vol. 35, no. 1, pp. 436–450, Jan. 2010, ISSN: 03605442. DOI: 10.1016/j.energy.2009.10.010.
- [7] H. Heshmat, J. F. Walton, C. D. Corte, and M. Valco, "Oil-free turbocharger demonstration paves way to gas turbine engine applications", in *Proceedings of the ASME Turbo Expo*, vol. 1, American Society of Mechanical Engineers (ASME), Aug. 2000, ISBN: 9780791878545. DOI: 10.1115/2000-GT-0620.
- [8] D. A. Kouremenos and X. K. Kakatsios, "The three isentropic exponents of dry steam", *Forschung im Ingenieurwesen*, vol. 51, no. 4, pp. 117–122, Jul. 1985, ISSN: 00157899. DOI: 10.1007/BF02558416.
- [9] R. Van den Braembussche, *Design and Analysis of Centrifugal Compressors*, 1st. Wiley, Apr. 2019.
- [10] A. Whitfield and N. Baines, *Design of radial turbomachines*. Longman, Jun. 1990.
- [11] D. Japikse, *Centrifugal Compressor Design and Performance*. Concepts Eti, Dec. 1996.
- [12] P. M. Came and C. J. Robinson, "Centrifugal compressor design", *Proceedings of the Institution of Mechanical Engineers, Part C: Journal of Mechanical Engineering Science*, vol. 213, no. 2, pp. 139–155, Feb. 1998, ISSN: 0954-4062. DOI: 10.1243/0954406991522239.
- [13] D. Rusch and M. Casey, "The design space boundaries for high flow capacity centrifugal compressors", *Journal of Turbomachinery*, vol. 135, no. 3, Mar. 2013, ISSN: 15288900. DOI: 10.1115/1.4007548.
- [14] H. S. Pham, N. Alpy, J. H. Ferrasse, *et al.*, "An approach for establishing the performance maps of the sc-CO₂ compressor: Development and qualification by means of CFD simulations", *International Journal of Heat and Fluid Flow*, vol. 61, pp. 379–394, Oct. 2016, ISSN: 0142-727X. DOI: 10.1016/J.IJHEATFLUIDFLOW.2016.05.017.
- [15] Y. Jeong, S. Son, S. K. Cho, S. Baik, and J. I. Lee, "Evaluation of supercritical CO₂ compressor off-design performance prediction methods", *Energy*, vol. 213, p. 119071, Dec. 2020, ISSN: 0360-5442. DOI: 10.1016/J.ENERGY.2020.119071.
- [16] A. Javed, C. Arpagaus, S. Bertsch, and J. Schiffmann, "Turbocompresseurs de petite taille pour un fonctionnement sur une large plage avec des jeux radiaux importants pour un concept de pompe à chaleur bi-étagée", *International Journal of Refrigeration*, vol. 69, pp. 285–302, Sep. 2016, ISSN: 01407007. DOI: 10.1016/j.ijrefrig.2016.06.015.
- [17] A. Giuffré and M. Pini, "Design Guidelines for Axial Turbines Operating With Non-Ideal Compressible Flows", *Journal of Engineering for Gas Turbines and Power*, vol. 143, no. 1, Jan. 2021, ISSN: 0742-4795. DOI: 10.1115/1.4049137.

-
- [18] D. Eckardt, "Instantaneous measurements in the jet-wake discharge flow of a centrifugal compressor impeller", *Journal of Engineering for Gas Turbines and Power*, vol. 97, no. 3, pp. 337–345, Jul. 1975, ISSN: 15288919. DOI: 10.1115/1.3445999.
- [19] D. Eckardt, "Detailed flow investigations within a high-speed centrifugal compressor impeller", *Journal of Fluids Engineering, Transactions of the ASME*, vol. 98, no. 3, pp. 390–399, Sep. 1976, ISSN: 1528901X. DOI: 10.1115/1.3448334.
- [20] D. Japikse, "A critical evaluation of three centrifugal compressors with pedigree data sets: Part 5—studies in component performance", *Journal of Turbomachinery*, vol. 109, no. 1, pp. 1–9, Jan. 1987, ISSN: 15288900. DOI: 10.1115/1.3262064.
- [21] X. Qiu, D. Japikse, J. Zhao, and M. R. Anderson, "Analysis and Validation of a Unified Slip Factor Model for Impellers at Design and Off-Design Conditions", *Journal of Turbomachinery*, vol. 133, no. 4, Apr. 2011, ISSN: 0889-504X. DOI: 10.1115/1.4003022.
- [22] A. Stodola, *Steam and Gas Turbines*. New York: McGraw-Hill, 1945.
- [23] E. J. Wiesner, "A Review of Slip Factors for Centrifugal Impellers", *Journal of Engineering for Power*, vol. 89, no. 4, pp. 558–566, Oct. 1967, ISSN: 0022-0825. DOI: 10.1115/1.3616734.
- [24] T. W. von Backström, "A unified correlation for slip factor in centrifugal impellers", *Journal of Turbomachinery*, vol. 128, no. 1, pp. 1–10, Jan. 2006, ISSN: 0889504X. DOI: 10.1115/1.2101853.
- [25] M. Casey and C. Robinson, *Radial Flow Turbocompressors: Design, Analysis, and Applications*, 1st. Cambridge University Press, 2021, ISBN: 1108416675. DOI: 10.1017/9781108241663.
- [26] E. W. Lemmon, I. H. Bell, M. L. Huber, and M. O. McLinden, *NIST Standard Reference Database 23: Reference Fluid Thermodynamic and Transport Properties-REFPROP, Version 10.0*, National Institute of Standards and Technology, 2018. DOI: <https://doi.org/10.18434/T4/1502528>. [Online]. Available: <https://www.nist.gov/srd/refprop>.
- [27] I. H. Bell, J. Wronski, S. Quoilin, and V. Lemort, "Pure and pseudo-pure fluid thermophysical property evaluation and the open-source thermophysical property library coolprop", *Industrial & Engineering Chemistry Research*, vol. 53, no. 6, pp. 2498–2508, 2014. DOI: 10.1021/ie4033999.
- [28] J. Tiainen, A. Jaatinen-Värri, A. Grönman, P. Sallinen, J. Honkatukia, and T. Hartikainen, "Validation of the Axial Thrust Estimation Method for Radial Turbomachines", *International Journal of Rotating Machinery*, vol. 2021, 2021, ISSN: 15423034. DOI: 10.1155/2021/6669193.
- [29] *CadQuery, Release 2*, 2022. [Online]. Available: <https://github.com/CadQuery/cadquery/>.
- [30] M. Van Der Geest, H. Polinder, J. A. Ferreira, and M. Christmann, "Power density limits and design trends of high-speed permanent magnet synchronous machines", *IEEE Transactions on Transportation Electrification*, vol. 1, no. 3, pp. 266–276, Oct. 2015, ISSN: 23327782. DOI: 10.1109/TTE.2015.2475751.
- [31] J. D. Denton, "Loss mechanisms in turbomachines", *Journal of Turbomachinery*, vol. 115, no. 4, pp. 621–656, Oct. 1993, ISSN: 15288900. DOI: 10.1115/1.2929299.
- [32] M. R. Galvas, "Fortran Program for Predicting Off-Design Performance of Centrifugal Compressors", Tech. Rep., 1973.
- [33] W. Jansen, "A method for calculating the flow in a centrifugal impeller when entropy gradient are present", *Inst. Mech. Eng. Internal Aerodynamics*, 1970.
- [34] R. H. Aungier, *Centrifugal Compressors: A Strategy for Aerodynamic Design and Analysis*. ASME Press, Aug. 2000. DOI: 10.1115/1.800938.
- [35] J. Coppage, F. Dallenbach, H. Eichenberger, G. Hlavaka, E. Knoernschild, and N. Van Lee, "Study of Supersonic Radial Compressors for Refrigeration and Pressurization on Systems", WADC 55–257, 1956.
- [36] J. J. Brasz, "Investigation into the Effect of Tip Clearance on Centrifugal Compressor Performance", in *Proceedings of the ASME Turbo Expo*, 1988. DOI: 10.1115/88-GT-190.
- [37] J. F. Johnston and R. C. Dean, "Losses an vaneless diffusers of centrifugal compressors and pumps: Analysis, experiment, and design", *Journal of Engineering for Gas Turbines and Power*, vol. 88, no. 1, pp. 49–60, Jan. 1966, ISSN: 15288919. DOI: 10.1115/1.3678477.

- [38] J. Stanitz, "One-dimensional compressible flow in vaneless diffusers of radial-and mixed-flow centrifugal compressors, including effects of friction, heat transfer and area change", Tech. Rep., 1952.
- [39] "AIR1168/1: Thermodynamics of Incompressible and Compressible Fluid Flow", SAE International, Tech. Rep., 2019.
- [40] C. F. Colebrook, "Turbulent Flow in Pipes, with Particular Reference to the Transition Region Between the Smooth and Rough Pipe Laws.", *Journal of the Institution of Civil Engineers*, vol. 11, no. 4, pp. 133–156, Feb. 1939, ISSN: 0368-2455. DOI: 10.1680/ijoti.1939.13150.
- [41] J. W. Daily and R. E. Nece, "Chamber dimension effects on induced flow and frictional resistance of enclosed rotating disks", *Journal of Fluids Engineering, Transactions of the ASME*, vol. 82, no. 1, pp. 217–230, Mar. 1960, ISSN: 1528901X. DOI: 10.1115/1.3662532.
- [42] H. W. Oh, E. S. Yoon, and M. K. Chung, "An optimum set of loss models for performance prediction of centrifugal compressors", *Proceedings of the Institution of Mechanical Engineers, Part A: Journal of Power and Energy*, vol. 211, no. 4, pp. 331–338, Jun. 1997, ISSN: 0957-6509. DOI: 10.1243/0957650971537231.
- [43] C. Freeman and N. A. Cumpsty, "Method for the prediction of supersonic compressor blade performance", *Journal of Propulsion and Power*, vol. 8, no. 1, pp. 199–208, May 1992, ISSN: 07484658. DOI: 10.2514/3.23461.
- [44] M. Marconcini, A. Bianchini, M. Checcucci, *et al.*, "A three-dimensional time-accurate computational fluid dynamics simulation of the flow field inside a vaneless diffuser during rotating stall conditions", *Journal of Turbomachinery*, vol. 139, no. 2, Feb. 2017, ISSN: 15288900. DOI: 10.1115/1.4034633.
- [45] H. Kobayashi, H. Nishida, T. Takagi, and Y. Fukushima, "A study on the rotating stall of centrifugal compressors. II - Effect of vaneless diffuser inlet shape on rotating stall", *JSMET*, vol. 56, pp. 2646–2651, 1990, ISSN: 0387-5016.
- [46] Y. Senoo and Y. Kinoshita, "Influence of inlet flow conditions and geometries of centrifugal vaneless diffusers on critical flow angle for reverse flow", *Journal of Fluids Engineering, Transactions of the ASME*, vol. 99, no. 1, pp. 98–102, Mar. 1977, ISSN: 1528901X. DOI: 10.1115/1.3448577.
- [47] D. Eckardt, "Investigation of the Jet-Wake Flow of a Highly-Loaded Centrifugal Compressor Impeller", Ph.D. dissertation, 1977, pp. 1–227.
- [48] A. Giuffrè, P. Colonna, and M. Pini, "Design Optimization of a High-Speed Twin-Stage Compressor for Next-Gen Aircraft Environmental Control System", *Journal of Engineering for Gas Turbines and Power*, vol. 145, no. 3, Mar. 2023, ISSN: 0742-4795. DOI: 10.1115/1.4056022.
- [49] ANSYS Inc., *ANSYS Academic Research CFX, Release 19.3*, Canonsburg, PA, 2019. [Online]. Available: <http://www.ansys.com>.
- [50] K. Deb, A. Pratap, S. Agarwal, and T. Meyarivan, "A fast and elitist multiobjective genetic algorithm: NSGA-II", *IEEE Transactions on Evolutionary Computation*, vol. 6, no. 2, pp. 182–197, Apr. 2002. DOI: 10.1109/4235.996017.
- [51] J. Blank and K. Deb, "Pymoo: Multi-Objective Optimization in Python", *IEEE Access*, vol. 8, pp. 89 497–89 509, 2020. DOI: 10.1109/ACCESS.2020.2990567.
- [52] O. Balje, *Turbomachines: a guide to design, selection and theory*. Wiley, New York, 1981.
- [53] ANSYS Inc., *ANSYS Academic Research BladeGen, Release 19.3*, Canonsburg, PA, 2019. [Online]. Available: <http://www.ansys.com>.
- [54] R. Otero, J. Gustavo, A. Patel, R. Diez S., and R. Pecnik, "Turbulence modelling for flows with strong variations in thermo-physical properties", *International Journal of Heat and Fluid Flow*, vol. 73, pp. 114–123, Oct. 2018, ISSN: 0142-727X. DOI: 10.1016/J.IJHEATFLUIDFLOW.2018.07.005.
- [55] T. Barth and D. Jespersen, "The design and application of upwind schemes on unstructured meshes", Jan. 1989. DOI: 10.2514/6.1989-366.
- [56] M. Elfert, A. Weber, D. Wittrock, A. Peters, C. Voss, and E. Nicke, "Experimental and numerical verification of an optimization of a fast rotating high-performance radial compressor impeller", *Journal of Turbomachinery*, vol. 139, no. 10, Oct. 2017, ISSN: 15288900. DOI: 10.1115/1.4036357/378792.

3

DESIGN OF THE TWIN-STAGE CENTRIFUGAL COMPRESSOR FOR THE IRIS TEST RIG

I don't know anything with certainty, but seeing the stars makes me dream.

Vincent Van Gogh

Parts of this chapter have been published in:

A. Giuffre', P. Colonna, and M. Pini, "Design Optimization of a High-Speed Twin-Stage Compressor for Next-Gen Aircraft Environmental Control System", *Journal of Engineering for Gas Turbines and Power*, vol. 145, no. 3, 2023, ISSN: 0742-4795. DOI: 10.1115/1.4056022.

Abstract

This chapter documents the fluid dynamic design optimization of the high-speed centrifugal compressor which will be installed in the IRIS, the heat pump test rig designed and commissioned at the Propulsion and Power Laboratory of Delft University of Technology. The compressor features a twin-stage configuration, consisting of two impellers mounted back-to-back on the same shaft and running on gas bearings operating with refrigerant vapor. First, the scaling analysis for single-stage centrifugal compressors is extended to provide guidelines for the design of twin-stage machines. The optimal set of non-dimensional parameters obtained from the scaling analysis suggests that the first stage of the twin-stage machine must be designed for a higher compression ratio and with a value of swallowing capacity in the proximity of the locus of optimal efficiency. In turn, by selecting the same value of the work coefficient for the two stages, the flow coefficient of the second stage lies in the region of optimal operating range. Next, the conceptual design optimization of the compressor prototype was performed by resorting to an in-house reduced-order model (ROM), coupled with a multi-objective optimization framework. Then, the flow path of the optimal design was refined based on the results of a throughflow method. Finally, the fluid dynamic performance of the optimal design was evaluated by means of a hybrid framework, encompassing CFD models and ROMs, and the structural integrity was assessed by means of FEA. The results show that it is possible to design a twin-stage compressor for the target application, featuring an overall efficiency higher than 65% and a maximum compression ratio exceeding 8.5, despite the detrimental effects of motor and bearings cooling, as well as the fluid dynamic performance penalty due to the small scale.

3.1. INTRODUCTION

The technical feasibility and the performance of an electrically-powered VCC system for next-generation aircraft ECS will be investigated through a series of experimental campaigns that will be performed by means of the IRIS test rig. At the core of the new facility, there is a high-speed twin-stage centrifugal compressor running on foil bearings, lubricated by refrigerant vapor. The reduced size, the absence of oil lubricant in the circuit, and the superior performance over traditional scroll compressors make this technology particularly suitable for airborne applications.

The feasibility of a miniature centrifugal compressor running on gas bearings for domestic heat pump applications has been demonstrated by Schiffmann et al. [1], [2]. Chapter 2 presents a systematic investigation on the influence of size and working fluid on various design aspects concerning single-stage high-speed compressors. However, the design of a twin-stage compressor, featuring two compressor wheels in series and mounted in back-to-back configuration on the same shaft involves additional considerations regarding the split of the duty among the two stages, the balance of axial thrust, the cooling of the bearings, and that of the electric motor. The objectives of this work are therefore:

- the extension of the scaling analysis to the case of twin-stage compressors to support the designer in the choice of the non-dimensional parameters characterizing the conceptual design of the two stages;
- the multi-objective conceptual design optimization of the twin-stage compressor to be installed in the IRIS test rig;

- the performance characterization of the optimal compressor design by means of computational fluid dynamics (CFD), and the preliminary structural assessment by means of finite element analysis (FEA).

This chapter is structured as follows. First, the extension of the scaling analysis and the conceptual design model for twin-stage compressors are described. Next, the results of the multi-objective conceptual design optimization are presented, and the differences between the optimal compressor configurations obtained as outcomes of two subsequent design iterations are discussed. Finally, the fluid dynamic performance of the selected designs, characterized by means of CFD, and a preliminary structural assessment, performed with FEA, are presented.

3.2. METHODOLOGY

3.2.1. SCALING ANALYSIS FOR TWIN-STAGE COMPRESSORS

The scaling law applied to single-stage centrifugal compressors can be expressed as [3]

$$\mathbf{y} = f(\phi_{t1}, \psi, \alpha_2, \beta, \overline{\gamma_{Pv}}, Re, \boldsymbol{\sigma}). \quad (3.1)$$

In Eqn. (3.1), the vector \mathbf{y} collects the compressor stage characteristics, e.g., rotational speed, impeller tip radius, and performance metrics, e.g., efficiency, operating range, and the vector $\boldsymbol{\sigma}$ groups of the non-dimensional geometrical parameters as listed in Table 3.1. The stage velocity triangles are univocally defined by the choice of ϕ_{t1} , ψ , and α_2 . The work input can be expressed as a function of the compression ratio β . Moreover, the influence of the working fluid and of flow non-ideality can be assessed by computing the average value of the isentropic pressure-volume exponent [4], [5], as reported in Chapter 2. Lastly, the impact of viscous effects is determined by evaluating the average value of the Reynolds number throughout the compressor stage.

For a twin-stage compressor, the design process encompasses additional requirements: the mass flow rate and the rotational speed must be equal for the two stages, and the designer has to decide how to split the compression ratio. In order to conceptually address the problem of determining the optimal duty of the two stages, the scaling analysis can be extended as follows. Starting from the definition of the swallowing capacity

$$\phi_{t1} = \frac{\dot{m}}{\rho_{t1} U_2 D_2^2} = \frac{2\dot{V}_{t1}}{D_2^3 \Omega}, \quad (3.2)$$

and imposing constant rotational speed, the ratio of the flow coefficients of the two stages can be written as

$$\frac{\phi_{t1}|_{s1}}{\phi_{t1}|_{s2}} = \frac{D_2^3|_{s2}}{D_2^3|_{s1}} \cdot \frac{\dot{V}_{t1}|_{s1}}{\dot{V}_{t1}|_{s2}}. \quad (3.3)$$

The split of the compression ratio among the two stages can be expressed as a function of the splitting factor κ_s

$$\begin{cases} \beta_{tt}|_{s1} = \kappa_s \sqrt{\beta_{tt}/\kappa_s} \\ \beta_{tt}|_{s2} = \sqrt{\beta_{tt}/\kappa_s} \end{cases} \quad (3.4)$$

Table 3.1: Non-dimensional geometrical characteristics of a single-stage centrifugal compressor, collected in the vector σ . The main geometrical features of the prescribed compressor configuration are displayed in Fig. 3.3.

Description	Definition
Impeller shape factor	$k = 1 - \left(\frac{R_{1,h}}{R_{1,s}}\right)^2$
Number of blades	N_{bl}, N_{split}
Diffuser radius ratio	R_3/R_2
Diffuser blade height ratio	$H_{r,pinch} = \frac{H_3 - H_2}{H_2(R_2/R_{pinch} - 1)}$
Diffuser pinch radius ratio	$R_{r,pinch} = \frac{R_{pinch} - R_2}{R_3 - R_2}$
Non-dimensional length	L_{ax}/R_2
Leading edge thickness ratio	$\frac{t_{le}(N_{bl} + N_{split})}{2\pi R_1}$
Trailing edge thickness ratio	$\frac{t_{te}(N_{bl} + N_{split})}{2\pi R_1}$
Relative tip clearance	c_t/H_2
Relative back face clearance	c_b/H_2
Relative surface roughness	$Ra/D_{hd,imp}$
Shaft radius ratio	$R_{shaft}/R_{1,h}$

In turn, for a fixed value of mass flow rate in the two stages, assuming constant pressure-volume isentropic exponent over the entire compression process, and neglecting total pressure losses between the outlet of the first impeller and the inlet of the second stage, the ratio of the volumetric flow rates defined at the impeller inlet can be expressed as a function of κ_s

$$\frac{\dot{V}_{t1}|_{s1}}{\dot{V}_{t1}|_{s2}} = \frac{\dot{m}|_{s1}}{\dot{m}|_{s2}} \cdot \frac{\rho_{t1}|_{s2}}{\rho_{t1}|_{s1}} = \left(\sqrt{\beta_{tt} \cdot \kappa_s}\right)^{\frac{1}{\gamma_{pv}}}. \quad (3.5)$$

Furthermore, by rearranging the definition of the work coefficient

$$\psi = \frac{\Delta h_{tt}}{U_2^2} = \frac{4\Delta h_{tt}}{\Omega^2 D_2^2} = \frac{4}{\Omega^2 D_2^2} \frac{P_{t1}}{\rho_{t1}} \frac{\overline{\gamma_{pv}}}{\overline{\gamma_{pv}} - 1} \left(\beta_{tt}^{\frac{\overline{\gamma_{pv}} - 1}{\overline{\gamma_{pv}}}} - 1 \right), \quad (3.6)$$

it is possible to make explicit the dependence of the ratio of the work coefficients on the splitting factor κ_s , and on the ratio between the impeller tip diameters, thus

$$\frac{\psi|_{s1}}{\psi|_{s2}} = \left(\sqrt{\beta_{tt} \cdot \kappa_s}\right)^{\frac{1}{\gamma_{pv}} - 1} \cdot \frac{\left(\sqrt{\beta_{tt} \cdot \kappa_s}\right)^{\frac{\overline{\gamma_{pv}} - 1}{\overline{\gamma_{pv}}}} - 1}{\left(\sqrt{\beta_{tt}}\right)^{\frac{\overline{\gamma_{pv}} - 1}{\overline{\gamma_{pv}}}} - 1} \cdot \frac{D_2^2|_{s2}}{D_2^2|_{s1}}. \quad (3.7)$$

Finally, by combining Eqn. (3.3), (3.5), (3.7), it is possible to relate the flow coefficients ratio with the ratio of the work coefficients, the splitting factor, the overall compression ratio,

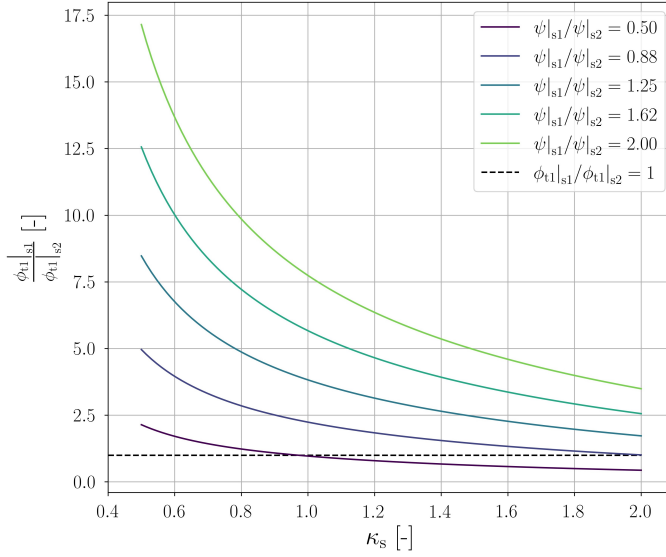


Figure 3.1: Trend of flow coefficients ratio, as a function of the splitting factor, and of the work coefficients ratio. The data have been generated considering an overall compression ratio $\beta_{tt} = 7$, and an average value of isentropic exponent $\overline{\gamma_{Pv}} = 1.075$, corresponding to the specifications set during the first design iteration of the IRIS compressor.

and the average value of the isentropic exponent over the thermodynamic transformation

$$\frac{\phi_{t1}|_{s1}}{\phi_{t1}|_{s2}} = f\left(\frac{\psi|_{s1}}{\psi|_{s2}}, \kappa_s, \beta_{tt}, \overline{\gamma_{Pv}}\right). \quad (3.8)$$

The relation expressed by Eqn. (3.8) is graphically displayed in Fig. 3.1 for a prescribed value of compression ratio and average isentropic exponent. By analyzing the trends, one can notice that the selection of an equal split of compression ratio among the two stages, i.e., $\kappa_s = 1$, combined with the choice of constant flow coefficient, i.e., $\phi_{t1}|_{s1}/\phi_{t1}|_{s2} = 1$, leads to a strong unbalance of the work coefficients, with the second stage affected by a larger non-dimensional duty. On the other hand, the higher the selected ratio of work coefficients, the larger the resulting flow coefficients ratio. The disparity in the flow coefficients of the two stages is attenuated by increasing the value of κ_s , i.e., by increasing the compression ratio of the first stage.

For high-speed miniature centrifugal compressors, the choice of the splitting factor is primarily driven by manufacturing constraints. Given that the second stage inherently features a lower volumetric flow rate, its efficiency and operating range are penalized by larger values of relative tip clearance, relative surface roughness, and blade blockage. A design approach to limit the impact of such detrimental effects consists in selecting $\kappa_s \geq 1$, and maximizing the efficiency of the first stage, i.e., the one providing most of the compression. Fig. 3.2 shows the contours of the total-to-total efficiency and operating range, i.e., $OR = (\dot{m}_{max} - \dot{m}_{min})/\dot{m}_{des}$ at Ω_{des} , of a miniature compressor stage operating with

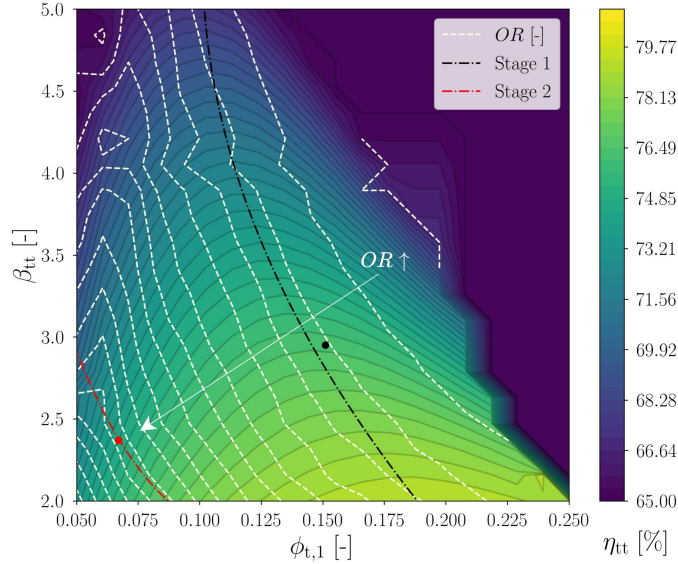


Figure 3.2: Design map of η_{tt} and OR determined for R1233zd(E) as working fluid at $P_{t1} = 0.5$ bar, $T_{t1} = 283.15$, $\psi_{is} = 0.8$. The dashed black and red lines correspond to the theoretical locii of optimal design for the two stages, computed by maximizing η_{tt} of stage 1 and fixing $\psi|_{s1}/\psi|_{s2} = 1$. The black and red dots correspond to the design points selected by the multi-objective optimizer during the first design iteration of the IRIS compressor. Calculations are performed with the compressor module of *TurboSim*.

R1233zd(E) as the working fluid[3]. The efficiency of the first stage can be maximized by selecting a design point lying on the locus of optimal ϕ_{t1} , namely the dashed black line. By selecting $\kappa_s \geq 1$, $\psi|_{s1}/\psi|_{s2} = 1$, and based on Eqn. (3.3), the flow coefficient of the second stage is located on the dashed red line, which lies within the region of optimal operating range. The consequence thereof is that the efficiency of the entire compression process is enhanced, without penalizing the operating range of the twin-stage machine.

3.2.2. EXTENSION OF THE COMPRESSOR DESIGN MODEL

The model used for the conceptual design of single-stage centrifugal compressors is presented in Chapter 2, together with the validation against experimental data and CFD simulation results. In this section, only the additional procedures needed to cope with the design of twin-stage compressors are discussed. The compressor configuration under analysis is schematically displayed in Fig. 3.3. A prototype of a twin-stage compressor developed by the industrial partner Aeronamic BV and operating with refrigerant R134a is shown in Fig. 3.4.

The two compressor wheels are mounted on the same shaft, thus the rotational speed of the second impeller is constrained by the design of the first stage. In other words, once the design of the first impeller is fixed, the choice of the work coefficient of the second stage univocally determines its flow coefficient, or viceversa. As a consequence, an ad-hoc design strategy is needed to comply with both the requirements of high efficiency and wide operating range, as discussed in the previous section. In addition, the use of

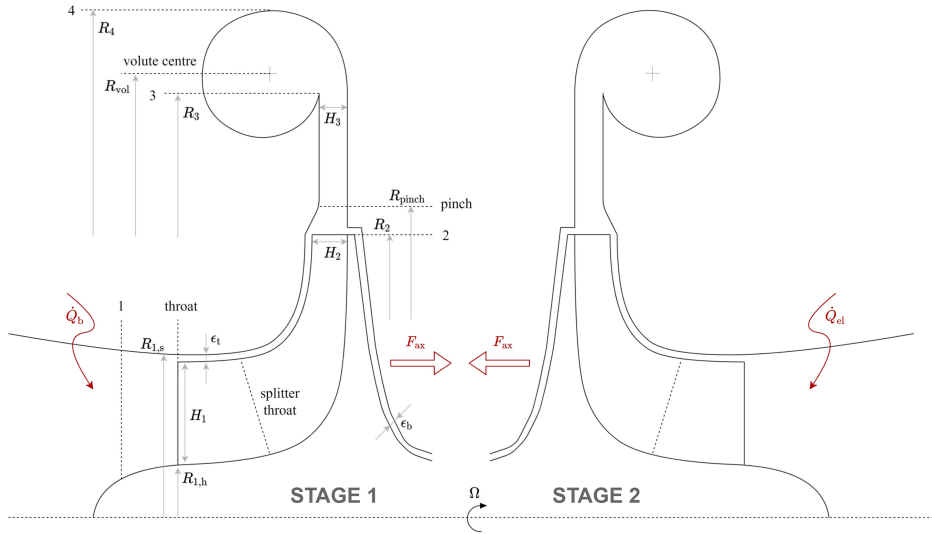


Figure 3.3: Meridional view of a twin-stage centrifugal compressor, featuring two stages mounted in back-to-back configuration on the same shaft.

gas bearings imposes stringent constraints on the maximum allowable axial thrust generated by the two compressor wheels. To cope with this limitation, it is necessary to adopt a back-to-back configuration and to carefully design the two impellers to balance their axial thrust. In the reduced-order compressor model, this is achieved by estimating the axial thrust of the two stages with the method proposed in [6], and by imposing a constraint on the maximum unbalance, computed over the entire operating range. Finally, the strong compactness requirement for the entire compressor assembly poses additional challenges with regard to bearings and electric motor cooling. In the proposed twin-stage configuration, a small portion of the refrigerant mass flow is bled at the outlet of the first stage and is recirculated at the inlet of the machine, after being used for bearings cooling. At the same time, the main portion of the pressurized refrigerant vapor leaving the first stage is used to cool the electric motor, before entering the second stage. In this way it is possible to obtain a very compact compressor assembly, which does not rely on external cooling flows for its thermal management, at the expenses of a fluid dynamic efficiency penalty, due to inter-stage flow heating. However, for future research and development of this technology, it is highly recommended to explore different cooling strategies for the bearings and electric motor, which stem from a higher level of integration between the twin-stage compressor and the heat pump. For example, the flow leaving the evaporator could be used to cool the electric motor before entering the first compressor stage. This solution simultaneously eliminates the need of superheating in the evaporator to avoid liquid ingestion in the compressor, and alleviates the performance penalty associated with inter-stage flow heating.

A summary of the design procedure implemented in the ROM is presented in Fig. 3.5. The design process starts by prescribing the set of specifications, constraints, and design

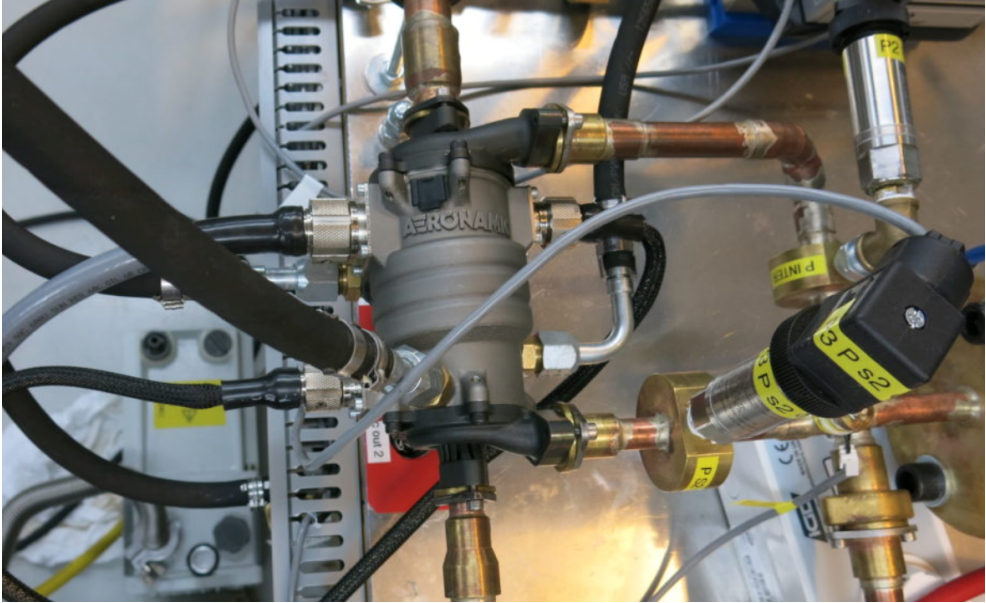


Figure 3.4: Prototype of a twin-stage high-speed centrifugal compressor operating with refrigerant R134a. The picture has been taken during a test campaign and is courtesy of Aeronamic BV.

variables, either as fixed values or as upper and lower bounds for optimization. First, the compression ratio is split between the two stages, according to the set value of the splitting factor. Then, the first compressor stage is designed at the nominal inlet conditions. Once the thermodynamic state at the outlet of the first stage is known, its inlet conditions are computed. This is accomplished by evaluating the mixing process occurring between the incoming flow and the stream of refrigerant vapor diverted for bearings cooling. Next, the first stage is re-designed at the updated inlet conditions, and its off-design performance is computed by accounting for the change in the thermodynamic state of the bearings cooling stream at each operating point. If the model is used to perform a design optimization, the off-design performance is computed only at the design rotational speed, to reduce the computational cost. Once this step is completed, the design of the second stage is addressed. The inlet conditions of the second stage are initially computed by prescribing a total pressure drop at the outlet of the first stage, to account for the presence of the return channel. Then, once the design of the second stage is set, the total electric power consumption is computed at the design point, together with the heat flow rate that must be dissipated to ensure safe operation of the electric motor. Subsequently, the inlet conditions of the second stage are adjusted, by accounting for the cooling of the electric motor by means of the inter-stage flow. Next, in the same fashion as for the first stage, the second stage is re-designed based on the updated inlet conditions, and its off-design performance is computed, by accounting for the change in the thermodynamic state of the inter-stage flow at each operating point. Finally, the operating map of the twin-stage compressor is computed by combining the performance data computed for the two stages.

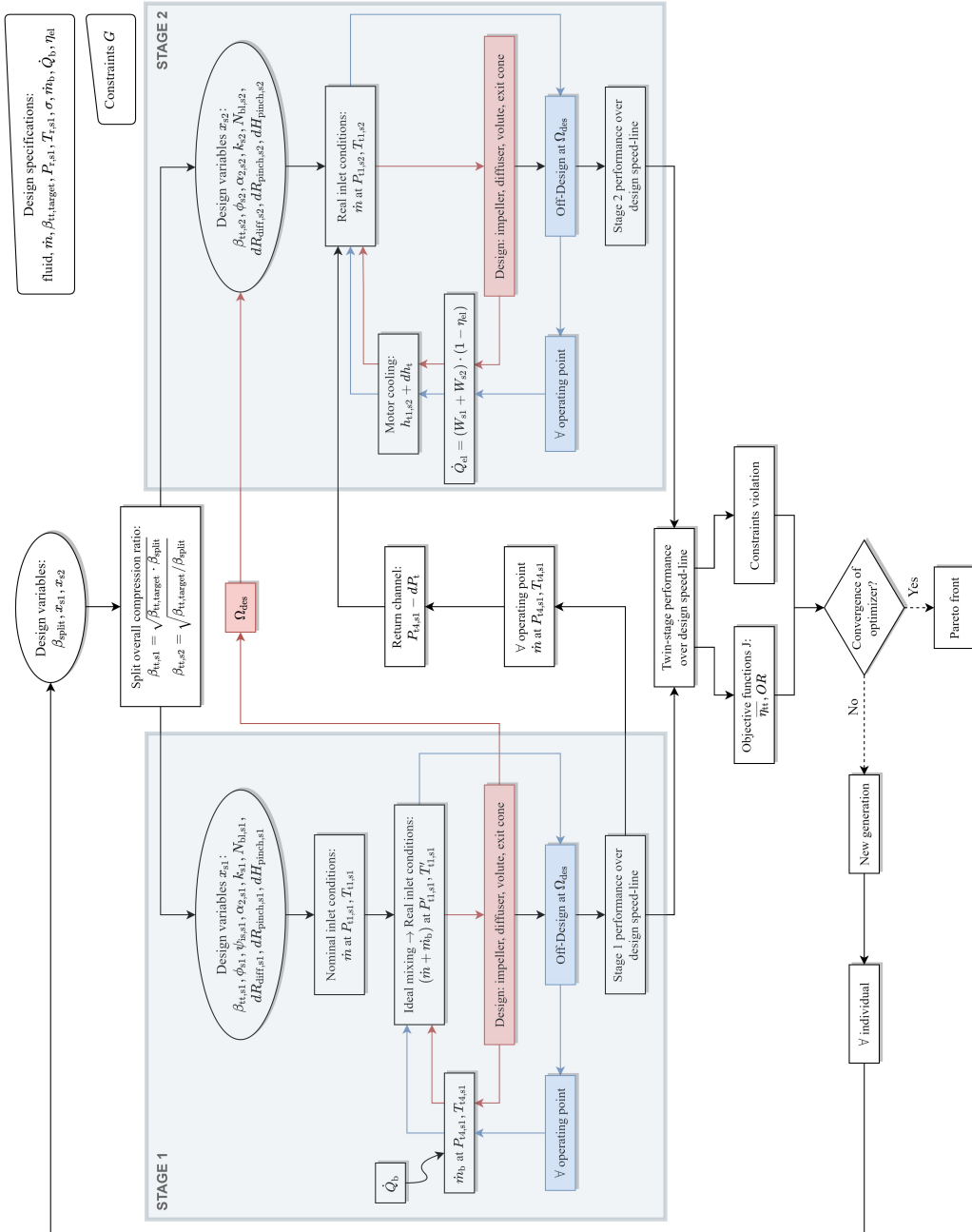


Figure 3.5: Flowchart of the conceptual design method for twin-stage compressors implemented in the reduced-order model.

3.3. FLUID DYNAMIC DESIGN OF THE IRIS COMPRESSOR

3.3.1. CONCEPTUAL DESIGN OPTIMIZATION

The in-house compressor model has been coupled with a multi-objective optimization framework and has been used to perform the conceptual design of the twin-stage compressor to be installed in the IRIS test rig. The prescribed objective functions are the operating range, i.e., $OR = (\dot{m}_{\max} - \dot{m}_{\min}) / \dot{m}_{\text{des}}$, and the compressor efficiency, both evaluated at the design rotational speed. To account for multiple operating points, the compressor efficiency is computed as the weighted average of the total-to-total efficiency, evaluated over the design speed-line. The weights used for this calculation are inversely proportional to the distance of each operating point from the selected design point. A set of non-linear constraints are imposed to ensure compressor manufacturability. Moreover, additional constraints are imposed on the rotational speed, axial thrust, power, and torque associated with the two impellers, to cope with the design requirements of the electric motor and the gas bearings. The values of these constraints are provided by the industrial partner Aeronamic BV and are compared with the maxima evaluated over the design speed-line.

The design of the IRIS compressor has been conducted in two steps. Given the power rating of the electric motor provided by Aeronamic BV, the mass flow rate and compression ratio defining the design point of the IRIS test rig could not be met simultaneously. In turn, to comply with the specifications of the electric motor, the first design iteration has been performed by setting a lower value of compression ratio, while matching the design point mass flow rate of the IRIS test rig. Then, once the design framework has been tested, the design of the twin-stage machine has been repeated by increasing the value of the target compression ratio, while lowering the design point mass flow rate. Moreover, based on the updated manufacturing constraints provided by the industrial partner, the second design iteration features more stringent requirements on the maximum rotational speed, impeller hub radius, and blade height at the impeller outlet. The parameters, design variables, equality, and inequality constraints set in the two design iterations are summarized in Table 3.2.

Overall, the optimization problem features 2 objectives, 16 design variables, and 17 non-linear constraints. The Pareto front is computed with the NSGA-II algorithm described in [7], and implemented in the open-source library Pymoo [8]. All the optimization variables are floating point, except for the number of blades of the two impellers, which are treated as integers. The initial population comprises ten individuals for each design variable and is sampled according to the Latin hypercube methodology along the floating point directions, and randomly along the integer axes. The population is evolved for 120 generations, leading to a total of 19,200 function evaluations. The optimal conceptual design has been selected as a trade-off between compressor efficiency and operating range, by giving priority to the operating range, as required by the target application. The resulting set of design variables for the two stages of the twin-stage compressor is reported in Table 3.3.

By analyzing the results of the first design iteration, it is possible to formulate the following considerations. The optimal value of the splitting factor is equal to 1.25. As a result, the first impeller is characterized by a higher compression ratio than the second, while the work coefficient is nearly the same for the two stages. Moreover, the first impeller features

Table 3.2: Settings used for the multi-objective optimization of the twin-stage compressor for the IRIS test rig.

Variable	Type	1 st design	2 nd design
$\beta_{tt,target}$	Parameter	7	9
\dot{m}	Parameter	0.114 kg/s	0.1 kg/s
fluid	Parameter	R1233zd(E)	R1233zd(E)
$P_{t1} _{s1}$	Parameter	47.79 kPa	47.79 kPa
$T_{t1} _{s1}$	Parameter	283.19 K	283.19 K
\dot{m}_b	Parameter	0.0044 kg/s	0.0044 kg/s
\dot{Q}_b	Parameter	360 W	360 W
$e_{t,le}$	Parameter	0.2 mm	0.4 mm
$e_{t,te}$	Parameter	0.15 mm	0.15 mm
e_b	Parameter	0.15 mm	0.15 mm
Ra	Parameter	3.2 μ m	3.2 μ m
$t_{b1,h}$	Parameter	0.6 mm	0.6 mm
$t_{b1,s}$	Parameter	0.3 mm	0.3 mm
R_{shaft}	Parameter	7.5 mm	7.5 mm
κ_s	Design variable	0.5-2	0.5-2
$\phi_{t1} _{s1-s2}$	Design variable	0.06-0.2	0.06-0.2
$\psi_{is} _{s1}$	Design variable	0.6-1.0	0.6-1.0
$\alpha_2 _{s1-s2}$	Design variable	60°-75°	60°-75°
$k _{s1-s2}$	Design variable	0.65-0.95	0.65-0.95
$N_{b1} _{s1-s2}$	Design variable	12-20	12-20
$R_3/R_2 _{s1-s2}$	Design variable	1.3-2	1.3-2
$R_{r,pinch} _{s1-s2}$	Design variable	0-1	0-1
$H_{r,pinch} _{s1-s2}$	Design variable	0-1	0-1
$R_{1,h} _{s1-s2}$	Equality constraint	-	4.5 mm
$\min(R_{1,h}) _{s1-s2}$	Inequality constraint	3.25 mm	-
$\min(a) _{s1-s2}$	Inequality constraint	1 mm	1 mm
$\min(H_2) _{s1-s2}$	Inequality constraint	1.35 mm	1.5 mm
$\max(R_4) _{s1-s2}$	Inequality constraint	50 mm	43 mm
$\max(M_3) _{s1-s2}$	Inequality constraint	0.6	0.7
$\min(\dot{m}_{max}/\dot{m}_{des}) _{s1-s2}$	Inequality constraint	1.1	1.1
$\min(\Omega) - \max(\Omega)$	Inequality constraint	50-112 krpm	50-103 krpm
$\max(\Delta F_{ax})$	Inequality constraint	26 N	26 N
$\max(P_{el})$	Inequality constraint	6.1 kW	6.5 kW
$\max(T)$	Inequality constraint	0.52 Nm	0.55 Nm

a value of swallowing capacity that is 2.25 times larger than the one of the second stage. These trends confirm the validity of the design guidelines derived from the extended scaling analysis for twin-stage compressors. The same trends are further corroborated by the results obtained as an outcome of the second design iteration. However, in the second design, the value of the splitting factor and the difference between the swallowing capacity of the two stages are smaller. This is due to the more stringent constraint imposed on the maximum rotational speed, which, in turn, imposes an upper limit to the compression ratio and to the swallowing capacity which can be set in the first stage without increasing the work coefficient. This leads to a higher work coefficient in the second stage, in line with what is reported in Fig. 3.1, i.e., a lower ratio of swallowing capacities leads to a lower ratio of work coefficients, given a fixed splitting factor κ_s . Furthermore, one can

Table 3.3: Design variables corresponding to the first and second stage of the IRIS compressor, obtained as a result of the multi-objective design optimization.

Variable	1 st design	2 nd design
κ_s	1.25	1.09
$\beta_{tt,target} _{s1-s2}$	2.95 - 2.37	3.13 - 2.87
$\phi_{t1} _{s1-s2}$	0.151 - 0.067	0.146 - 0.066
$\psi_{is} _{s1-s2}$	0.83 - 0.76	0.81 - 0.94
$\psi _{s1-s2}$	0.66 - 0.65	0.63 - 0.79
$\alpha_2 _{s1-s2}$	64.2° - 67.4°	65° - 70.4°
$k _{s1-s2}$	0.95 - 0.90	0.91 - 0.79
$N_{b1} _{s1-s2}$	7 - 9	6 - 10
$N_{split} _{s1-s2}$	7 - 9	6 - 10
$R_3/R_2 _{s1-s2}$	1.52 - 1.44	1.34 - 1.37
$R_{pinch}/R_2 _{s1-s2}$	1.46 - 1.38	1.24 - 1.31
$H_3/H_2 _{s1-s2}$	0.72 - 0.75	0.9 - 0.88

notice that both the optimal designs feature a larger value of the impeller absolute outflow angle of the second stage. This is inherently related to the value of the tip clearance gap set by manufacturing limitations. Note that the second impeller systematically features a lower blade height, as a result of the lower volumetric flow rate. In turn, the second stage is always characterized by a higher value of the relative clearance gap, leading to a significant efficiency drop. A viable strategy to limit this efficiency decay is to decrease the meridional component of the velocity at the impeller outlet, in order to increase the outlet blade span. This is achieved by increasing the value of α_2 . Lastly, the conceptual design optimization leads to a lower number of blades in the first impeller. The reason thereof can be attributed to the larger value of the inlet relative Mach number in the first stage, which is a direct consequence of the larger value of the swallowing capacity. As a result, the choice of a lower number of blades is dictated by the requirement of a minimum choke margin at the design point.

3.3.2. 3D BLADE DESIGN

The three-dimensional geometry of the two stages has been designed according to the following methodology. First, the baseline geometry is constructed using a commercial software for turbomachinery geometry generation [9], starting from the main compressor dimensions obtained as an outcome of the conceptual design optimization. The shape of the main and the splitter blades are controlled by specifying the hub, mid, and shroud profiles, and by stacking them along the radial direction at the leading edge. The meridional location of the splitter blade leading edge has been selected to ensure that the geometrical throat is located in the main blade passage. The blades feature a constant thickness of 0.6 mm at the hub section and a linear thickness distribution from 0.3 to 0.5 mm at the shroud section. Furthermore, a linear tapering is set in the span-wise direction, to increase the natural frequency and reduce the stresses on the blades [10]. Then, the shape of the meridional channel and the blade angle distributions at the hub, mid, and shroud sections are manually refined based on the results computed with a commercial through-

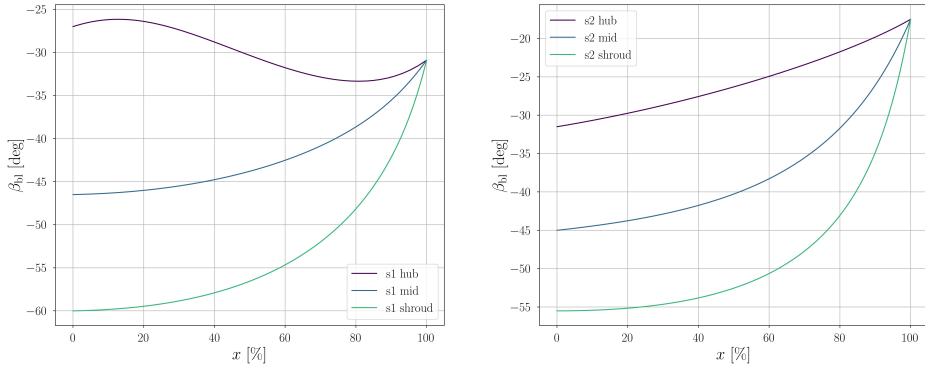


Figure 3.6: Impeller blade angle distribution at the hub, mid, and shroud section of the first (left chart) and second (right chart) stage of the compressor prototype obtained as a result of the second design iteration.

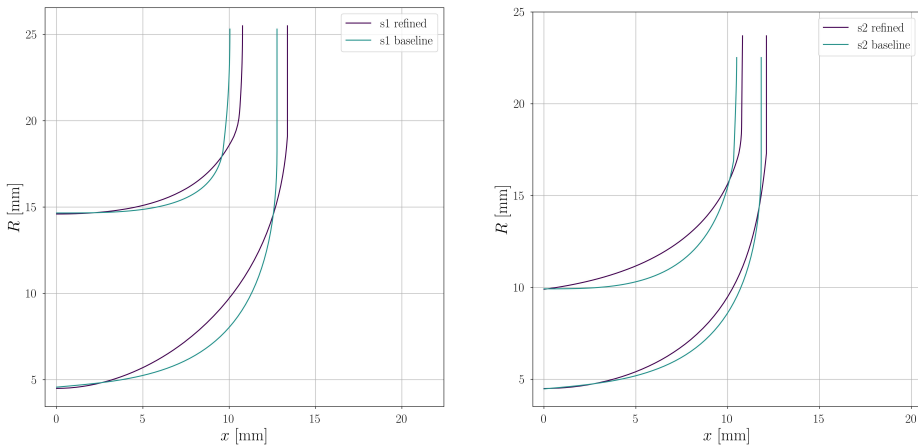


Figure 3.7: Meridional channel of the first (left chart) and second (right chart) stage of the compressor prototype obtained as a result of the second design iteration.

flow solver for radial turbomachinery [11]. For the sake of brevity, only the results of the second design iteration are reported in this section.

The first objective of the detailed fluid dynamic design is to limit flow separation at the shroud section, due to excessive diffusion of the flow within the impeller passage. This is achieved by imposing a lower limit of 0.55 to the de Haller number, computed as the ratio of the relative flow velocity at the inducer shroud and the mean relative velocity at the impeller outlet [12]. The threshold imposed in this work is slightly lower than the value of 0.6 suggested in [10]. However, this is necessary to cope with the prescribed design point pressure ratio and the constraint set on the maximum allowable rotational speed. The second target of the three-dimensional geometry refinement is to control the incidence angle at the hub and shroud sections, to ensure both a high design point efficiency, as well

as a wide operating range. For this purpose, the maximum design point incidence at the shroud section is set at 2° , to avoid excessive leading edge loading and the corresponding local flow acceleration. At the hub section, the maximum allowable incidence is set to 12° , to increase the stall margin and maximize the compressor operating range. Furthermore, the blade angle distributions and the shape of the meridional channel have been adjusted to limit the maximum flow acceleration occurring at the inducer shroud and to avoid flow separation and recirculation at the hub section. The first target is achieved by minimizing both the curvature of the shroud profile as well as the rate of change of the blade angle in the inducer section. Conversely, the second objective is accomplished by increasing the curvature of the hub section. The resulting blade angle distributions and meridional channel profiles characterizing the design of the two stages are shown in Fig. 3.6 and Fig. 3.7, respectively.

The three-dimensional geometry of the two impellers obtained as a result of the detailed design phase is displayed in Fig. 3.8. The design of the two impellers features remarkable differences, as a consequence of the different regime of operation, namely $M_{w1,s}|_{s1} = 1.24$, $M_{w1,s}|_{s2} = 0.84$, and to the discrepancy in volumetric flow rate, i.e., $\dot{V}_1|_{s1} = 0.051$, $\dot{V}_1|_{s2} = 0.016$. Given that the inducer of the first stage is transonic, the blades are designed to be aft-loaded at the shroud, to improve the choke margin and reduce the shock losses [10]. As discussed in Section 3.3.1, the second stage is inherently characterized by a larger relative tip clearance gap, i.e., 18.3%, thus by the unavoidable presence of a massive tip leakage flow. In turn, the design of the second impeller should be aimed at mitigating the interaction of secondary flows with the tip leakage vortex, in order to limit the efficiency penalty induced by viscous mixing. This is achieved by shaping the blades of the second impeller to minimize the difference in span-wise blade loading.

3.3.3. PRELIMINARY STRUCTURAL ASSESSMENT

In order to enhance the structural integrity of backswept impeller blades, the wrap angle distributions at the hub, mid, and shroud sections are commonly selected to ensure a positive value of the rake angle, i.e., the lean angle measured in the direction of rotation at the impeller outlet. However, the wrap angle profile is linked to the blade angle distribution, thus the design problem is overconstrained. In conventional applications, the blade angle distribution at the shroud section is prescribed according to fluid dynamic considerations, and the one at the hub is selected to comply with structural requirements. The result thereof is an s-shaped blade angle profile at the hub section, as displayed in Fig. 3.6 for the first stage.

In the second design iteration, the first impeller blade features a rake angle of 23° . As discussed in Section 3.3.2, for the second stage, the blade angle distribution at the hub has been selected to minimize the interaction of the secondary flows with the tip leakage vortex. This is particularly important in the target application, due to the magnitude of the relative tip clearance gap. As a result, the wrap angle distributions are such to obtain a slightly negative rake angle, i.e., -4° .

To assess the implications of the fluid dynamic design choices on the mechanical integrity of the two impellers, a static structural analysis has been carried out by means of FEA. In analogy with Section 3.3.2, only the structural analysis performed during the second design iteration is discussed here. The prescribed loads are the pressure force acting

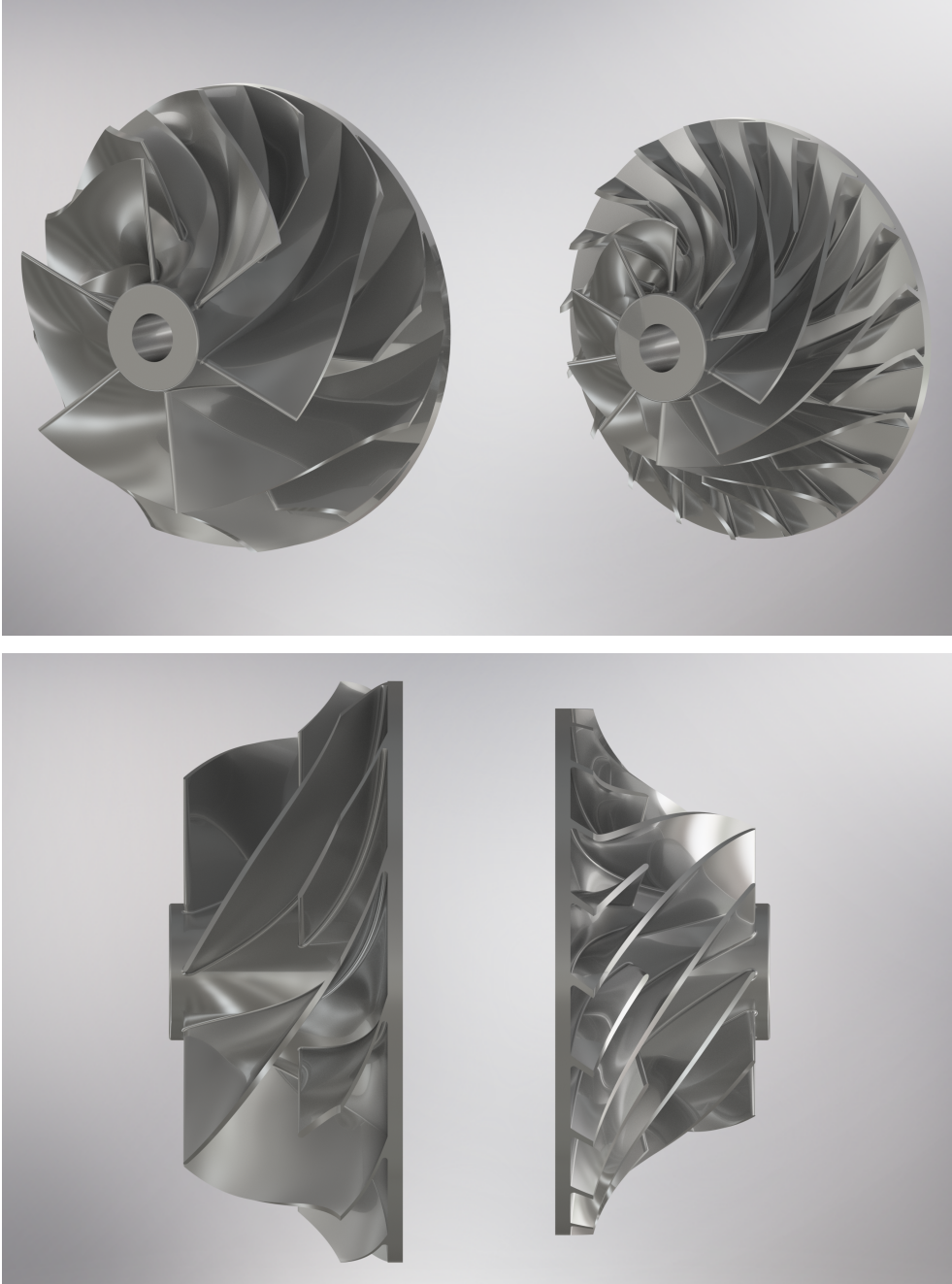


Figure 3.8: Three-dimensional rendering of the two impellers obtained as a result of the detailed design phase of the second design iteration.

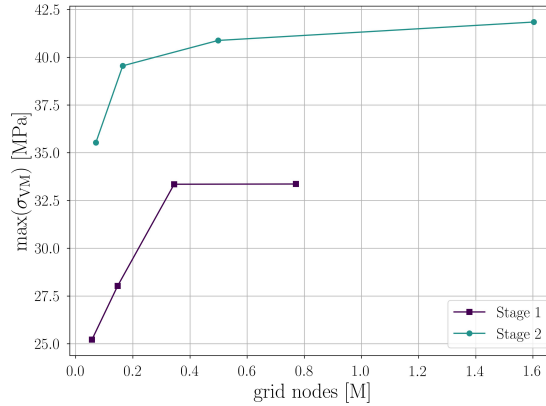


Figure 3.9: Structural grid sensitivity analysis performed on the two impellers obtained as an outcome of the second design iteration.

Table 3.4: Properties of the material selected to manufacture the impellers of the IRIS compressor, i.e., the aluminum alloy Al 2219-T852.

Property	Value	Property	Value
ρ	3100 kg/m ³	T_m	913 K
E	72 GPa	ν	0.33
σ_y	360 MPa	σ_{uts}	460 MPa

on the back disk, the pressure and impulse forces acting on the inlet, the fluid dynamic pressure distribution over the hub and the blades, and the centrifugal force established at the maximum rotational speed, set at 105 krpm. The properties of the selected material, an aluminum alloy, are listed in Table 3.4. The geometry of the two impellers has been discretized by means of second-order 10 nodes tetrahedral elements (TET10). The optimal number of nodes has been computed by means of a grid convergence study, adopting the adaptive mesh refinement feature implemented in [13]. The results displayed in Fig. 3.9 show that a grid of approximately 350k and 500k elements is sufficient to guarantee an accurate estimation of the maximum von Mises stress in the first and second impeller, respectively.

The results of the structural analysis are shown in Fig. 3.10, in terms of equivalent von-Mises stress. Note that the computations have been performed on the entire blisks, but only the contour of the equivalent stress on the blades is displayed. As expected, the maximum stress is located at the blade root and its position is shifted toward the impeller outlet in the second stage, which features a negative rake angle. Nevertheless, the maximum stresses computed for stage 1 and stage 2 are approximately 33.4 Mpa, and 40.9 Mpa, leading to a high safety margin with respect to the yielding stress of the selected material. These results demonstrate that, for small-scale impellers featuring low outlet blade

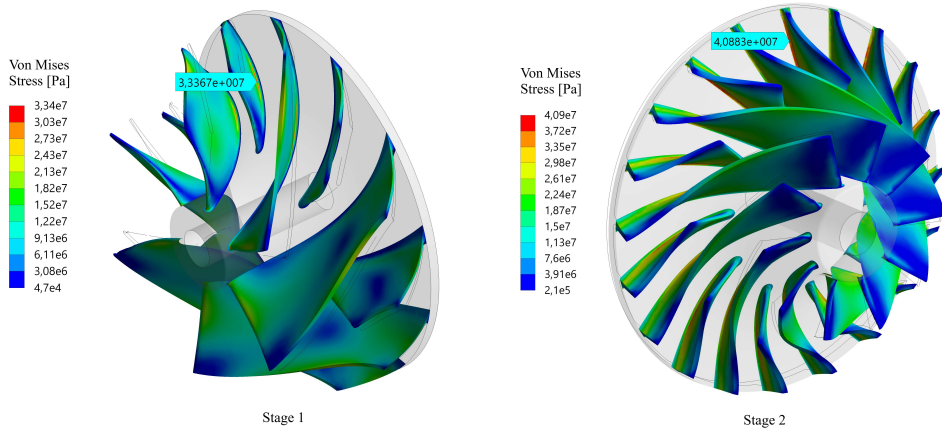


Figure 3.10: Equivalent von Mises stress computed by means of FEA on the grids featuring the optimal number of nodes. The markers highlight the location of the maximum von Mises stress in the two impellers.

height and high relative blade thickness, it is possible to specify a negative rake angle without compromising structural integrity. A more detailed mechanical analysis, including the influence of the shaft and the gas bearings on the rotordynamic characteristics of the system, will be performed by Aeronamic BV.

3.4. FLUID DYNAMIC PERFORMANCE ANALYSIS

3.4.1. HYBRID COMPUTATIONAL METHOD

The fluid dynamic performance of the compressor prototype has been characterized by resorting to a hybrid framework encompassing CFD and reduced-order models, as schematically described in Fig. 3.11. The flow field throughout the impeller and the diffuser of the two stages are simulated with CFD. The fluid dynamic performance of the remaining components along the main flow path, namely the volute, the exit cone, and the return channel, is determined by means of lumped-parameter models [3]. The choice of this modeling approach is motivated as follows. First, the use of a single CFD model of the flow field throughout the entire machine would entail full annulus simulations, at least within the volutes, the exit cones, and the return channel. However, this would lead to a sizeable computational overhead, making the simulation of multiple operating points significantly more challenging. Moreover, the adoption of a single CFD model would require the modeling of the cooling channels of the electric motor and the bearings, whose detailed design has not been addressed yet. Finally, in the compressor configuration under study, the flow field at the inlet of the second stage is only weakly coupled to the one at the outlet of the first stage. Hence, the benefits deriving from the use of a single CFD model for the entire compressor are not deemed sufficient to justify the considerable increase in computational cost and complexity.

Single passage RANS computations [14] with a frozen-rotor interface are used to assess the fluid dynamic performance of the impeller and the diffuser of the two stages.

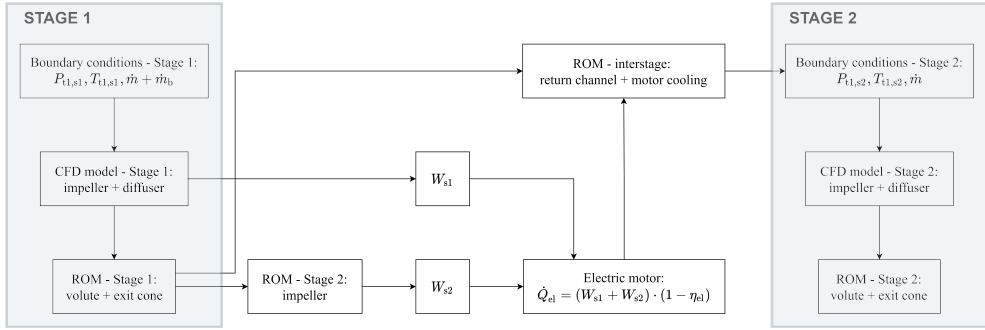


Figure 3.11: Flowchart of the hybrid computational method used to compute the operating map of the IRIS compressor.

The boundary conditions are imposed in terms of flow direction, total pressure, and total temperature at the inlet, whereas the mass flow rate is assigned at the outlet. The flow direction is assumed to be normal at the inlet of the two stages. The $k - \omega$ SST turbulence model is employed, together with adequate cell clustering near the walls to guarantee $y^+ \leq 1$. Turbulence boundary conditions are set in terms of inlet turbulence intensity ($k = 5\%$), and eddy viscosity ratio ($\mu/\mu_t = 10$), while the turbulent Prandtl number is set to $Pr_t = 1$, in accordance with what documented in [15]. The advective and turbulent fluxes are discretized with a total variation diminishing scheme [16]. A look-up table method is employed to reduce the computational time for the evaluation of the thermo-physical fluid properties. The property values are calculated using the multi-parameter equation of state model available in [17]. Fig. 3.12 shows the tabulated region of thermodynamic states in the pressure-temperature diagram of the working fluid, together with the saturation curve, the spinodal line, and the target isentropic compression processes. As one can notice, the two thermodynamic transformations happen in the proximity of the saturation curve. As a result, if the lower temperature boundary of the tabulated region is defined by the saturation temperature, the robustness of the CFD solver is remarkably reduced. To overcome this issue, in the present study the vapor properties are extended up to the spinodal line, implying the existence of meta-stable thermodynamic states. On the one hand, this minimizes the number of thermodynamic state evaluations outside of the tabulated region in the initial phase of the calculation. On the other hand, it does not affect the accuracy of the converged solution, which features only thermodynamic states lying in the superheated vapor region. During the first design iteration, a grid sensitivity analysis has been performed on the first compressor stage, simulated at the design point. Based on the results shown in Fig. 3.13, a grid of approximately 3.7 million nodes and a thermodynamic mesh of 1 million elements are selected as an optimal trade-off between accuracy and computational cost. The computational grid of the second stage has been scaled, accounting for the variation of the average Reynolds number, and of the number of blade passages, leading to a grid size of approximately 3.3 million nodes. The same procedure has been applied during the second design iteration, obtaining a grid size of 3.5 and 4.3 million nodes for the first and the second stage, respectively.

The fluid dynamic performance of the twin-stage compressor is computed as follows.

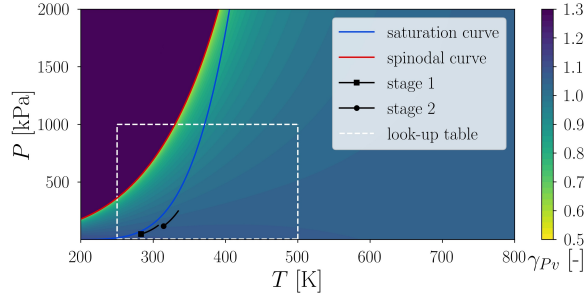


Figure 3.12: Contours of the isentropic pressure-volume exponent computed for refrigerant R1233zd(E) and displayed on the pressure-temperature thermodynamic diagram. The blue and the red lines correspond to the saturation and the spinodal curves, respectively. The region where the thermo-physical properties are computed by means of a look-up table approach is delimited by the white dashed line.

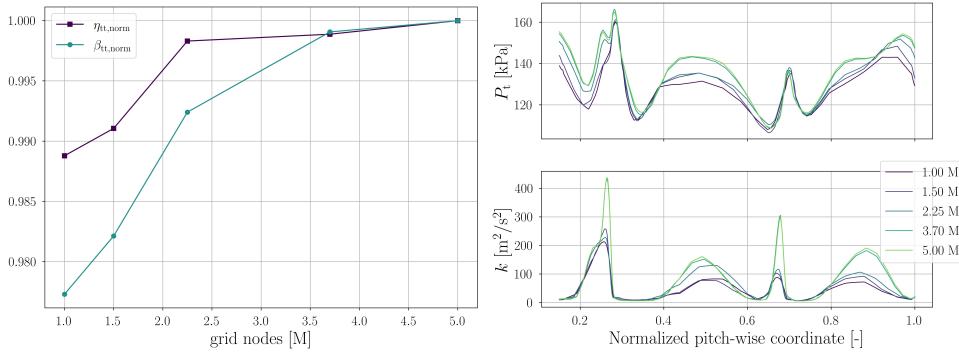


Figure 3.13: Results of the grid sensitivity analysis related to the CFD simulation of the first stage designed during the first design iteration and simulated at the design point. The grid sensitivity is evaluated in terms of stage performance metrics and the pitch-wise distribution of total pressure and turbulence kinetic energy at the outlet of the impeller.

First, the operating maps of the two stages are computed at the nominal inlet conditions by means of CFD, disregarding the presence of the volute and the exit cone. Then the operating maps are scaled in terms of corrected mass flow rate and rotational speed, according to

$$\dot{m}_r = \dot{m} \cdot T_{t,1}^{1/2} \cdot P_{t,1}^{-1} \cdot M_U^{-7.834} \quad (3.9)$$

$$N_r = \Omega \cdot T_{t,1}^{-1/2}, \quad (3.10)$$

where $M_U = U_2/a_{t,1}$ is the peripheral Mach number at the impeller outlet. Eqn. 3.9 is an extension of the standard formulation used for air compressors, featuring one additional term to account for the effect of the working fluid. The exponent of M_U has been computed based on a database of compressors operating with refrigerant R1233zd(E) at variable inlet conditions and simulated with the model described in Chapter 2. Once the

mass-flow averaged flow properties evaluated by means of CFD at the outlet of the first diffuser are available, they are set as boundary conditions in the ROMs of the volute, exit cone, and return channel. This provides a first estimate of the total conditions at the inlet of the second stage, disregarding the effect of electric motor cooling. Then, the power absorbed by the second impeller is estimated under the assumption of isentropic flow, and the overall power input of the electric motor is calculated. Next, the total thermodynamic state at the inlet of the second stage is computed again, this time by taking into account the effect of electric motor cooling, determined by assuming a constant electrical efficiency equal to $\eta_{el} = 95\%$. Subsequently, the total inlet conditions are used to compute the corrected mass flow rate and rotational speed of the second stage, and the entire procedure is repeated for each operating point. Once the entire operating envelope is known in terms of $\dot{m}_r = \dot{m}$ and N_r , the performance of the second stage can be characterized by interpolating the CFD simulation results in the corrected reference system. Finally, the flow conditions at the outlet of the second stage are evaluated with the ROMs of the volute and the exit cone.

3.4.2. RESULTS

The hybrid computational framework described in the previous section has been used to predict the fluid dynamic performance expected from the designs of the compressor prototypes obtained from the first and second design iterations. The results of the first design iteration are documented in [18], whereas, for the sake of conciseness, only the results of the second design iteration are discussed here.

The operating maps of the first and second stages have been computed by means of a total of 20 and 28 CFD simulations, respectively, with a rotational speed ranging from 95 to 105 krpm. The nominal total conditions prescribed at the inlet of the two stages are $P_{t,1}|_{s1-s2} = 0.478 - 1.485$ bar and $T_{t,1}|_{s1-s2} = 283.9 - 317.6$ K. The left and right boundaries of each speed-line are defined by the numerical prediction of the onset of unsteady flow phenomena, and by the establishment of choking conditions, respectively. To get a more accurate estimation of the inception of rotating stall, it is necessary to perform higher-order calculations, e.g., full annulus URANS. However, this is beyond the scope of this phase of the project and will be considered for the following phase.

The resulting stable operating points are displayed in Fig. 3.14, along with the corresponding η_{tt} predictions. The efficiency values result from CFD simulations and account only for the fluid dynamic losses in the impeller and diffuser passages. The first stage features a higher total-to-total efficiency, whereas the second stage is characterized by a wider operating range, as a result of the difference in swallowing capacity. This corroborates the findings of the extended scaling analysis. Moreover, the second stage is characterized by flatter speed-lines as compared to the ones of the first stage. This characteristic can be primarily attributed to the higher work coefficient of the second stage, which, in turn, leads to a lower impeller backsweep angle.

The calculated operating map of the entire twin-stage compressor is shown in Fig. 3.15, both in terms of total-to-total compression ratio and efficiency. In this case, the computation of the efficiency values accounts for the losses in the volute and exit cone of the two stages, the parasitic losses, and the detrimental effect of electric motor cooling. Notably, it is not possible to achieve the design point mass flow rate ($\dot{m} = 0.1$ kg/s) and compression

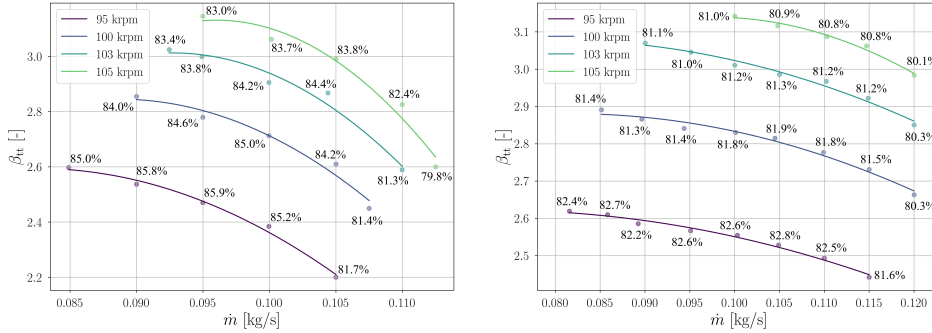


Figure 3.14: Predicted operating map of the first (left) and second (right) IRIS compressor stage obtained as an outcome of the second design iteration. The stage performance is computed with CFD accounting only for the presence of the impeller and the vaneless diffuser. The results are reported in terms of mass-flow averaged β_{tt} and η_{tt} .

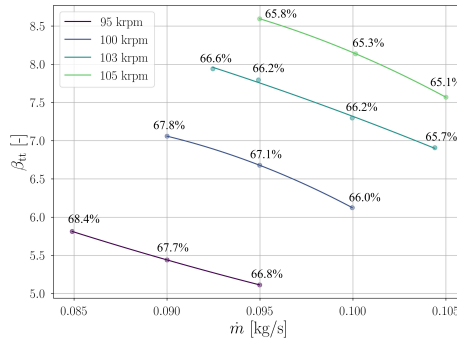


Figure 3.15: Operating map of the twin-stage compressor obtained as an outcome of the second design iteration. The compressor performance is computed with the method schematically displayed in Fig. 3.11. The results are reported in terms of mass-flow averaged β_{tt} and η_{tt} .

ratio ($\beta_{tt} = 9$) within the prescribed range of rotational speed. The reason is twofold. First, the design of the twin-stage compressor is heavily constrained. In particular, the equality constraint imposed on the impeller hub radii and the upper threshold set on the rotational speed significantly limit the design space. In addition, the large values of relative tip clearance gaps, e.g., 18.3% for the second stage, lead to a reduction of both efficiency and compression ratio, due to the occurrence of reverse flow in the proximity of the shroud.

The effect of the tip clearance magnitude has been investigated during the first design iteration, by means of a parametric CFD-based analysis. Specifically, three different values of tip clearance gap ($\epsilon_{t,le} = 0.4 - 0.2 - 0.0$ mm, $\epsilon_{t,te} = 0.3 - 0.15 - 0.0$ mm) have been prescribed for the impeller and the CFD simulations of the first stage have been systematically repeated at the design rotational speed. The results are compared in Fig. 3.16 in terms of mass-flow averaged compression ratio and efficiency. Moreover, the flow field observed

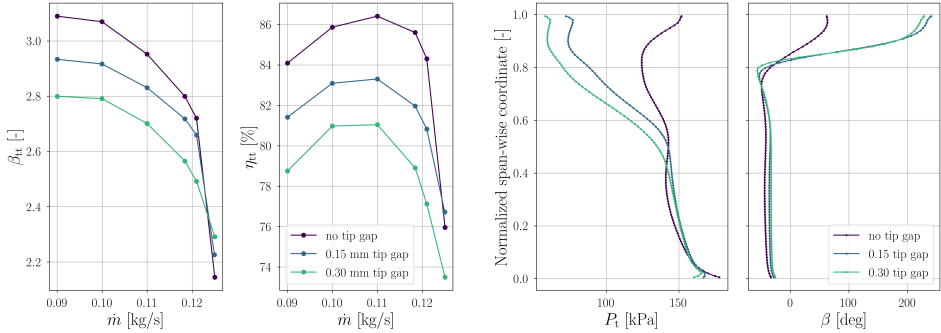


Figure 3.16: Mass-flow averaged total-to-total compression ratio and efficiency of the first stage, computed by 3D RANS at design rotational speed, in presence of variable tip clearance gap. Moreover, the span-wise distribution of total pressure and relative flow angle at the outlet of the first impeller is displayed at the design point.

downstream of the impeller at the design point is displayed in terms of total pressure and relative flow angle.

The following considerations can be drawn from these results. In the absence of tip clearance gap, the impeller outflow angle is nearly constant over the blade span, with the exception of the shroud region, where flow separation takes place. The leakage flow has a negligible effect on the spanwise distribution of the outflow angle, up to approximately 80% of the blade channel height, where backflow starts to occur. This effect is nearly invariant with respect to the size of the tip clearance gap. Moreover, in the absence of tip gap, the profile of the total pressure is flat away from the boundary layers, with some fluctuations induced by flow separation. Conversely, the effect of tip clearance is such that the total pressure decreases from midspan to shroud. This phenomenon is more prominent in the presence of a larger clearance gap. Similar trends are observed over the entire speed-line. It can be concluded that, when designing small-scale impellers featuring a large relative clearance gap, one should account not only for a reduction of η_{tt} but also for a decrease of β_{tt} , that is proportional to the relative tip gap and the work performed by the impeller, hence to the compression ratio. Based on these results, the following empirical correction of the impeller work has been implemented in the in-house compressor model, to match the performance trends obtained with CFD, as reported in Chapter 2.

$$|\Delta h_{tt}| = |\Delta h_{tt, \text{no gap}}| \cdot \left(1 - 0.2 \frac{\epsilon_t}{H_2}\right). \quad (3.11)$$

Despite the stringent constraints imposed by manufacturing limitations and the detrimental effects of motor cooling and small size, this work demonstrates that it is possible to design a twin-stage compressor for the target application featuring an overall efficiency higher than 65% and a maximum compression ratio exceeding 8.5. A higher margin for design optimization can be achieved by relaxing the equality constraint set on the impellers' hub radii, at the expense of a re-design of the tie-shaft. Moreover, a remarkable increase in the achievable pressure ratio can be obtained by reducing the tip clearance gap and by relaxing the upper limit set on the rotational speed. However, this entails a re-design of

the electric motor and a detailed rotordynamic assessment by the industrial partner.

3.5. CONCLUSIONS

The fluid dynamic design method developed to realize the high-speed twin-stage compressor that will be installed in the IRIS test rig at the Propulsion and Power Laboratory of Delft University of Technology is documented. The scaling analysis for single-stage centrifugal compressors has been extended to address the optimal design of twin-stage machines. The conceptual design has been performed by means of an in-house model, coupled with a multi-objective optimization framework. Then, the flow path of the optimal design has been manually refined based on the results of the application of a throughflow method. Finally, the fluid dynamic performance and the structural integrity of the final design have been assessed by means of a hybrid framework coupling 3D RANS and ROMs, and by FEA. The outcomes of this study can be summarized as follows.

1. As far as the design of miniature twin-stage compressors is concerned, the efficiency and the operating range of the second stage are inherently penalized by lower values of volumetric flow rate, thus by larger values of relative tip clearance, relative surface roughness, and blade blockage. As a result, the optimal set of non-dimensional parameters is such that the first stage features a larger compression ratio and a value of swallowing capacity in the proximity of the locus of optimal efficiency. In turn, by selecting the same value of work coefficient for the two stages, the flow coefficient of the second impeller lies in the region of optimal operating range. Consequently, the efficiency of the entire compression process is enhanced, without penalizing the operating range of the twin-stage machine.
2. The results of the multi-objective optimization corroborate the outcomes of the extended scaling analysis. This finding confirms both the suitability of the proposed methodology for the conceptual design optimization of twin-stage compressors and the validity of the design guidelines derived from similarity principles.
3. It is possible to design a twin-stage compressor for the target application featuring an overall efficiency higher than 65% and a maximum compression ratio exceeding 8.5, despite the detrimental effects of motor cooling and miniature size.
4. Setting the impellers' hub radii to a fixed value significantly limits the feasible design space. Moreover, the maximum achievable compression ratio is very sensitive to the tip clearance gap and the maximum allowable rotational speed. Relaxing these constraints would imply a re-design of the electric motor, gas bearings, and shaft. However, it would also promote a substantial improvement in fluid dynamic performance, highlighting the importance of a coupled multi-disciplinary optimization of this type of device.

NOMENCLATURE

Roman symbols

a	Throat length [m]
c	Specific heat capacity [$\text{J kg}^{-1} \text{K}^{-1}$]
D	Diameter [m]
E	Young modulus [Pa]
F_{ax}	Axial thrust acting on bearings [N]
H	Blade height [m]
h	Specific enthalpy [J kg^{-1}]
k	Impeller shape factor [-]
L_{ax}	Impeller axial length [m]
M	Mach number [-]
\dot{m}	Mass flow rate [kg s^{-1}]
N_{bl}	Number of main blades [-]
N_{split}	Number of splitter blades [-]
OR	Operating range [-]
P	Pressure [Pa]
Pr	Prandtl number [-]
\dot{Q}	Heat flow rate [W]
R	Radius [m]
Ra	Surface roughness [m]
Re	Reynolds number [-]
T	Temperature [K]
	Torque [Nm^{-1}]
T_{m}	Melting point temperature [K]
t	Thickness [m]
U	Peripheral speed [m s^{-1}]
V	Absolute velocity [m s^{-1}]
\dot{V}	Volumetric flow rate [$\text{m}^3 \text{s}^{-1}$]
v	Specific volume [$\text{m}^3 \text{kg}^{-1}$]
W	Power [W]
	Relative velocity [m s^{-1}]

Greek symbols

α	Absolute flow angle [deg]
β	Pressure ratio [-]
	Relative flow angle [deg]
γ	Heat capacity ratio [$\text{J kg}^{-1} \text{K}^{-1}$]
γ_{pv}	Isentropic pressure-volume exponent [$\text{J kg}^{-1} \text{K}^{-1}$]
e_{b}	Back face clearance [m]
e_{t}	Tip clearance gap [m]
η	Efficiency [-]
μ	Dynamic viscosity [Pa s^{-1}]
ν	Poisson's ratio [-]

ρ	Density [kg m^{-3}]
σ	Stage geometrical characteristics [-]
σ_{y}	Yielding stress [Pa]
σ_{uts}	Ultimate tensile strength [Pa]
ϕ_{t1}	Swallowing capacity [-]
ψ	Work coefficient [-]
Ω	Rotational speed [rpm]
ω	Turbulence specific dissipation rate [s^{-1}]
κ	Turbulence kinetic energy [J kg^{-1}]
κ_{s}	Compression ratio splitting factor [-]

Subscripts

b	Bearings
bl	Blade
choke	Choking point
des	Design point
el	Electric
h	Hub
hd	Hydraulic
is	Isentropic
le	Leading edge
r	Ratio
s	Shroud
s1	First stage
s2	Second stage
t	Total - turbulent
te	Trailing edge
ts	Total-to-static
tt	Total-to-total
1	Inducer
2	Exducer - diffuser inlet
3	Diffuser outlet - volute inlet
4	Volute outlet - cone inlet
P	Evaluated at constant pressure
v	Evaluated at constant volume

Abbreviations

ACM	Air cycle machine
ECS	Environmental control system
IRIS	Inverse Rankine integrated system
ROM	Reduced-order model
R1233zd(E)	Trifluoropropene
VCC	Vapor compression cycle

BIBLIOGRAPHY

- [1] J. Schiffmann and D. Favrat, "Experimental investigation of a direct driven radial compressor for domestic heat pumps", *International Journal of Refrigeration*, vol. 32, no. 8, pp. 1918–1928, Dec. 2009, ISSN: 01407007. DOI: 10.1016/j.ijrefrig.2009.07.006.
- [2] J. Schiffmann and D. Favrat, "Design, experimental investigation and multi-objective optimization of a small-scale radial compressor for heat pump applications", *Energy*, vol. 35, no. 1, pp. 436–450, Jan. 2010, ISSN: 03605442. DOI: 10.1016/j.energy.2009.10.010.
- [3] A. Giuffr , P. Colonna, and M. Pini, "The Effect of Size and Working Fluid on the Multi-Objective Design of High-Speed Centrifugal Compressors", *International Journal of Refrigeration*, vol. 143, pp. 43–56, Nov. 2022, ISSN: 0140-7007. DOI: 10.1016/J.IJREFRIG.2022.06.023.
- [4] D. A. Kouremenos and X. K. Kakatsios, "The three isentropic exponents of dry steam", *Forschung im Ingenieurwesen*, vol. 51, no. 4, pp. 117–122, Jul. 1985, ISSN: 00157899. DOI: 10.1007/BF02558416.
- [5] A. Giuffr  and M. Pini, "Design Guidelines for Axial Turbines Operating With Non-Ideal Compressible Flows", *Journal of Engineering for Gas Turbines and Power*, vol. 143, no. 1, Jan. 2021, ISSN: 0742-4795. DOI: 10.1115/1.4049137.
- [6] D. Rusch and M. Casey, "The design space boundaries for high flow capacity centrifugal compressors", *Journal of Turbomachinery*, vol. 135, no. 3, Mar. 2013, ISSN: 15288900. DOI: 10.1115/1.4007548.
- [7] K. Deb, A. Pratap, S. Agarwal, and T. Meyarivan, "A fast and elitist multiobjective genetic algorithm: NSGA-II", *IEEE Transactions on Evolutionary Computation*, vol. 6, no. 2, pp. 182–197, Apr. 2002. DOI: 10.1109/4235.996017.
- [8] J. Blank and K. Deb, "Pymoo: Multi-Objective Optimization in Python", *IEEE Access*, vol. 8, pp. 89 497–89 509, 2020. DOI: 10.1109/ACCESS.2020.2990567.
- [9] ANSYS Inc., *ANSYS Academic Research BladeGen, Release 21.2*, Canonsburg, PA, 2021. [Online]. Available: <http://www.ansys.com>.
- [10] M. Casey and C. Robinson, *Radial Flow Turbocompressors: Design, Analysis, and Applications*, 1st. Cambridge University Press, 2021, ISBN: 1108416675. DOI: 10.1017/9781108241663.
- [11] M. Casey and C. Robinson, "A New Streamline Curvature Throughflow Method for Radial Turbomachinery", *Journal of Turbomachinery*, vol. 132, no. 3, Apr. 2010, ISSN: 0889-504X. DOI: 10.1115/1.3151601.
- [12] P. De Haller, "Das verhalten von tragflugelgittern in axialverdichtern und in windkanal", *BWK Zeitschrift*, vol. 5, no. 10, pp. 333–337, 1953.
- [13] ANSYS Inc., *ANSYS Academic Research Mechanical, Release 21.2*, Canonsburg, PA, 2021. [Online]. Available: <http://www.ansys.com>.
- [14] ANSYS Inc., *ANSYS Academic Research CFX, Release 21.2*, Canonsburg, PA, 2021. [Online]. Available: <http://www.ansys.com>.
- [15] R. Otero, J. Gustavo, A. Patel, R. Diez S., and R. Pecnik, "Turbulence modelling for flows with strong variations in thermo-physical properties", *International Journal of Heat and Fluid Flow*, vol. 73, pp. 114–123, Oct. 2018, ISSN: 0142-727X. DOI: 10.1016/J.IJHEATFLUIDFLOW.2018.07.005.
- [16] T. Barth and D. Jespersen, "The design and application of upwind schemes on unstructured meshes", Jan. 1989. DOI: 10.2514/6.1989-366.
- [17] E. W. Lemmon, I. H. Bell, M. L. Huber, and M. O. McLinden, *NIST Standard Reference Database 23: Reference Fluid Thermodynamic and Transport Properties-REFPROP, Version 10.0*, National Institute of Standards and Technology, 2018. DOI: <https://doi.org/10.18434/T4/1502528>. [Online]. Available: <https://www.nist.gov/srd/refprop>.

-
- [18] A. Giuffrè, P. Colonna, and M. Pini, "Design Optimization of a High-Speed Twin-Stage Compressor for Next-Gen Aircraft Environmental Control System", *Journal of Engineering for Gas Turbines and Power*, vol. 145, no. 3, Mar. 2023, ISSN: 0742-4795. DOI: 10.1115/1.4056022.

4

DYNAMIC THERMAL MODEL OF PRESSURIZED AIRCRAFT FUSELAGE

4

Every man takes the limits of his own field of vision for the limits of the world.

Arthur Schopenhauer

The Environmental Control System (ECS) of modern passenger aircraft is designed to operate in a wide range of flight phases and climatic conditions, spanning from nominal cruise operation to ground service on a hot and humid day. The characterization of the thermal behavior of the aircraft's pressurized areas is essential to compute the operating envelope of the ECS, which entails both steady-state and transient operating points. Therefore, a dynamic thermal model of the air distribution system and the pressurized compartments of the aircraft, which can be used for both ECS preliminary sizing and control design, is needed. The fuselage thermal model documented in this work has been implemented in the acausal, object-oriented, equation-based programming language Modelica, and has been validated with proprietary data provided by Airbus. The choice of the acausal modeling paradigm, together with the adoption of a modeling approach based on first principles, rather than on semi-empirical correlations, make the model scalable and easily extendable. The validated aircraft thermal model has been used to identify the operating envelope of the ECS of an Airbus A320 and to simulate a case study involving the dynamic thermal behavior of the system. Future work will entail the modeling of alternative aircraft configurations, including the simultaneous control of multiple ventilation zones, as well as the study of additional thermal management applications, i.e., rotorcraft, more electric aircraft, and all-electric aircraft.

4.1. INTRODUCTION

MODERN commercial airliners fly at an altitude higher than eleven km to reduce drag and fuel consumption. The environmental conditions at these altitude are incompatible with human life, due to the scarcity of oxygen, and the low pressure and temperature of the air. To make high-altitude flight possible, the Environmental Control System (ECS) is responsible for providing dry, sterile, and dust-free conditioned air to the airplane cabin at the proper temperature, flow rate, and pressure [1]. The technology of ECS's is well-established and very limited innovation has occurred in the last sixty years, with few exceptions, e.g., the bleedless air cycle machine equipping the Boeing 787 [2]. However, the assessment and improvement of the air quality in commercial aviation is still an active field of research and development, especially after the COVID-19 pandemic. Unlike other indoor spaces, the aircraft cabin is characterized by high occupant density, and the passengers are not allowed to leave the enclosed space for the entire duration of the flight mission. Moreover, in modern passenger aircraft, part of the pressurized air is filtered and recirculated in the air distribution system, instead of being entirely replenished by fresh air, to reduce the fuel consumption associated with the ECS. As a result, if not properly monitored, the concentration of gaseous and microbiological contaminants may overcome the safety limits, leading to an increased probability of viral infections, and an exacerbation of chronic respiratory problems. Furthermore, the rapid changes in the cabin air pressure occurring during take-offs and landings may lead to ear and sinus problems, often accompanied by dental pain [3].

In addition to the safety and comfort concerns, the knowledge of the thermal loads associated with the prescribed environmental conditions within the aircraft's pressurized spaces is crucial for the correct sizing of the ECS. The ECS of modern passenger aircraft is designed not only to operate at nominal cruise conditions but also in other extreme atmospheric states, such as ground service on a hot and humid day. In this context, the avail-

ability of a model simulating the thermal characteristics of the pressurized aircraft compartments, i.e., cabin, cockpit, electronic and equipment (E/E) bay, and cargo, is essential to estimate the operating envelope of the ECS. This is testified by the various attempts to develop a thermal model for passenger aircraft documented in the scientific literature. In [4], the author presents a general overview of a one-dimensional Modelica thermal model developed at Airbus [5]. As stated by the author, the objective of the work was to highlight the challenges related to providing a complete, accurate, and user-friendly thermal model of a complex thermal system, such as a commercial aircraft, rather than to provide a detailed description of the proposed model. Similarly, the development and validation of a model used to size the ECS of passenger aircraft, named FLECS (Functional Model Library of the ECS), is documented in [6]. The article provides a list of data related to the considered aircraft configuration, but lacks a detailed description of the modeling approach, thus hindering the reproducibility of the model and its results. Another attempt to devise a dynamic thermal model of the air distribution system and the pressurized compartments can be found in [7]. The authors investigated a new ducting concept, which enables the simultaneous control of many independent temperature zones. The focus of the article is on the rapid development of an efficient control strategy, obtained by coupling the Matlab and Modelica simulation environments. In particular, the design of the control logic was performed with Matlab, while Modelica was used to create a simplified thermal model of the pressurized aircraft compartments and to test the proposed control strategies. Further examples of one-dimensional thermal models developed for automotive applications are documented in [8], [9]. An alternative approach to model the heat and mass transfer occurring within the pressurized spaces of a commercial airliner is documented in [10]. In this paper, the authors rely on the results of high-fidelity Computational Fluid Dynamics (CFD) simulations to create fast and accurate reduced-order models. However, the proposed methodology is application-specific and requires the CFD simulation of each considered zone. As a consequence, it is deemed inappropriate for the purpose of this work.

The objective of the work documented here is to develop a dynamic thermal model of the air distribution system and of the pressurized compartments of a generic commercial aircraft, allowing for the estimation of the operating envelope of the ECS, given limited information about the aircraft type and the flight mission. Such model should therefore satisfy the specific requirements of the preliminary design of the ECS and of its control strategy. Differently from the models documented in the literature, the present modeling library, named *DynTherM* (Dynamic Thermal Management), has to be scalable and easily extendable to cover additional applications, e.g., rotorcraft. To achieve these targets, the new model has been coded in Modelica, i.e., an equation-based programming language created to simulate physical systems, supporting the acausal modeling paradigm [11] to facilitate modeling from first principles [5]. Moreover, it provides object-oriented constructs to facilitate the systematic reuse of models. The structure and the basic components of the novel aircraft model are largely inspired by the ThermoPower library, i.e., an open-source Modelica library for the dynamic modeling of thermal power plants and energy conversion systems [12], [13]. All the basic components of *DynTherM* are zero-dimensional, i.e., they do not feature a discretization of the governing physical equations in any spatial direction. To facilitate the reproducibility of results and promote future ex-

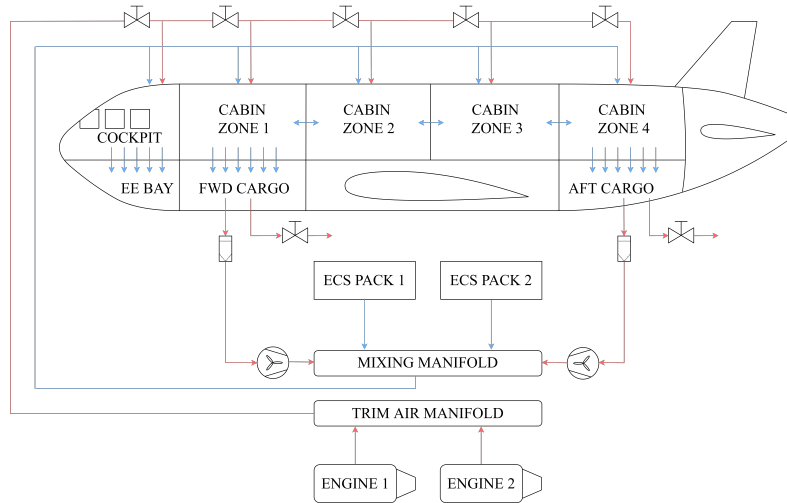


Figure 4.1: Simplified schematic of the air distribution system of an exemplary passenger aircraft.

tension by means of collaborative software development, the aircraft model documented in the following sections will be released open-source upon publication of this work.

The remainder of the chapter is structured as follows. First, the approach used to develop the thermal model is discussed and the main components of the *DynTherM* library are described. Next, a validation test case based on proprietary data provided by the industrial partner Airbus is documented. Then, two different examples of usage of the aircraft thermal model are presented. Finally, concluding remarks summarize the content of the chapter and provide an outlook of future work.

4.2. METHODOLOGY

4.2.1. SYSTEM MODEL

The air distribution system of a generic passenger aircraft is schematically displayed in Fig. 4.1. The details of this system may vary depending on the aircraft type and the manufacturer.

Two ECS packs, located in the unpressurized volume below the center wing box, provide conditioned and pressurized air to the mixing manifold. In the mixing unit, usually located under the cabin floor and in front of the center wing box, the fresh air is mixed with the recirculated cabin air. The recirculated air is extracted at the cabin floor level through dado panels, depurated by means of a HEPA filter, and fed to the mixing manifold with a recirculation fan. The aircraft is equipped with two recirculation loops located in the forward and aft sections of the cabin, for redundancy. Moreover, to guarantee a higher degree of temperature control, the aircraft cabin is divided into separate ventilation zones. The mixture of conditioned and recirculated air is distributed to the cockpit and to each cabin zone by means of dedicated supply ducts provided with orifices, and the mass flow rate is adjusted as a function of the temperature set points and of the cor-

responding heat loads. Furthermore, the air temperature is regulated by mixing hot trim air, bled from the compressors of the main engines, with the air stream coming from the mixing unit. To fine-tune the local air temperature, the flow rate of trim air is controlled by means of a separate trim-air valve installed in each zone. In addition, the air distribution system provides ventilation to the cargo and the electronics (E/E) bays, by means of dado panels located on the floor of the cabin and cockpit, respectively. The pressurization level is regulated by the opening of the outflow valves positioned in the forward and aft cargo compartments, as a function of the altitude.

To describe the modeling approach adopted in this work, it is convenient to analyze the heat and mass transfer processes occurring within one section of the fuselage, which corresponds to one ventilation zone, as depicted in Fig. 4.2. From the outer to the inner surface, the overall heat transfer can be decomposed into the following contributions:

- external radiative and convective heat transfer established between the environment and the outer skin of the fuselage;
- heat conduction through the fuselage composite structure;
- radiative and convective heat transfer between the fuselage inner surface and the pressurized air volume.

The temperature difference between the fuselage interior and the pressurized air volume is negligible, due to the presence of an insulation layer within the fuselage composite structure. Moreover, the temperature is low, since it is directly regulated by the ECS. As a result, the internal radiative heat transfer can be neglected as a first approximation. Additional heat transfer mechanisms must be accounted for due to the presence of cabin windows and cockpit windshields. The external radiative heat transfer is subdivided into the absorbed, transmitted, and reflected components. The transmitted component is directed to the cabin and cockpit interiors. This thermal power is then partly transferred to the surrounding air by convection.

Furthermore, the following processes involving mass transfer take place within the prescribed fuselage section:

- a mixture of fresh, recirculated, and trim air is supplied to the prescribed ventilation zone by the air distribution system;
- mass transfer occurs between the upper and lower sections of the fuselage by means of the dado panels located on the cabin floor;
- part of the air in the cargo bay is vented overboard by means of the outflow valve and the rest is fed to the recirculation loop.

The model of the entire fuselage can be assembled by coupling together multiple sections, characterized by the heat and mass transfer processes described above. Following this approach, each instance corresponds to a separate ventilation zone. The cockpit and the E/E bay can be modeled in the same fashion as the cabin and cargo compartments, with only minor modifications, accounting for the variation of the shape of the fuselage, the presence of larger transparencies in the cockpit, and the internal heat loads due to the

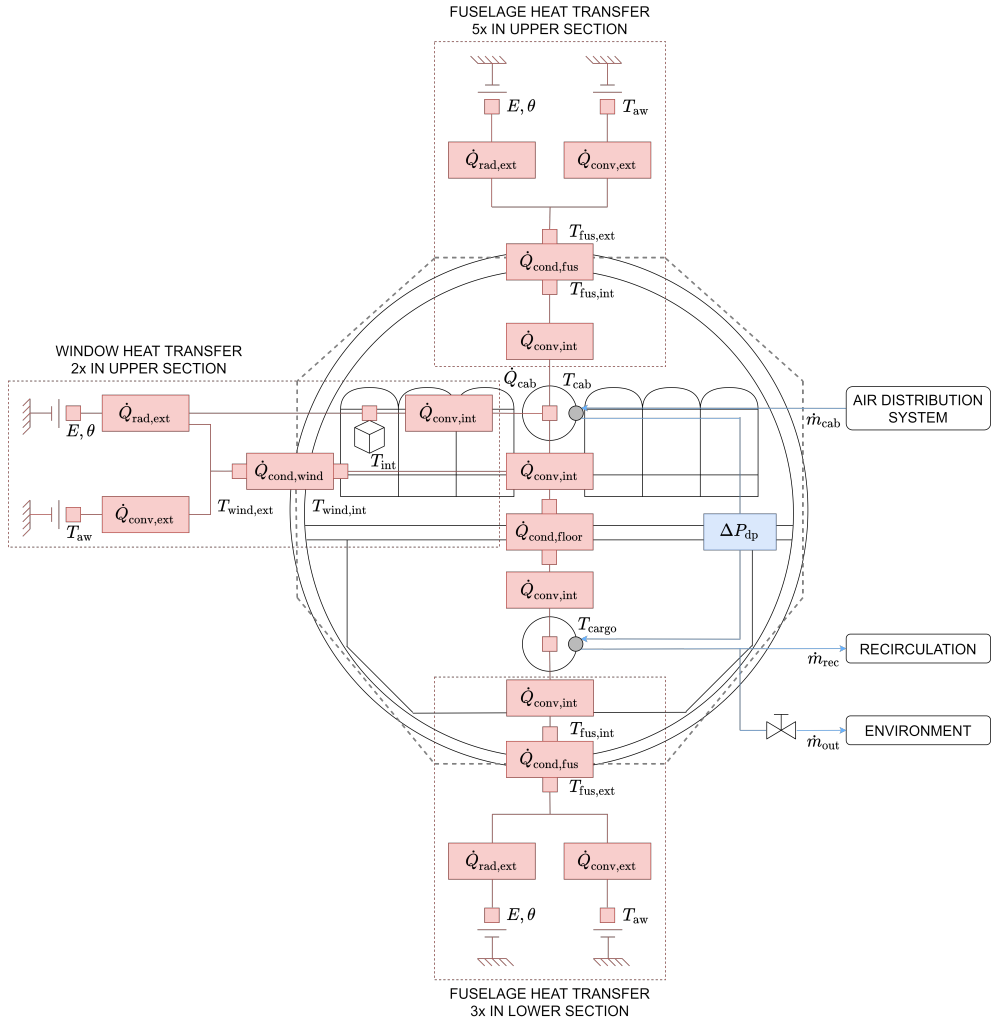


Figure 4.2: Diagram of the model decomposition of the heat and mass transfer processes occurring in one section of the fuselage, corresponding to one ventilation zone.

flight deck electronics and avionics. This modeling approach complies with the requirements of the development of a library featuring a modular structure (or object-oriented), as displayed in Fig. 4.3. In the current implementation, the lowest hierarchical layer, labeled as utilities, collects the packages defining the interfaces of each component and the boundary conditions used for the simulations. Moreover, it gathers the material properties and the sensors. The intermediate layer contains the implementation of the basic components. These are organized in two packages, collecting the models related to heat and mass transfer. Moreover, a model to predict the atmospheric conditions, called environment, is included in the intermediate layer. Finally, the models of the aircraft and

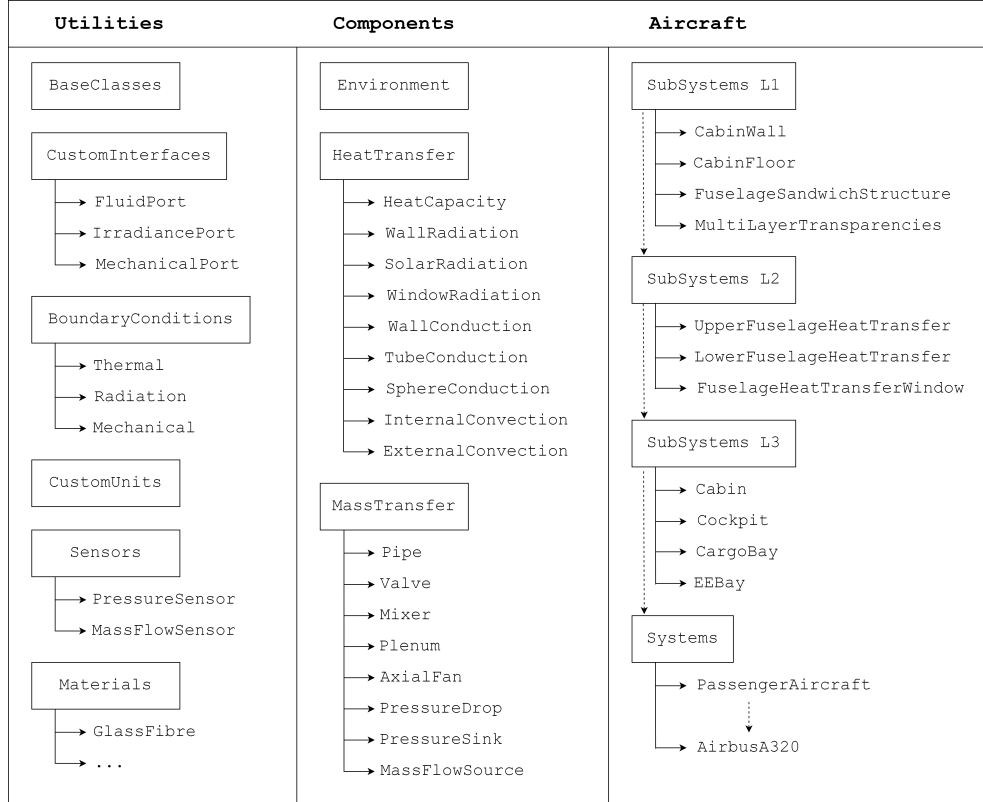


Figure 4.3: Structure of the *DynTherM* library. The solid arrows indicate the list of models collected within a package. The dashed arrows indicate model inheritance.

the related subsystems are collected within the top hierarchical layer. In particular, the packages of the aircraft subsystems are organized into three levels featuring an increasing degree of complexity and inheritance. Following the notation of Fig. 4.3, the package SubSystems L1 collects the models of the composite structures of the fuselage, cabin floor, and wall. Moreover, it includes the model of the transparent surfaces. In SubSystems L2, the models of the composite structures and the windows are coupled to those of convective and radiative heat transfer to create the building blocks of the upper and lower fuselage. At the third level, the models of the pressurized aircraft compartments are created by assembling multiple instances of the upper and lower fuselage, featuring different orientations. Finally, the air distribution system is modeled by resorting to the components of the mass transfer package, and the model of the aircraft is created by connecting the third-level subsystems. This modular modeling approach is illustrated in Fig. 4.4 and Fig. 4.5.

The total mass, air species (mass fractions), and energy conservation equations applied to the pressurized air volume of one ventilation zone within the fuselage are

$$\frac{dm}{dt} = V \cdot \frac{d\rho}{dt} = \dot{m}_{\text{in}} + \dot{m}_{\text{out}} + N_p \dot{m}_{\text{H}_2\text{O}}, \quad (4.1)$$

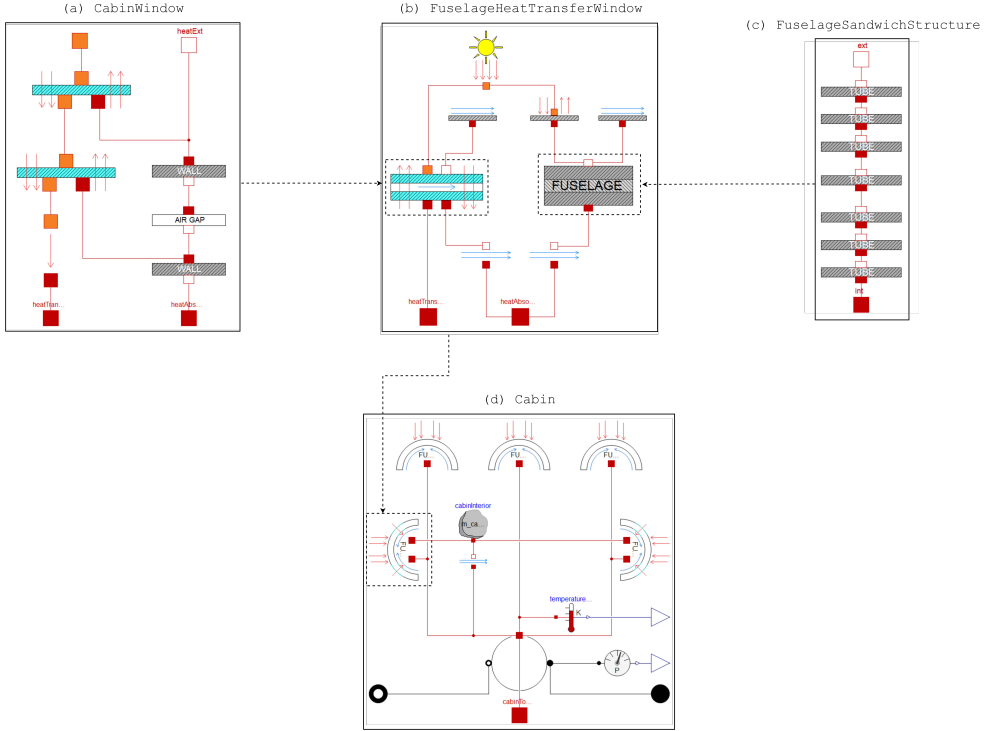


Figure 4.4: Graphical user interface of the Modelica model of the aircraft cabin and its main submodels, as implemented in the *DynTherM* library. The dashed arrows indicate the usage of a submodel in a higher hierarchical layer.

$$\frac{dU}{dt} = V \cdot \frac{d(\rho u)}{dt} = \dot{m}_{in} h_{in} + \dot{m}_{out} h_{out} + \dot{Q}_{in} + \dot{Q}_{out} + N_p (\dot{Q}_{sens} + \dot{Q}_{lat}) + \dot{Q}_{int}, \quad (4.2)$$

$$m \cdot \frac{dx_w}{dt} = \dot{m}_{in} (x_{in,w} - x_w) + \dot{m}_{out} (x_{out,w} - x_w) + N_p \dot{m}_{H_2O} (1 - x_w),$$

$$m \cdot \frac{dx_{air}}{dt} = \dot{m}_{in} (x_{in,air} - x_{air}) + \dot{m}_{out} (x_{out,air} - x_{air}) - N_p \dot{m}_{H_2O} x_{air}, \quad (4.3)$$

$$x_w + x_{air} = 1.$$

The heat flow rate terms which, once summed up, give the total internal heat flow rate \dot{Q}_{int} depend on the considered ventilation zone. In the case of a cabin sector, the terms are the heat flow rate associated with the cabin lights, that related to the in-flight entertainment, and the heat flow rate provided by the galleys. Conversely, for the cockpit and the related underfloor compartment, i.e., the E/E bay, the sources of internal heat flow rate are the flight deck electronics and the avionics.

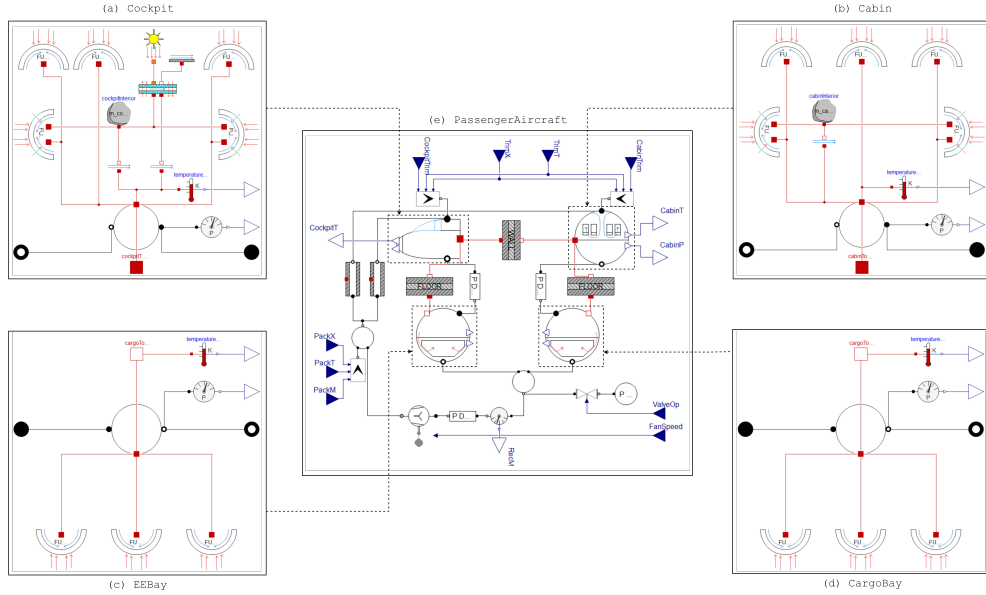


Figure 4.5: Graphical user interface of the Modelica model of a passenger aircraft and its main submodels, as implemented in the *DynTherM* library. The dashed arrows indicate the usage of a submodel in a higher hierarchical layer.

The presence of occupants, i.e., pilots (cockpit), passengers, and crew members (cabin), leads to the generation of water vapor within the pressurized air volume. As reported in [14], the rate of evaporative heat generation from the human body can be expressed as

$$E_{hb} = E_{rsw} + E_{diff} + E_{res}, \quad (4.4)$$

where E_{rsw} , E_{diff} , and E_{res} are the rates of heat generation due to sweating, water diffusion through the skin, and respiration, respectively. They can be computed as

$$\begin{aligned} E_{rsw} &= 0.42(M_{hb} - W_{hb} - 58.15), \\ E_{diff} &= 3.05(5.73 - 0.007(M_{hb} - W_{hb}) - P_v/1000), \\ E_{res} &= 0.0173M_{hb}(5.87 - P_v/1000), \end{aligned} \quad (4.5)$$

where P_v is the water vapor pressure in the pressurized air volume, whereas M_{hb} and W_{hb} are the rate of metabolic heat production and the rate of mechanical work accomplished by one individual, respectively. According to the guidelines reported in [15], M_{hb} can be set to 60, 115, and 70 W m^{-2} for passengers, crew members, and pilots, respectively. Moreover, as a first approximation, W_{hb} can be neglected. The rate of water vapor generation per person can be calculated by considering the average surface area of the human body, i.e., $A_{hb} = 1.75 \text{ m}^2$, and the rate of the evaporative heat loss

$$\dot{m}_{\text{H}_2\text{O}} = \frac{E_{\text{hb}} A_{\text{hb}}}{h_v(T) - h_l(T_{\text{skin}})}. \quad (4.6)$$

In Eqn. (4.6), T is the temperature of the pressurized air volume, and T_{skin} is the skin temperature of the human body, estimated as [16]

$$T_{\text{skin}} = 273.15 + 37.5 - 0.0275(M_{\text{hb}} - W_{\text{hb}}). \quad (4.7)$$

The sensible and latent components of the heat flow rate associated with the generation of water vapor in the prescribed air volume can be computed as

$$\dot{Q}_{\text{sens}} = A_{\text{hb}} \cdot (M_{\text{hb}} - E_{\text{hb}}), \quad (4.8)$$

$$\dot{Q}_{\text{lat}} = \dot{m}_{\text{H}_2\text{O}}(h_v(T) - h_l(T_{\text{skin}})). \quad (4.9)$$

The pressurized air volumes of the upper and lower fuselage sections, i.e., cabin and cargo, or cockpit and E/E bay, exchange heat and mass through the dado panels and the cabin floor. Furthermore, the cabin and the cockpit sections exchange energy as heat via the wall separating the two environments. The dado panels are modeled as simple elements featuring a lumped pressure drop, that scales linearly with the mass flow rate of air. The floor and the wall are heat conduction elements featuring a planar composite structure. The cabin can be discretized into multiple ventilation zones connected in series, without additional modeling effort, by leveraging the modularity of the *DynTherM* library. However, for the sake of simplicity, the cabin is assumed to be constituted by a single ventilation zone. To keep the internal pressure at the prescribed set point value, part of the air in the underfloor compartment is vented overboard by means of the outflow valve. In the current implementation, the valve features a simple linear characteristic. The remaining airflow is fed to the recirculation loop, amounting to the HEPA filter, the recirculation fan, and the mixing manifold. These components are modeled as a pressure drop, a turbo-machine with a linear characteristic, and a plenum featuring accumulation of mass and energy. Finally, the mix of fresh and recirculated air at the outlet of the mixing manifold is provided to each ventilation zone by means of a separate distribution pipe. The pressure drop in the air distribution system is modeled with the Darcy-Weisbach equation and the heat transfer is neglected, due to the thick thermal insulation. The graphical representation of the complete model of a passenger aircraft featuring two ventilation zones, i.e., cockpit and cabin, is depicted in Fig. 4.5.

4.2.2. MODEL OF EXTERNAL ENVIRONMENT

The International Standard Atmosphere (ISA) [17] is used to model the variation of the atmospheric conditions with altitude. Within this model, the atmosphere is divided into layers, in which the ambient temperature is computed as a function of altitude. In particular, until the Tropopause, located at eleven kilometers above Mean Sea Level (MSL), the ambient temperature is evaluated as

$$T_{\text{ISA}} = T_0 - \frac{6.5z}{1000}, \quad (4.10)$$

where $T_0 = 15^\circ \text{C}$ is the average ambient temperature at MSL. Then, between the Tropopause and the edge of the Stratosphere, located at 20 kilometers above MSL, the ambient temperature is assumed to be constant and equal to $T_{\text{ISA}} = -56.5^\circ \text{C}$. The ambient pressure and density are computed by sequentially solving the hydrostatic equilibrium, which relates the rate of change of pressure with geopotential altitude, and the ideal gas law, therefore

$$\begin{aligned}
 P_{\text{ISA}} &= P_0 \frac{T_{\text{ISA}}^{\frac{1000g}{6.5R}}}{T_0} & \text{if } z \leq 11 \text{ km} \\
 P_{\text{ISA}} &= P_0 \frac{T_{\text{ISA}}^{\frac{1000g}{6.5R}}}{T_0} e^{-\frac{g}{T_{\text{ISA}}R}(z-11000)} & \text{if } 11 \text{ km} < z \leq 20 \text{ km} \\
 \rho_{\text{ISA}} &= \frac{P_{\text{ISA}}}{T_{\text{ISA}}R},
 \end{aligned} \tag{4.11}$$

where $P_0 = 1 \text{ bar}$ is the ambient pressure at MSL. In the ISA model, the ambient air is assumed to be dry and of constant composition. Humidity effects are accounted for by adopting a standard moist air thermodynamic model in which the air pressure and temperature are defined according to the ISA model. Non-standard days are modeled by adding a prescribed temperature delta to T_{ISA} , whereas the ambient pressure remains unaltered. Then, density is recalculated as a function of the new ambient temperature using the ideal gas equation of state. Once the ambient conditions are defined, the set-point pressure of the pressurized spaces of the aircraft can be computed by imposing a maximum pressure differential of 50 kPa with respect to the external environment. Moreover, for safety reasons, the minimum pressure within the ventilation zones is fixed at 76.2 kPa.

In addition to the standard atmospheric conditions, the model of the environment is used to compute the clear-sky temperature and emissivity, which are used for the radiative heat transfer calculation, as described in Section 4.2.5. The vapor pressure of ambient air is computed according to [18] as

$$\begin{aligned}
 P_v &= \Phi_{\text{amb}} e^{\frac{29.06-6211.88}{T_{\text{amb}}+274.35}} & \text{if } T_{\text{amb}} < 0^\circ \text{C}, \\
 P_v &= \Phi_{\text{amb}} e^{\frac{23.3-3890.94}{T_{\text{amb}}+230.4}} & \text{if } T_{\text{amb}} \geq 0^\circ \text{C},
 \end{aligned} \tag{4.12}$$

with T_{amb} expressed in Celsius. The clear-sky temperature and emissivity can be derived, see [19], as

$$\begin{aligned}
 \epsilon_{\text{sky}} &= \left(0.48 + 0.17 \left(\frac{P_v}{100} \right)^{0.22} \right) \left(\frac{P_{\text{amb}}}{P_0} \right)^{0.45} & \text{if } T_{\text{amb}} < 0^\circ \text{C}, \\
 \epsilon_{\text{sky}} &= \left(\frac{T_{\text{sky}}}{T_{\text{amb}}} \right)^4 & \text{if } T_{\text{amb}} \geq 0^\circ \text{C}.
 \end{aligned} \tag{4.13}$$

4.2.3. MODEL OF COMPOSITE STRUCTURES

The geometry of the composite structures of a passenger aircraft can be approximated with two simple geometries, i.e., a planar element, and a hollow cylinder. The planar ele-

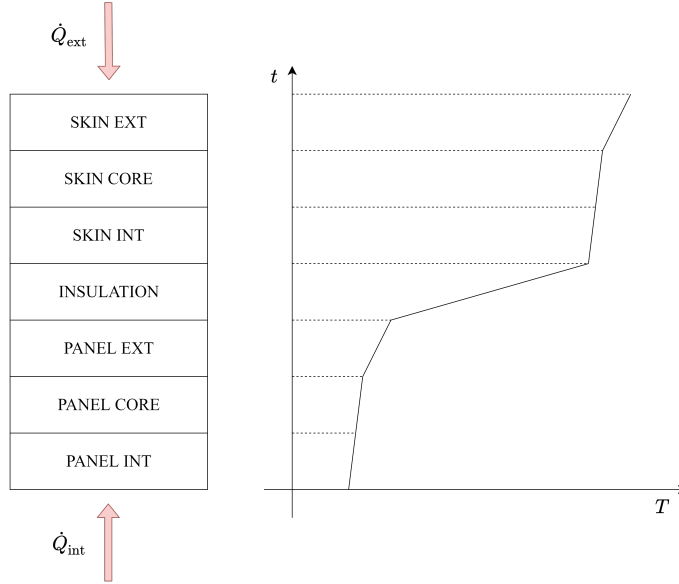


Figure 4.6: Heat conduction and qualitative temperature distribution evaluated through the layers of the fuselage composite structure.

ment is used to model the cabin floor and the wall separating the cockpit from the cabin. The heat conduction equations for a planar surface of thickness t reads

$$\begin{aligned}\dot{Q}_{\text{in}} &= \frac{2k_t A(T_{\text{in}} - T)}{t}, \\ \dot{Q}_{\text{out}} &= \frac{2k_t A(T_{\text{out}} - T)}{t}.\end{aligned}\quad (4.14)$$

The hollow cylinder is used to model the fuselage structure in between the forward and aft pressure bulkheads. The thermal energy balance equations for the heat conduction in a hollow cylindrical section can be expressed as

$$\begin{aligned}\dot{Q}_{\text{in}} &= \frac{2\pi L_{\text{fus}} k_t (T_{\text{in}} - T)}{\log \frac{R_{\text{int}} + R_{\text{ext}}}{2R_{\text{int}}}}, \\ \dot{Q}_{\text{out}} &= \frac{2\pi L_{\text{fus}} k_t (T_{\text{out}} - T)}{\log \frac{2R_{\text{ext}}}{R_{\text{int}} + R_{\text{ext}}}}.\end{aligned}\quad (4.15)$$

The surface areas occupied by transparent surfaces, e.g., cabin windows, are excluded from this computation, as they are characterized by different physical properties and heat transfer mechanisms. Further information about the methodology used to model the heat transfer mechanisms for transparent surfaces is described in Section 4.2.4. Once the heat

conduction mechanisms characterizing the two basic geometries have been derived, the corresponding composite structures can be modeled by connecting in series multiple planar or cylindrical elements, featuring different dimensions and material properties, as displayed in Fig. 4.4c and Fig. 4.6.

4.2.4. MODEL OF TRANSPARENT SURFACES

The external surface of the fuselage of a passenger aircraft features two types of transparencies: cabin windows and flight deck windshields. Cabin windows consist of an outer panel flush with the fuselage skin, an inner panel featuring a breather hole, and a thinner non-structural scratch panel, separating the passengers from the actual window assembly. The scratch panel is made of plastic and is not airtight. The inner and outer panels are made of stretched acrylic, and feature a non-ventilated air cavity between them. During the climb phase, the pressure differential established between the interior of the fuselage and the external environment gradually increases. The breather hole on the inner panel allows some of the pressurized air to leak into the air cavity, gradually equalizing the pressure differential. This causes the thicker outer panel to progressively carry the pressurization load, whereas the inner panel acts only as a buffer.

The model of the heat transfer through the cabin windows is adapted from [20] and its graphical representation is illustrated in Fig. 4.4a. The solar radiation acting on the outer panel is split into the absorbed, transmitted, and reflected components, yielding

$$\begin{aligned} E_r &= (r_{\text{eff}} + r_{\text{eff}}(1 - r_{\text{eff}})\tau^2)E_{\text{t,b}}, \\ E_{\text{tr}} &= (1 - r_{\text{eff}})^2\tau E_{\text{t,b}}, \\ E_a &= E_{\text{t,b}} - E_r - E_{\text{tr}}. \end{aligned} \quad (4.16)$$

If $\cos\theta \leq 0$, the incident solar radiation is entirely reflected by the surface, leading to $E_{\text{tr}} = E_a = 0$. The reflection coefficient r_{eff} can be computed by applying the Snell's law

$$n_1 \sin\theta_i = n_2 \sin\theta_t, \quad (4.17)$$

and the Fresnel equations

$$\begin{aligned} r_s &= \left| \frac{n_1 \cos\theta_i - n_2 \cos\theta_t}{n_1 \cos\theta_i + n_2 \cos\theta_t} \right|, \\ r_p &= \left| \frac{n_1 \cos\theta_t - n_2 \cos\theta_i}{n_1 \cos\theta_t + n_2 \cos\theta_i} \right|, \end{aligned} \quad (4.18)$$

at the interface between the external air and the outer panel. In this case, subscript 1 corresponds to the air side, and subscript 2 refers to the stretched acrylic side. Moreover, r_s and r_p are the reflection coefficients computed for s-polarized and p-polarized light. r_s refers to the polarization of a wave's electric field normal to the plane of incidence, whereas r_p refers to the polarization of the electric field parallel to the plane of incidence. Unpolarized natural light has an equal amount of power in each of the two linear polarizations, thus its reflection coefficient can be simply estimated as $r_{\text{eff}} = (r_s + r_p)/2$.

The absorbed component of the incident solar radiation contributes to the conductive heat balance through the outer panel, which is modeled as a planar element, according to the method described in Section 4.2.3. The convective heat transfer coefficient in the air cavity is computed according to the correlation documented in [21], namely

$$h_t = \frac{Nu \cdot k_t}{t}, \quad (4.19)$$

where t is the thickness of the air cavity, the Nusselt number is evaluated as

$$\begin{aligned} Nu &= 0.0673838 \cdot Ra^{1/3} & \text{if } Ra > 5 \cdot 10^4, \\ Nu &= 0.028154 \cdot Ra^{0.4134} & \text{if } 10^4 < Ra \leq 5 \cdot 10^4, \text{ and} \\ Nu &= 1 + 1.75967 \cdot 10^{-10} \cdot Ra^{2.2984755} & Ra \leq 10^4, \end{aligned} \quad (4.20)$$

while the Rayleigh number is computed as

$$Ra = \rho^2 t^3 g \frac{2c_p |T_{in} - T_{out}|}{\mu k_t (T_{in} + T_{out})}. \quad (4.21)$$

The transmitted component of the incident radiation acts directly on the inner panel. Therefore, the computation described by Eqn. (4.18) is repeated, accounting for the change of media at the interface. The heat transfer mechanisms established in the inner panel are equivalent to those acting on the outer panel. As a result, also the modeling approach is the same. However, in the case of the inner panel the transmitted component of radiation contributes to the heat balance of the cabin interiors.

Flight deck windshields are made of glass-faced acrylic, i.e., an outer layer of glass bonded to one or multiple layers of stretched acrylic. In between the glass and the acrylic, there is a thin urethane layer. The stretched acrylic layers are equivalent to the ones of the cabin windows, albeit much thicker. The methodology used to model the heat transfer through the flight deck windshields is the same as the one adopted for the cabin windows, with minor modifications due to the presence of multiple layers and the absence of the air gap. Therefore, the detailed description of the windshield model is omitted here for the sake of conciseness.

4.2.5. FUSELAGE MODEL

The heat flow rate due to solar radiation acting on the outer skin of the fuselage scales as a function of the total clear-sky irradiance impinging on the receiving surface E_t and the incidence angle θ . In particular, the total irradiance is the sum of the direct beam, diffuse, and ground-reflected components. These quantities can be estimated with the methodology documented in [22], [23] and reported in Appendix A for brevity. As an alternative, they can be computed by means of external software implementing more advanced algorithms, such as the open-source program SMARTS [24]–[26]. In turn, the incidence angle depends on the sun position in the sky, and the altitude and orientation of the receiver, i.e., the fuselage, see Fig. 4.7. To capture the variation of the incidence angle along the circumferential direction, the fuselage section can be conveniently discretized as a series

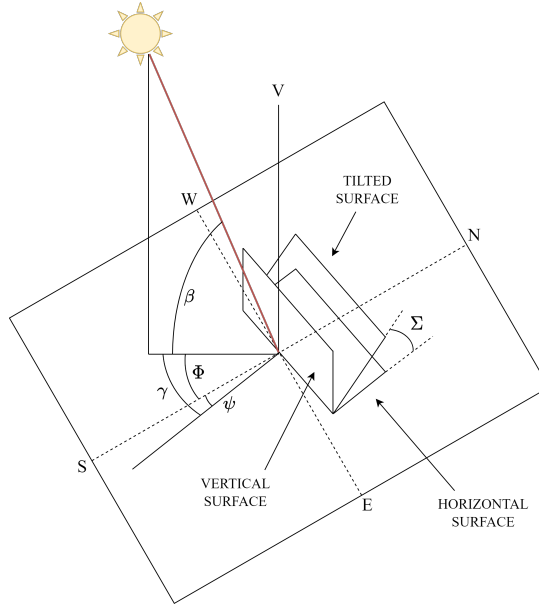


Figure 4.7: Angles formed by solar radiation incident on a tilted surface.

of circular sectors characterized by the composite structure described in Section 4.2.3. In this way, the average orientation of each sector is equivalent to that of the associated segment, as represented by the dashed lines in Fig. 4.2c. Each circular sector is subject to

$$\dot{Q}_{\text{rad}} = \dot{Q}_{\text{abs}} + \dot{Q}_{\text{em}}, \quad (4.22)$$

where

$$\begin{aligned} \dot{Q}_{\text{abs}} &= -\alpha A E_t, \\ \dot{Q}_{\text{em}} &= \dot{Q}_{\text{em,sky}} + \dot{Q}_{\text{em,air}} + \dot{Q}_{\text{em,ground}}. \end{aligned} \quad (4.23)$$

In particular, the different components of the emitted radiation can be expressed as [27]

$$\begin{aligned} \dot{Q}_{\text{em,sky}} &= \epsilon A \sigma \left(\frac{1 + \cos \Sigma}{2} \right)^{3/2} \left(T_{\text{fus,ext}}^4 - T_{\text{sky}}^4 \right), \\ \dot{Q}_{\text{em,air}} &= \epsilon A \sigma \frac{1 + \cos \Sigma}{2} \left(1 - \sqrt{\frac{1 + \cos \Sigma}{2}} \right) \left(T_{\text{fus,ext}}^4 - T_{\text{amb}}^4 \right), \\ \dot{Q}_{\text{em,ground}} &= \epsilon A \sigma \frac{1 - \cos \Sigma}{2} \left(T_{\text{fus,ext}}^4 - T_{\text{ground}}^4 \right). \end{aligned} \quad (4.24)$$

For the sake of clarity, the different components contributing to the radiative heat transfer between the fuselage and the external environment are schematically displayed in Fig. 4.8.

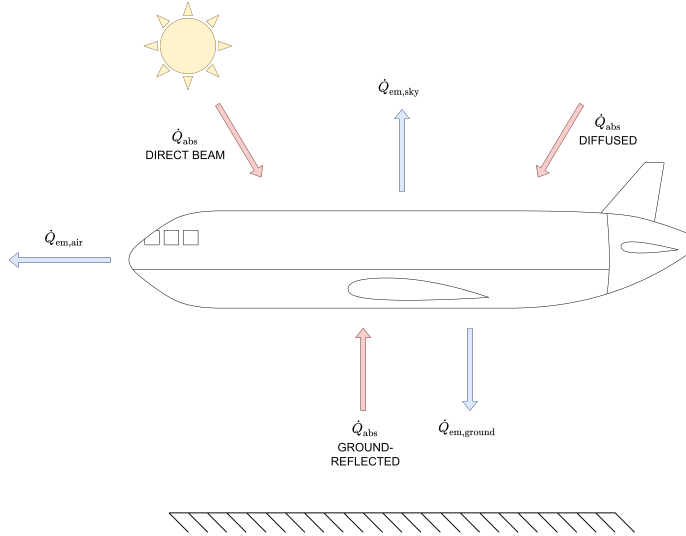


Figure 4.8: Absorbed and emitted components of the radiative heat transfer between the aircraft fuselage and the external environment.

In addition to solar radiation, each circular sector is subject to convection heat transfer from the inside and from the outside. According to the guidelines reported in [28], the physical mechanism driving the convective heat transfer between the outer skin of the fuselage and the environment depends on the flight phase and the environmental conditions. During flight, the cold ambient air adjacent to the outer skin of the aircraft is heated through the ram effect. Given that the properties of air can be estimated according to the polytropic ideal gas model, the adiabatic wall temperature can be computed as

$$T_{aw} = T_{amb} \left(1 + Pr_{aw}^{1/3} \frac{\gamma_{amb} - 1}{2} M_{\infty}^2 \right). \quad (4.25)$$

In turn, the heat flow rate reads

$$\dot{Q}_{conv,ext} = h_t A (T_{fus,ext} - T_{aw}). \quad (4.26)$$

During flight, the fuselage is at free-stream static pressure with a very good degree of approximation, thus the flat-plate analogy applies and the convective heat transfer coefficient can be conveniently computed as

$$h_t = 0.185 \rho^* c_p^* V_{\infty} \cdot (\log_{10} Re_x^*)^{-2.584} \cdot Pr^{*-2/3}, \quad (4.27)$$

where Re_x^* is the Reynolds number evaluated at x , that is the distance from the fuselage nose; its value is bounded between 10^7 and 10^9 . In this formulation, the quantities denoted by $*$ are evaluated at the thermodynamic state defined by the ambient pressure and the temperature T^* , given by [22]

$$T^* = \frac{T_{aw} + T_{amb}}{2} + 0.22(T_{aw} - T_{amb}). \quad (4.28)$$

Conversely, when the aircraft is stationary on the ground, the heat flow rate due to external convection is equal to

$$\dot{Q}_{\text{conv,ext}} = h_t A (T_{\text{fus,ext}} - T_{\text{amb}}). \quad (4.29)$$

In the limiting case of buoyancy-driven free convection, the heat transfer coefficient can be expressed as

$$h_{t,\text{free}} = \frac{0.13 k_t (Gr \cdot Pr)^{1/3}}{D_{\text{fus,ext}}}, \quad (4.30)$$

where the Prandtl number is computed at the thermodynamic state defined by the ambient pressure and the temperature T_f , given by

$$T_f = \frac{T_{\text{fus,ext}} + T_{\text{amb}}}{2}. \quad (4.31)$$

In this context, the Grashof number is evaluated as

$$Gr = \frac{g}{T_f} \frac{|T_{\text{fus,ext}} - T_{\text{amb}}| \cdot D_{\text{fus,ext}}^3}{\nu_f^2}, \quad (4.32)$$

and the convective heat transfer correlation is valid for $10^9 < Gr \cdot Pr < 10^{12}$. In the presence of wind, forced convection is the heat transfer mechanism, and the heat transfer coefficient can be estimated as

$$h_{t,\text{forced}} = \frac{0.0266 k_{t,f} \cdot Re_f^{0.805} \cdot Pr^{1/3}}{D_{\text{fus,ext}}}. \quad (4.33)$$

In this expression, the Reynolds number is evaluated as

$$Re_f = \frac{\rho_f V_{\text{wind}} D_{\text{fus,ext}}}{\mu_f}, \quad (4.34)$$

and its value is bounded between $4 \cdot 10^4$ and $4 \cdot 10^5$.

In the case of convection heat transfer occurring between the inner surfaces of the fuselage and the air volume inside the pressurized aircraft compartments, the heat flow rate is expressed as

$$\dot{Q}_{\text{conv,int}} = h_{t,\text{int}} A (T_{\text{int}} - T_{\text{fus,int}}), \quad (4.35)$$

and the heat transfer coefficient can be simply computed according to [29]

$$h_{t,\text{int}} = 5.6783 \cdot (2 + 0.314 \cdot 3.2808 \cdot V_{\text{int}}), \quad (4.36)$$

where V_{int} can assume values up to 1 m/s in an occupied compartment.

According to this discretization method, heat transfer can be modeled with the same thermal network in the upper and lower sections of the fuselage, with exception of the heat transfer occurring in presence of transparencies, e.g., cabin windows. To account for transparent surfaces, the upper section of the fuselage is discretized with five elements,

Table 4.1: Data of the validation test cases. The aircraft under analysis is an Airbus A320. Some of the data entries are normalized to preserve confidentiality.

Test Case	Hot Ground	Cruise	Faulty Pack
$\frac{\dot{m}_{\text{ECS}}}{\dot{m}_{\text{ECS,ground}}}$ [%]	100	106	88
$\frac{\dot{m}_{\text{rec}}}{\dot{m}_{\text{ECS}} + \dot{m}_{\text{rec}}}$ [%]	50	50	50
ϕ_{ECS}	0	0	0
T_{target} [°C]	27	24	27
z [km]	0	11.89	11.89
Ma_{∞}	0	0.78	0.78
ΔT_{ISA} [°C]	23	0	16
LAT [°]	33.754	33.754	33.754
LON [°]	-84.39	-84.39	-84.39
n	200	200	200
h	12	12	12
N_{pax}	196	180	180
N_{crew}	6	6	6
N_{pilots}	3	3	3
\dot{Q}_{el} [kW]	1.2	1.2	1.2
\dot{Q}_{gal} [kW]	1.5	1.5	1.5
\dot{Q}_{av} [kW]	10	0	0
\dot{Q}_{el} [kW]	1.15	1.15	1.15
\dot{Q}_{ife} [kW]	5.88	5.40	5.40

whereby the two lateral segments include suitable models for the heat transfer related to the windows. The complete thermal network used to model the upper fuselage sector corresponding to a cabin ventilation zone is displayed in Fig. 4.4d. The fuselage sector corresponding to the cockpit is modeled in the same fashion, with models for the lateral and frontal flight deck windshields in place of the cabin windows models.

4.3. VALIDATION

In order to assess the accuracy of the thermal model of the passenger aircraft fuselage, the simulation results have been compared with proprietary data provided by the industrial partner Airbus. The validation test cases comprise the most relevant operating points defining the design of the ECS of an Airbus A320. The operating conditions on which the ECS design is based are: i) standard cruise conditions, ii) ground operation on a hot and humid day, and iii) flying conditions in case of a faulty ECS pack. The characteristics of the aircraft considered for the validation test cases are reported in Tab. B.1 of Appendix B. Moreover, the specifications of the aircraft composite structures, cabin windows and flight deck windshields are listed in Tab. B.2, Tab. B.3, Tab. B.4, and Tab. B.5 of Appendix B. The three considered operating points are defined by the data reported in Tab. 4.1. These include:

Table 4.2: Results of the validation test cases. The aircraft under analysis is an Airbus A320. The results are normalized or expressed as deviation with respect to proprietary data to preserve confidentiality.

Test Case	Hot Ground	Cruise	Faulty Pack
ΔT_{ECS} [°C]	2.42	1.14	0.74
ΔP_{ECS} [kPa]	0.07	0.58	4.47
$\dot{m}_{\text{cpt}}/\dot{m}_{\text{cab}}$ [%]	12.6	11.7	11.7
\dot{Q}_{tot} [kW]	n.a.	n.a.	n.a.
$\dot{Q}_{\text{cpt}}/\dot{Q}_{\text{tot}}$ [%]	6.8	1.8	2.7
$\dot{Q}_{\text{cpt,int}}/\dot{Q}_{\text{cpt}}$ [%]	45.1	266	186.9
$\dot{Q}_{\text{cpt,ext}}/\dot{Q}_{\text{cpt}}$ [%]	54.9	-166	-86.9
$\dot{Q}_{\text{cab}}/\dot{Q}_{\text{tot}}$ [%]	62.9	69.3	78.4
$\dot{Q}_{\text{cab,int}}/\dot{Q}_{\text{cab}}$ [%]	94.3	123.1	116.3
$\dot{Q}_{\text{cab,ext}}/\dot{Q}_{\text{cab}}$ [%]	5.7	-23.1	-16.3
$\dot{Q}_{\text{ufloor}}/\dot{Q}_{\text{tot}}$ [%]	30.3	28.9	18.9
$\dot{Q}_{\text{ufloor,int}}/\dot{Q}_{\text{ufloor}}$ [%]	64.6	0.0	0.0
$\dot{Q}_{\text{ufloor,ext}}/\dot{Q}_{\text{ufloor}}$ [%]	35.4	100	100

- the total mass flow rate of fresh air provided by the ECS, together with the relative humidity at the outlet of the pack and the recirculation ratio;
- the temperature set point, assumed that it is the same for all the ventilation zones;
- the altitude and speed of the aircraft;
- the data about the climate, including the geographic location, date and time, and deviation from the ISA standard conditions;
- the number of occupants onboard the aircraft, namely, passengers, crew members, and pilots;
- the thermal energy generated inside the fuselage, namely that due to flight deck electronics, avionics, galleys, in-flight entertainment, and cabin lights.

The model is used to compute the conditions at the outlet of the ECS packs required to comply with the pressure and temperature set points prescribed for each ventilation zones. The absolute deviations between the predictions of the model and the data provided by Airbus are reported in Tab. 4.2, whereas the actual values are omitted for confidentiality. The maximum absolute deviations in terms of temperature and pressure at the discharge of the ECS packs are equal to 2.4 K and 4.5 kPa, respectively. Accounting for the uncertainty in the data about the climate or external environment and the uncertainty related to the technical specifications of the aircraft, which have not been provided by the industrial partner, the accuracy of the model is deemed acceptable for the purpose of this study.

In addition to the absolute deviations between the model predictions and the validation data, Tab. 4.2 lists the ratio between the airflow delivered to the cockpit and cabin, as well as the total heat flow rate computed for the entire fuselage and the individual compartments, i.e., cockpit, cabin, and underfloor, comprising both cargo and E/E bays. Furthermore, to comply with the format of the validation data provided by the industrial partner, these are divided into two contributions, depending on whether the corresponding thermal energy source is internal or external to the fuselage. The external heat flow rate is considered positive when entering the considered control volume. As can be noticed in Tab. 4.2, most of the thermal energy that must be removed by the ECS can be attributed to the cabin. While the aircraft is flying, part of the thermal energy coming from the sources internal to the fuselage is transferred to the external cold environment. Instead, during ground operation on a hot and humid day, the heat transfer with the environment is in the opposite direction and further increases the total heat load of the ECS. The same considerations apply to the cockpit section, with a higher relative influence of the heat transfer with the external environment, due to the relatively larger transparent surfaces. The underfloor volumes do not feature any source of thermal energy, except for the avionics. During flight, the avionics are cooled by the skin heat exchanger, therefore they are not accounted for in the model. However, the avionics heat generation must be taken into account in case of hot ground operation, the most critical operating condition, which defines the sizing point of the ECS.

4.4. APPLICATIONS

To showcase the capabilities of the *DynTherM* library, two examples of applications are documented. The selected aircraft configuration is the same used for model validation, i.e., an Airbus A320. However, the library can be used to model the fuselage thermal fluxes of any other commercial aircraft.

4.4.1. ECS OPERATING ENVELOPE

The operating envelope of the Airbus A320 ECS is identified by simulating 50 operating points, belonging to widely different operating scenarios, namely ground, climb, cruise, and faulty pack operations, and simulated at variable climate conditions. The data defining these operating points are listed in Tab. 4.3. In particular, each of the 10 selected flight phases is simulated for 5 different climate conditions. The results are displayed in Fig. 4.9. The chart on the left shows that the temperature at the discharge of the ECS is almost insensitive to the change of flight phase. The only exception is ground operation, which is always characterized by higher cooling demand. Conversely, T_{ECS} strongly scales with the change of the environmental conditions, with temperature variations of up to $\approx 25^\circ\text{C}$ for the same flight condition. Furthermore, the cabin pressure delivered by the ECS is only a function of the aircraft altitude, thus of the flight phase. According to industry best practices, the ECS of passenger aircraft must be sized to meet the extreme operating points of the envelope. At the same time, the ECS should be optimized for the most common operating conditions. Therefore, the information displayed in the $P - T$ diagram of Fig. 4.9, together with the corresponding mass flow rate of fresh air provided for each operating point, is essential to tackle the multi-point design optimization of the system.

Table 4.3: Data of the operating points used to identify the operating envelope of the ECS of an Airbus A320. The parameters T_{target} , z , Ma_{∞} , ΔT_{ISA} , n , h , N_{pax} , \dot{Q}_{av} , \dot{Q}_{ife} assume different values in the range defined by the lower bound (lb) and the upper bound (ub). Some of the data entries are normalized to preserve confidentiality.

Test Case	Ground	Climb	Cruise	Faulty Pack
$\frac{\dot{m}_{\text{ECS}}}{\dot{m}_{\text{ECS,ground}}}$ [%]	100	106	106	88
$\frac{\dot{m}_{\text{rec}}}{\dot{m}_{\text{ECS}} + \dot{m}_{\text{rec}}}$ [%]	50	50	50	50
ϕ_{ECS}	0	0	0	0
T_{target} [°C]	24 : 27	24	24	24
z [km]	0	6 : 9	11.89	11.89
Ma_{∞}	0	0.6 : 0.78	0.78	0.78
ΔT_{ISA} [°C]	-23 : 23	-23 : 23	-23 : 23	-23 : 23
LAT [°]	33.754	33.754	33.754	33.754
LON [°]	-84.39	-84.39	-84.39	-84.39
n	20 : 200	20 : 200	20 : 200	20 : 200
h	9 : 12	9 : 12	9 : 12	9 : 12
N_{pax}	100 : 196	100 : 196	100 : 196	100 : 196
N_{crew}	6	6	6	6
N_{pilots}	3	3	3	3
\dot{Q}_{el} [kW]	1.2	1.2	1.2	1.2
\dot{Q}_{gal} [kW]	1.5	1.5	1.5	1.5
\dot{Q}_{av} [kW]	0 : 10	0	0	0
\dot{Q}_{cl} [kW]	1.15	1.15	1.15	1.15
\dot{Q}_{ife} [kW]	0 : 5.88	0 : 5.88	0 : 5.88	0 : 5.88

The characterization of the operating envelope is complemented by the chart displayed on the right side of Fig. 4.9, where the temperature of the fresh air at the pack discharge is correlated with the total thermal load, as well as with the individual components related to the cabin, cockpit, and underfloor compartments. In accordance with what reported in Section 4.3, the cabin is responsible for the largest share of the ECS duty, followed by the underfloor areas, and the cockpit. Interestingly, the relationship between T_{ECS} and the total heat load can be approximated by linear regression with good accuracy. For this example, the linear correlation reads

$$\dot{Q}_{\text{tot}} = 31.028 - 1.227T_{\text{ECS}}, \quad (4.37)$$

where \dot{Q}_{tot} and T_{ECS} are expressed in kilowatt and degree Celsius, respectively. In turn, if an estimate of the total heat load related to another operating point is available, this simple equation can be used to compute a first guess of the temperature at the ECS discharge, or vice versa. This approach is significantly less time-consuming than setting up a new test case and running the fuselage thermal model, thus it can be conveniently used to assess the ECS operating envelope during the preliminary design phase. However, this correlation cannot be generalized to a different aircraft configuration.

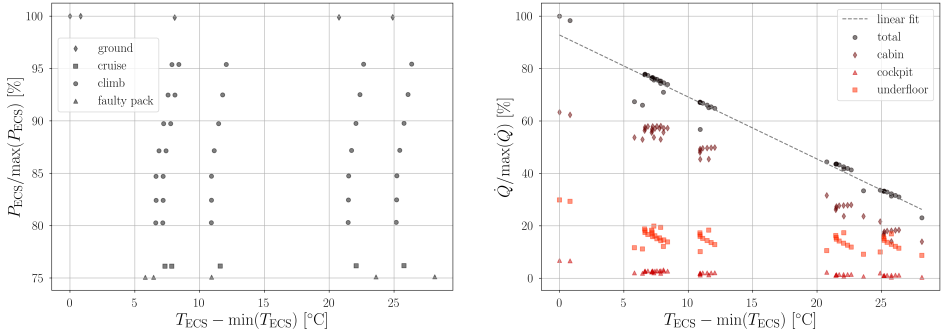


Figure 4.9: Operating envelope of the ECS of an Airbus A320 calculated with a model obtained with the *Dyn-TherM* library. The boundary conditions at the pack discharge, defined in terms of pressure and temperature, are shown in the left chart. The total and individual components of the heat load are displayed versus the temperature at the pack discharge in the right chart. The results are normalized or expressed as absolute differences to preserve confidentiality.

4.4.2. PULL-DOWN OPERATING POINT

This case study is concerned with the simulation of a *pull-down operating point*, that is, an operating point for which the aircraft is on the ground on a hot day, but empty of passengers, and with minimal heat loads internal to the fuselage. The initial temperature is set to 40°C in all the ventilation zones and the ECS must lower it to the set point within 30 minutes. Differently from the operating conditions analyzed in Sections 4.3 and 4.4.1, which require only steady-state simulations, this test case is about the dynamics of the system. Although the pull-down operating point is not extreme, it is included in the requirements for the certification of the ECS. Therefore, the accurate simulation of the ECS dynamics is of paramount importance.

The simulation setup is similar to the one used for the hot ground case reported in Tab. 4.1. The only differences are the absence of passengers in the cabin, the absence of thermal energy input due to galleys, avionics, and in-flight entertainment, and the lower value of recirculation ratio, set to $\dot{m}_{rec} / (\dot{m}_{ECS} + \dot{m}_{rec}) = 0.2$. The temperature at the outlet of the ECS pack is set to $T_{ECS} = -15^\circ\text{C}$, in accordance with the operating point featuring the highest cooling requirement reported in Fig. 4.9. The following considerations can be drawn from the results displayed in Fig. 4.10. First, the ECS is capable of meeting the temperature set point of 24°C in the prescribed time for both ventilation zones. In the absence of trim air and active control of the airflow delivered to the different ventilation zones, the cockpit reaches the temperature set point in approximately 23.3 minutes, whereas the cabin requires 30 minutes, due to its higher thermal inertia. Moreover, a temperature rise is observed in the underfloor compartments during the initial transient. To explain this phenomenon, it is important to notice that the initial temperature has been set to the same value in all the ventilation zones without accounting for thermal equilibrium. An alternative approach to avoid the initial temperature rise in the underfloor compartments consists in using the results of a steady-state simulation without the ECS to initialize the transient simulation of the pull-down case.

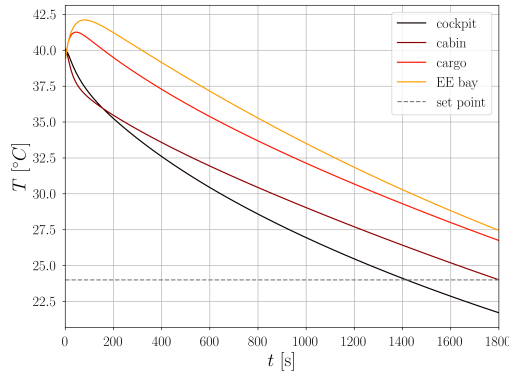


Figure 4.10: Pull-down case study: temporal evolution of the temperature in the main aircraft compartments computed with the Airbus A320 fuselage thermal model obtained with the *DynTherM* library.

Additional insights about the time-dependent evolution of the temperature distribution in the cabin and cargo compartments can be gained by analyzing Fig. 4.11. In accordance with what documented in Section 4.2 and displayed in Fig. 4.2, the fuselage is discretized with eight elements along the circumferential direction. Each element is a circular sector of the composite structure described in Section 4.2.3, featuring the properties reported in Tab. B.2 of Appendix B. The temperature of the air in the cabin and cargo volumes is displayed in the central part of the polar plot. The outer portion of the polar plot corresponds to the fuselage skin. In between them, the temperature distribution is shown for the different portions of the fuselage composite structure.

At the initial time instant of the simulation, the temperature is uniform and equal to the prescribed initial condition of 40°C. Afterwards, the simulation evolves with the injection of a mixture of fresh and recirculated air into the cabin and a radial temperature gradient is progressively established between the internal air volume and the fuselage skin. At the same time, the conditioned air is circulated to the cargo bay by means of the dado panels located on the cabin floor, leading to a higher temperature in the lower sections of the fuselage. At the last time instant, the highest temperature, i.e., 56.9°C, is measured in the lower right part of the fuselage skin, whereas the coldest portion of the skin, i.e., 43.6°C, is located in the opposite corner. At the same locations, the radial temperature gradient evaluated through the fuselage composite structure is equal to 30.1°C and 19.6°C, respectively. This highlights the presence of a non-symmetric solar radiation field acting on the fuselage at the specified climate conditions. Moreover, the non-uniformity shows the influence of ground-reflected solar radiation and ground-emitted radiation on the fuselage temperature distribution when operating the aircraft on the ground during a hot day. This information can be used to assess the influence of the layout and the materials used for the fuselage composite structure on the thermal dynamics of the aircraft.

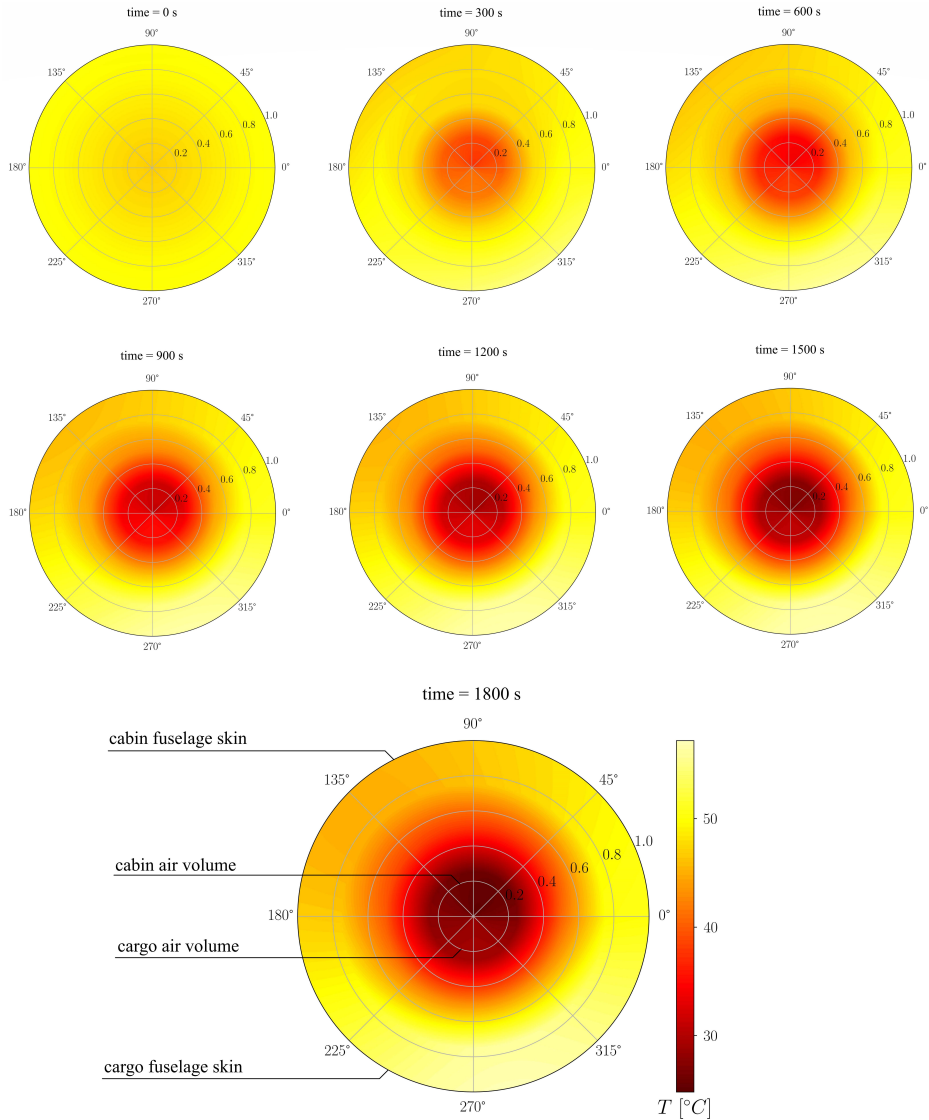


Figure 4.11: Pull-down case study: temperature distribution in the cabin and cargo compartments computed at different time instants using the Airbus A320 fuselage thermal model obtained with the *DynTherM* library. The fuselage is discretized with eight elements along the circumferential direction. The inner section of the polar plot corresponds to the pressurized air volumes, whereas the outer section represents the fuselage skin.

4.5. CONCLUSIONS

This chapter documents the development, validation, and use of the *DynTherM* Modelica library. The modules of this library allow to compose the dynamic thermal model of the air distribution system and the pressurized compartments of a passenger aircraft. The *DynTherM* library has been validated with proprietary data concerning the fuselage thermal characteristics of an A320 aircraft provided by the industrial partner Airbus. For the considered validation case studies, the results computed by the model show maximum absolute deviations of 2.4 K and 4.5 kPa with respect to the actual temperature and pressure evaluated at the discharge of the ECS pack. The validated thermal model has been used to compute the operating envelope of the ECS of an Airbus A320. The outcomes show that the thermodynamic state at the discharge of the pack varies substantially as a function of the flight phase and climate conditions. This confirms the need for a fast and accurate thermal model to provide the specifications for the multi-point design optimization of a novel ECS configuration. Finally, the study is complemented with the simulation of a test case involving a pull-down operating point. The results reveal the ability of the model to capture the dynamic thermal behavior of the system and provide additional insights about the evolution of the temperature distribution throughout the different sections of the fuselage as a function of time.

Currently, the modeling method at the basis of the *DynTherM* library is affected by the following limitations:

- the leakage of pressurized air through the fuselage is neglected, leading to a possible underestimation of the ECS pressurization requirements;
- the heat transfer through the fuselage is modeled as one dimensional, i.e., only heat transfer along the radial direction is considered, as the thermal resistance in the circumferential direction is negligible if compared to the radial one. However, to simulate more accurately the temperature distribution in the presence of a non-symmetric solar field, also the heat transfer in the circumferential direction must be modeled, at the expenses of increased complexity and computational cost;
- the temperature at the ECS pack discharge is computed to match the temperature set point in one ventilation zone, e.g., the cabin. Then the trim air flow rate is prescribed to achieve the set temperature in the remaining ventilation zones, e.g., the cockpit. To simplify the use of the model, it is necessary to automatically vary the opening of the trim air valves to match the temperature set point in all the ventilation zones.

Future work will entail the study of non-conventional ECS architectures for aircraft configurations alternative to the Airbus A320. For this purpose, the dynamic thermal model of the aircraft fuselage developed with the *DynTherM* library and documented in this chapter, will be tailored for each aircraft configuration and applied to retrieve the corresponding ECS operating envelope. A similar study will be performed for large rotorcraft applications. Moreover, future research will target the development of thermal management systems for disruptive aircraft layouts, aimed at accelerating the transition to net

zero emissions by the aviation sector, such as battery-powered and fuel cell-powered aircraft. To tackle the design of such systems, the *DynTherM* library will be extended to include models for characterizing the dynamic thermal behavior of battery packs, as well as that of hydrogen storage and distribution systems.

NOMENCLATURE

Roman symbols

A	Surface area [m^2]
c_p	Specific heat capacity [$\text{J kg}^{-1} \text{K}^{-1}$]
D	Diameter [m]
E	Irradiance [W m^{-2}]
Gr	Grashof number [-]
g	Gravitational acceleration [m s^{-2}]
h	Specific enthalpy [J kg^{-1}] Hour of the day [-]
h_t	Heat transfer coefficient [$\text{Wm}^{-2}\text{K}^{-1}$]
k_t	Thermal conductivity [$\text{Wm}^{-1}\text{K}^{-1}$]
L	Length [m]
M	Metabolic heat production [Wm^{-2}] Mach number [-]
m	Mass [kg]
\dot{m}	Mass flow rate [kg s^{-1}]
N	Number of elements [-]
Nu	Nusselt number [-]
n	Day of the year [-] Refractive index [-]
Pr	Prandtl number [-]
\dot{Q}	Heat flow rate [W]
R	Radius [m] Specific gas constant [$\text{J kg}^{-1} \text{K}^{-1}$]
Ra	Rayleigh number [-]
Re	Reynolds number [-]
r	Reflection coefficient [-]
T	Temperature [K]
t	Transmittance [-] Thickness [m] Time [s]
U	Internal energy [J]
u	Specific internal energy [Jkg^{-1}]
V	Velocity [ms^{-1}] Volume [m^3]
x	Mass fraction [-]
z	Altitude [m]

Greek symbols

α	Absorptivity [-]
ϵ	Emissivity [-]
θ	Incidence angle [deg]
μ	Dynamic viscosity [Pa s^{-1}]
ν	Kinematic viscosity [$\text{m}^2 \text{s}^{-1}$]
ρ	Density [kg m^{-3}]
Σ	Tilt angle [deg]

σ	Boltzmann constant [$\text{m}^2\text{kgs}^{-2}\text{K}^{-1}$]
Φ	Relative humidity [-]

Subscripts

abs	Absorbed
amb	Ambient
aw	Adiabatic wall
av	Avionics
b	Direct beam component
cab	Cabin
cl	Cabin lights
conv	Convection
cpt	Cockpit
diff	Water diffusion
el	Flight deck electronics
em	Emitted
fus	Fuselage
gal	Galley
hb	Human body
ife	In-flight entertainment
l	Liquid
lat	Latent
p	P-polarized light
pax	Passengers
r	Reflected
rad	Radiation
rec	Recirculated
res	Respiration
rsw	Sweating
s	S-polarized light
sens	Sensible
t	Component acting on the receiver surface
tot	Total
tr	Transmitted
ufloor	Underfloor
v	Vapor
w	Water

Abbreviations

CFD	Computational fluid dynamics
ECS	Environmental control system
E/E	Electronics and equipment
LAT	Site latitude
LON	Site longitude
MSL	Mean sea level

BIBLIOGRAPHY

- [1] M. Dechow and C. Nurcombe, "Aircraft Environmental Control Systems", in *Air Quality in Airplane Cabins and Similar Enclosed Spaces*, M. Hocking, Ed., Berlin, Heidelberg: Springer Berlin Heidelberg, 2005, pp. 3–24, ISBN: 978-3-540-31491-2. DOI: 10.1007/b107234.
- [2] A. Pollok, "Modelling and control of aircraft environmental control systems", Ph.D. dissertation, Politecnico di Milano, 2018.
- [3] C. Giaconia, A. Orioli, and A. Di Gangi, "Air quality and relative humidity in commercial aircrafts: An experimental investigation on short-haul domestic flights", *Building and Environment*, vol. 67, pp. 69–81, 2013, ISSN: 0360-1323. DOI: 10.1016/j.buildenv.2013.05.006.
- [4] B. Oehler, "Modeling and simulation of global thermal and fluid effects in an aircraft fuselage", in *4th International Modelica Conference*, Harburg, Germany, 2005, pp. 497–506.
- [5] *The Modelica Association*. [Online]. Available: <https://modelica.org/>.
- [6] C. Müller, D. Scholz, and T. Giese, "Dynamic simulation of innovative aircraft air conditioning", in *1st CEAS European Air and Space Conference*, 2007.
- [7] A. Pollok, D. Bender, I. Kerling, and D. Zimmer, "Rapid development of an aircraft cabin temperature regulation concept", in *12th International Modelica Conference*, Jul. 2017, pp. 151–159. DOI: 10.3384/ecp17132151.
- [8] M. A. Fayazbakhsh and M. Bahrami, "Comprehensive Modeling of Vehicle Air Conditioning Loads Using Heat Balance Method", *SAE Technical Papers*, 2013. DOI: 10.4271/2013-01-1507.
- [9] F. Brèque and M. Nemer, "Cabin Thermal Needs: Modeling and Assumption Analysis", in *Proceedings of the 12th International Modelica Conference*, Prague, Czech Republic, 2017, pp. 771–781. DOI: 10.3384/ecp17132771.
- [10] M. Geron, C. Butler, J. Stafford, and D. Newport, "Development and validation of a compact thermal model for an aircraft compartment", *Applied Thermal Engineering*, vol. 61, no. 2, pp. 65–74, 2013. DOI: 10.1016/j.applthermaleng.2013.07.012.
- [11] G. Schweiger, H. Nilsson, J. Schoeggel, W. Birk, and A. Posch, "Modeling and simulation of large-scale systems: A systematic comparison of modeling paradigms", *Applied Mathematics and Computation*, vol. 365, Jan. 2020, ISSN: 0096-3003. DOI: 10.1016/J.AMC.2019.124713.
- [12] F. Casella and A. Leva, "Modelica open library for power plant simulation: design and experimental validation", in *Proceedings of the 3rd International Modelica Conference*, P. Fritzson, Ed., Linköping, 2003, pp. 41–50.
- [13] F. Casella and A. Leva, "Modelling of thermo-hydraulic power generation processes using Modelica", *Mathematical and Computer Modelling of Dynamical Systems*, vol. 12, no. 1, pp. 19–33, Feb. 2006, ISSN: 13873954. DOI: 10.1080/13873950500071082.
- [14] P. O. Fanger *et al.*, *Thermal comfort. Analysis and applications in environmental engineering*. McGraw-Hill, 1970.
- [15] "Thermal comfort", in *ASHRAE Handbook - Fundamentals*, American Society of Heating, Refrigerating and Air-Conditioning Engineers - ASHRAE, 2013, ISBN: 978-1-936504-46-6.
- [16] F. Rohles and R. Nevins, "The nature of thermal comfort for sedentary man", *ASHRAE Transactions*, vol. 77, no. 1, pp. 239–246, 1971.
- [17] "Standard atmosphere", International Organization for Standardization, Geneva, CH, Standard, 1975.
- [18] X. D. Fang, "Study on saturation water-vapor pressure equations for calculation of aircraft air-conditioning systems", *Journal of Aerospace Power*, 1995. DOI: 10.329-300.

-
- [19] Q. Dai and X. Fang, "A new model for atmospheric radiation under clear sky condition at various altitudes", *Advances in Space Research*, vol. 54, no. 6, pp. 1044–1048, 2014, ISSN: 0273-1177. DOI: 10.1016/j.asr.2014.05.028.
- [20] F. Zanghirella, M. Perino, and V. Serra, "A numerical model to evaluate the thermal behaviour of active transparent façades", *Energy and Buildings*, vol. 43, no. 5, pp. 1123–1138, 2011, ISSN: 0378-7788. DOI: 10.1016/j.enbuild.2010.08.031.
- [21] J. L. Wright, "A correlation to quantify convective heat transfer between vertical window glazings", *ASHRAE Transaction*, vol. 102, no. 1, pp. 940–946, 1996.
- [22] "Climatic design information", in *ASHRAE Handbook - Fundamentals*, American Society of Heating, Refrigerating and Air-Conditioning Engineers - ASHRAE, 2013, ISBN: 978-1-936504-46-6.
- [23] G. Comini and S. Savino, *La Captazione dell'Energia Solare*. Udine: International Center for Mechanical Sciences, 2013, ISBN: 978-88-85137-45-5.
- [24] C. A. Gueymard, "Smarts2, a simple model of the atmospheric radiative transfer of sunshine: Algorithms and performance assessment", Tech. Rep., 1995.
- [25] C. A. Gueymard, "Parameterized transmittance model for direct beam and circumsolar spectral irradiance", *Solar Energy*, vol. 71, no. 5, pp. 325–346, 2001, ISSN: 0038-092X. DOI: [https://doi.org/10.1016/S0038-092X\(01\)00054-8](https://doi.org/10.1016/S0038-092X(01)00054-8).
- [26] C. A. Gueymard, "Interdisciplinary applications of a versatile spectral solar irradiance model: A review", *Energy*, vol. 30, no. 9, pp. 1551–1576, 2005, ISSN: 0360-5442. DOI: <https://doi.org/10.1016/j.energy.2004.04.032>.
- [27] F. Goia, M. Perino, and M. Haase, "A numerical model to evaluate the thermal behaviour of pcm glazing system configurations", *Energy and Buildings*, vol. 54, pp. 141–153, 2012, ISSN: 0378-7788. DOI: 10.1016/j.enbuild.2012.07.036.
- [28] "Aircraft", in *ASHRAE Handbook - Heating, Ventilating, and Air-Conditioning Applications*, American Society of Heating, Refrigerating and Air-Conditioning Engineers - ASHRAE, 2019, ISBN: 978-1-947192-13-3.
- [29] "AIR1168/3 - Aerothermodynamic Systems Engineering and Design", SAE Aerospace, Tech. Rep., 2011.

5

INTEGRATED DESIGN OPTIMIZATION OF ECS FOR NEXT-GENERATION AIRCRAFT

5

*Nature uses only the longest threads to weave her patterns,
so that each small piece of her fabric reveals the organization of the entire tapestry.*

Richard Phillips Feynman

The use of an electrically-driven Vapor Compression Cycle (VCC) system in place of the conventional Air Cycle Machine (ACM) for the Environmental Control System (ECS) of next-generation aircraft could lead to a substantial reduction in fuel consumption. The interest in the adoption of VCC systems for airborne applications is further enhanced by the advent of new refrigerants, featuring low Global Warming Potential (GWP), low toxicity, and flammability, and by the latest development of high-speed centrifugal compressors and ultra-compact heat exchangers. This chapter documents the development of an integrated design optimization method for aircraft ECS, whereby the preliminary design and performance evaluation of the system is performed along with the conceptual design of its main components. This novel methodology is applied to carry out the multi-point and multi-objective design optimization of a bleedless ACM and an electrically-driven VCC system for a single-aisle, short-haul aircraft. The comparison between the performance of the two optimal ECS architectures show that the VCC system is characterized by lower weight and electric power consumption than the bleedless ACM layout, but features a higher drag penalty. Overall, the optimal VCC system is predicted to burn approximately 20% less fuel than the bleedless ACM for the prescribed application. In addition, the optimization study provides insights into the trends characterizing the design of the main components of the two systems. This information can be used to draw general design guidelines or as a starting point for the detailed design phase. With the appropriate modifications, the same methodology can be generally applied to design and optimize the performance of any energy conversion system.

5.1. INTRODUCTION

THE Environmental Control System (ECS) is the user of the largest amount of onboard non-propulsive power, accounting for up to 3-5% of the total fuel burn [1]. To reduce the fuel consumption due to the ECS, the Boeing 787 has been equipped with a so-called *bleedless ECS* driven by an electrical motor. This solution eliminates the extraction of pneumatic power generated by the engines and enables a reduction of specific fuel consumption in the range of 1-2% at cruise conditions [2]. In addition to fuel savings, adopting an electrically-powered ECS is expected to reduce maintenance costs and increase system reliability, due to the removal of the maintenance-intensive bleed system [2], [3]. Furthermore, the replacement of the traditional Air Cycle Machine (ACM), based on the inverse Brayton cycle, with a Vapor Compression Cycle (VCC) system, based on the inverse Rankine cycle, may lead to a substantial reduction of the electric power consumption. However, the adoption of this technology in the aerospace sector has been historically very limited, due to safety concerns and regulations regarding the Ozone depleting potential, toxicity and flammability of the working fluids used as refrigerants, as well as because of the larger weight associated with VCC systems, which are commonly designed for stationary applications. With the advent of next-generation refrigerants, featuring low Global Warming Potential (GWP), low toxicity, and no or low flammability, together with the recent development of high-speed centrifugal compressors and ultra-compact heat exchangers, there is renewed interest in the possibility of adopting VCC systems for airborne applications.

A dynamic model for the simulation of both steady-state and transient operations of VCC systems for aircraft ECS was developed and is documented in Ref. [4]. The au-

thors state that the main efforts were focused on the development of two-phase heat exchangers models, whereas the performance of other components, e.g., the refrigerant compressor, were calculated by means of look-up tables. Ref. [5] presents a graph-theory steady-state model to investigate arbitrary layouts of the refrigeration cycle and the cooling fluid loop used for the thermal management of galleys and avionics of commercial aircraft. The model was validated experimentally, resulting in a difference between calculated and measured values of $\pm 8\%$ for the cooling capacity, $\pm 8^\circ\text{C}$ for the system temperatures, and $\pm 10\%$ for the system pressures. The possibility of using a VCC system to heat the aircraft cabin in cold environments has been investigated experimentally by Xu et al [6]. The authors proposed to integrate the VCC-based ECS with the engine oil lubrication loop through a refrigerant-oil heat exchanger. During normal operation of the ECS, the refrigerant-oil heat exchanger is bypassed and the two systems are decoupled. When cabin heating is required, the heat coming from the lubricating oil is used for the evaporation of the refrigerant, and the air at the outlet of the condenser is supplied to the cabin. From a more theoretical perspective, a thorough attempt to derive an analytical formulation of the COP of aircraft ECS can be found in [7]. The authors obtained an explicit expression of the COP for five different ACM configurations. However, the COP derivation is based on the assumption of dry air and of fluids whose properties obey to the ideal gas law, thus it is not applicable to VCC systems, because the working fluid undergoes phase changes, and its properties cannot be estimated with the ideal gas thermodynamic model. In all the aforementioned studies, the researchers did not account for the conceptual design of the main components of the ECS, namely, the heat exchangers and the turbomachines. However, as reported in Ref. [8], the performance of the ECS strongly depends on the design and performance of its components. Therefore, the optimal design of the system can arguably only be achieved by resorting to an integrated design approach, i.e., a computational framework in which the design variables of the system and those related to the preliminary design of the main components are optimized simultaneously.

A pioneering application of the integrated design method to the optimization of a simplified ECS configuration is documented in Ref. [9]. Following this work, numerous attempts have been made to apply the integrated design approach to more complex and more realistic ECS configurations. In [10], the authors showcase the multi-objective optimization of a two-wheel bootstrap ACM, including the preliminary design of the two offset strip fin heat exchangers. The objectives selected for the optimization were the minimization of the volume of the heat exchangers, and the minimization of the total entropy generation at cruise conditions. The study has been subsequently extended to include a thermo-economic analysis, as documented in Ref. [11]. More recently, the multi-objective optimization of an unconventional ECS architecture, featuring a hybrid ACM-VCC system, has been studied by Sielemann et al. [12]. In this work, the ECS has been simulated under three different operating conditions, and the specific fuel consumption (SFC) has been computed as the weighted average of the values obtained in the three scenarios. An alternative strategy to compute the thermodynamic characteristics of a conventional ECS configuration has been proposed by Li et al. [13]. By adopting the heat current method, in place of the energy flow method, the authors were able to reduce the number of independent variables and governing equations of the system, thus simplifying its solution for analysis and optimization purposes. Ref. [14] reports the multi-objective optimization of

a three-wheel bootstrap ACM, including the high-pressure water separation loop. The optimization procedure featured four design variables, namely, the effectiveness of the four heat exchangers, two objectives, i.e., the entropy generation rate due to the ECS and the number of transfer units (*NTU*) of its heat exchangers, and five non-linear constraints.

All the studies concerning the integrated design optimization of aircraft ECS have treated conventional or hybrid ACM configurations, focusing the modeling effort on the heat exchangers. However, in a VCC system featuring a high-speed centrifugal compressor operating with gas bearings, the most critical component is arguably the compressor. The operating range of the VCC system is limited by the choke and stall margins of the compressor, and the COP is strongly affected by the efficiency of the turbomachine. Therefore, in order to perform an integrated design optimization of a VCC-based ECS, it is necessary to include a model of the turbo-compressor. Furthermore, the ECS is characterized by a broad operating envelope, ranging from cruise operation to extreme operating points, such as ground operation on a hot and humid day, and flight operation in the presence of a faulty ECS pack. As a result, the optimal preliminary design of the ECS can be only obtained with a multi-point optimization strategy.

The objective of this work is therefore twofold. The first goal is to advance the state-of-the-art regarding the methodologies used for the integrated design optimization of energy conversion systems in general, and airborne VCC systems in particular. This is achieved by demonstrating the capabilities of a new multi-objective and multi-point optimization framework, hereinafter referred to as DesOptECS (Design Optimization of Energy Conversion Systems), embedding the preliminary design of the compact heat exchangers, the cabin air compressor, and the refrigerant compressor within the design of the system. The second target is to compare the performance metrics of two optimized ECS configurations featuring different architectures: a bleedless ACM, and an electrically-driven VCC system. The ultimate goal is to evaluate if the theoretical benefits of the envisaged novel ECS architecture can be realized. The remainder of the chapter is structured as follows. First, the methodology used to model the main components of the two systems is introduced. Then, the structure of DesOptECS is presented. Next, the results of the optimization of the bleedless ACM and the VCC system are discussed and compared. Finally, the main outcomes of this study are summarized in the form of concluding remarks and an outlook for future work is provided.

5.2. METHODOLOGY

5.2.1. SYSTEM MODEL

The capabilities of DesOptECS are demonstrated by performing the preliminary design of two ECS's for a single-aisle, short-haul aircraft, e.g., the Airbus A320. One ECS configuration is based on a bleedless three-wheel ACM, i.e., the system equipping the Boeing 787; the other features an electrically-driven VCC system powered by a twin-stage centrifugal compressor. The ACM-based configuration has been selected to assess the performance of state-of-the-art ECS technology. The VCC system configuration has been chosen as a trade-off between system complexity and performance: the COP could be improved by adopting a configuration featuring multiple pressure levels, however the increased number of components would lead to larger weight and a higher risk of failures, thus requiring

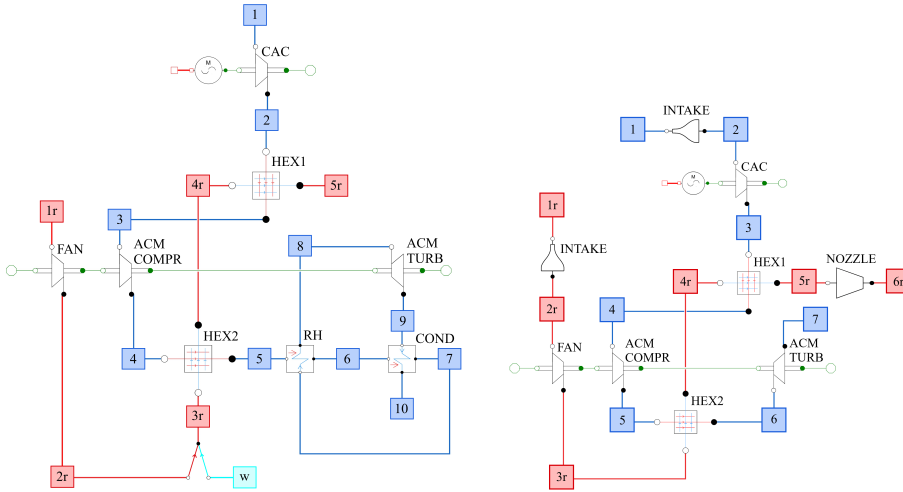


Figure 5.1: Graphical representation of the modular Modelica models of the bleedless three-wheel bootstrap air cycle machine used to simulate ground (left) and flying (right) operation. The thermodynamic states of the ram air stream are highlighted in red, whereas the ones of the cabin air stream are displayed in blue. Image adapted from the graphical user interface of the DeSimECS library.

more frequent maintenance. The description of the exemplary ACM and VCC systems is reported in Chapter 1 and is omitted here for the sake of conciseness.

The models of the two ECS configurations have been coded using the *acasual* [15], object-oriented, equation-based Modelica language and its implementation in the Dymola commercial software. The models of the system components are implemented in the in-house Modelica library for the Design and Simulation of Energy Conversion Systems (DeSimECS). All the components are treated as steady-state and zero-dimensional, and can be used without adaptations for both design and off-design simulations, due to the adoption of an *acasual* modeling paradigm. The only exception is the centrifugal compressor, whose performance at the design point and operating map is computed with the Python model documented in Ref. [16], [17], using a lumped parameters approach. The adoption of a different modeling paradigm and programming language for the centrifugal compressor is dictated by two reasons: i) the availability of an established and validated compressor model; ii) the reduced complexity of the system model implemented in Modelica and thus the increased robustness of the Dymola numerical solver.

The graphical representation of the modular models used to simulate ground operation of the ACM and VCC system are displayed in Fig. 5.1 and Fig. 5.2, respectively. The models used to evaluate the performance of the ECS during flight feature two main differences. First, they include a model of the air intake of the cabin air and ram air sides. Secondly, they do not feature the de-humidification loop, due to the negligible water content in the ambient air at high altitudes.

The working fluid selected for the VCC system is the standard refrigerant used for helicopter applications, i.e., the R134a. This refrigerant belongs to the class of hydrofluorocarbons (HFCs). It is characterized by null Ozone Depletion Potential (ODP) but fea-

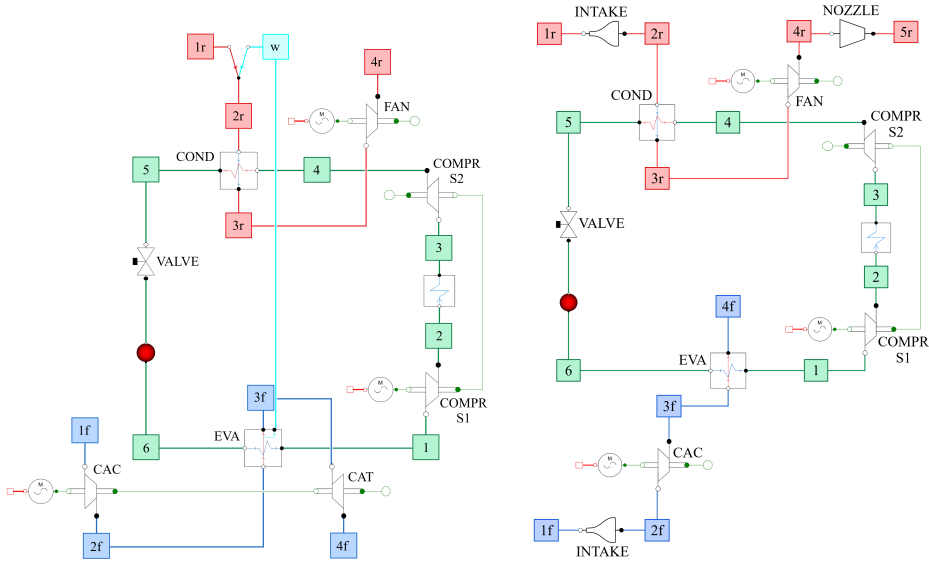


Figure 5.2: Graphical representation of the modular Modelica models of the electrically-driven vapor compression cycle system used to simulate ground (left) and flying (right) operation. The thermodynamic states of the ram air stream, cabin air stream, and refrigerant loop are highlighted in red, blue, and green. Image adapted from the graphical user interface of the DeSimECS library.

tures a GWP^1 equal to 1300. In view of the phase-out of HFCs by 2036 in developed countries [18], hydrofluoroolefins (HFOs) and hydrochlorofluoro-olefins (HCFOs) are targeted as the next-generation refrigerants also for this type of systems. Thanks to their chemistry, these compounds have a short atmospheric lifetime, hence GWP values lower than one [19]. However, the selection of the optimal working fluid will be addressed in a future study, if the VCC system shows superior performance with respect to the ACM technology.

5.2.2. MODEL OF AIR INTAKES

Air intakes are used to supply the cabin with cabin air and to provide ram air to the heat exchangers of the ECS packs. The inlet of air intakes can be of two types:

- scoop inlets, i.e., emergent air intakes characterized by high total pressure recovery over a broad range of Mach numbers, at the expense of high drag;
- flush inlets, i.e., submerged air intakes generating less drag and featuring lower total pressure recovery.

As reported in Ref. [20], the minimization of the drag penalty is a primary concern in the optimization of thermal management systems, therefore flush inlets are usually preferred when the amount of total pressure recovery is not a stringent constraint. The selected air

¹The authors refer to the index GWP_{100} , which estimates the environmental impact of a substance with respect to that of CO_2 over a time horizon of 100 years.

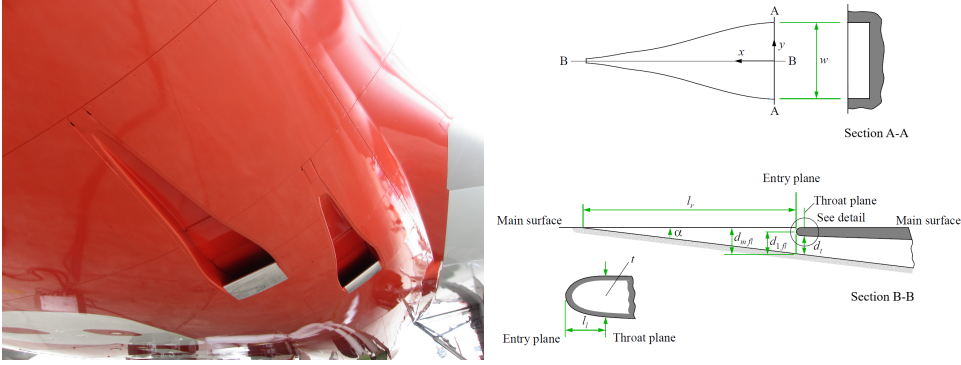


Figure 5.3: Schematic representation of the main geometrical characteristics of a submerged air intake featuring a rectangular entry and a NACA curved-divergent ramp. For exemplary purposes, the use of this type of air intake is shown on the lower fuselage section of a Boeing 747.

intake features a rectangular entry and a NACA curved-divergent ramp. The details of the prescribed geometry are displayed in Fig. 5.3.

The air intake is modeled according to the methodology documented in Ref. [21]. The main non-dimensional parameters characterizing the geometry of the flush inlet are selected to maximize the pressure recovery, as suggested in [20]. In particular, an aspect ratio $AR = w/d_t$ equal to 4 and a ramp angle α equal to 7° are set as optimal values. The first step in the design procedure is the evaluation of the boundary layer momentum thickness at the entry plane of the intake. This can be either measured in wind tunnel experiments, computed with high-fidelity CFD, or estimated with simple correlations. Following the methodology outlined in [20] for the preliminary sizing of flush intakes, the boundary layer thickness is estimated as

$$\delta = \frac{0.3747 \cdot l_r^{0.8}}{\left(\frac{\rho_\infty V_\infty}{\mu_\infty}\right)^{0.2}}, \quad (5.1)$$

and the momentum thickness is simply computed as $\theta = \delta/10$. Once the value of θ is known, the mass flow parameter \dot{m}_{bl} can be computed as a function of the design point mass flow rate

$$\dot{m}_{bl} = \frac{\dot{m}}{\rho_\infty V_\infty \theta^2}. \quad (5.2)$$

As reported in Ref. [21], the mass flow parameter \dot{m}_{bl} is correlated with the ratio between the momentum thickness and the height of the intake in the throat plane, thus $\dot{m}_{bl} = f(\theta/d_t)$. Once the value of d_t is known, the geometry of the flush inlet can be evaluated as

$$d_{m,fl} = d_t + t - l_t \tan(\alpha), \quad (5.3)$$

$$d_{1,fl} = d_t + 0.5t - l_t \tan(\alpha), \quad (5.4)$$

$$A_1 = d_{1,\text{fl}} w. \quad (5.5)$$

Next, the ideal mass flow rate that can be processed by the intake in free-stream conditions can be computed as

$$\dot{m}_\infty = \rho_\infty V_\infty A_1. \quad (5.6)$$

The corresponding drag penalty reads

$$D_{\text{fl}} = \dot{m}_\infty V_\infty \frac{C_{D,\text{fl}}}{2}, \quad (5.7)$$

where the drag coefficient is the sum of the ram drag term, the spillage drag coefficient, and a correction accounting for the increase of drag at values of mass flow rate close to the choking point of the intake

$$C_{D,\text{fl}} = 2k_{\text{fl}} \frac{\dot{m}}{\dot{m}_\infty} + k_\alpha k_m k_{\text{sp,fl}} C'_D + \Delta C_D. \quad (5.8)$$

The coefficients of Eqn. (5.8) are evaluated with the semi-empirical correlation reported in Ref. [21]. In particular, k_{fl} determines the ram drag component, and its value is determined by the geometry of the intake. Moreover, the coefficients k_α , k_m , and $k_{\text{sp,fl}}$ are used to correct the value of the spillage drag coefficient at zero mass flow C'_D , accounting for the actual values of the ramp angle, Mach number, and mass flow ratio \dot{m}/\dot{m}_∞ . Finally, the incremental drag term ΔC_D scales only as a function of the mass flow ratio.

The pressure recovery factor of the air intake is expressed as

$$C_{P,\text{fl}} = \frac{P_{t,1} - P_\infty}{P_{t,\infty} - P_\infty}. \quad (5.9)$$

In the same fashion as for the drag coefficient, the pressure recovery factor is evaluated as the sum of different coefficients evaluated with the semi-empirical correlations documented in Ref. [21]

$$C_{P,\text{fl}} = C_{P,m} + \Delta C_{P,\text{mf}} + \Delta C_{P,\alpha} + \Delta C_{P,w}. \quad (5.10)$$

In particular, $C_{P,m}$ corresponds to the maximum value of the pressure recovery factor that can be obtained with an intake geometry optimized for the design point mass flow rate. This value is then corrected by accounting for the actual values of the mass flow ratio, ramp angle, and aspect ratio through the coefficients $\Delta C_{P,\text{mf}}$, $\Delta C_{P,\alpha}$, and $\Delta C_{P,w}$.

The same methodology can be used to evaluate the performance of the flush intake both in design and off-design conditions. In design mode, the geometry of the intake is determined to achieve a certain target, e.g., maximum pressure recovery factor or minimum drag, at the design point mass flow rate. Conversely, in off-design mode, the geometry of the intake is assigned and the performance metrics of the intake are computed as a function of the prescribed operating point, i.e., mass flow ratio \dot{m}/\dot{m}_∞ . This procedure can be iterated by varying the operating point until reaching the value of mass flow rate leading to choking of the intake. This can be computed as

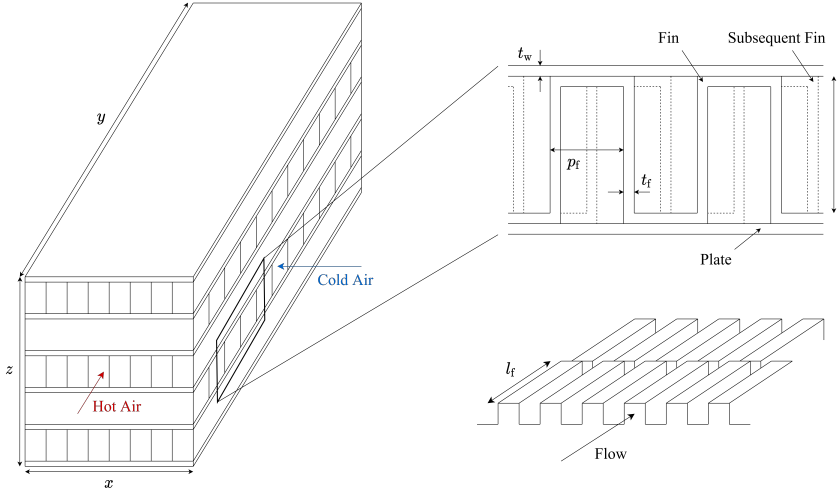


Figure 5.4: Schematic view of the internal and external geometry of a plate-fin heat exchanger, featuring offset strip fins.

$$\frac{\dot{m}_{\text{choke}}}{\dot{m}_{\infty}} = \frac{0.579}{M_{\infty}} (1 + 0.2M_{\infty}^2)^3 \left(C_{P,\text{fl}} + \frac{1 - C_{P,\text{fl}}}{(1 + 0.2M_{\infty}^2)^{7/2}} \right) \frac{d_t w}{A_1}, \quad (5.11)$$

where $C_{P,\text{fl}}$ is evaluated at the design point.

5.2.3. AIR-TO-AIR HEAT EXCHANGER MODEL

The topology selected for the primary and secondary heat exchangers of the bleedless three-wheel bootstrap ACM is that of plate-fin heat exchangers. In this device, the hot and cold streams flow according to an unmixed cross-flow arrangement. The flow passages are formed by corrugated fins, featuring triangular or rectangular cross sections, sandwiched between parallel plates. The fins are attached to the plates by brazing, soldering, welding, or adhesive bonding. The shape and density of the fins can be selected to meet the design specifications in terms of compactness and pressure drops. In the present work, offset strip fins are prescribed on the hot and cold sides, as displayed in Fig. 5.4. The heat transfer coefficient of this type of fins is 1.5 to 4 times higher than that of plain fin geometries, at the expense of a larger friction factor [22]. For this reason, offset strip fins are widely used in the aerospace sector, as well as in other industries that do not require mass production.

The geometry of offset strip fins is characterized by their length l_f , height b , pitch p_f , and thickness t_f . These geometrical parameters can be conveniently converted into non-dimensional numbers, to simplify the development of empirical correlations derived from experimental data, as documented in Ref. [23]. The resulting non-dimensional groups are the fin pitch to height ratio $\alpha = p_f/b$, fin thickness to length ratio $\delta = t_f/l_f$, and fin thickness to pitch ratio $\gamma = t_f/p_f$. As a result, the vector of parameters characterizing the design of plate-fin heat exchangers featuring offset strip fins can be expressed as

$$\mathbf{X}_{\text{hex}} = [x, y, z, \alpha_{\text{hot}}, \alpha_{\text{cold}}, \delta_{\text{hot}}, \delta_{\text{cold}}, \gamma_{\text{hot}}, \gamma_{\text{cold}}]. \quad (5.12)$$

The heat transfer coefficient and the pressure drop occurring in the core of the plate-fin heat exchanger are computed as a function of the Colburn factor j and the friction factor f , as follows

$$h = j \frac{c_p G}{Pr^{2/3}}, \quad (5.13)$$

$$\Delta P = f \frac{l_{\text{core}}}{D_{\text{hyd}}} \frac{\rho V^2}{2}. \quad (5.14)$$

In turn, j and f are estimated with the correlations documented in Ref. [24]. The heat transfer rate is computed with the $\epsilon - NTU$ method. The effectiveness can be interpreted as a thermal efficiency denoting the ratio between the actual heat transfer rate between the hot and cold fluid to the maximum possible heat transfer rate occurring in the ideal case. For an unmixed cross-flow heat exchanger, it is expressed as

$$\epsilon = 1 - \exp \left\{ \frac{NTU^{0.22}}{C_r} [\exp(-C_r NTU^{0.78}) - 1] \right\}. \quad (5.15)$$

The thermal capacity ratio $C_r = C_{\min}/C_{\max}$ is a dimensionless parameter defined as the ratio between the maximum and the minimum heat transfer capacity of the two media. The NTU is defined as the product of the overall heat transfer coefficient U and the total heat transfer surface A , divided by the minimum heat transfer capacity between the two working fluids.

$$NTU = \frac{UA}{C_{\min}} = \frac{1}{C_{\min}(R_{\text{hot}} + R_w + R_{\text{cold}})}, \quad (5.16)$$

where the thermal resistance of the plate is equal to

$$R_w = \frac{t_w}{k_w A_w}, \quad (5.17)$$

and that of the two media is expressed as

$$R = \frac{1}{\eta h A}. \quad (5.18)$$

Notably, η , h , and A assume different values on the hot and cold sides. The efficiency of the extended surface is computed as

$$\eta = 1 - \left\{ 1 - \frac{\tanh[m(b/2 - t_f)]}{m(b/2 - t_f)} \right\} \frac{A_f}{A_{\text{tot}}}, \quad (5.19)$$

where

$$m = \sqrt{2 \frac{h}{k_w t_f} \left(1 + \frac{t_f}{l_f} \right)}, \quad (5.20)$$

Table 5.1: Comparison between the predictions of the heat transfer and pressure drop correlations adopted in the plate-fin heat exchanger model, and a case study reported in Ref. [25].

Working fluid	Property	Deviation
Air: hot side	Heat transfer coefficient	±0.9%
Air: cold side	Heat transfer coefficient	±7.1%
Air: hot side	Pressure drop	±2.9%
Air: cold side	Pressure drop	±0.3%

and the ratio between the fin area and the total heat transfer surface is evaluated as reported in Ref. [22].

In addition to the friction through the heat exchanger core, the hot and cold streams experience pressure drops due to the sudden flow contraction and expansion occurring at the inlet and outlet of the flow passage. This effect is induced by the change in the free-flow area, as a result of the blockage introduced by the presence of the fins and plates. According to the methodology documented in Ref. [22], these pressure drops can be expressed as

$$\Delta P_{\text{in}} = \frac{(\dot{m}/A_{\text{ff}})^2}{2\rho_{\text{in}}} (1 - \sigma^2 + K_c) \quad (5.21)$$

$$\Delta P_{\text{out}} = \frac{(\dot{m}/A_{\text{ff}})^2}{2\rho_{\text{out}}} (1 - \sigma^2 - K_e),$$

where σ represents the ratio between the minimum free-flow area and the frontal area, while K_c and K_e are the contraction and expansion coefficients, which are computed as a function of σ and the Reynolds number. The correlations used for the calculation of the heat transfer coefficient and the pressure drops have been verified using a case study documented in Ref. [25]. The results are reported in Tab. 5.1.

In design mode, the conditions at the inlet and outlet of the heat exchanger are known, but the geometry is not completely specified. For example, the model can be used to compute the height of the heat exchanger, which is equivalent to determining the number of flow passages, in order to meet the prescribed heat duty. Conversely, in off-design mode, the geometry of the heat exchanger is given, and the model is used to compute the heat transfer at the corresponding operating conditions. Moreover, the models include a method to estimate the dry weight of the heat exchangers. Once the geometry has been fully determined, the volume of the material forming the core can be computed as the sum of the volume occupied by the fins V_f , and that of the plates V_p . With reference to Fig. 5.4, these two volumes can be expressed as

$$V_f = (b_{\text{hot}} - t_{f,\text{hot}} + p_{f,\text{hot}}) t_{f,\text{hot}} N_{f,\text{hot}} y + (b_{\text{cold}} - t_{f,\text{cold}} + p_{f,\text{cold}}) t_{f,\text{cold}} N_{f,\text{cold}} x, \quad (5.22)$$

$$V_p = t_w x y (N_p + 2) + b_{\text{hot}} y t_w (N_p + 1) + b_{\text{cold}} x t_w N_p.$$

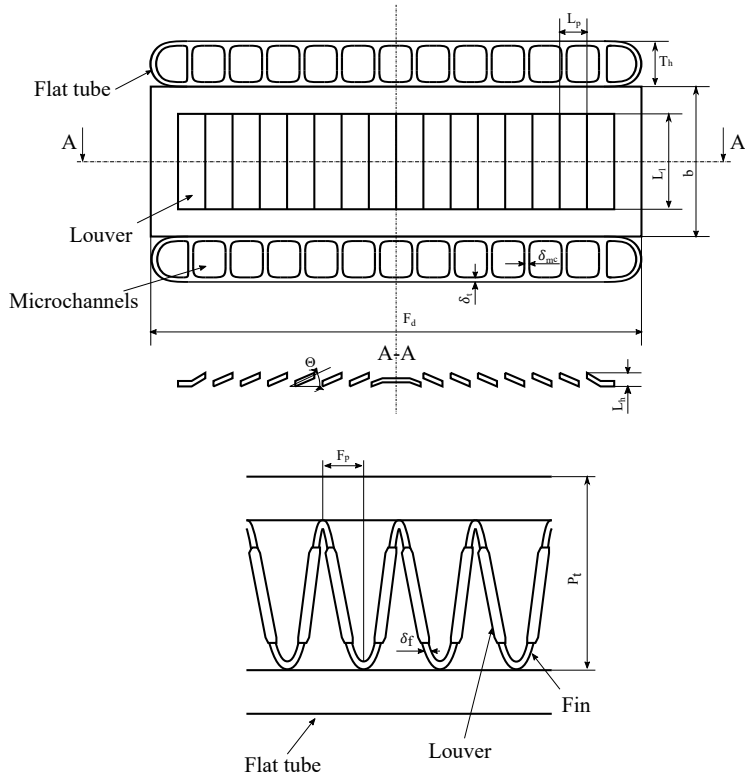


Figure 5.5: Schematic view of the internal geometry of a heat exchanger featuring multi-louvered fins and flat tubes with microchannels.

Then, based on the prescribed material, the weight of the heat exchanger is computed as the product of the material density and the total volume of the core. Finally, the result is multiplied by an empirical coefficient, to account for the presence of the casing, manifold, and soldering.

5.2.4. AIR-TO-REFRIGERANT HEAT EXCHANGER MODEL

The two compact heat exchangers featured in the VCC system, i.e., the condenser and the evaporator, share the same topology. This consists of a stack of alternate flat tubes with an internal microchannel structure and multi-louvered fins brazed on the external surface. The air and the refrigerant flow according to an unmixed cross-flow arrangement. In particular, the air flows through the passages created by the fins, where the boundary layer is continuously broken up, thus enhancing the heat transfer rate [26]. On the other side, the refrigerant undergoes a phase change along the microchannels, which are used to increase the heat transfer surface. This HEX geometry, displayed in Fig. 5.5, is typically employed for automotive applications, due to its high compactness factor (i.e., $\beta \approx 1100 \text{ m}^2/\text{m}^3$) and high thermal efficiency [27]. With reference to Fig. 5.5, the vector of parameters characterizing the geometry of this type of heat exchanger reads

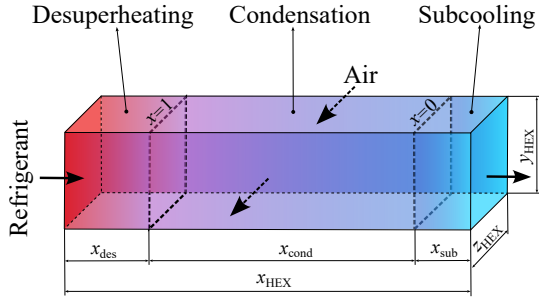


Figure 5.6: Schematic of the condenser channel model based on the moving boundary approach. The vapor quality of the working fluid x determines the subdivision among the different phases.

$$\mathbf{X}_{\text{hex}} = \left[x, y, z, b, F_p, F_d, l_f, l_t, L_h, L_l, L_p, N_{\text{mc}}, N_f, N_t, T_h, \delta_f, \delta_t, \delta_{\text{mc}}, \Theta \right]. \quad (5.23)$$

To correctly estimate the variation of fluid properties along the channel where phase change occurs, the model features a number of control volumes equal to the number of working fluid phases, i.e., liquid, saturated fluid and vapor. The condenser thus is divided into three sections: desuperheating (superheated vapor), condensing (liquid-vapor in thermodynamic equilibrium), and subcooling (subcooled liquid), as displayed in Fig. 5.6. This modeling approach, known as Moving Boundary (MB) method, has been selected in place of the finite volume method, since it provides a better trade-off between model complexity and accuracy, as demonstrated by Pangborn et al. [28]. The length of each control volume is computed as a function of the phase of the refrigerant and the corresponding enthalpy change. A linear distribution of the thermodynamic properties is assumed within each control volume. Hence, the flow properties at each station can be calculated by averaging the values at the boundaries of each control volume.

By adopting the MB method, it is possible to estimate the heat transfer coefficient and the pressure drop occurring in the HEX using the most appropriate correlations for each refrigerant phase. These equations are based on non-dimensional numbers, i.e., the Colburn factor j and the Nusselt number Nu for the heat transfer coefficient, and the friction factor f for the pressure drop. The Colburn factor j of the air passing through the multi-louvered fins is retrieved using the correlation by Chang et al. [29], and is computed with Eqn. (5.13). The heat transfer coefficient of the single-phase refrigerant flow is computed as a function of the Nusselt number, estimated with the correlation by Gnielinski [30], namely

$$h = Nu \frac{k}{D_{\text{hyd}}}. \quad (5.24)$$

In the case of a condensing and evaporating refrigerant flow, the heat transfer coefficient is determined according to Ref. [31] and [32], respectively. The heat transfer rate is estimated using the $\epsilon - NTU$ method, where the definition of the effectiveness ϵ depends on both the flow arrangement and the phase of the refrigerant [33]. The effectiveness is computed

with Eqn. (5.15). If evaporation or condensation occurs within the heat exchanger tubes, the heat capacity ratio C_r is null, and the effectiveness can be simply expressed as

$$\epsilon = 1 - e^{-NTU}. \quad (5.25)$$

The overall heat transfer coefficient UA used in the expression of the NTU accounts for both the effect of convection and of conduction, due to the presence of the fins and the tubes

$$\frac{1}{UA} = \frac{1}{h_{\text{air}}\eta A_{\text{air}}} + \frac{1}{h_{\text{refr}}A_{\text{refr}}} + R_t. \quad (5.26)$$

The effectiveness of the extended surface η is a function of the fin efficiency η_f [33] and is given by

$$\eta = 1 - \frac{A_f}{A_{\text{air}}} (1 - \eta_f) = 1 - \frac{A_f}{A_{\text{air}}} \left(1 - \frac{\tanh ml_f}{ml_f} \right), \quad (5.27)$$

where

$$m = \sqrt{\frac{2h_{\text{air}}}{k_f\delta_f} \left(1 + \frac{\delta_f}{F_d} \right)}, \quad (5.28)$$

$$l_f = \frac{H}{2} - \delta_f. \quad (5.29)$$

The thermal resistance of the microchannel walls, see [34], is estimated as

$$R_t = \frac{1}{2\pi k} \left(\frac{1}{l_t N_{\text{mc}} N_t} \right) \log \left(\frac{D_{\text{ext,mc}}}{D_{\text{ext,mc}} - 2\delta_{\text{mc}}} \right). \quad (5.30)$$

The pressure loss due to friction depends on both the fluid phase and the heat exchanger geometry. In this work, the friction coefficient f of the airflow is computed using the correlation proposed by Kim et al. [33]. On the refrigerant side, the model proposed by Schmidt et al. [35] has been selected as the most suitable for the case of two-phase flow. A well-established set of correlations for pressure drops in straight tubes has been implemented to characterize single-phase flows, depending on the Reynolds number. The complete list of references is reported in Ref. [36]. Finally, once the tube geometry and the fluid mass flow rate are fixed, the total pressure drop, neglecting inlet and outlet effects associated with flow contraction and expansion, can be calculated as

$$\Delta P = f \frac{l_t}{D_{\text{hyd}}} \frac{\rho V^2}{2}. \quad (5.31)$$

All the correlations used in the evaporator and condenser models have been verified using experimental data available in the literature, and the results of the comparison are reported in Tab. 5.2. Moreover, the condenser model has been validated against the experimental data published by Kim et al. [37]. The results show a 10% discrepancy in the estimation of the pressure drop and a deviation lower than 4% in the calculation of the heat transfer surface.

Table 5.2: Comparison between the predictions of the correlations adopted in the evaporator and condenser models, and the experimental data available in the literature.

Working fluid	Property	Experimental data	Deviation
Air	Heat transfer coefficient	[33]	±17%
Air	Pressure drop	[33]	±14%
Refrigerant: single phase	Nusselt number	[38]	±5%
Refrigerant: condensation	Heat transfer coefficient	[39]	±8%
Refrigerant: evaporation	Heat transfer coefficient	[40]	±10%
Refrigerant: two-phase flow	Pressure drop	[39], [40]	±10%

Similarly to the model of the air-to-air plate fin heat exchanger (Sec. 5.2.3), the models of the condenser and evaporator can be used for both design and off-design simulations. In design mode, the model computes the width of the air side cross section, which corresponds to the length of the microchannels. This is different from the model of the air-to-air heat exchanger, in which the height of the HEX is computed in design mode. This modeling choice is driven by the different physical mechanisms governing the heat transfer in the two devices. In the air-to-air heat exchanger, the same working fluid is used on both sides, and no phase change occurs. Therefore, any of the three dimensions characterizing the volume of the HEX can be selected as free variable in design mode. The height has been chosen as free variable in this work, as it determines the number of identical flow passages that are required to comply with the design point heat flow rate. In the case of the condenser and evaporator, however, one of the two working fluids undergoes phase change inside the microchannels. The result thereof is that the length of the microchannels is the most natural choice of free geometrical variable in design mode. For weight estimation purposes, the volume occupied by the fins V_f , and that of the microchannel tubes V_t can be expressed as

$$V_f = \delta_f \left[\left(b^2 + F_p^2 \right)^{1/2} - \delta_f \right] F_d N_f, \quad (5.32)$$

$$V_t = x \left[\frac{\pi}{2} \delta_t N_t (T_h + F_d - 2\delta_t) + \delta_{mc} (T_h - 2\delta_t) (N_{mc} - 1) \right].$$

The weight of the two-phase heat exchanger, similarly to the air-to-air heat exchanger, is computed as the product of the material density and the total volume of the core multiplied by an empirical coefficient, accounting for the additional weight of the casing, manifold, and soldering.

5.2.5. CENTRIFUGAL COMPRESSOR MODEL

The cabin air compressor (CAC) and the refrigerant compressor (RC) are the critical turbomachines of the two considered ECS configurations. The CAC is the main consumer of electric power of the ECS, whereas the design of the RC significantly affects the COP and defines the operating range of the VCC system. The methodology used to model single-stage and twin-stage centrifugal compressors is thoroughly described in Chapter 2 and

Chapter 2, respectively. For the sake of conciseness, only the main aspects of the models are treated in this section.

With reference to the nomenclature of Fig. 5.7, a centrifugal compressor stage can be sized as a function of eight design variables, namely, the swallowing capacity

$$\phi_{t1} = \frac{\dot{m}}{\rho_{t1} U_2 D_2^2}, \quad (5.33)$$

the isentropic work coefficient

$$\psi_{is} = \frac{\Delta h_{tt,is}}{U_2^2}, \quad (5.34)$$

the impeller shape factor

$$k = 1 - \left(\frac{R_{1,h}}{R_{1,s}} \right)^2, \quad (5.35)$$

the impeller outlet absolute flow angle α_2 , the number of blades N_{bl} , the diffuser radius ratio R_3/R_2 , and the non-dimensional parameters characterizing the shape of the diffuser

$$R_{r,pinch} = \frac{R_{pinch} - R_2}{R_3 - R_2}, \quad (5.36)$$

$$H_{r,pinch} = \frac{H_3 - H_2}{H_2(R_2/R_{pinch} - 1)}.$$

Moreover, the model requires the specification of the working fluid, the total-to-total pressure ratio β_{tt} , the mass flow rate \dot{m} , the total inlet conditions, and a list of geometrical parameters related to manufacturing constraints, e.g., the impeller tip clearance gap.

In a twin-stage centrifugal compressor, the two compressor wheels are mounted on the same shaft, thus the rotational speed of the second impeller is constrained to be the same as the one of the first stage. Therefore, once the design of the first impeller is fixed, the choice of the work coefficient of the second stage univocally determines also its flow coefficient, or viceversa. Moreover, the value of the intermediate pressure between the two stages is an additional design variable, if it is not constrained by the design of the VCC system. As documented in Chapter 3, this can be expressed as a function of the splitting factor κ_s

$$\begin{cases} \beta_{tt}|_{s1} = \kappa_s \sqrt{\beta_{tt}/\kappa_s} \\ \beta_{tt}|_{s2} = \sqrt{\beta_{tt}/\kappa_s} \end{cases} \quad (5.37)$$

In turn, the vector of parameters characterizing the design of a twin-stage centrifugal compressor reads

$$\begin{aligned} \mathbf{X}_c = & \left[\beta_{tt}, \dot{m}, \kappa_s, \phi_{t1}|_{s1-s2}, \psi_{is}|_{s1}, \alpha_2|_{s1-s2}, k|_{s1-s2}, N_{bl}|_{s1-s2}, \right. \\ & \left. R_3/R_2|_{s1-s2}, R_{r,pinch}|_{s1-s2}, H_{r,pinch}|_{s1-s2} \right]. \end{aligned} \quad (5.38)$$

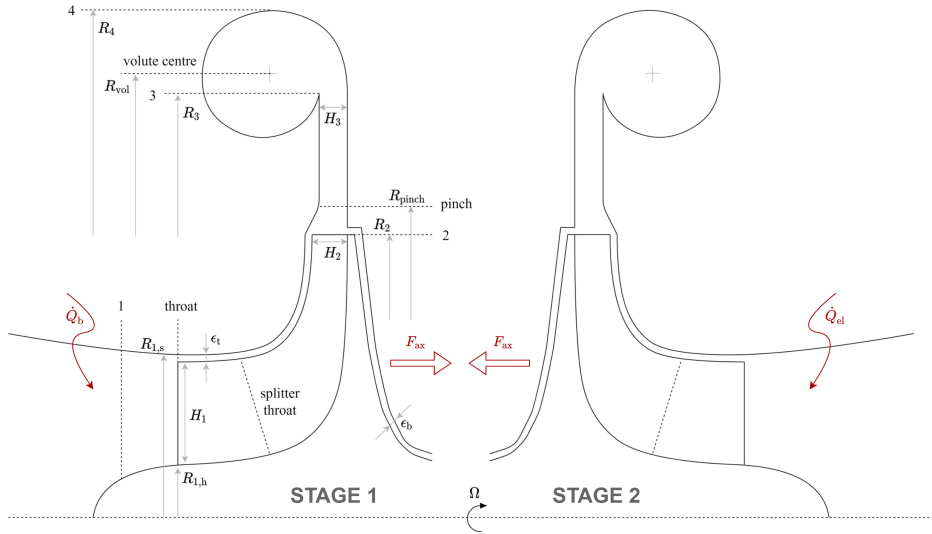


Figure 5.7: schematic meridional view of a twin-stage centrifugal compressor, featuring two stages mounted back-to-back on the same shaft.

The two impellers are mounted back-to-back, see Fig. 5.7, such that their axial thrust on the shaft can be balanced by gas bearings, which cannot sustain high axial loads. Furthermore, the cooling of the electric motor must be properly modeled, as it can significantly affect the performance of the machine. In the configuration adopted in this work, the flow at the outlet of the first stage is used to cool the motor, before entering the second stage. The resulting compressor assembly is very compact and does not rely on external cooling flows for thermal management. As a drawback, the refrigerant vapor is heated in between the two compressor stages, causing a fluid dynamic efficiency penalty in the order of five percentage points. Conversely, the cooling of the bearings is neglected to limit the complexity of the VCC system model.

The compressor design methodology is implemented in Python and is based on the lumped parameters modeling approach. However, it features a spanwise discretization of the flow quantities at the inducer section. The slip factor and the losses are predicted by means of the set of semi-empirical correlations reported in Ref. [17]. The thermo-physical fluid properties are evaluated by means of the reference thermodynamic library developed by NIST [41], which is also included in the open-source CoolProp library [42]. The flow in the vaneless diffuser is modeled by integrating the system of two-dimensional differential equations derived by Stanitz [43]. The axial thrust acting on gas bearings is computed following the approach devised by Tiainen2021 et al. [44]. The model can be used for both design and off-design simulations, as documented in Chapter 2. To assess the accuracy of the compressor model, the predictions of the in-house tool have been compared with the experimental data of three reference test cases available in literature [45]–[50], and with the CFD simulation results of the first compressor stage of the IRIS test rig, obtained during the first design iteration. The outcome of the validation study is that more

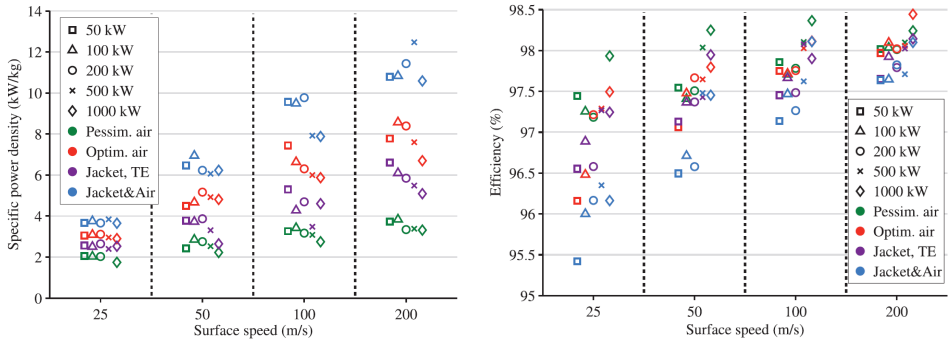


Figure 5.8: Model predictions of power density and efficiency of high-speed permanent magnet synchronous electric motors as a function of rotor surface speed, cooling scenario and power rating, see Ref. [51].

than 95% of the experimental and CFD data fall within the $\pm 5\%$ uncertainty bands of the values predicted by the model. Further details are reported in Chapter 2.

The compressor model is complemented with a method for preliminary weight estimation. The weight of the compressor assembly is computed by resorting to CadQuery [52], i.e., an open-source Python library for the creation of parametric CAD models. Once the dimensions of the main components are set, a simplified CAD model of the compressor assembly is automatically generated. Next, the weight of each component is computed according to the volume associated with the CAD model and the density of the prescribed material. Moreover, the weight of the electric motor is estimated based on the predicted values of power density for high-speed permanent magnet synchronous machines, according to the method documented in Ref. [51] and displayed in Fig. 5.8. The correlations implemented in the model of the electric motor are derived by assuming liquid jacket cooling and are valid for rotor surface speeds up to 200 m/s and electrical power ratings as high as 1 MW. The rotor outer radius, used to compute the surface speed, is set to match the maximum mechanical power required by the compressor, after accounting for the electrical efficiency and the windage losses. The electrical efficiency is estimated by means of the values reported in Fig. 5.8, while the windage loss is computed according to the method documented in Ref. [53].

5.2.6. INTEGRATED DESIGN OPTIMIZATION

The design optimization problem involves three counteracting objectives: the minimization of the electric power consumption, of the weight, and of the drag penalty associated with the two ECS packs. For the bleedless ACM architecture, the weight of each pack is calculated as the sum of the weight of the CAC and that of the primary and secondary HEXs. In the case of the VCC system, the weight of each pack accounts for the contributions of the CAC, RC, evaporator, condenser, and working fluid charge. The working fluid charge is computed considering the amount circulating in the system during steady-state operation plus an additional quantity used to ensure safe start-up of the VCC system. The material considered for the heat exchangers of the ACM and the VCC system is the Aluminium alloy 3003, whereas the CAC and the RC are assumed to be made with the Aluminium alloy

Table 5.3: Specifications of the ECS operating points selected for the multi-point design optimization.

Variable	Hot ground	Cruise	Faulty pack
T_{amb} [K]	311.15	216.65	216.65
P_{amb} [kPa]	102.4	76.266	76.247
Φ_{amb} [%]	22	0	0
\dot{m}_{pack} [kg/s]	0.5	0.5	0.88
T_{pack} [K]	256.95	276.55	273.69
P_{pack} [kPa]	101.325	19.679	19.679

2219-T852. These materials were indicated as optimal choices by the industrial partners of this project. The weight of the remaining components of the two systems is disregarded in this analysis.

The multi-objective design optimization targets three operating conditions of the ECS: standard cruise conditions, ground operation on a hot and humid day, and flying operation in case of a faulty pack. The ECS thermal load associated with the operating points defining the optimal design have been computed with the thermal model of the pressurized aircraft compartments described in Chapter 4 and are reported in Tab. 5.3. The main components of the system, namely, the heat exchangers and the centrifugal compressors, are sized at hot ground conditions. Then, their off-design performance is evaluated for cruise and faulty pack operation. Similarly, the air intakes are sized to accommodate the maximum mass flow rate, obtained in faulty pack conditions, and their off-design performance is evaluated in cruise conditions. The electric power consumption and the drag penalty associated with the two ECS packs have different values at each operating point. In turn, the objective functions used for the multi-objective optimization are computed as a weighted average of these quantities. In particular, the average electric power consumption is evaluated as

$$\overline{P_{\text{el}}} = 0.3P_{\text{el,hg}} + 0.6P_{\text{el,cr}} + 0.1P_{\text{el,fp}}, \quad (5.39)$$

and the average drag penalty is expressed as

$$\overline{D} = 0.8D_{\text{cr}} + 0.2D_{\text{fp}}. \quad (5.40)$$

The vector of objective functions reads

$$\mathbf{J} = \left[\overline{P_{\text{el}}}, W, \overline{D} \right]. \quad (5.41)$$

In Eqn. (5.39) and Eqn. (5.40) the electric power consumption and the drag penalty must be doubled at ground and cruise conditions, in order to account for the simultaneous operation of two ECS packs. Moreover, the choice of the weights assigned to each operating point is arbitrary and directly affects the result of the optimization. In this work, more relevance has been given to the performance metrics computed at cruise conditions, followed by those obtained during hot ground operation. Conversely, the power consumption and

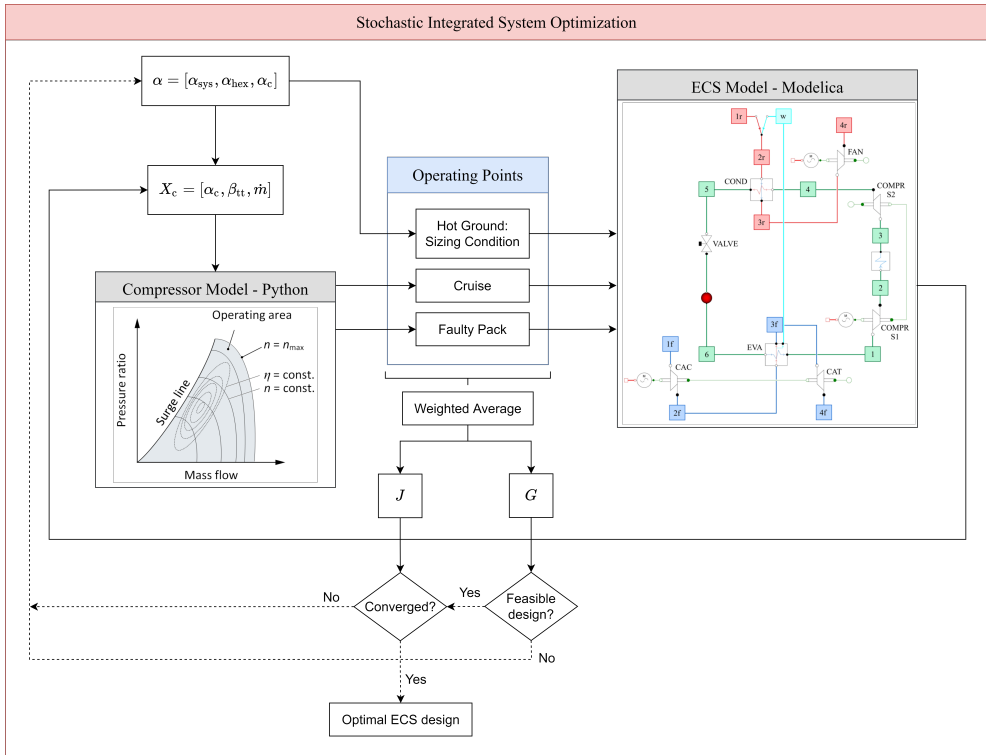


Figure 5.9: Flowchart of DesOptECS, coupling the ACM and VCC system models implemented in Modelica with the centrifugal compressor model implemented in Python.

the drag penalty computed for the faulty pack case have a limited influence on the objective functions, since the performance of the ECS should not be optimal in such conditions. Nevertheless, to ensure the required level of redundancy for certification purposes, each of the optimal solutions needs to meet the prescribed set point also in faulty pack conditions.

The flowchart of DesOptECS is displayed in Fig. 5.9. It consists of a Python program coupling the ECS models developed in Modelica, the compressor model implemented in Python, and an open-source toolbox for multi-objective design optimization [54]. With reference to the figure, the vector α includes both the variables related to the design of the system, heat exchangers, and compressors

$$\alpha = [\alpha_{\text{sys}}, \alpha_{\text{hex}}, \alpha_c]. \quad (5.42)$$

Some of the parameters characterizing the design of the compressors and heat exchangers can be set to fixed values to reduce the size of the optimization problem and therefore to expedite the calculation. As a result, α_{hex} and α_c may include less elements than X_{hex} and X_c , see Eqn. (5.12), Eqn. (5.23), and Eqn. (5.38). For example, when performing the optimization of the VCC system, only the y and z dimensions of the condenser and evaporator

have been included in the vector α_{hex} , whereas the parameters characterizing the design of the fins and microchannels have been set to constant values, since they have only a secondary influence on the values of the objective functions. The design variables and the corresponding upper and lower bounds prescribed for the optimization of the two ECS configurations are reported in Tab. 5.4 and Tab. 5.6. The total number of design variables pertaining to the ACM and VCC optimization is equal to 25 and 27, respectively.

Two sets of non-linear constraints have been prescribed for the design optimization of the two ECS configurations. In particular, the constraints are set to ensure the manufacturability of the system components, i.e., heat exchangers and compressors, and to define an upper threshold for the speed of the air and the refrigerant in the circuit, as well as for the corresponding pressure drops. Overall, the design optimization of the ACM and the VCC system features 17 and 41 non-linear constraints, as summarized in Tab. 5.4 and Tab. 5.6, respectively.

The optimization algorithm used in this study is the NSGA-II [55], i.e., a well-established evolutionary algorithm suited for multi-objective constrained optimization problems. A genetic algorithm has been preferred over a gradient-based approach because

- the gradients of the objectives and the constraints cannot be obtained analytically;
- the large number of design variables and non-linear constraints makes the numerical computation of the gradients prohibitively expensive;
- gradient-based algorithms are inherently limited if applied to the solution of multi-objective optimization problems.

The initial population comprises ten individuals for each design variable. The corresponding design space is sampled according to the latin hypercube methodology. The population is evolved until either the maximum number of generations is reached, or the relative improvement evaluated with respect to the precedent five generations is below a pre-defined threshold.

5.3. RESULTS

The three-dimensional Pareto fronts identified by the optimization algorithm for the two ECS configurations are displayed in Fig. 5.10. To facilitate the quantitative comparison between the performance metrics of the two systems, the same results are illustrated on the power-weight, power-drag, and weight-drag planes in Fig. 5.11. Moreover, the optimal design point leading to the minimum fuel weight penalty W_{f0} is highlighted with a red marker. In this work, the fuel weight penalty associated with the ECS is computed as the sum of three contributions [56]:

- penalty due to additional weight

$$W_{f0} = W \left[\exp \left(\frac{SFC_{\text{th}} \tau}{L/D} \right) - 1 \right]; \quad (5.43)$$

- penalty associated with shaft power off-take

$$W_{f0} = P_{\text{el}} SFC_{\text{p}} \frac{L/D}{SFC_{\text{th}}} \left[\exp \left(\frac{SFC_{\text{th}} \tau}{L/D} \right) - 1 \right]; \quad (5.44)$$

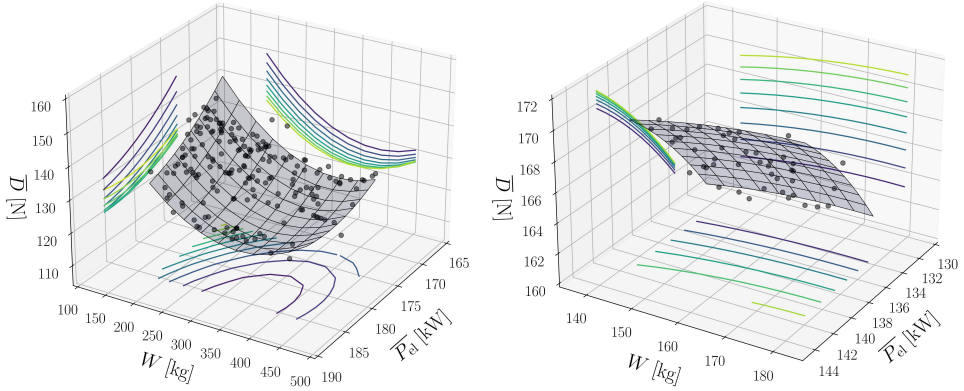


Figure 5.10: Three-dimensional Pareto front computed for the ECS based on the bleedless ACM architecture (left) and on the VCC system (right). The three objective functions displayed in the figure are the weight of the system, the average electric power consumption, and the average drag penalty evaluated at three operating points: hot ground, cruise, and faulty pack.

- penalty associated with additional drag

$$W_{f0} = D \frac{L/D}{g} \left[\exp\left(\frac{SFC_{th}\tau}{L/D}\right) - 1 \right]. \quad (5.45)$$

The values of the parameters in Eqn. (5.43) - Eqn. (5.45) depend on the aircraft type, the engine specifications, and the prescribed flight phase. In this work, the required set of aircraft parameters is representative of an Airbus A320 [1] and they are:

- thrust-specific fuel consumption: $SFC_{th} = 0.514 \text{ lb}/(\text{lb}\cdot\text{h})$;
- power-specific fuel consumption: $SFC_p = 0.5 \text{ lb}/(\text{hp}\cdot\text{h})$;
- lift-to-drag ratio: $L/D = 15.32$;
- mission time: $\tau = 1.5 \text{ h}$.

By comparing the Pareto fronts associated with the optimal designs of the bleedless ACM and the VCC system, it is possible to observe that the VCC system is characterized by lower weight and lower electric power consumption but features a higher drag penalty. However, if the design of the ACM characterized by lower weight is considered, the difference between the drag penalty computed for the two systems reduces only to $\bar{D} \approx 30 \text{ N}$. As a result, the fuel weight penalty associated with the optimal VCC system configuration is approximately 20% lower than the one of the optimal bleedless ACM. This is a conservative estimate since the ACM compressor and turbine, as well as the reheater and condenser, are not accounted for in the weight computation of the bleedless ACM.

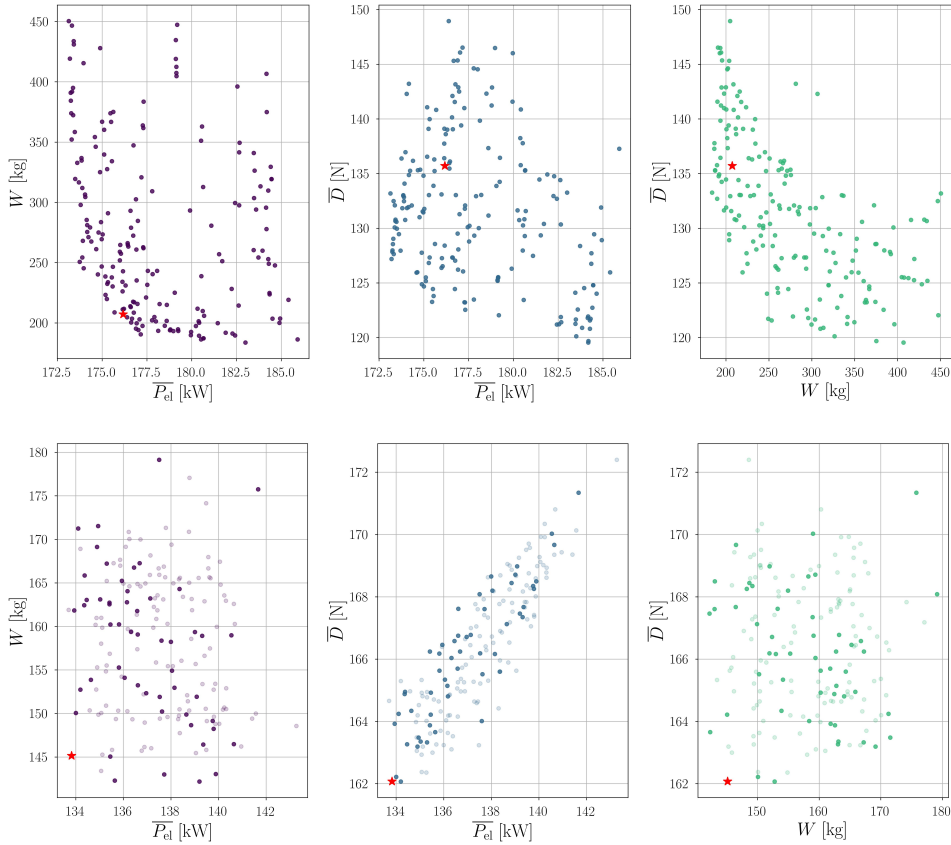


Figure 5.11: Weight, average electric power consumption, and average drag penalty computed for the ECS based on the bleedless ACM architecture (top) and on the VCC system (bottom). The red marker identifies the optimal design leading to the minimum fuel weight penalty. The shaded dots identify the optimal solutions that do not respect all the prescribed constraints.

To gain further insights, it is possible to analyze the influence of each objective function on the value of the fuel weight penalty, as displayed in Fig. 5.12. The fuel weight penalty of the bleedless ACM features a linear dependency with the weight and an inverse proportionality with the drag. These trends are mainly affected by the design of the primary and secondary heat exchangers. A more compact design of the heat exchangers leads to lower weight and higher pressure drops. The increase of the pressure drops leads to a higher drag penalty, but also to a higher power consumption of the CAC to meet the pressure set point at the pack discharge. However, as one can notice in Fig. 5.12, the design points associated with lower drag or lower electric power consumption feature a remarkable increase in the system weight. In turn, the higher weight offsets any potential reduction of fuel consumption due to lower drag and lower electric power consumption, leading to a sub-optimal design. As a result, the optimal design of the bleedless ACM cor-

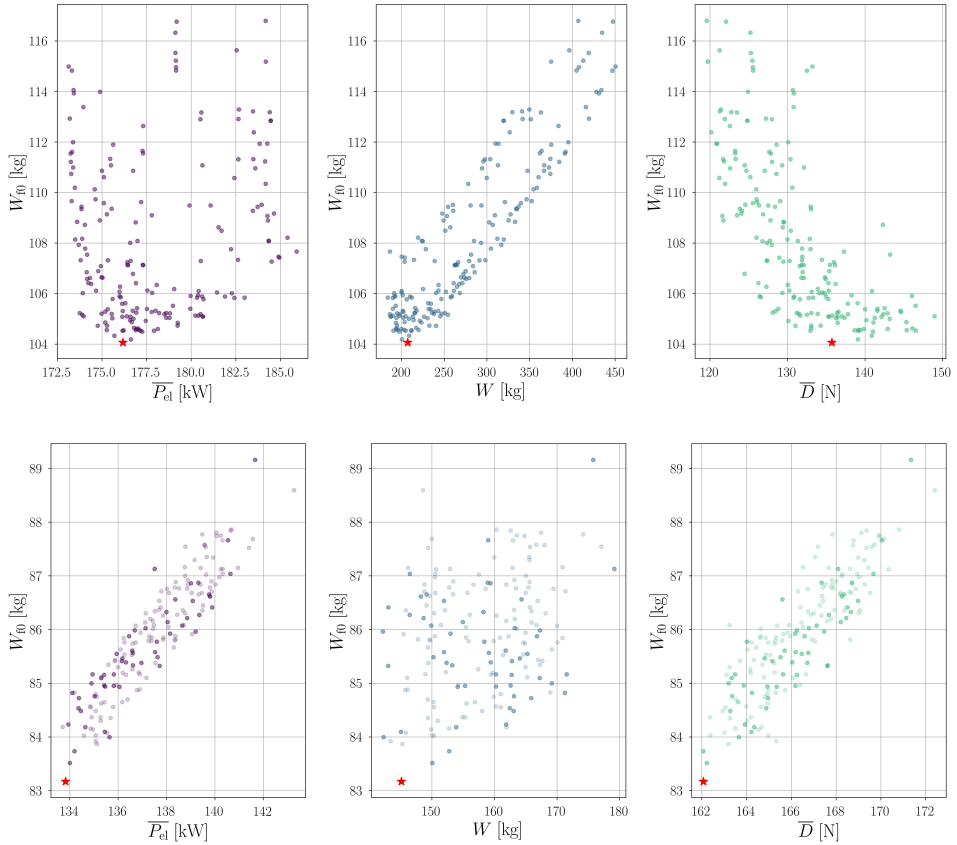


Figure 5.12: Variation of the fuel weight penalty as a function of the three objectives for the ECS based on the bleedless ACM architecture (top) and on the VCC system (bottom). The red marker identifies the optimal design leading to the minimum fuel weight penalty. The shaded dots identify the optimal solutions that do not respect all the prescribed constraints.

responds to the one characterized by the minimum weight.

The design of the evaporator and the condenser of the VCC system is affected by the same trade-off between compactness and pressure drops that characterizes the design of the air-to-air heat exchangers of the ACM. However, in the case of the VCC system, the combined weight of the two heat exchangers is comparable to the sum of the weights of the CAC and the RC. Therefore, the minimization of the weight and the drag penalty of the VCC system can be partially decoupled. The electric power consumption of the VCC system is affected by both the CAC and the RC. An increase in the pressure ratio of the refrigerant compressor leads to a rise of the temperature lift², and ultimately to a higher temperature difference in the condenser. On the one hand, this allows the use of a more

²Evaluated as the difference between the condensation and the evaporation temperature of the refrigerant in the vapor compression cycle.

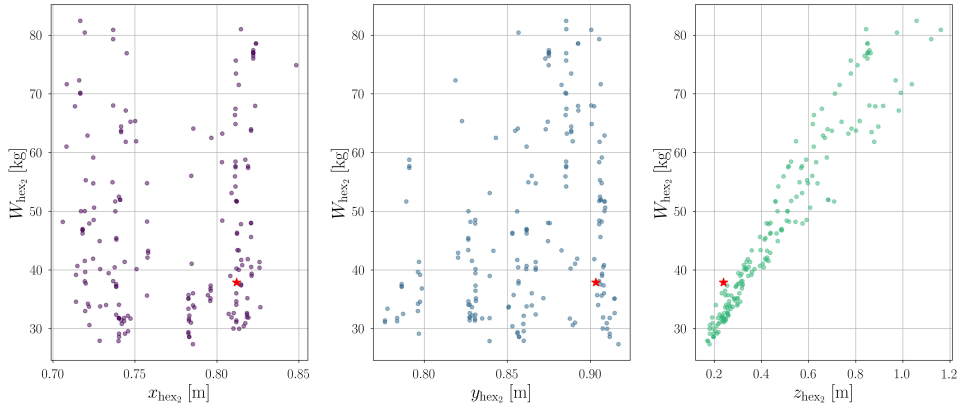


Figure 5.13: Variation of the weight of the secondary heat exchanger as a function of its main dimensions. The red marker identifies the optimal design leading to the minimum fuel weight penalty.

compact and lighter condenser, featuring a lower heat transfer surface. On the other hand, it leads to higher electric power consumption.

5.3.1. AIR CYCLE MACHINE

The ECS pack based on the ACM features four heat exchangers, namely, the primary and secondary HEXs, the reheater, and the condenser. The primary and secondary HEXs are responsible for providing cooling of the cabin air, whereas the reheater and the condenser are used in the dehumidification loop, and are bypassed during flight. The design of the primary and secondary HEXs mainly affects the trade-off between the weight and the drag penalty associated with the ACM. This analysis is focused on the secondary HEX, i.e., the one characterized by the highest heat load in the optimal ACM configuration. However, design parameters vary in the same way also for the primary heat exchanger, therefore the same qualitative result are applicable.

The influence of the main dimensions of the secondary heat exchanger on its weight is displayed in Fig. 5.13. The weight primarily scales with the height z_{hex2} of the HEX, which defines the number of flow passages. As a result, to minimize the weight, designs featuring large values of width and depth, i.e., $x_{hex2} \approx 0.8$ m, $y_{hex2} \approx 0.9$ m, are optimal as they lead to a lower height, i.e., $z_{hex2} \approx 0.2$ m. However, a lower height implies a smaller frontal area on the cabin air and the ram air sides, leading to higher pressure drop. To illustrate this issue, Fig. 5.14 shows the variation of the pressure drop with the frontal area of the secondary heat exchanger on the ram air side. Moreover, the chart displays the variation of the average drag evaluated at the three operating points as a function of the frontal area. As displayed in the figures, a reduction of the frontal area below the value associated with the design featuring the minimum fuel weight penalty produces an exponential increase of the drag penalty. The associated reduction of weight is not sufficient to compensate for the increase in drag, leading to a sub-optimal design.

The variables that mostly affect the design and the performance of the cabin air com-

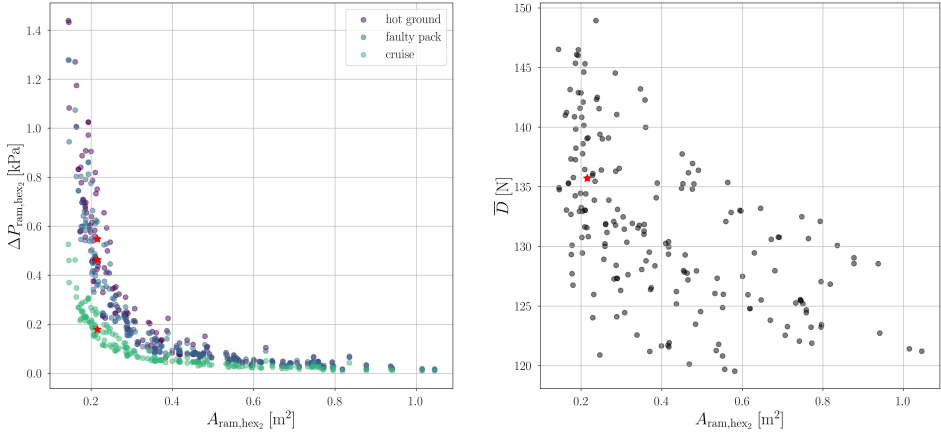


Figure 5.14: Variation of the pressure drop and the average drag penalty with respect to the frontal area of the secondary heat exchanger on the ram air side. The red marker identifies the optimal design leading to the minimum fuel weight penalty.

pressor are the swallowing capacity $\Phi_{t1,cac}$ and the isentropic work coefficient $\psi_{is,cac}$. Figure 5.15 shows the influence of these design variables on the weight of the CAC, the average rotational speed, and the average compressor efficiency evaluated over the three operating points. A higher value of swallowing capacity leads to higher values of rotational speed and efficiency. Moreover, compressor designs featuring higher rotational speed are more compact and lightweight, leading to an inverse proportionality between $\Phi_{t1,cac}$ and W_{cac} . This is in accordance with the design guidelines documented in Ref. [17]. In this study, the maximum value of $\Phi_{t1,cac}$ has been limited to 0.1 for the CAC since higher values lead to diminishing returns in terms of efficiency and negatively affect the compressor operating range.

The relations between the compressor performance metrics and work coefficient are more complicated and require further explanation. $\psi_{is,cac}$ measures the share of the work performed by the flow deflection within the impeller blade passage with respect to the contribution of the centrifugal potential $U_2^2/2$. A compressor featuring a higher value of $\psi_{is,cac}$ is characterized by higher blade loading and lower peripheral speed, thus lower rotational speed. However, as displayed in Fig. 5.15, the rotational speed is mostly affected by the value of the swallowing capacity. An increase in blade loading is usually associated with higher fluid-dynamic losses and lower compressor efficiency. Moreover, a higher blade loading implies a higher flow deflection, thus a higher impeller blade turning. This may lead to an unfeasible design of the impeller, characterized by forward-swept blades at the outlet. Conversely, the work coefficient cannot be arbitrarily reduced, since the impeller peripheral speed must be kept below a threshold, e.g., 600 m/s, to avoid structural issues, and the back-sweep at the impeller outlet cannot exceed 45–50° for manufacturing reasons.

The set of design variables and the values of the constraints characterizing the ACM layout leading to the minimum fuel weight penalty is reported in Tab. 5.4. Moreover, the

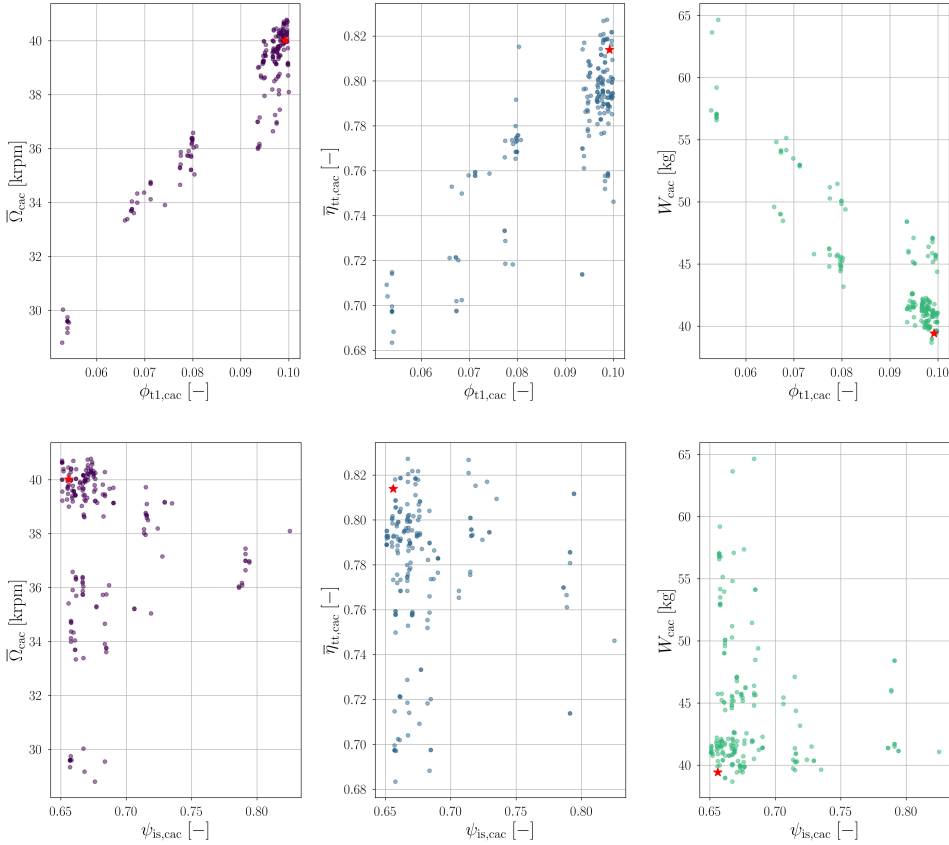


Figure 5.15: Influence of the swallowing capacity (top) and the isentropic work coefficient (bottom) on the main performance metrics of the cabin air compressor. The red marker identifies the optimal design leading to the minimum fuel weight penalty.

corresponding temperature-entropy diagrams for ground and cruise operations are displayed in Fig. 5.16. Inspection of the thermodynamic diagrams shows that, during ground operation, the total heat load is split between the primary and secondary heat exchangers, with the secondary heat exchanger featuring a slightly higher duty, i.e., $\dot{Q}_{hex_1} = 44.9$ kW and $\dot{Q}_{hex_2} = 52.6$ kW. As a result, the two heat exchangers are characterized by a similar design, but the secondary HEX features larger dimensions. Conversely, when the aircraft is at cruise conditions and the total heat load of the ECS pack is lower, the secondary HEX is responsible for most of the heat transfer, i.e., $\dot{Q}_{hex_1} = 6.1$ kW and $\dot{Q}_{hex_2} = 69.1$ kW. This is due to the small temperature difference between the fresh and ram air streams established in the primary HEX at cruise, see states 3-4 and 4r-5r in the right chart of Fig. 5.16. In such operating conditions, the primary HEX could be bypassed and the cabin air could be cooled only with the secondary HEX. As a result, the drag penalty associated with the pressure drops on the ram air side could be further reduced. However, this would require

Table 5.4: Design variables and non-linear constraints used for the integrated design optimization of the three-wheel bleedless air cycle machine. The set of optimal values corresponds to the ACM design leading to the minimum fuel weight penalty.

Design variable	Category	Range	Optimal value
$T_r _{hg}$ [-]	System - hot ground	0.45 - 0.65	0.49
$\dot{m}_{ram} _{hg}$ [kg/s]	System - hot ground	1.6 - 2.0	1.91
$\beta_{tt,cac} _{cr}$ [-]	System - cruise	3.5 - 4.5	3.54
$\beta_{tt,cac} _{fp}$ [-]	System - faulty pack	5.0 - 5.5	5.05
$\phi_{t1,cac}$ [-]	Compressor	0.05 - 0.1	0.099
$\psi_{is,cac}$ [-]	Compressor	0.65 - 0.85	0.66
$\alpha_{2,cac}$ [deg]	Compressor	60 - 70	66
$R_{3,cac}/R_{2,cac}$ [-]	Compressor	1.3 - 1.8	1.31
k_{cac} [-]	Compressor	0.75 - 0.95	0.86
$x_{hex_1-hex_2}$ [m]	Heat exchanger	0.6 - 1.1	0.6 - 0.81
$y_{hex_1-hex_2}$ [m]	Heat exchanger	0.6 - 1.1	0.65 - 0.9
α_{hot,hex_1-hex_2} [-]	Heat exchanger	0.1 - 1	0.447 - 0.293
δ_{hot,hex_1-hex_2} [-]	Heat exchanger	0.01 - 0.05	0.017 - 0.016
γ_{hot,hex_1-hex_2} [-]	Heat exchanger	0.01 - 0.15	0.047 - 0.068
$\alpha_{cold,hex_1-hex_2}$ [-]	Heat exchanger	0.1 - 1	0.211 - 0.428
$\delta_{cold,hex_1-hex_2}$ [-]	Heat exchanger	0.01 - 0.05	0.024 - 0.018
$\gamma_{cold,hex_1-hex_2}$ [-]	Heat exchanger	0.01 - 0.15	0.019 - 0.016
Constraint	Category	Threshold	Optimal value
$\max(P_{m,fan})$ [kW]	System	10	3.44
$\min(R_{1,h,cac})$ [mm]	Compressor	3.25	29.2
$\min(H_{2,cac})$ [mm]	Compressor	1.4	12.1
$\min(\beta_{2,bl,cac})$ [deg]	Compressor	-50	-49.7
$\max(\beta_{2,bl,cac})$ [deg]	Compressor	-10	-49.7
$\max(M_{3,cac})$ [-]	Compressor	0.7	0.61
$\min(\Omega_{cac})$ [krpm]	Compressor	30	36.63
$\max(\Omega_{cac})$ [krpm]	Compressor	250	42.54
$\max(U_{2,cac})$ [m/s]	Compressor	600	482.5
$\min(z_{hex_1-hex_2})$ [m]	Heat exchanger	0.05	0.34 - 0.24
$\max(z_{hex_1-hex_2})$ [m]	Heat exchanger	1.2	0.34 - 0.24
$\max(V_{hot,hex_1-hex_2})$ [m/s]	Heat exchanger	50	16.25
$\max(V_{cold,hex_1-hex_2})$ [m/s]	Heat exchanger	50	17.01

substantial modifications of the ram air duct and the implementation of an active control strategy.

5.3.2. VAPOR COMPRESSION CYCLE SYSTEM

The VCC system features two heat exchangers, i.e., the evaporator and the condenser. The design of the evaporator affects the trade-off between the weight of the VCC system and the electric power consumption of the CAC. Conversely, the trade-off between the weight and the drag penalty generated by the pressure drop on the ram air side depends on the design of the condenser.

The sensitivity of the weight of the evaporator with respect to its main dimensions is displayed in Fig. 5.17. The weight scales linearly with the width of the evaporator, which

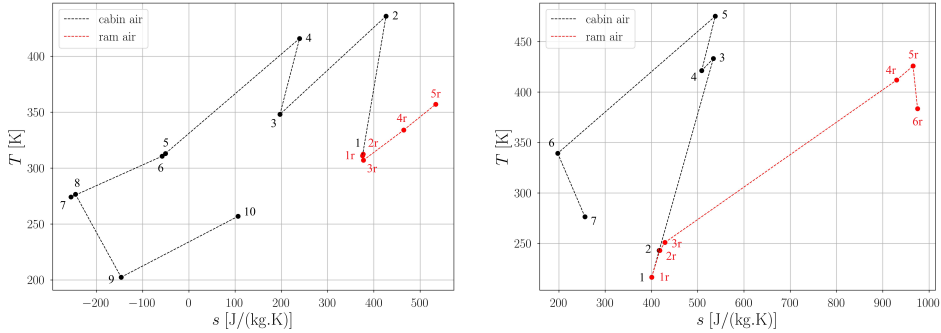


Figure 5.16: Temperature-entropy diagrams of the optimal ACM architecture, operating on the ground (left) and in cruise conditions (right). The thermodynamic states are numbered with reference to the system schematic displayed in Fig. 5.1.

defines the length of the microchannels. Most of the optimal designs populating the Pareto front feature approximately the same value of evaporator height ($y_{\text{eva}} \approx 0.5$ m), and depth ($z_{\text{eva}} \approx 0.1$ m). Moreover, the Pareto front is complemented by a group of optimal designs characterized by a higher value of the height ($y_{\text{eva}} \approx 0.7 - 0.8$ m). Within this cluster of design points, the linear proportionality between the evaporator weight and its width is characterized by a higher slope, as displayed in the left chart of Fig. 5.17. The lack of optimal solutions between the two groups featuring $y_{\text{eva}} \approx 0.5$ m and $y_{\text{eva}} \approx 0.7 - 0.8$ can be explained by investigating the dependence of y_{eva} on the evaporator characteristics. For this purpose, a test case has been set up. The set of variables characterizing the design of the VCC system has been prescribed according to the solution leading to the minimum fuel weight penalty. Moreover, the evaporator depth has been set to $z_{\text{eva}} = 0.1$ m, and the height has been linearly varied in the range $y_{\text{eva}} = 0.5 - 1$ m. The resulting values of the evaporator width and weight are shown in Fig. 5.18, together with the corresponding pressure drops computed for the air and the refrigerant sides. Given a fixed heat duty, the higher the evaporator height, the lower the corresponding width. However, in this case, the decrease of x_{eva} does not compensate for the increase of y_{eva} , leading to a higher evaporator weight and a higher frontal area on the air and the refrigerant sides. In turn, this yields a reduction of the pressure drops on both sides, which ultimately reduces the electric power consumption of the CAC and the RC. In light of these considerations, the existence of two groups of optimal y_{eva} values, as shown in Fig. 5.17, can be interpreted as follows. To minimize the weight of the VCC system, it is necessary to design a compact and lightweight evaporator, which can be achieved by selecting $y_{\text{eva}} \approx 0.5$ m. Conversely, if the primary objective is to minimize the electric power consumption, the designer should select a higher value of evaporator height, in order to minimize pressure drops. Intermediate values of the evaporator height lead to feasible, but sub-optimal solutions.

The dependence of the condenser frontal area on the ram-air-side pressure drop is reported on the left chart of Fig. 5.19. Moreover, the variation of the pressure drops on the refrigerant side as a function of the condenser width is displayed on the right chart of Fig. 5.19. As expected, the air-side pressure drop is inversely proportional to the frontal

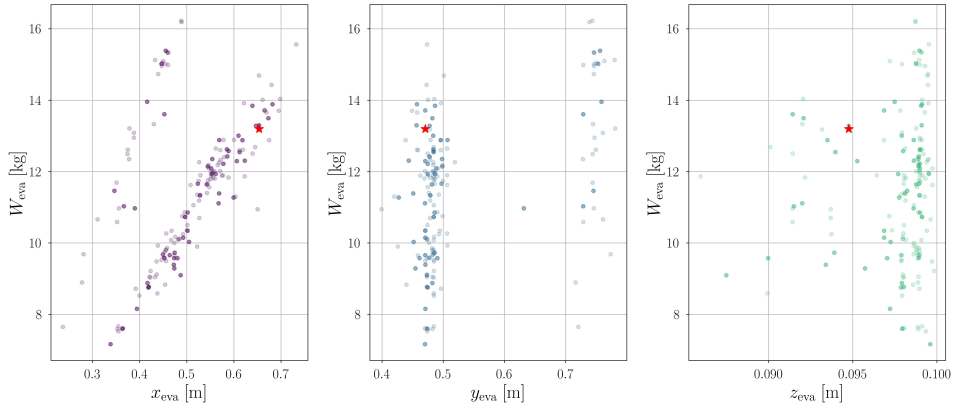


Figure 5.17: Variation of the weight of the evaporator as a function of its main dimensions. The red marker identifies the optimal design leading to the minimum fuel weight penalty. The shaded dots identify the optimal solutions that do not comply with all the specified constraints.

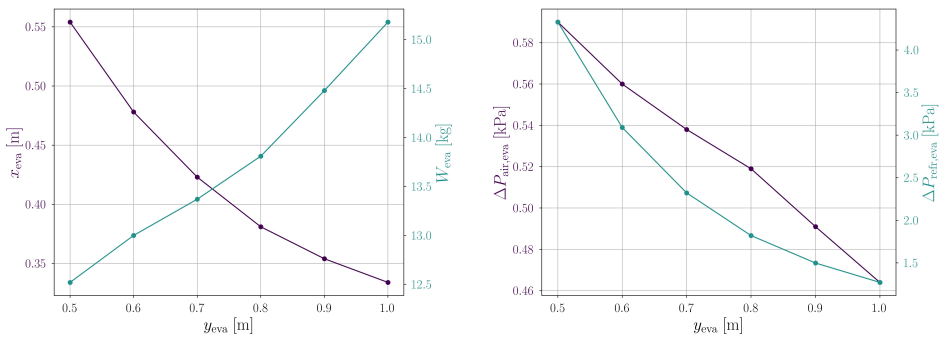


Figure 5.18: Influence of the evaporator height on the weight (left) and the pressure drops (right) on the cabin air and the refrigerant sides.

area, while the refrigerant-side pressure drop is linearly dependent on the length of the microchannels, i.e., the condenser width. Red markers put into evidence how optimal designs are obtained by minimizing ram-air-side pressure drops, thus by maximizing the frontal area, at the expense of higher pressure drops along the refrigerant side. This is in accordance with the results reported in the lower chart of Fig. 5.12, which shows that the optimal VCC design corresponds to the design associated with the lowest drag penalty.

In the VCC system, the only function of the CAC is to provide the required pressurization of the cabin air. Thus, the CAC is characterized by a lower pressure ratio than in the case of the ACM. This allows the selection of a higher value of swallowing capacity, in accordance with the design guidelines reported in Chapter 2. The resulting design therefore features low rotational speed, low weight of the electric motor, and, on average, higher efficiency than, for example, the air compressor of the bleedless ACM.

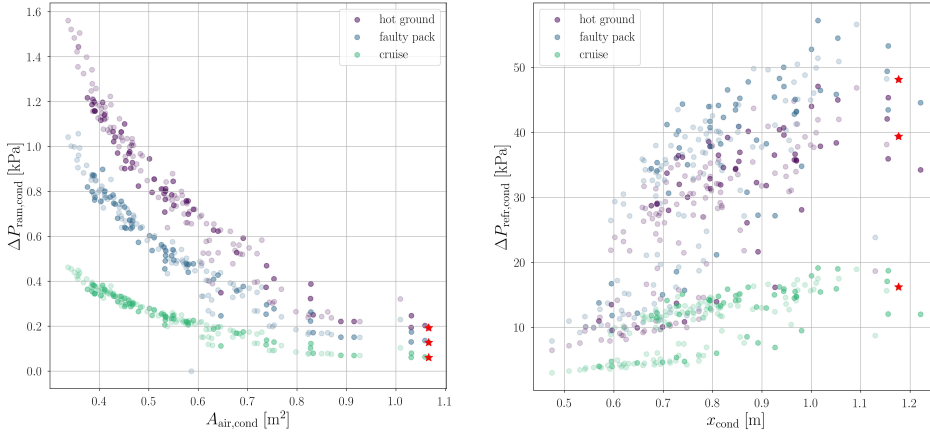


Figure 5.19: Condenser design: air-side and refrigerant-side pressure drop as a function of frontal area and width. The red marker identifies the optimal design leading to the minimum fuel weight penalty. The shaded dots identify optimal solutions violating some of the specified constraints.

Differently from the CAC, the optimal design of the refrigerant compressor strongly depends on the operating envelope dictated by the design of the VCC system. Consequently, the analysis of the Pareto front does not allow to isolate the influence of α_{sys} and α_c on the performance of the refrigerant compressor. However, insights on the mutual influence of design aspects can be gained by means of a case study, i.e., the design of the compressor of the VCC system configuration characterized by the minimum fuel weight penalty. The set of design variables and the data related to the design point and the operating conditions of the refrigerant twin-stage compressor are reported in Tab. 5.5. The operating map computed for the nominal inlet conditions is displayed in Fig. 5.20 in terms of total-to-total pressure ratio and efficiency. The first stage is characterized by a value of swallowing capacity that is more than double that of the second stage, whereas the two stages feature similar values of the isentropic work coefficient. Moreover, the pressure ratio of the first stage at design point is higher, leading to a value of the splitting factor κ_s larger than one. These results comply with the design guidelines for twin-stage compressors reported in Chapter 3. Furthermore, the operating map shows that some compressor designs are characterized by a pressure ratio that is as high as 13 with a value of the efficiency above 70%. The superior performance of high-speed radial compressors as compared to conventional volumetric compressors, combined with the wide operating range and extreme compactness, are deemed key enablers of the adoption of VCC technology in aerospace applications.

To evaluate the compressor performance at variable inlet conditions, the operating maps of the two stages are scaled in terms of corrected mass flow rate and rotational speed, according to

$$\dot{m}_r = \dot{m} \cdot T_{t,1}^{1/2} \cdot P_{t,1}^{-1} \cdot M_U^{-9.58} \quad (5.46)$$

Table 5.5: Design variables, design point, and operating conditions of the two stages of the refrigerant compressor corresponding to the optimal VCC system configuration, leading to the minimum fuel weight penalty.

Design Variable	Stage 1	Stage 2	
ϕ_{t1} [-]	0.158	0.065	
ψ_{is} [-]	0.813	0.728	
α_2 [deg]	67.58	67.69	
k [-]	0.95	0.85	
N_{bl} [-]	14	18	
R_3/R_2 [-]	1.5	1.5	
$R_{r,pinch}$ [-]	0.9	0.9	
$H_{r,pinch}$ [-]	0.9	0.9	
Design Point	Stage 1	Stage 2	
\dot{m} [kg/s]	0.55	0.55	
T_{t1} [K]	273.8	312.8	
P_{t1} [kPa]	248.83	694.16	
β_{tt} [-]	2.8	2.6	
Operating Point	Hot ground	Cruise	Faulty pack
\dot{m} [kg/s]	0.443	0.317	0.516
$\dot{m}_{r,s1}$ [-]	$7.04 \cdot 10^{-7}$	$7.03 \cdot 10^{-7}$	$9.43 \cdot 10^{-7}$
$\dot{m}_{r,s2}$ [-]	$5.28 \cdot 10^{-7}$	$4.94 \cdot 10^{-7}$	$7.35 \cdot 10^{-7}$
$T_{t1,s1}$ [K]	273.5	282.5	274
$T_{t1,s2}$ [K]	323.3	331.2	319.5
$P_{t1,s1}$ [kPa]	214.6	287.2	219.7
$P_{t1,s2}$ [kPa]	701.8	889.6	662.6
Ω [krpm]	110	110.6	105.9
$\beta_{tt,s1}$ [-]	3.22	3.01	3.07
$\beta_{tt,s2}$ [-]	2.74	2.92	2.51

$$N_r = \Omega \cdot T_{t,1}^{-1/2}, \quad (5.47)$$

where $M_U = U_2/a_{t,1}$ is the peripheral Mach number at the impeller outlet. The exponent of M_U has been computed based on a database of compressors operating with refrigerant R134a at variable inlet conditions created with the model described in Chapter 2. The corrected operating maps of the two stages are shown in Fig. 5.21, together with the operating conditions corresponding to hot ground, cruise, and faulty pack operation of the VCC system. The following considerations can be drawn from the analysis of the two charts. The three operating points are characterized by a smaller range of variability of \dot{m}_r if compared to \dot{m} , leading to a less stringent requirement on the operating range of the compressor. Moreover, the three operating points are located on the speed-lines characterized by higher Ω and lower \dot{m}_r . In particular, the operating points corresponding to cruise and faulty pack operations are in the proximity of the choking point of the first and second stage, respectively. As a result, the efficiency of the compressor stage decreases with respect to the design point efficiency. The design point mass flow rate should be further increased to mitigate this effect. In general, the data related to the design point of

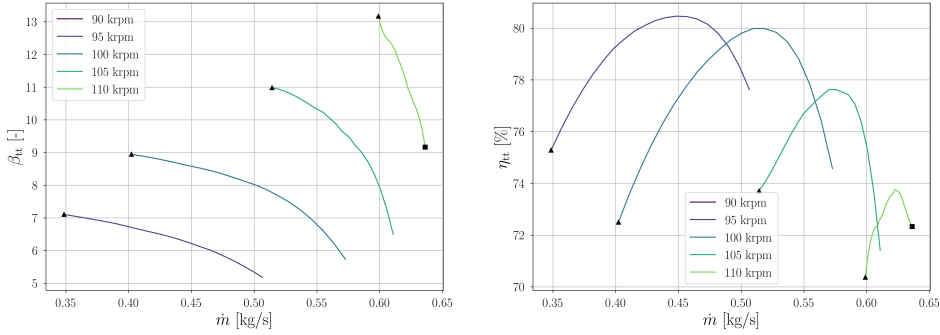


Figure 5.20: Operating map of the twin-stage refrigerant compressor computed at the nominal inlet conditions, i.e., $P_{t1,s1} = 248.83$ kPa, $T_{t1,s1} = 273.8$ K, and corresponding to the optimal VCC design leading to the minimum fuel weight penalty.

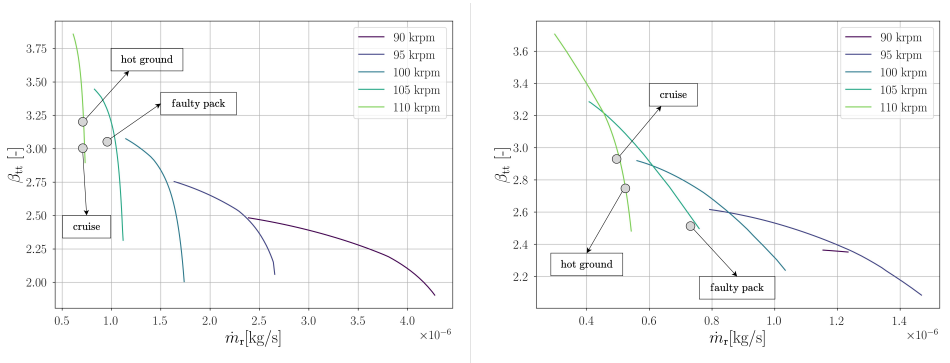


Figure 5.21: Reduced operating map of the first (left) and second (right) stage of the refrigerant compressor corresponding to the optimal VCC design leading to the minimum fuel weight penalty.

the two stages should be included in the set of compressor optimization variables α_c , to maximize the performance of the VCC system.

The set of design variables and the values of the constraints characterizing the optimal VCC system configuration is reported in Tab. 5.6. The associated temperature-entropy diagrams evaluated at ground and cruise conditions are displayed in Fig. 5.22. The heat load of the condenser and the evaporator is approximately 45% higher on ground than in cruise conditions and this is primarily due to a 33% increase in the mass flow rate of refrigerant in ground conditions. This effect, combined with the large variation of the environmental conditions between the two operating points, leads to a sizeable increase in the ram air mass flow rate, i.e., from $\dot{m}_{ram}|_{cr} = 0.46$ kg/s to $\dot{m}_{ram}|_{hg} = 2.86$ kg/s. As a result, the minimization of the condenser air side pressure drop is of paramount importance not only to reduce the drag penalty but also the power consumption of the ram air fan during ground operation. Conversely, the variation of the evaporation and condensation temperatures between the two operating points is limited to 7.8° C and 12.9° C, respectively. As

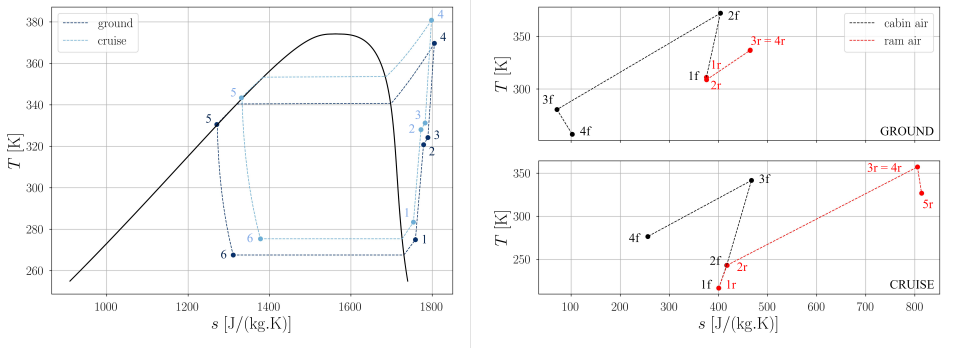


Figure 5.22: Temperature-entropy diagrams of R134a indicating the refrigeration cycle (left) and of air indicating the relevant processes occurring in the cabin and in the ram duct (right). The thermodynamic states of the fluids are those calculated for the optimal VCC system if operating on the ground and in cruise conditions. The thermodynamic states are numbered with reference to process flow diagram of Fig. 5.2.

a consequence, the change in the temperature lift and the pressure ratio provided by the refrigerant compressor is only minor. This is due to the presence of the cabin air turbine downstream of the evaporator, which enables cooling of the cabin air below 0° T during ground operation, without significantly altering the evaporation temperature.

5.4. CONCLUSIONS

A novel integrated design method for aircraft ECS, named DesOptECS, has been developed and is presented in this chapter. The methodology encompasses a multi-point and multi-objective optimization strategy that simultaneously accounts for the preliminary design of the system, thus its thermodynamic cycle, and its main components. The models of the ECS components have been implemented in the in-house Modelica library DeSimECS, which supports the acausal modeling paradigm. The only exception is the centrifugal compressor, whose design and operating map are computed with the Python model documented in Chapter 2 and Chapter 3. The integrated design framework has been used to optimize and compare the simulated performance of two different ECS configurations: a bleedless three-wheel bootstrap ACM, and an electrically-driven VCC system. The vehicle providing the main system specifications is a single-aisle, short-haul aircraft, e.g., the Airbus A320, and the prescribed operating points are hot ground, cruise, and high-altitude flight in the presence of a faulty ECS pack.

The main outcomes of this study can be summarized as follows.

1. The ECS configuration based on the electrically-driven VCC system, featuring compact heat exchangers and high-speed centrifugal compressors, can be both lighter and more energy-efficient than the state-of-the-art bleedless ACM architecture. However, if compared to the most compact ACM designs, the air intake of the VCC system causes a higher average drag penalty evaluated over the three operating points. Overall, the fuel weight penalty computed for the optimal VCC system is approximately 20% lower than the one evaluated for the optimal bleedless ACM.

Table 5.6: Design variables and non-linear constraints used for the integrated design optimization of the electrically-driven vapor compression cycle system. The set of optimal values corresponds to the VCC design leading to the minimum fuel weight penalty.

Design variable	Category	Range	Optimal value
$\Delta T_{sh} _{hg}$ [K]	System - hot ground	3 - 10	8.6
$\Delta T_{sc} _{hg}$ [K]	System - hot ground	3 - 10	9.8
$\Delta T_{sh} _{cr}$ [K]	System - cruise	3 - 10	8.5
$\Delta T_{sc} _{cr}$ [K]	System - cruise	3 - 10	9.6
$\Delta T_{sh} _{fp}$ [K]	System - faulty pack	3 - 10	9.9
$\Delta T_{sc} _{fp}$ [K]	System - faulty pack	3 - 10	9.2
$\dot{m}_{ram} _{hg}$ [kg/s]	System - hot ground	2.8 - 3.5	3.06
$T_{eva} _{hg}$ [K]	System - hot ground	253.15 - 268.15	267.8
$\beta_{tt,cac} _{hg}$ [-]	System - hot ground	1.5 - 2	1.72
$\beta_{tt,s1} _{hg}$ [-]	System - hot ground	2.9 - 3.3	3.22
$\beta_{tt,s2} _{hg}$ [-]	System - hot ground	2.7 - 3.1	2.85
$\beta_{tt,s1} _{cr}$ [-]	System - cruise	2.7 - 3.1	3.02
$\beta_{tt,s2} _{cr}$ [-]	System - cruise	2.5 - 2.9	2.82
$\beta_{tt,s1} _{fp}$ [-]	System - faulty pack	2.7 - 3.1	3.07
$\beta_{tt,s2} _{fp}$ [-]	System - faulty pack	2.5 - 2.9	2.73
$\phi_{t1,cac}$ [-]	Compressor	0.08 - 0.15	0.149
$\psi_{is,cac}$ [-]	Compressor	0.75 - 0.9	0.79
$\phi_{t1,s1}$ [-]	Compressor	0.1 - 0.18	0.157
$\psi_{is,s1}$ [-]	Compressor	0.65 - 0.85	0.81
$\phi_{t1,s2}$ [-]	Compressor	0.04 - 0.1	0.065
$\alpha_{2,cac-s1-s2}$ [deg]	Compressor	60 - 70	69.6 - 67.6 - 67.7
y_{eva} [m]	Heat exchanger	0.3 - 1	0.47
y_{cond} [m]	Heat exchanger	0.5 - 1.2	0.9
$z_{eva-cond}$ [m]	Heat exchanger	0.03 - 0.4	0.095 - 0.027
Constraint	Category	Threshold	Optimal value
$\max(P_{m,fan})$ [kW]	System	10	0.82
$\min(R_{1,h,cac-s1-s2})$ [mm]	Compressor	3.25	26.56 - 3.33 - 4.07
$\min(H_{2,cac-s1})$ [mm]	Compressor	1.4	25.14 - 3.53
$\min(H_{2,s2})$ [mm]	Compressor	1.2	1.48
$\min(\beta_{2,bl,cac-s1-s2})$ [deg]	Compressor	10	35 - 45.9 - 40.32
$\max(\beta_{2,bl,cac-s1-s2})$ [deg]	Compressor	50	35 - 45.9 - 40.32
$\max(M_{3,cac-s1-s2})$ [-]	Compressor	0.7	0.42 - 0.6 - 0.64
$\min(\Omega_{cac})$ [krpm]	Compressor	10	20.67
$\min(\Omega_{s1-s2})$ [krpm]	Compressor	30	105.62
$\max(\Omega_{cac-s1-s2})$ [krpm]	Compressor	250	27.81 - 112.02
$\max(U_{2,cac-s1-s2})$ [m/s]	Compressor	600	304.93 - 216.51 - 205.27
$\max(\Delta F_{ax,s1-s2})$ [N]	Compressor	400	367.9
$\min(x_{eva-cond})$ [m]	Heat exchanger	0.05	0.65 - 1.18
$\max(x_{eva-cond})$ [m]	Heat exchanger	1.25	0.65 - 1.18
$\min(\Delta T_{pp,eva-cond})$ [K]	Heat exchanger	0.5	1.18 - 0.8
$\max(V_{air,eva-cond})$ [m/s]	Heat exchanger	40	3.63 - 2.44
$\max(V_{refr,eva-cond})$ [m/s]	Heat exchanger	40	10.65 - 5.03
$\max(\Delta P_{air,eva-cond})$ [kPa]	Heat exchanger	1.5	0.92 - 0.19
$\max(\Delta P_{refr,eva-cond})$ [kPa]	Heat exchanger	50	11.54 - 48.14

2. The VCC system design leading to the minimum fuel weight penalty corresponds to the design point associated with the minimum average electric power consumption and drag penalty. Conversely, the minimization of the fuel weight penalty related to the bleedless ACM is primarily driven by the minimization of the system weight.
3. The design of the primary and secondary heat exchangers of the ACM is dictated by the trade-off between weight and pressure drop, which directly affects the drag penalty. For both the heat exchangers, the design leading to the minimum fuel weight penalty is characterized by similar width and depth, and a lower height. At the sizing condition, i.e., hot ground operation, the heat load is split between the two HEXs, with the secondary HEX featuring a slightly higher duty, thus larger dimensions. At cruise conditions, the whole thermal heat load can be theoretically processed by the secondary HEX, while the primary HEX can be bypassed to reduce the drag penalty generated by the pressure drop on the ram air side.
4. The design of the evaporator affects the trade-off between the weight of the VCC system and the electric power consumption of the cabin air compressor and the refrigerant compressor. Conversely, the design of the condenser determines the trade-off between the weight and the drag penalty. For both heat exchangers, the minimization of the pressure drop on the air side is more beneficial than the reduction of the refrigerant-side pressure drop. As a result, the optimal design features a large frontal area on the air side, long microchannels, and a short airflow path.
5. The optimal design of the twin-stage refrigerant compressor of the VCC system is in line with the design guidelines reported in Chapter 3. In particular, the first stage is characterized by a value of swallowing capacity that is more than double of that of the second stage, whereas the isentropic work coefficient has similar values for the two stages. Moreover, the first stage is always characterized by a higher pressure ratio than the second stage. For the prescribed ECS operating points, the mass flow rate of refrigerant is approximately 60% higher during faulty pack operation than at cruise conditions, whereas the variation of the compression ratio of the two stages is minor. However, by computing the corrected mass flow rate for the three operating points, it is possible to show that the difference between the values of \dot{m}_r associated with the two stages is significantly lower than that of \dot{m} , leading to a less stringent requirement on the operating range of the machine.

The results of this research reveal the importance of adopting an integrated design approach when pursuing the optimization of complex energy conversion systems, such as the ECS of passenger aircraft. Moreover, the results of this work, albeit only numerical, prove the potential of an electrically-driven VCC system, featuring compact heat exchangers and high-speed centrifugal compressors. Therefore, this technology is envisaged to replace partly or completely bleedless ACM systems in next-generation aircraft. Future work will investigate the performance of more complex VCC system architectures, featuring multiple pressure levels, and will include the selection of the working fluid as an additional degree of freedom of the integrated design optimization.

NOMENCLATURE

Roman symbols

A	Surface area [m ²]
b	Fins height [m]
C_r	Heat capacity ratio [-]
c_p	Specific heat capacity at constant pressure [kg m ² s ⁻² K ⁻¹]
D	Diameter [m] Drag force [N]
F_{ax}	Axial thrust [N]
F_d	Flow depth [m]
F_p	Fins pitch [m]
f	Friction factor [-]
G	Mass flux [kg m ⁻² s ⁻¹]
\mathbf{G}	Vector of constraints [-]
g	Gravitational acceleration [m/s ²]
H	Blade height [m]
h	Specific enthalpy [J kg ⁻¹] Heat transfer coefficient [W m ⁻² K ⁻¹]
\mathbf{J}	Vector of objective functions [-]
j	Colburn factor [-]
k	Impeller shape factor [-] Thermal conductivity [W m ⁻¹ K ⁻¹]
L_p	Louver pitch [m]
L_l	Louver length [m]
L_h	Louver height [m]
L/D	Lift to drag ratio [-]
l_f	Fin length [m]
l_t	Tube length [m]
M	Mach number [-]
\dot{m}	Mass flow rate [kg s ⁻¹]
NTU	Number of Transfer Units [-]
Nu	Nusselt number [-]
OR	Operating range [-]
P	Pressure [Pa] Power [W]
Pr	Prandtl number [-]
P_t	Tubes pitch [m]
\dot{Q}	Heat flow rate [W]
R	Radius [m] Thermal resistance [K W ⁻¹]
Re	Reynolds number [-]
SFC_{th}	Thrust specific fuel consumption [lb/(h.lbf)]
SFC_p	Power specific fuel consumption [lb/(hp.h)]
T	Temperature [K]
T_h	Tube height [m]
t	Thickness [m]
U	Peripheral speed [m s ⁻¹] Overall heat transfer coefficient [W m ⁻² K ⁻¹]
V	Velocity [m s ⁻¹] Volume [m ³]
W	Weight [kg]

W_{f0}	Fuel weight penalty [kg]
x	Width [m]
y	Height [m]
z	Depth [m]

Greek symbols

α	Absolute flow angle [°]
$\mathbf{\alpha}$	Vector of design variables [-]
β	Pressure ratio [-]
δ	Thickness [m]
ϵ	Effectiveness [-]
η	Efficiency [-]
Θ	Louver angle [°]
ρ	Density [kg m ⁻³]
τ	Aircraft mission time [h]
ϕ_{t1}	Swallowing capacity [-]
ψ_{is}	Isentropic loading coefficient [-]
Ω	Rotational speed [rpm]

Subscripts

1	Impeller inlet
2	Impeller outlet
3	Diffuser outlet
4	Volute outlet
air	Air stream
bl	Impeller blade
cond	Condensation
cr	Cruise operating point
el	Electrical
eva	Evaporation
f	Fin
fp	Faulty pack operating point
h	Hub
hg	Hot ground operating point
hyd	Hydraulic
is	Isentropic
m	Mechanical
mc	Microchannel
pp	Pinch point
refr	Refrigerant stream
s1	First compressor stage
s2	Second compressor stage
sc	Subcooling
sh	Superheating
t	Tube
tt	Total-to-total

Abbreviations

ACM	Air Cycle Machine
CAC	Cabin Air Compressor
COP	Coefficient Of Performance
DeSimECS	Design and Simulation of Energy Conversion Systems
DesOptECS	Design Optimization of

ECS	Energy Conversion Systems	R134a	Tetrafluoroethane
HEX	Environmental Control System	RC	Refrigerant Compressor
MB	Heat Exchanger	VCC	Vapor Compression Cycle
	Moving Boundary		

BIBLIOGRAPHY

- [1] D. Bender, “Exergy-based analysis of aircraft environmental control systems and its integration into model-based design”, Ph.D. dissertation, Technische Universität Berlin, 2018. DOI: 10.14279/DEPOSITONCE-8101.
- [2] Boeing, “AERO magazine, 4th quarter”, 2007.
- [3] V. Cavalcanti and C. de Andrade, “A Trade-off Study of a Bleedless and Conventional Air Conditioning Systems”, in *SAE Brasil Congress and Exhibit*, 2008. DOI: doi.org/10.4271/2008-36-0001.
- [4] N. Ablanque, S. Torras, C. Olliet, J. Rigola, and C.-D. Perez-Segarra, “Vapor compression system modelica library for aircraft ecs”, in *International Refrigeration and Air Conditioning Conference*, 2018.
- [5] H. Hu, H. Sun, C. Wu, X. Wang, and Z. Lv, “A steady-state simulation model of supplemental cooling system integrated with vapor compression refrigeration cycles for commercial airplane”, *Applied Thermal Engineering*, vol. 166, p. 114 692, 2020, ISSN: 1359-4311. DOI: 10.1016/j.applthermaleng.2019.114692.
- [6] Y. Xu, Z. Yan, and W. Xia, “A novel system for aircraft cabin heating based on a vapor compression system and heat recovery from engine lubricating oil”, *Applied Thermal Engineering*, vol. 212, p. 118 544, 2022, ISSN: 1359-4311. DOI: 10.1016/j.applthermaleng.2022.118544.
- [7] H. Yang and C. Yang, “Derivation and comparison of thermodynamic characteristics of endoreversible aircraft environmental control systems”, *Applied Thermal Engineering*, vol. 180, p. 115 811, Nov. 2020, ISSN: 1359-4311. DOI: 10.1016/J.APPLTHERMALENG.2020.115811.
- [8] H. Yang and C. Yang, “Application of scaling-endoreversible thermodynamic analysis model to aircraft environmental control system-methodology development”, *International Journal of Refrigeration*, vol. 112, pp. 90–99, Apr. 2020, ISSN: 0140-7007. DOI: 10.1016/J.IJREFRIG.2019.12.006.
- [9] J. V. Vargas and A. Bejan, “Integrative thermodynamic optimization of the environmental control system of an aircraft”, *International Journal of Heat and Mass Transfer*, vol. 44, no. 20, pp. 3907–3917, Oct. 2001, ISSN: 0017-9310. DOI: 10.1016/S0017-9310(01)00033-3.
- [10] I. Pérez-Grande and T. J. Leo, “Optimization of a commercial aircraft environmental control system”, *Applied Thermal Engineering*, vol. 22, no. 17, pp. 1885–1904, Dec. 2002. DOI: 10.1016/S1359-4311(02)00130-8.
- [11] T. J. Leo and I. Pérez-Grande, “A thermoeconomic analysis of a commercial aircraft environmental control system”, *Applied Thermal Engineering*, vol. 25, no. 2-3, pp. 309–325, Feb. 2005, ISSN: 1359-4311. DOI: 10.1016/J.APPLTHERMALENG.2004.06.011.
- [12] M. Sielemann, T. Giese, B. Oehler, and M. Gräber, “Optimization of an Unconventional Environmental Control System Architecture”, *SAE International Journal of Aerospace*, vol. 4, no. 2, pp. 1263–1275, Oct. 2011, ISSN: 1946-3855. DOI: 10.4271/2011-01-2691.
- [13] X. Li, Q. Chen, J. H. Hao, X. Chen, and K. L. He, “Heat current method for analysis and optimization of a refrigeration system for aircraft environmental control system”, *International Journal of Refrigeration*, vol. 106, pp. 163–180, Oct. 2019, ISSN: 0140-7007. DOI: 10.1016/J.IJREFRIG.2019.06.004.
- [14] Z. Duan, H. Sun, C. Wu, and H. Hu, “Multi-objective optimization of the aircraft environment control system based on component-level parameter decomposition”, *Energy*, vol. 245, p. 123 330, Apr. 2022, ISSN: 0360-5442. DOI: 10.1016/J.ENERGY.2022.123330.
- [15] G. Schweiger, H. Nilsson, J. Schoegg, W. Birk, and A. Posch, “Modeling and simulation of large-scale systems: A systematic comparison of modeling paradigms”, *Applied Mathematics and Computation*, vol. 365, Jan. 2020, ISSN: 0096-3003. DOI: 10.1016/J.AMC.2019.124713.

- [16] A. Giuffr  and M. Pini, "Design Guidelines for Axial Turbines Operating With Non-Ideal Compressible Flows", *Journal of Engineering for Gas Turbines and Power*, vol. 143, no. 1, Jan. 2021, ISSN: 0742-4795. DOI: 10.1115/1.4049137.
- [17] A. Giuffr , P. Colonna, and M. Pini, "The Effect of Size and Working Fluid on the Multi-Objective Design of High-Speed Centrifugal Compressors", *International Journal of Refrigeration*, vol. 143, pp. 43–56, Nov. 2022, ISSN: 0140-7007. DOI: 10.1016/J.IJREFRIG.2022.06.023.
- [18] E. A. Heath, "Amendment to the montreal protocol on substances that deplete the ozone layer (Kigali Amendment)", *International Legal Materials*, vol. 56, no. 1, pp. 193–205, Feb. 2017, ISSN: 0020-7829, 1930-6571. DOI: 10.1017/ilm.2016.2.
- [19] M. O. McLinden and M. L. Huber, "(R)Evolution of Refrigerants", *Journal of Chemical & Engineering Data*, vol. 65, no. 9, pp. 4176–4193, Sep. 2020, ISSN: 0021-9568, 1520-5134. DOI: 10.1021/acs.jced.0c00338. (visited on 01/28/2022).
- [20] T. Plan s, V. Habrard, S. Delbecq, V. Pommier-Budinger, and E. Benard, "Thermal management system models for overall aircraft design", in *AIAA AVIATION 2021 FORUM*, Jul. 2021. DOI: 10.2514/6.2021-2428.
- [21] "Drag and pressure recovery characteristics of auxiliary air inlets at subsonic speeds", ESDU 86002, Tech. Rep., 2004.
- [22] R. K. Shah and D. P. Sekuli , *Fundamentals of heat exchanger design*. Hoboken, NJ: John Wiley & Sons, Ltd, 2003, ISBN: 978-0-471-32171-2.
- [23] H. M. Joshi and R. L. Webb, "Heat transfer and friction in the offset stripfin heat exchanger", *International Journal of Heat and Mass Transfer*, vol. 30, no. 1, pp. 69–84, 1987, ISSN: 0017-9310. DOI: 10.1016/0017-9310(87)90061-5.
- [24] R. M. Manglik and A. E. Bergles, "Heat transfer and pressure drop correlations for the rectangular offset strip fin compact heat exchanger", *Experimental Thermal and Fluid Science*, vol. 10, no. 2, pp. 171–180, 1995, ISSN: 0894-1777. DOI: 10.1016/0894-1777(94)00096-Q.
- [25] R. K. Shah and D. P. Sekuli , "Chapter 9 - heat exchanger design procedures", in *Fundamentals of heat exchanger design*, John Wiley & Sons, Ltd, 2003, pp. 608–617, ISBN: 978-0-471-32171-2.
- [26] W. M. Kays and A. L. London, *Compact heat exchangers*, 3rd ed. Krieger Pub Co, 1984, ISBN: 1-57524-060-2.
- [27] B. Zohuri, *Compact Heat Exchangers*. Springer International Publishing, 2017, ISBN: 978-3-319-29834-4. DOI: 10.1007/978-3-319-29835-1.
- [28] H. Pangborn, A. G. Alleyne, and N. Wu, "A comparison between finite volume and switched moving boundary approaches for dynamic vapor compression system modeling", *International Journal of Refrigeration*, vol. 53, pp. 101–114, May 2015, ISSN: 0140-7007. DOI: 10.1016/J.IJREFRIG.2015.01.009.
- [29] Y.-J. Chang and C.-C. Wang, "A generalized heat transfer correlation for louver fin geometry", *International Journal of Heat and Mass Transfer*, vol. 40, no. 3, pp. 533–544, 1997, ISSN: 0017-9310. DOI: 10.1016/0017-9310(96)00116-0.
- [30] V. Gnielinski, "On heat transfer in tubes", *International Journal of Heat and Mass Transfer*, vol. 63, pp. 134–140, 2013, ISSN: 0017-9310. DOI: 10.1016/j.ijheatmasstransfer.2013.04.015.
- [31] M. Shah, "A general correlation for heat transfer during film condensation inside pipes", *International Journal of Heat and Mass Transfer*, vol. 22, no. 4, pp. 547–556, 1979, ISSN: 0017-9310. DOI: 10.1016/0017-9310(79)90058-9.
- [32] S. G. Kandlikar, "A general correlation for saturated two-phase flow boiling heat transfer inside horizontal and vertical tubes", *Journal of Heat Transfer*, vol. 112, no. 1, pp. 219–228, Feb. 1990, ISSN: 0022-1481, 1528-8943.
- [33] M.-H. Kim and C. W. Bullard, "Air-side thermal hydraulic performance of multi-louvered fin aluminum heat exchangers", *International Journal of Refrigeration*, vol. 25, no. 3, pp. 390–400, 2002, ISSN: 0140-7007. DOI: 10.1016/S0140-7007(01)00025-1.
- [34] M. S. Yadav, S. A. Giri, and V. C. Momale, "Sizing analysis of louvered fin flat tube compact heat exchanger by genetic algorithm", *Applied Thermal Engineering*, vol. 125, pp. 1426–1436, 2017, ISSN: 1359-4311. DOI: 10.1016/j.applthermaleng.2017.07.119.

- [35] J. Schmidt and L. Friedel, "Two-phase pressure drop across sudden contractions in duct areas", *International Journal of Multiphase Flow*, vol. 23, no. 2, pp. 283–299, 1997, ISSN: 0301-9322. DOI: 10.1016/S0301-9322(96)00056-0.
- [36] F. Ascione, C. M. De Servi, O. Meijer, V. Pommé, and P. Colonna, "Assessment of an inverse organic rankine cycle system for the ecs of a large rotorcraft adopting a high-speed centrifugal compressor and a low GWP refrigerant", in *Proceedings of the 6th International Seminar on ORC Power Systems*, Technical University of Munich, 2021. DOI: 10.14459/2021mp1633127.
- [37] M. H. Kim and C. W. Bullard, "Performance Evaluation of a Window Room Air Conditioner With Microchannel Condensers", *Journal of Energy Resources Technology*, vol. 124, no. 1, pp. 47–55, Mar. 2002, ISSN: 0195-0738. DOI: 10.1115/1.1446072.
- [38] M. Sheikholeslami, M. Hatami, M. Jafaryar, F. Farkhadnia, D. D. Ganji, and M. Gorji-Bandpy, "Thermal management of double-pipe air to water heat exchanger", *Energy and Buildings*, vol. 88, pp. 361–366, 2015, ISSN: 0378-7788. DOI: 10.1016/j.enbuild.2014.11.076.
- [39] A. Cavallini, G. Censi, D. Del Col, L. Doretti, G. Longo, and L. Rossetto, "Experimental investigation on condensation heat transfer and pressure drop of new hfc refrigerants (R134a, R125, R32, R410A, R236ea) in a horizontal smooth tube", *International Journal of Refrigeration*, vol. 24, no. 1, pp. 73–87, 2001, ISSN: 0140-7007. DOI: 10.1016/S0140-7007(00)00070-0.
- [40] Y.-Y. Yan and T.-F. Lin, "Evaporation heat transfer and pressure drop of refrigerant r-134a in a small pipe", *International Journal of Heat and Mass Transfer*, vol. 41, no. 24, pp. 4183–4194, 1998, ISSN: 0017-9310. DOI: 10.1016/S0017-9310(98)00127-6.
- [41] E. W. Lemmon, I. H. Bell, M. L. Huber, and M. O. McLinden, *NIST Standard Reference Database 23: Reference Fluid Thermodynamic and Transport Properties-REFPROP, Version 10.0*, National Institute of Standards and Technology, 2018. DOI: <https://doi.org/10.18434/T4/1502528>. [Online]. Available: <https://www.nist.gov/srd/refprop>.
- [42] I. H. Bell, J. Wronski, S. Quoilin, and V. Lemort, "Pure and pseudo-pure fluid thermophysical property evaluation and the open-source thermophysical property library coolprop", *Industrial & Engineering Chemistry Research*, vol. 53, no. 6, pp. 2498–2508, 2014. DOI: 10.1021/ie4033999.
- [43] J. Stanitz, "One-dimensional compressible flow in vaneless diffusers of radial-and mixed-flow centrifugal compressors, including effects of friction, heat transfer and area change", Tech. Rep., 1952.
- [44] J. Tiainen, A. Jaatinen-Värri, A. Grönman, P. Sallinen, J. Honkatukia, and T. Hartikainen, "Validation of the Axial Thrust Estimation Method for Radial Turbomachines", *International Journal of Rotating Machinery*, vol. 2021, 2021, ISSN: 15423034. DOI: 10.1155/2021/6669193.
- [45] D. Eckardt, "Instantaneous measurements in the jet-wake discharge flow of a centrifugal compressor impeller", *Journal of Engineering for Gas Turbines and Power*, vol. 97, no. 3, pp. 337–345, Jul. 1975, ISSN: 15288919. DOI: 10.1115/1.3445999.
- [46] D. Eckardt, "Detailed flow investigations within a high-speed centrifugal compressor impeller", *Journal of Fluids Engineering, Transactions of the ASME*, vol. 98, no. 3, pp. 390–399, Sep. 1976, ISSN: 1528901X. DOI: 10.1115/1.3448334.
- [47] D. Eckardt, "Investigation of the Jet-Wake Flow of a Highly-Loaded Centrifugal Compressor Impeller", Ph.D. dissertation, 1977, pp. 1–227.
- [48] D. Japikse, "A critical evaluation of three centrifugal compressors with pedigree data sets: Part 5-studies in component performance", *Journal of Turbomachinery*, vol. 109, no. 1, pp. 1–9, Jan. 1987, ISSN: 15288900. DOI: 10.1115/1.3262064.
- [49] J. Schifmann and D. Favrat, "Experimental investigation of a direct driven radial compressor for domestic heat pumps", *International Journal of Refrigeration*, vol. 32, no. 8, pp. 1918–1928, Dec. 2009, ISSN: 01407007. DOI: 10.1016/j.ijrefrig.2009.07.006.
- [50] J. Schifmann and D. Favrat, "Design, experimental investigation and multi-objective optimization of a small-scale radial compressor for heat pump applications", *Energy*, vol. 35, no. 1, pp. 436–450, Jan. 2010, ISSN: 03605442. DOI: 10.1016/j.energy.2009.10.010.

-
- [51] M. Van Der Geest, H. Polinder, J. A. Ferreira, and M. Christmann, "Power density limits and design trends of high-speed permanent magnet synchronous machines", *IEEE Transactions on Transportation Electrification*, vol. 1, no. 3, pp. 266–276, Oct. 2015, ISSN: 23327782. DOI: 10.1109/TTE.2015.2475751.
- [52] *CadQuery, Release 2*, 2022. [Online]. Available: <https://github.com/CadQuery/cadquery/>.
- [53] J. Saari, "Friction losses and heat transfer in high-speed electrical machines", Helsinki University of Technology, Tech. Rep., Dec. 1996.
- [54] J. Blank and K. Deb, "Pymoo: Multi-Objective Optimization in Python", *IEEE Access*, vol. 8, pp. 89497–89509, 2020. DOI: 10.1109/ACCESS.2020.2990567.
- [55] K. Deb, A. Pratap, S. Agarwal, and T. Meyarivan, "A fast and elitist multiobjective genetic algorithm: NSGA-II", *IEEE Transactions on Evolutionary Computation*, vol. 6, no. 2, pp. 182–197, Apr. 2002. DOI: 10.1109/4235.996017.
- [56] SAE, *Aircraft fuel weight penalty due to air conditioning*, Jun. 2004. DOI: 10.4271/ATR1168/8.

6

DATA-DRIVEN COMPRESSOR MODELING FOR ECS DESIGN OPTIMIZATION

*The greater danger for most of us lies not in setting our aim too high and falling short;
but in setting our aim too low, and achieving our mark.*

Michelangelo

6

Parts of this chapter have been published in:

A. Giuffre, F. Ascione, C. De Servi, and M. Pini, "Data-Driven Modeling of High-Speed Centrifugal Compressors for Aircraft Environmental Control Systems", *International Journal of Refrigeration*, vol. 151, pp. 354-369, 2023, ISSN: 0140-7007. DOI: 10.1016/j.ijrefrig.2023.03.019.

The optimal design of the Environmental Control System (ECS) of passenger aircraft can be arguably achieved only by simultaneously optimizing the design variables of the system and those associated with the conceptual design of the main components, i.e., heat exchangers and turbomachines. However, adopting an integrated design approach leads to a remarkable increase in the number of design variables and constraints characterizing the optimization problem. As a result, the computational cost associated with the optimization becomes prohibitive, even for relatively simple ECS configurations. Moreover, the increased complexity of the mathematical problem associated with the ECS design reduces the robustness of the numerical solver. These shortcomings can be mitigated by replacing the conceptual design models of the most critical components with data-driven surrogate models. In this work, a data-driven model for high-speed centrifugal compressors was developed. The model is based on artificial neural networks and has been trained on a synthetic dataset of 165k compressor designs, generated with an in-house tool. The case study selected to demonstrate the capabilities of the proposed methodology is the multi-objective design optimization of an electrically-driven VCC system for the ECS of a single-aisle, short-haul aircraft, flying at cruise conditions. The results show that the number of function evaluations needed to identify the Pareto front reduces by a factor of three when using the data-driven model. At the same time, the robustness of the numerical solver is improved, leading to the identification of optimal solutions covering a wider design space.

6.1. INTRODUCTION

THE performance of the Environmental Control System (ECS) of a passenger aircraft is largely affected by the design of its main components. Therefore, the optimal design of the system can be arguably achieved only by resorting to an integrated design approach, i.e., a framework in which the design variables of the system and those related to the preliminary design of the main components are optimized simultaneously. An extended literature review concerning design optimization studies targeting aircraft ECS is reported in Chapter 5 and is omitted here for brevity. In the case of an electrically-driven Vapor Compression Cycle (VCC) system, the most critical components are the evaporator, condenser, Refrigerant Compressor (RC), and Cabin Air Compressor (CAC). Among them, the most critical component is arguably the high-speed centrifugal compressor powering the refrigerant loop. Hence, it is necessary to include a preliminary design model of the turbo-compressor in the integrated design framework. However, this is often overlooked in the existing body of literature regarding the design optimization of aircraft ECS. The reason thereof is that the introduction of such a model further complicates the mathematical problem associated with the ECS design and increases the number of design variables and non-linear constraints to be included in the optimization. As a result, the robustness of the numerical solver decreases, due to the higher likelihood of an ill-conditioned matrix associated with the system of equations representing the model, and the computational cost of the optimization problem quickly becomes prohibitive, even for relatively simple ECS configurations. For these reasons, the availability of a strategy to reduce the complexity of the numerical system model including the conceptual design of the RC, without decreasing the accuracy of the solution, is of paramount importance. The development of such a strategy is the objective of the research presented here. This target is achieved through two intermediate steps. First, a methodology to derive a data-driven model for high-speed

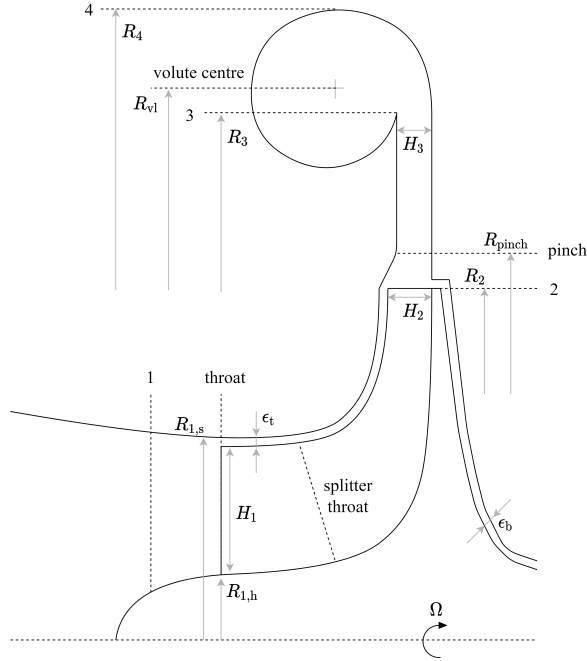


Figure 6.1: Schematic meridional view of a centrifugal compressor stage featuring splitter blades, pinched vaneless diffuser, overhung volute, and no inlet guide vanes.

centrifugal compressors operating with gas bearings is proposed. Second, the capabilities of an optimization methodology, exploiting the data-driven model for the integrated design of an exemplary ECS based on the electrically-driven VCC system, are demonstrated.

The remainder of the chapter is structured as follows. First, the development of the data-driven compressor model is documented. Then, the integrated design methodology is described and the modifications required to couple the data-driven compressor model are discussed. Next, the multi-objective design optimization of an electrically-powered ECS is described, including two different methodologies: a conventional approach, whereby the compressor preliminary design is addressed by means of a meanline code, and the proposed method, in which the meanline code is replaced with the data-driven model. The results are compared in terms of optimal solutions and computational cost. Moreover, a sensitivity analysis is performed to assess the robustness of the optimal solutions to changes in the values of the design variables and to identify the design variables which mostly affect the objective functions. Finally, concluding remarks summarize the lessons learned and provide an outlook on future work.

6.2. DATA-DRIVEN COMPRESSOR MODEL

The development of a surrogate model for small-scale single-stage centrifugal compressors has been recently documented in Ref. [1]. Using a symbolic regression tool, the authors obtained an analytical expression of the isentropic efficiency at the design point, as

Table 6.1: Design space selected to create the dataset used to train the data-driven compressor model.

Variable	Range	Fluid	N	T_r	P_r
β_{tt}	2.0 - 5.0	H ₂	3.0	2.0	0.08
\dot{m} [kg/s]	0.05 - 0.25	CO ₂	7.0	0.9	0.2
ϕ_{t1}	0.05 - 0.2	Propane	19.08	0.65	0.015
ψ_{is}	0.6 - 1.2	R134a	21.64	0.65 - 0.81	0.015 - 0.15
α_2 [deg]	60 - 75	Isobutane	28.43	0.65	0.015
k	0.65 - 0.95	R1233zd(E)	28.77	0.65 - 0.82	0.015 - 0.15
N_{bl}	10 - 20				
R_3/R_2	1.2 - 2.0				
$H_{r,pinch}$	0.0 - 1.0				
$R_{r,pinch}$	0.0 - 1.0				

a function of five non-dimensional groups and the total inlet pressure. The data-driven regression has been performed on a dataset comprising approximately 12.5k compressor designs, obtained by means of a meanline tool, validated with experimental data. However, the proposed reduced-order model has the following limitations. All the compressor stages featured in the dataset have been designed to operate with the same working fluid, i.e., refrigerant R134a. Moreover, a number of geometrical parameters characterizing the shape and the performance of the compressor stage, e.g., the impeller outlet blade angle, have been set to constant values, or have been determined by prescribing a constant ratio among two geometrical parameters, e.g., the diffuser radius ratio. Therefore, the dataset is biased, and the resulting analytical expression of the efficiency is not applicable to a compressor stage operating with an arbitrary working fluid and featuring a generic shape. Furthermore, the proposed data-driven model does not provide any prediction of the operating range of the machine, thus it may lead to compressor configurations that are unfeasible for systems that require a broad operating envelope, such as the ECS of passenger aircraft.

To overcome these limitations, a new methodology to derive a data-driven model for single-stage centrifugal compressors is proposed. In the same fashion as in Ref. [1], the dataset has been generated with a validated compressor model, which is documented in Chapter 2. The synthetic dataset comprises 240k unique compressor stage designs, characterized by different combinations of the design variables listed in Tab. 6.1, and sampled according to the latin hypercube method. Following the notation adopted throughout this dissertation and with reference to Fig. 6.1, the swallowing capacity of the compressor is defined as

$$\phi_{t1} = \frac{\dot{m}}{\rho_{t1} U_2 D_2^2}, \quad (6.1)$$

whereas the isentropic work coefficient reads

$$\psi_{is} = \frac{\Delta h_{tt,is}}{U_2^2}. \quad (6.2)$$

The non-dimensional geometrical characteristics of the compressor stage are expressed in terms of the impeller shape factor

$$k = 1 - \left(\frac{R_{1,h}}{R_{1,s}} \right)^2, \quad (6.3)$$

the diffuser radius ratio R_3/R_2 , and the diffuser pinch radius and height ratio

$$R_{r,pinch} = \frac{R_{pinch} - R_2}{R_3 - R_2}, \quad (6.4)$$

$$H_{r,pinch} = \frac{H_3 - H_2}{H_2(R_2/R_{pinch} - 1)}.$$

Differently from the study reported in Ref. [1], none of the main geometrical characteristics of the stage has been fixed to a constant value. Nevertheless, the number of design variables considered to create the dataset is relatively limited, thanks to the adoption of a non-dimensional approach based on scaling analysis. The additional compressor design parameters related to manufacturing constraints have been set to constant values, namely, $\epsilon_b = \epsilon_t = 0.15$ mm, $Ra = 3.2$ μ m. Finally, to cope with the design of compressors of different sizes, the ratio between the shaft and the inlet hub radii has been fixed throughout the design space, instead of prescribing a constant value of shaft radius.

The working fluids considered in this work are synthetic and natural refrigerants selected from a parametric study conducted for an electrically-driven VCC for the ECS of large helicopters [2]. To enrich the dataset, the compressor stages operating with the refrigerants R134a and R1233zd(E) have been designed for two different total inlet thermodynamic states, resembling the conditions encountered in a conventional and a high-temperature heat pump. To reduce bias in the dataset and to extend the range of applicability of the data-driven compressor model, the database has been complemented with compressor stages designed for simpler molecule fluids, i.e., CO₂ and H₂. Additional working fluids and thermodynamic conditions will be included as part of future work. The complete list of fluids and of the corresponding reduced inlet conditions, i.e., total inlet conditions normalized with respect to critical state properties, considered in this work is reported in Tab. 6.1.

Several techniques are suitable for data-driven regression, e.g., symbolic regression, Artificial Neural Networks (ANN), Support Vector Machines (SVM), and Gaussian Processes (GP). In this work, a Multi-Layer Perceptron (MLP), i.e., a feedforward ANN featuring one or multiple fully connected hidden layers, has been selected to accomplish this task. The reason is twofold. First, the computational overhead associated with the evaluation of the data-driven model is of primary importance for the target application. In general terms, the computational cost of an MLP model scales with the total number of neurons and is lower than the cost of evaluating, for instance, a model based on a GP or an SVM. At the same time, an MLP model requires a larger amount of training data to reach the same level of accuracy as a GP or an SVM. However, the availability of data is not a limiting factor in this case, since the dataset is generated with a numerical model.

To reduce the number of input features used to train the ANN and to avoid the use of categorical input, i.e., a string identifying the name of the fluid, the data associated with the working fluid and the inlet thermodynamic conditions have been synthesized in two parameters. These are the fluid molecular complexity, measured as the number of active degrees of freedom of a molecule [3]

$$N = \frac{2Mc_{v,id}(T_c)}{R}, \quad (6.5)$$

and the average value of the isentropic pressure-volume exponent [4] over the compression process

$$\overline{\gamma_{Pv}} = \frac{\log\left(\frac{P_{in}}{P_{out}}\right)}{\log\left(\frac{\rho_{in}}{\rho_{out}}\right)}. \quad (6.6)$$

A detailed analysis of the influence of these parameters on the design of centrifugal compressors can be found in Ref. [5], and it is omitted here for brevity. The resulting vector of input features for the ANN reads

$$\mathbf{X} = \left[\phi_{t1}, \psi_{is}, \alpha_2, \frac{R_3}{R_2}, k, N_{bl}, H_{r,pinch}, R_{r,pinch}, \beta_{tt,target}, \dot{m}, N, \overline{\gamma_{Pv}}, \frac{\epsilon_b}{H_2}, \frac{\epsilon_t}{H_2} \right]. \quad (6.7)$$

The original dataset has been pre-processed by removing the compressor designs that are considered unfeasible or do not meet the required specifications. The criteria used to filter the dataset are:

- minimum acceptable efficiency at design point $\eta_{tt} \geq 0.5$;
- minimum acceptable operating range at the design rotational speed

$$OR = \frac{\dot{m}_{max} - \dot{m}_{min}}{\dot{m}_{des}} \Big|_{\Omega_{des}} \geq 0.05;$$
- maximum allowable blade angle at impeller outlet to ensure stable compressor operation $\beta_{2,bl} \leq 0^\circ$;
- maximum allowable deviation between the target and the computed values of pressure ratio $\Delta\beta_{tt} \leq 20\%$.

The filtered dataset is composed of 165k samples, thus reducing the computational cost associated with the training of the data-driven model by about 30%, without any loss of useful information. In order to enhance the accuracy of the MLP model, input features standardization has been applied prior to training. Moreover, to further simplify the multivariate regression function to be learned by the ANN, the labels have been categorized according to their use in the ECS optimization process, i.e., objectives or constraints. Then, two separate MLP models have been trained to predict the vector of objective functions and constraints, namely:

Table 6.2: Design space and set of optimal hyperparameters.

Hyperparameter	Range	MLP _{obj}	MLP _{con}
L	4 - 6	5	6
$n^{[1]}$	5 - 200	199	60
$n^{[2]}$	5 - 200	199	94
$n^{[3]}$	5 - 200	200	44
$n^{[4]}$	5 - 200	144	63
$n^{[5]}$	5 - 200	42	68
$n^{[6]}$	5 - 200	-	70
α	$10^{-4} - 10^{-1}$	$10^{-2.75}$	$10^{-2.89}$
mini-batch size	$2^6 - 2^{10}$	2^6	2^6

$$Y_{\text{obj}} = [\beta_{\text{tt}}, \eta_{\text{tt}}, OR, \dot{m}_{\text{choke}}], \quad (6.8)$$

$$Y_{\text{con}} = [\Omega_{\text{des}}, R_{1,h}, H_2, \beta_{2,\text{bl}}, R_4].$$

Upon pre-processing, the dataset has been split into training, development, and test sets, counting 145k, 10k, and 10k samples, corresponding to approximately 88%, 6%, and 6% of the total amount of data, respectively. The space of hyperparameters investigated to optimize the accuracy of the ANN is summarized in Tab. 6.2. The hyperparameters search is performed by resorting to NOMAD [6], [7], i.e., an optimization algorithm suited for mixed-integer non-linear programming problems, featuring an expensive black-box function evaluation. For each combination of hyperparameters, an MLP model is created leveraging the open-source programming framework TensorFlow [8]. The model is trained for 80 epochs, and its performance is evaluated on the development set, using the mean squared error loss function

$$L(\theta) = \frac{1}{n} \sum_{i=1}^n (\hat{y}_i - y_i)^2, \quad (6.9)$$

where θ , n , and \hat{y} denote the space of the hyperparameters, the number of samples, and the model prediction, respectively. The optimal architecture is selected after a maximum of 750 different MLP models have been trained and evaluated. The process is repeated for both the models trained to predict Y_{obj} and Y_{con} . The hyperparameters search has been performed using a computer equipped with an Intel® Xeon® Gold 5220R chipset, featuring 48 logical threads, leading to a total computational cost of about 380 hours. The arrays of optimal hyperparameters are reported in Tab. 6.2 for the two MLP models. The training histories of the MLP models featuring the optimal set of hyperparameters are displayed in Fig. 6.2.

The accuracy of the optimal MLP models is evaluated for each label on the test set, i.e., the 10k samples not used for training or hyperparameters search, in terms of both mean absolute error (mae), and mean absolute percentage error (mape). The results are listed in Tab. 6.3. Furthermore, to provide a more comprehensive overview of the predictive

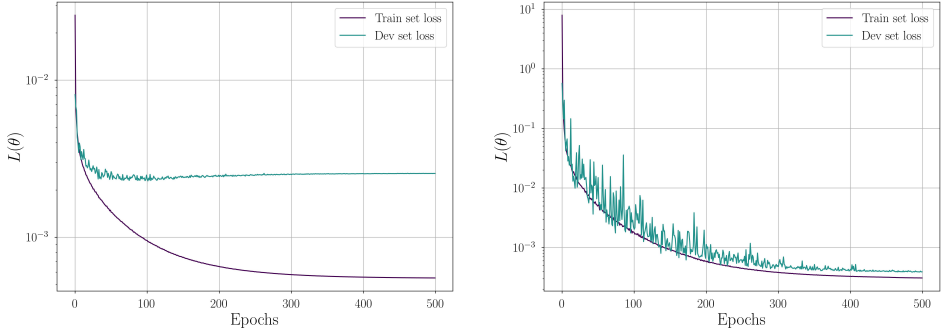


Figure 6.2: Training history of MLP models trained to predict Y_{obj} (left) and Y_{con} (right), and featuring the optimal set of hyperparameters.

Table 6.3: Accuracy of the two MLP models evaluated on the test set.

Y	$mae = \frac{1}{n} \sum_{i=1}^n \hat{Y} - Y $	$mape = \frac{1}{n} \sum_{i=1}^n \frac{ \hat{Y} - Y }{Y} \cdot 100$
β_{tt}	0.031 [-]	0.96 %
η_{tt}	0.007 [-]	0.97 %
OR	0.013 [-]	4.97 %
\dot{m}_{choke}	0.004 [kg/s]	2.41 %
Ω_{des}	1670 [rpm]	1.01 %
$R_{1,h}$	10^{-5} [m]	0.31 %
H_2	10^{-5} [m]	0.84 %
$\beta_{2,bl}$	0.02 [deg]	0.37 %
R_4	$7 \cdot 10^{-4}$ [m]	1.06 %

capabilities of the MLPs, the deviation between the model predictions and the true labels of the test set is reported in Fig. 6.3. The comparison shows that the mape is in the order of 1% or lower for each label except for the choking point mass flow rate. A further inspection of Fig. 6.3 reveals that the maximum prediction errors related to \dot{m}_{choke} occur when the value of the operating range is close to zero, thus are related to compressor designs that are unfeasible for ECS applications.

6.3. INTEGRATED DESIGN OPTIMIZATION

The test case selected to demonstrate the capabilities of the data-driven compressor model is the multi-objective optimization of the ECS of a single-aisle, short-haul aircraft, e.g., the Airbus A320. For the sake of simplicity, one ECS architecture and one operating condition are considered: a single-pressure level, electrically-driven VCC system, operating at cruise, i.e., $M_\infty = 0.78$ at an altitude of 11.88 km. The inlet conditions of the mixing manifold of the air distribution system, which corresponds to the outlet of the VCC system, are specified in terms of mass flow rate, pressure, and temperature: $\dot{m}_{mix} = 0.5$ kg/s, $P_{mix} = 76.25$

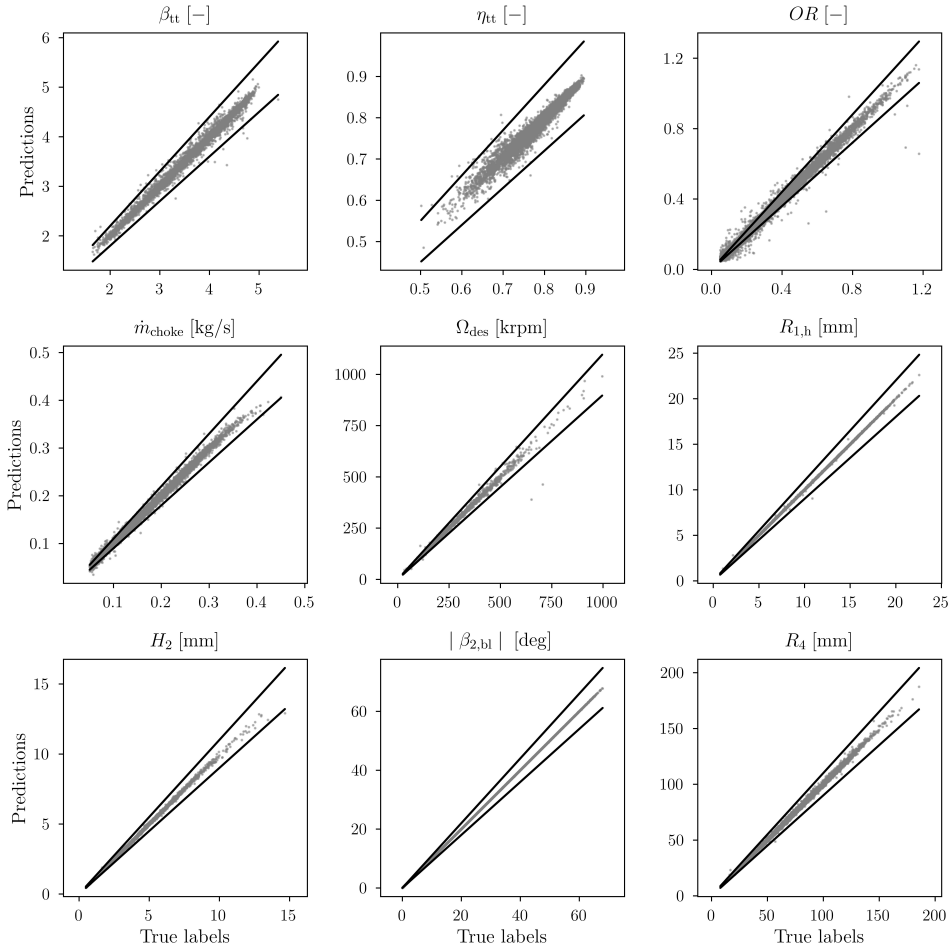


Figure 6.3: Comparison between the predictions of the optimal MLP models and the true labels of the test set. The data points are displayed in grey, whereas the black lines correspond to the $\pm 10\%$ error bands.

kPa, $T_{\text{mix}} = 13.14^{\circ}\text{C}$, and correspond to a mild cooling operating point [9]. As discussed in Chapter 5, the ECS of passenger aircraft is characterized by a broad operating envelope, ranging from cruise to extreme operating points, such as ground operation on a very hot and humid day, and flight operation in the presence of a faulty ECS pack. Therefore, a VCC system powered by a single-stage refrigerant compressor is arguably incapable to meet the pressure ratio required at the extreme operating points of the envelope. However, the development of a data-driven model for a multi-stage centrifugal compressor is beyond the scope of the present work and will be addressed in a future study.

The ECS based on the electrically-driven VCC technology has been modeled by means of the in-house DeSimECS (Design and Simulation of Energy Conversion Systems) library

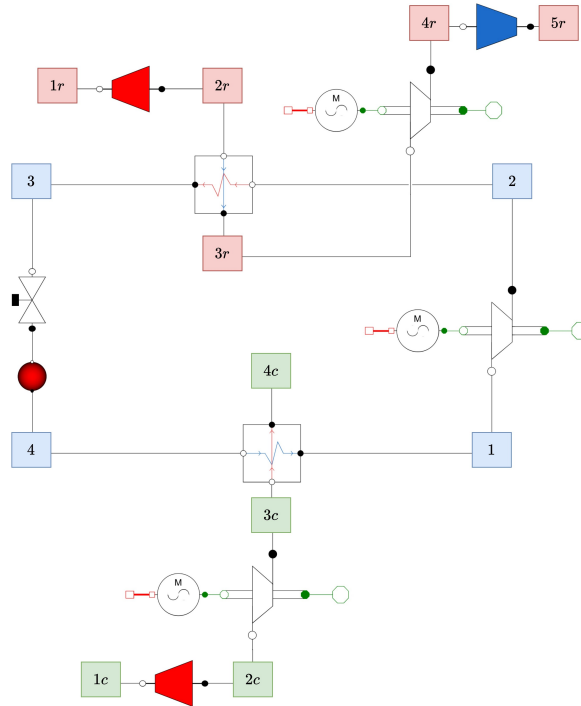


Figure 6.4: Simplified process flow diagram of the electrically-driven VCC system obtained from the graphical user interface of DeSimECS. The thermodynamic states are highlighted as follows: ram air stream in red, cabin air stream in green, and refrigerant loop in blue.

coded in the *acasual* [10], object-oriented, equation-based Modelica language, see Fig. 6.4. The main components of the VCC system are: two compact heat exchangers (CHEXs), namely the condenser and the evaporator, the expansion valve, and the refrigerant compressor. The additional components needed to simulate the performance of the ECS are: two intakes for the ram air and the cabin air, respectively, the cabin air compressor, the ram air fan, and the nozzle, used to accelerate the ram airflow at the exhaust. The refrigerant selected for the application is the R134a, i.e., the standard working fluid used for VCC-based ECS, such as those of helicopters. The approach adopted to model the main components is described in Chapter 5 and is omitted here for brevity. In this work, the intakes feature a simplified model as compared to the one documented in Chapter 5. In particular, a constant value of 0.8 is assumed for the pressure recovery factor, and the drag penalty is simply computed as the difference between the momentum of the flow entering and leaving the ram air duct.

The objective functions selected for this demonstration of capabilities are the maximization of the system COP and the minimization of the weight and the drag penalty associated with the ram airflow. With the purpose of evaluating the overall performance of the ECS, the COP is defined as the ratio of the power required for cabin cooling and pressurization in ideal conditions, over the total electric power consumption of the system,

Table 6.4: Settings of the ECS multi-objective design optimization: upper and lower bounds prescribed for the design variables and maximum or minimum thresholds set for the non-linear constraints.

Design variable	Type	Range	Constraint	Value
\dot{m}_{ram} [kg/s]	System	0.4 - 1.0	$\min(R_{1,h})$ [mm]	3.25
\dot{m}_{refr} [kg/s]	System	0.1 - 0.25	$\min(H_2)$ [mm]	1.5
β_{tt}	System	2.0 - 5.0	$\min(\beta_{2,\text{bl}})$ [deg]	-45
ΔT_{sh} [K]	System	3.0 - 10.0	$\max(\beta_{2,\text{bl}})$ [deg]	-10
ΔT_{sc} [K]	System	3.0 - 10.0	$\max(\Omega)$ [krpm]	250
ϕ_{t1}	Compressor	0.05 - 0.2	$\min(x_{\text{eva-cond}})$ [mm]	50
ψ_{is}	Compressor	0.6 - 1.0	$\max(x_{\text{eva-cond}})$ [mm]	800
α_2 [deg]	Compressor	60 - 75	$\min(\Delta T_{\text{pp,eva}})$ [K]	3
k	Compressor	0.65-0.95	$\min(\Delta T_{\text{pp,cond}})$ [K]	5
N_{bl}	Compressor	10 - 20	$\max(V_{\text{air,eva-cond}})$ [m/s]	30
R_3/R_2	Compressor	1.2 - 2.0	$\max(V_{\text{refr,eva-cond}})$ [m/s]	30
$R_{r,\text{pinch}}$	Compressor	0.0 - 1.0		
$H_{r,\text{pinch}}$	Compressor	0.0 - 1.0		
$y_{\text{eva-cond}}$ [mm]	Heat exchanger	100 - 300		
z_{eva} [mm]	Heat exchanger	20 - 70		
z_{cond} [mm]	Heat exchanger	10 - 60		

due to the cabin air compressor, the ram air fan and the high-speed centrifugal compressor, i.e.,

$$\text{COP} = \frac{\dot{Q}_{\text{cooling}} + \dot{W}_{\text{p,id}}}{\dot{W}_{\text{el,CAC}} + \dot{W}_{\text{el,fan}} + \dot{W}_{\text{el,CC}}}. \quad (6.10)$$

To further simplify the problem, only the dry weight of the two CHEXs is accounted for as an objective in the optimization process. The weight of the remaining components of the ECS is assumed to be constant throughout the design space. Due to the low operating temperature of the prescribed application, the material selected for both the condenser and the evaporator is the 6061 Aluminium alloy. The non-linear constraints are imposed to ensure the manufacturability of the system components, i.e., heat exchangers and compressor, and to define an upper threshold for the speed of the air and the refrigerant in the circuit. Overall, the optimization problem comprises 17 design variables, 3 objectives, and 15 inequality constraints, as summarized in Tab. 6.4. In line with what is reported in the introduction, this demonstrates that the size of the optimization problem rapidly increases even for a simple VCC configuration, when including the design of the centrifugal compressor in the integrated design framework together with a set of realistic manufacturing constraints.

The in-house optimization framework DesOptECS (Design Optimization of Energy Conversion Systems) consists of a Python program coupling the ECS model developed in Modelica with an open-source toolbox for multi-objective design optimization [11]. The Pareto front of optimal solutions is computed by means of the NSGA-II algorithm described in Ref. [12]. The initial population comprises ten individuals for each design variable, and is sampled according to the latin hypercube methodology along the floating-point directions, and randomly along the integer axis, i.e., the one corresponding to the

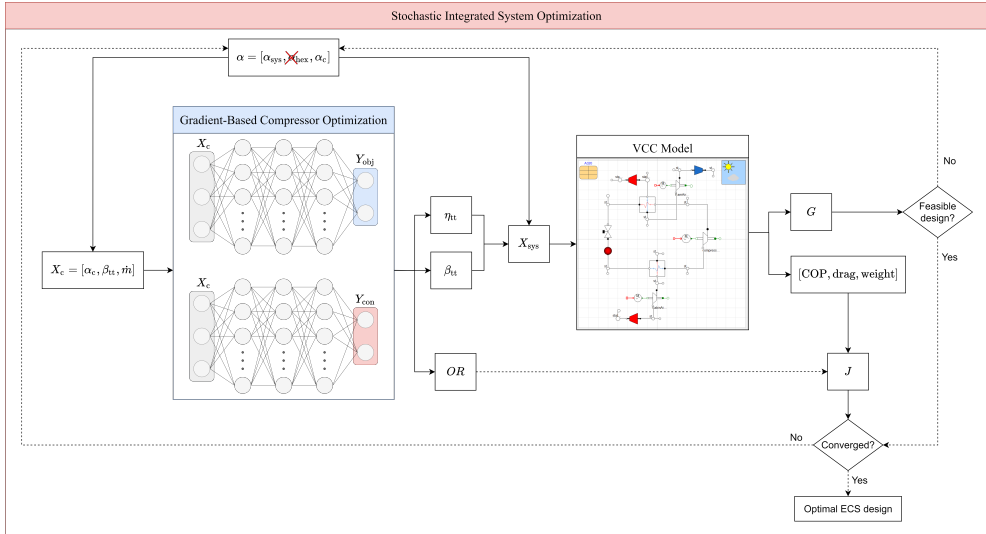


Figure 6.5: Flowchart of the modified version of DesOptECS. The data-driven model is used to decouple the optimization of the high-speed centrifugal compressor, highlighted in blue, from the optimization of the VCC system, highlighted in red.

number of compressor blades. The population is evolved for a maximum of 170 generations, leading to a maximum of 28900 evaluations of the Modelica model. The result thereof is that the computational cost quickly becomes prohibitive when increasing the number of design variables, even if resorting to parallel computing to evaluate the individuals of each generation.

To overcome this limitation, DesOptECS has been modified by replacing the compressor model implemented in Modelica with the pre-trained MLP models described in Section 6.2. The computational cost of the optimization problem can be significantly reduced by limiting the number of design variables selected by the stochastic algorithm NSGA-II. This can be achieved by leveraging the computational efficiency of the pre-trained MLP models, as described in the following. As discussed in Chapter 5, the vector of design variables α can be conveniently split into three subsets, corresponding to the design variables of the system, the heat exchangers, and the high-speed compressor:

$$\begin{aligned}
 \alpha_{\text{sys}} &= [\dot{m}_{\text{ram}}, \dot{m}_{\text{refr}}, \beta_{\text{tt}}, \Delta T_{\text{sh}}, \Delta T_{\text{sc}}], \\
 \alpha_{\text{HEX}} &= [y_{\text{eva}}, y_{\text{cond}}, z_{\text{eva}}, z_{\text{cond}}], \\
 \alpha_{\text{c}} &= [\phi_{\text{t1}}, \psi_{\text{is}}, \alpha_2, k, N_{\text{bl}}, R_3/R_2, R_{\text{r,pinch}}, H_{\text{r,pinch}}].
 \end{aligned} \tag{6.11}$$

The vector of input features for the data-driven model can be assembled by combining α_{c} with two variables of α_{sys} , namely, \dot{m}_{refr} , β_{tt} , and with two parameters related to compressor manufacturability, i.e., ϵ_b/H_2 , ϵ_t/H_2 , and two parameters related to the prescribed

working fluid and thermodynamic state, i.e., $N, \overline{\gamma_{Pv}}$. As a result, the set of compressor design variables α_c can be decoupled from the array of optimization variables selected by the stochastic algorithm, and can be treated separately. In this implementation, once the values of β_{tt} and \dot{m}_{refr} have been selected by the stochastic algorithm for each individual of a generation, the set of α_c is optimized separately, by resorting to a constrained gradient-based algorithm [13]. The values of the objectives and constraints are evaluated by means of the MLP models, and the objective function is expressed as a linear combination of η_{tt} and OR . After the gradient-based optimization, the resulting values of η_{tt} and β_{tt} are appended to the vectors α_{sys} and α_{HEX} , and the values of the objectives and the constraints of the VCC system are evaluated by means of the Modelica model. Eventually, the compressor operating range can be included into the vector of objective functions J . However, this is not done here, since the aim is to compare the Pareto front identified by means of the original and the modified versions of DesOptECS, without altering the vector of the objective functions. The proposed optimization methodology is schematically illustrated in Fig. 6.5.

Thanks to the use of data-driven modeling, the cost of the gradient-based compressor design optimization for each individual of the population is negligible, as compared to the cost associated with the evaluation of the VCC system model. On the other hand, the number of design variables selected by the stochastic algorithm is reduced from 17 to 9, leading to a sizeable reduction in the number of objective function evaluations required to reach convergence.

6.4. RESULTS

The multi-objective optimization performed with the original version of DesOptECS, namely the one adopting the compressor meanline model embedded in Modelica, reached convergence after a total of 13050 function evaluations. The number of function evaluations reduces to 4500 when resorting to the modified version of DesOptECS, leveraging the data-driven compressor model. This enables a reduction of the total computational time from approximately 125 hours to 37.5 hours when running the optimization in parallel on a computer equipped with a Intel® Xeon® E5-1620 v3 CPU, featuring 8 logical threads. Differently from Chapter 5, the results presented in the following are computed for a single ECS pack. The Pareto front computed with the modified version of DesOptECS is displayed in Fig. 6.6. The COP of the entire ECS, see Eqn. (6.10), is reported on the x-axis of the left figure, whereas the COP of the VCC system, i.e., the ratio between the cabin cooling duty ($\dot{Q}_{cooling}$) and the electrical power required to drive the centrifugal compressor ($\dot{W}_{el,CC}$), is reported on the x-axis of the right chart. The same results are illustrated on the weight-drag, COP-weight, and COP-drag planes in Fig. 6.7.

By comparing the optimal design points identified with and without the use of the data-driven model, it is possible to observe that:

- similar trends are computed for the three objective functions, i.e., COP, weight and drag penalty;
- the range of variation of weight and drag penalty over the Pareto front identified by the two methods are comparable;

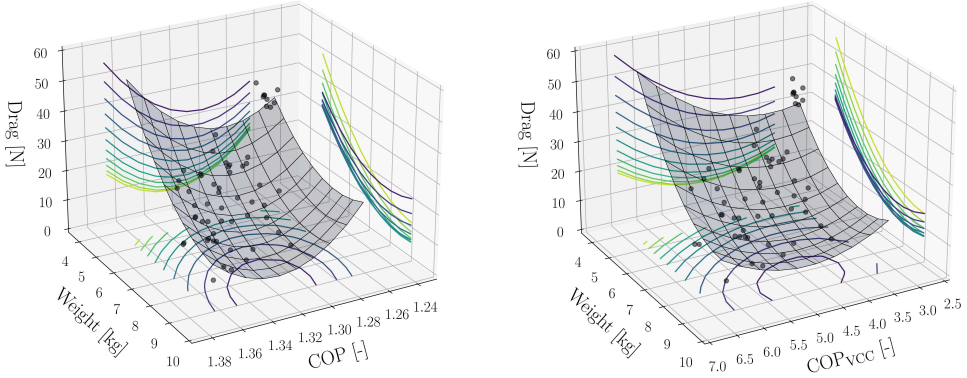


Figure 6.6: Three-dimensional Pareto front computed with the modified version of DesOptECS, embedding the data-driven compressor model. The three objective functions displayed in the figure are the weight of the CHEXs, the drag penalty, and the COP computed for the entire ECS (left) and only for the VCC system (right).

- the integration of the data-driven compressor model in DesOptECS allows to identify optimal solutions characterized by higher COP.

6

Moreover, it is important to emphasize that the Pareto front displayed in Fig. 6.6 and Fig. 6.7 differs both qualitatively and quantitatively with respect to that reported in Chapter 5 for the VCC system. This discrepancy is due to the following reasons:

- the results presented here are computed for a single ECS pack, whereas in Chapter 5 they refer to the two packs;
- the drag penalty is evaluated only for the ram air duct in this case, and the intake features a simplified model;
- only the weight of the CHEXs is accounted for in the objective function;
- the CHEXs are sized for a mild cooling requirement in cruise conditions, thus they feature lower dimensions and lower weight than those considered in Chapter 5.

Additional insights regarding the optimal VCC system configurations identified with the modified version of DesOptECS can be inferred by examining the data reported in Tab. 6.5. In particular, the table lists the design variables and the main performance metrics corresponding to the design points leading to maximum COP, minimum drag penalty, and minimum weight. Moreover, the set of design variables corresponding to the VCC system configuration leading to the minimum fuel weight penalty is reported in Tab. 6.5. In line with what is documented in Chapter 5, the fuel weight penalty associated with the ECS is computed as the sum of three contributions [14]:

- penalty due to additional weight

$$W_{f0} = W_{ECS} \left[\exp \left(\frac{SFC_{th} \tau}{L/D} \right) - 1 \right]; \quad (6.12)$$

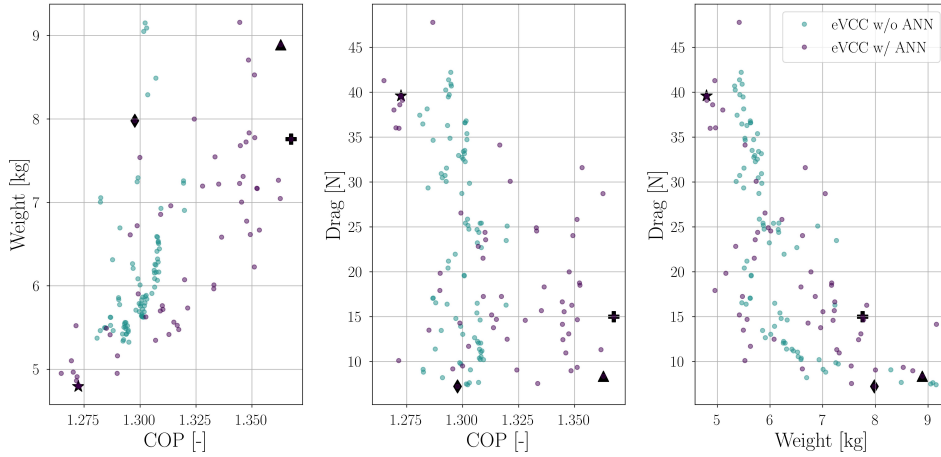


Figure 6.7: Weight, drag penalty, and COP computed with the original and the modified version of DesOptECS, embedding the data-driven compressor model. The markers identify the optimal solutions whose details are reported in Tab. 6.5.

- penalty associated with shaft power off-take

$$W_{f0} = P_{el} SFC_p \frac{L/D}{SFC_{th}} \left[\exp\left(\frac{SFC_{th}\tau}{L/D}\right) - 1 \right]; \quad (6.13)$$

- penalty associated with ram air drag

$$W_{f0} = \dot{m}_{ram} V_{air} \frac{L/D}{g} \left[\exp\left(\frac{SFC_{th}\tau}{L/D}\right) - 1 \right]. \quad (6.14)$$

The values of the parameters in Eqn. (6.12-6.14) are equal to the ones reported in Chapter 5.

By analyzing the design parameters related to the optimal VCC system configurations reported in Tab. 6.5, the following considerations can be derived. As the cabin cooling requirement is fixed, the COP of the system is inversely proportional to the power demand of the refrigerant compressor. It follows that, to maximize the COP, the pressure ratio provided by the compressor has to be minimized, as displayed in Fig. 6.8. This design choice implies that the condenser operates at a lower pressure level and its core dimensions become larger, with a consequent reduction of the pressure losses on the refrigerant side. This can be achieved by increasing the core width on the refrigerant side z_{eva} and z_{cond} , thus lowering the refrigerant velocity in the microchannels. The analysis of Fig. 6.8 reveals also the main reason for the difference in the COP computed with the original and the modified versions of DesOptECS. The use of the data-driven compressor model leads to optimal solutions featuring a wider range of β_{tt} , thus a wider range of COP values. The root cause of this difference can be arguably attributed to the higher complexity of the

Table 6.5: Most influential design variables and performance metrics corresponding to the optimal VCC system configurations selected over the Pareto front computed with the modified version of DesOptECS, embedding the data-driven compressor model. The optimal design points leading to maximum COP, minimum drag, minimum weight, and minimum fuel weight penalty are marked with different symbols.

Symbol	Type	♣ max(COP)	♦ min(drag)	★ min(weight)	▲ min(W_{f0})
\dot{m}_{ram} [kg/s]	System - variable	0.99	0.97	0.99	0.86
\dot{m}_{refr} [kg/s]	System - variable	0.19	0.19	0.22	0.19
β_{tt} [-]	System - variable	2.8	4.5	4.9	2.9
COP [-]	System - result	1.4	1.3	1.3	1.4
COP _{VCC} [-]	System - result	6.4	3.8	3.4	6.2
Weight [kg]	System - result	7.8	8.0	4.8	8.9
Drag [N]	System - result	15.0	7.2	39.6	8.4
W_{f0} [kg]	System - result	32.2	33.2	36.0	31.6
P_{el} [kW]	System - result	65.3	68.8	69.7	65.0
\dot{Q}_{eva} [kW]	System - result	32.3	32.3	32.0	32.0
\dot{Q}_{cond} [kW]	System - result	37.1	40.2	41.1	36.8
P_{eva} [bar]	System - result	2.07	1.34	2.23	2.17
P_{cond} [bar]	System - result	5.72	6.15	10.70	6.14
T_{eva} [K]	System - result	263.9	253.4	265.8	265.2
T_{cond} [K]	System - result	293.1	295.5	315.1	295.5
z_{eva} [mm]	HEX - variable	70	60	60	61
z_{cond} [mm]	HEX - variable	51	41	51	51
$A_{eva,air}$ [m ²]	HEX - result	0.10	0.08	0.11	0.12
$A_{cond,air}$ [m ²]	HEX - result	0.21	0.33	0.09	0.26
$\Delta P_{air,eva}$ [kPa]	HEX - result	2.13	2.05	1.38	1.29
$\Delta P_{air,cond}$ [kPa]	HEX - result	2.71	1.07	8.28	1.82
$\Delta P_{refr,eva}$ [kPa]	HEX - result	3.67	4.59	4.64	3.72
$\Delta P_{refr,cond}$ [kPa]	HEX - result	0.59	1.37	1.06	0.59
ϕ_{t1} [-]	RC - variable	0.07	0.10	0.06	0.05
ψ_{is} [-]	RC - variable	0.81	0.80	0.79	0.83
α_2 [deg]	RC - variable	70.1	69.5	70	67.3
η_{tt} [-]	RC - result	0.85	0.81	0.84	0.85
Ω [krpm]	RC - result	52	100	55	39
$R_{1,h}$ [mm]	RC - result	5.3	6.8	5.5	5.3
H_2 [mm]	RC - result	3.0	3.0	2.9	2.8
$\beta_{2,bl}$ [deg]	RC - result	-33.5	-33.1	-35.6	-25.7

VCC system model when embedding the compressor meanline code. This makes the solution of the underlying non-linear system of equations more susceptible to failure during the optimization process, narrowing the design space explored by the optimizer.

If the main objective is to design compact and lightweight heat exchangers, it is necessary to minimize the heat transfer surfaces, i.e., minimize the x , y , and z dimensions of the condenser and the evaporator. This can be accomplished by raising the pressure ratio provided by the refrigerant compressor, which results in an increase of the temperature lift, i.e., the difference between T_{cond} and T_{eva} . This design choice does not lead only to higher electric power consumption, but also to a larger drag penalty due to larger pressure drops in the airflow. The increase of P_{el} is exacerbated by the increment of the refrigerant mass flow rate occurring in the case of more compact heat exchanger designs, as depicted

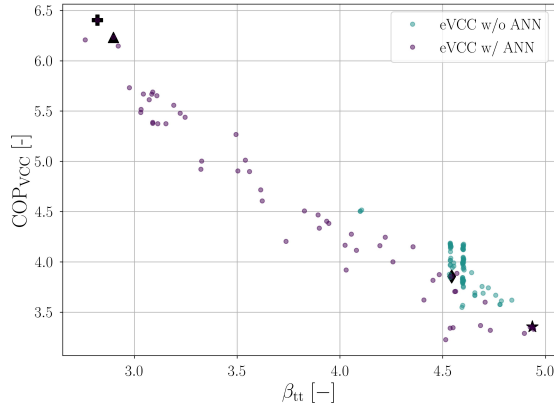


Figure 6.8: COP of the VCC system vs. total-to-total pressure ratio, computed with the original and the modified version of DesOptECS. The markers identify the optimal solutions whose main characterizing parameters are reported in Tab. 6.5.

in Fig. 6.9. This trend can be explained by observing that, given a value of evaporation pressure, the latent heat of condensation decreases with an increase in the pressure ratio and temperature lift. In turn, since the condenser heat duty does not vary significantly throughout the Pareto front, a higher refrigerant mass flow rate is required when higher values of pressure ratio are chosen.

Conversely, in order to minimize the drag penalty, the designer has to select an intermediate value of the pressure ratio and minimize the pressure drops on the ram air side. This can be achieved by increasing the condenser frontal area on the air side, i.e., $A_{\text{cond,air}} = x_{\text{cond}} \cdot y_{\text{cond}}$, which results in lower air velocity throughout the condenser, at a given mass flow rate. This argument is corroborated by the trend displayed in Fig. 6.10.

The trade-off solution leading to the minimum fuel weight penalty can be interpreted as a linear combination of the VCC system configurations associated with maximum COP and minimum drag penalty. In particular, the pressure ratio and the refrigerant mass flow rate delivered by the compressor resemble the values leading to maximum COP. In the same fashion, the frontal area of the condenser on the ram air side is close to the value associated with minimum drag penalty. Moreover, the values of the pressure drop on the refrigerant side are comparable to those leading to maximum COP, whereas the values of the pressure drop on the air side are similar to those computed for the system layout featuring minimum drag. Nevertheless, it should be noted that in real applications the ECS must be sized not only to operate at cruise conditions but also at critical operating points, such as ground operation on a very hot and humid day. To comply with such extreme cooling requirements, the heat exchangers are oversized with respect to what is reported here. Moreover, additional weight contributions, e.g., the weight of the turbomachines, can be included in Eqn. (5.43). As a result, the weight of the ECS of an actual passenger aircraft has a higher influence on the fuel weight penalty than estimated by applying the method described in this chapter, as extensively discussed in Chapter 5.

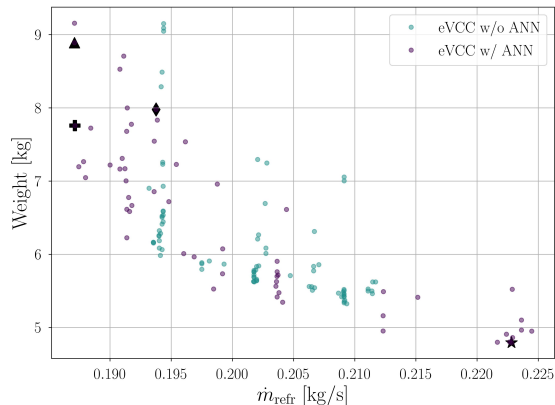


Figure 6.9: CHEXs weight vs. refrigerant mass flow rate, computed with the original and the modified version of DesOptECS. The markers identify the optimal solutions reported in Tab. 6.5.

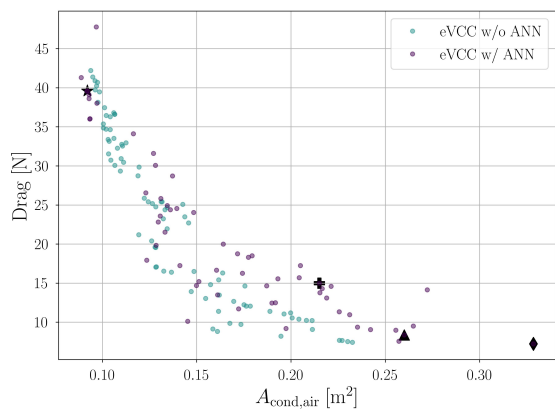


Figure 6.10: Drag penalty vs. condenser frontal area on the air side, computed with the original and the modified version of DesOptECS. The markers identify the optimal solutions reported in Tab. 6.5.

A detailed analysis of the trends relating the most influential performance metrics of the refrigerant compressor is displayed in Fig. 6.11. The values of η_{tt} depicted in the figure correspond to the internal efficiency, which only accounts for the losses occurring within the main flow passage. The external losses, e.g., the windage loss, are taken into account when calculating the power demand of the compressor. As expected, the compressor efficiency is inversely proportional to the pressure ratio. Moreover, the design points associated with ECS configurations featuring maximum COP and minimum fuel weight penalty lie in the region of maximum compressor efficiency. In general terms, an increase in the pressure ratio leads to compressor designs featuring higher values of the rotational speed. This can be mainly attributed to the need for a higher value of peripheral

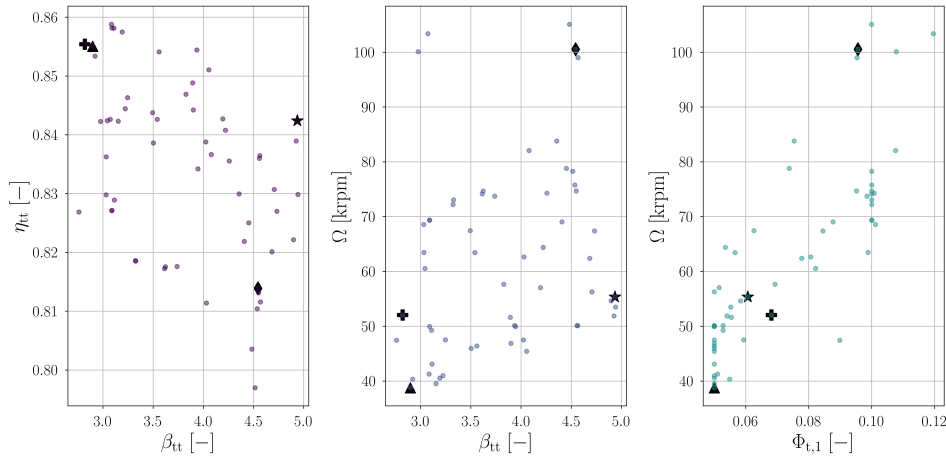


Figure 6.11: Variation of compressor efficiency and rotational speed as a function of pressure ratio, and variation of rotational speed as a function of swallowing capacity established over the Pareto front computed with the data-driven model. The markers identify the optimal solutions reported in Tab. 6.5.

speed to achieve a higher specific work. The ECS configuration featuring the compressor with the highest rotational speed is the one leading to minimum drag. This can be explained by the fact that the compressor weight is not taken into account in the objective function and by the fact that the evaporating pressure P_{eva} is lower at the compressor inlet. In turn, this leads to a higher volumetric flow rate processed by the compressor, and, consequently, to a higher swallowing capacity selected by the optimizer. As documented in [5], higher values of $\Phi_{t,1}$ are associated with higher rotational speeds, but also with lower values of the operating range, thus limiting the operating envelope of the VCC system. To overcome this issue, in the modified version of DesOptECS, the compressor optimization has been performed by setting a linear combination of η_{tt} and OR as one of the objective functions. As a result, the values of swallowing capacity selected by the optimizer are not clustered around the region of optimal compressor efficiency but are spread between the range 0.05-0.12, leading to a trade-off between efficiency and operating range for the values of pressure ratio under analysis.

To conclude this study, a sensitivity analysis of the objective functions with respect to the prescribed set of design variables was performed. The purpose was to assess the robustness of the obtained optimal solutions with respect to changes in the values of the design variables, as well as to identify those variables which mostly affect the objective functions. The analysis was carried out as follows. First, five design points were selected over the Pareto front computed with the modified version of DesOptECS. Then, a perturbation of $\pm 10\%$ was applied to each design variable independently, and the vector of objective functions was re-evaluated. This process was repeated for each prescribed design point, and the averaged results are displayed in Fig. 6.12. The sensitivity of the objective functions is evaluated with respect to the compressor efficiency η_{tt} , rather than to the compressor design variables α_c . Moreover, the COP of the ECS is replaced with the COP of

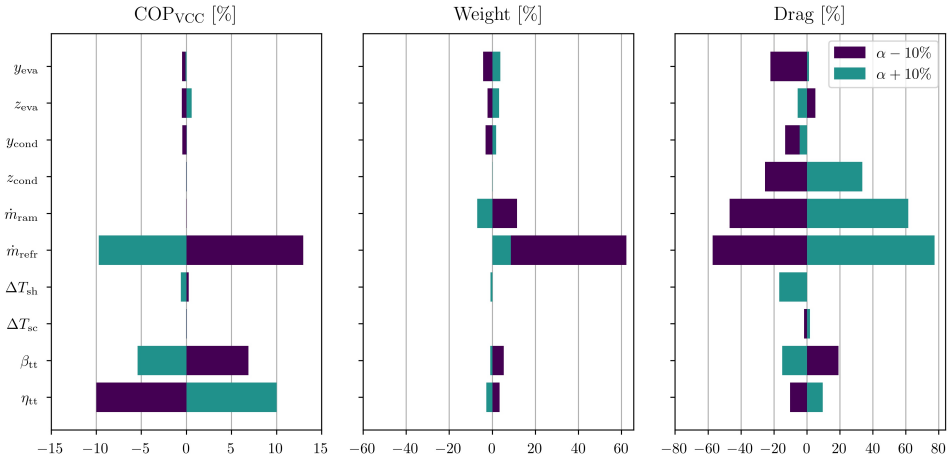


Figure 6.12: Sensitivity of the objective functions with respect to a $\pm 10\%$ perturbation in the vector of design variables.

the VCC system, since the COP of the ECS is mainly affected by the terms $\dot{W}_{p,id}$ and $\dot{W}_{el,CAC}$ in Eqn. (6.10), whose values are almost constant.

The outcomes of the sensitivity analysis can be summarized as follows. The COP shows the highest sensitivity with respect to the mass flow rate of the refrigerant, and to the pressure ratio and the efficiency of the refrigerant compressor. The weight of the CHEXs is mostly affected by the mass flow rates of refrigerant and ram air. The value of drag penalty is mostly sensitive to \dot{m}_{refr} , \dot{m}_{ram} , z_{cond} , y_{eva} , and β_{tt} . As a result, the computational cost of the optimization process can be further reduced by removing z_{eva} , y_{cond} , ΔT_{sh} , and ΔT_{sc} from the vector of design variables, without significantly affecting the optimal solutions. Moreover, the COP of the optimal designs shows a variation of the order of $\pm 10\%$ when changing the values of the compressor efficiency and the refrigerant mass flow rate by the same order of magnitude. These results corroborate the consideration that the compressor is one of the most critical components of the VCC system, and highlight the need of performing its conceptual design along with that of the system.

6.5. CONCLUSIONS

This chapter documents a novel methodology for the integrated design optimization of aircraft ECS, based on the electrically-driven VCC system. The main novelty lies in the integration of a data-driven compressor model into the optimization procedure. This allows for both a reduction of the computational cost associated with the solution of the optimization problem and for an increase in the robustness of the numerical solver used to size and evaluate the performance of the ECS. The case study selected to demonstrate the capabilities of the proposed methodology is the multi-objective design optimization of an electrically-driven VCC system for the ECS of a single-aisle, short-haul aircraft, flying at cruise conditions. The prescribed objectives are the maximization of the system COP,

the minimization of the weight of the heat exchangers, and the minimization of the drag penalty associated with the ram airflow. The optimization has been performed with and without the use of the data-driven compressor model, to highlight the advantages offered by the proposed methodology. The main outcomes can be summarized as follows.

1. A data-driven compressor model can be developed using a dataset of about 165k compressor designs. The number of design variables used to create the dataset is relatively small, thanks to the adoption of a non-dimensional approach based on scaling principles. To enhance the accuracy of the data-driven model, and to facilitate its integration into the ECS optimization framework, two MLP models have been trained to predict the compressor performance parameters and the relevant geometrical constraints. The mean absolute percentage error of the two MLP models evaluated on the test set is 2.32% and 0.72%, respectively.
2. The complexity of the VCC system model, and the likelihood of an ill-conditioned matrix when the associated mathematical problem is solved, can be reduced by replacing the meanline model of the high-speed centrifugal compressor with a data-driven surrogate model. A similar approach could be adopted to replace also the models of the compact heat exchangers.
3. The use of a data-driven model enables the partial decoupling between the optimization of the VCC system and the compressor. For each set of system design variables selected by the stochastic algorithm, the compressor design variables are optimized by resorting to a constrained gradient-based algorithm. The computational cost associated with compressor optimization is negligible, thanks to the use of a pre-trained data-driven model. As a result, the number of design variables selected by the stochastic algorithm drops from 17 to 9, and the number of function evaluations needed to identify the Pareto front reduces from 13050 to 4500.
4. The objective functions selected for the optimization of the VCC system are in trade-off. In particular, the use of very compact heat exchangers leads to higher drag penalties. Nevertheless, it is possible to achieve a lightweight design of the heat exchangers, without incurring in large drag penalties, at the expense of a reduction in the COP. The range of variation of the objective functions and the variations among them remain virtually unaltered, regardless of the adopted compressor model. Moreover, the modified framework can identify optimal solutions over a wider design space, thanks to the improved robustness of the underlying VCC system model.
5. The results show that the ram airflow and the condenser thermal load do not vary significantly over the Pareto front. Therefore, the use of heavier condenser units, featuring a larger frontal area on the ram air side, leads to a reduction of the drag penalty. On the other hand, the adoption of compact and lightweight heat exchangers requires a higher temperature lift and a higher refrigerant mass flow rate to comply with the prescribed heat duty.
6. An increase in the temperature lift of the VCC system produces a rise in the pressure ratio of the refrigerant compressor. In turn, this leads to a rapid deterioration

of the compressor efficiency and to an increase in the rotational speed. A higher rotational speed, thus a more compact compressor design, can be also attained by increasing the value of the swallowing capacity. However, this comes at the expense of a reduced operating range.

7. As pointed out by a sensitivity analysis, the computational cost of the optimization process can be further reduced by removing z_{eva} , y_{cond} , ΔT_{sh} , and ΔT_{sc} from the vector of design variables, without significantly affecting the solution. Furthermore, the analysis shows that the COP of the VCC system is mostly influenced by the compressor efficiency. This demonstrates the need for an integrated design optimization methodology embedding a model for the conceptual design of the compressor.

The results of this research showcase the large potential of adopting data-driven models for the simultaneous optimization of the ECS and the preliminary design of its components. The substantial reduction of the computational cost associated with the optimization process, combined with the improved robustness of the underlying system model, make this approach suitable for large-scale, industrial-strength energy system design problems. Future works will target the improvement of the data-driven compressor model by extending the dataset with additional working fluids and thermodynamic conditions. Furthermore, the proposed integrated design methodology will be applied to assess the performance of different non-conventional ECS architectures over multiple operating points.

NOMENCLATURE

Roman symbols

A	Surface area [m ²]
F_{ax}	Axial thrust [N]
g	Gravitational acceleration [m/s ²]
H	Blade height [m]
h	Specific enthalpy [J kg ⁻¹]
k	Impeller shape factor [-]
L	Loss function [-]
L/D	Lift to drag ratio [-]
\dot{m}	Mass flow rate [kg s ⁻¹]
Ma	Mach number [-]
N	Fluid molecular complexity [-]
n	Number of samples [-]
OR	Operating range [-]
P	Pressure [Pa]
\dot{Q}	Heat flow rate [W]
R	Radius [m]
Re	Reynolds number [-]
SFC_{th}	Thrust specific fuel consumption [lb/(h.lbf)]
SFC_P	Power specific fuel consumption [lb/(hp.h)]
T	Temperature [K]
\dot{V}	Volumetric flow rate [m ³ s ⁻¹]
U	Peripheral speed [m s ⁻¹]
V	Absolute velocity [m s ⁻¹]
\dot{W}	Power [W]
W	Weight [kg]
W_{f0}	Fuel weight penalty [kg]
x	Width [m]
Y	Vector of true labels [-]
\hat{Y}	Vector of model predictions [-]
y	Height [m]
z	Depth [m]

Greek symbols

α	Absolute flow angle [°]
$\boldsymbol{\alpha}$	Vector of design variables [-]
β	Pressure ratio [-]
γ_{Pv}	Isentropic pressure-volume exponent [-]
ϵ_b	Back face clearance [m]
ϵ_t	Tip clearance gap [m]
η	Efficiency [-]
$\boldsymbol{\theta}$	Vector of hyperparameters [-]
Φ_{t1}	Swallowing capacity [-]
ψ_{is}	Isentropic loading coefficient [-]

ρ	Density [kg m ⁻³]
τ	Aircraft mission time [h]
Ω	Rotational speed [rpm]

Subscripts

1	Impeller inlet
2	Impeller outlet
3	Diffuser outlet
4	Volute outlet
bl	Blade
cond	Condensation
el	Electrical
eva	Evaporation
ext	External
h	Hub
is	Isentropic
ram	Ram air stream
refr	Refrigerant stream
ts	Total-to-static
tt	Total-to-total

Abbreviations

ACM	Air Cycle Machine
ANN	Artificial Neural Network
CAC	Cabin Air Compressor
CHEX	Compact Heat Exchanger
CO ₂	Carbon Dioxide
COP	Coefficient Of Performance
con	Constraints
DeSimECS	Design and Simulation of Energy Conversion Systems
DesOptECS	Design Optimization of Energy Conversion Systems
ECS	Environmental Control System
FV	Finite Volume
H ₂	Hydrogen
HEX	Heat Exchanger
MB	Moving Boundary
MLP	Multi-Layer Perceptron
mae	Mean absolute error
mape	Mean absolute percentage error
obj	Objectives
pp	Pinch point
R-1233zd(E)	Trifluoropropene
R-134a	Tetrafluoroethane
VCC	Vapor Compression Cycle

BIBLIOGRAPHY

- [1] V. Mounier, C. Picard, and J. Schiffmann, “Data-Driven Predesign Tool for Small-Scale Centrifugal Compressor in Refrigeration”, *Journal of Engineering for Gas Turbines and Power*, vol. 140, no. 12, Dec. 2018, ISSN: 15288919. DOI: 10.1115/1.4040845/457767.
- [2] F. Ascione, C. M. De Servi, O. Meijer, V. Pommé, and P. Colonna, “Assessment of an inverse organic rankine cycle system for the ecs of a large rotorcraft adopting a high-speed centrifugal compressor and a low GWP refrigerant”, in *Proceedings of the 6th International Seminar on ORC Power Systems*, Technical University of Munich, 2021. DOI: 10.14459/2021mp1633127.
- [3] P. Colonna and A. Guardone, “Molecular interpretation of nonclassical gas dynamics of dense vapors under the van der Waals model”, *Physics of Fluids*, vol. 18, no. 5, p. 056 101, May 2006, ISSN: 1070-6631. DOI: 10.1063/1.2196095.
- [4] D. A. Kouremenos and X. K. Kakatsios, “The three isentropic exponents of dry steam”, *Forschung im Ingenieurwesen*, vol. 51, no. 4, pp. 117–122, Jul. 1985, ISSN: 00157899. DOI: 10.1007/BF02558416.
- [5] A. Giuffré, P. Colonna, and M. Pini, “The Effect of Size and Working Fluid on the Multi-Objective Design of High-Speed Centrifugal Compressors”, *International Journal of Refrigeration*, vol. 143, pp. 43–56, Nov. 2022, ISSN: 0140-7007. DOI: 10.1016/J.IJREFRIG.2022.06.023.
- [6] C. Audet, S. Le Digabel, and C. Tribes, “The Mesh Adaptive Direct Search Algorithm for Granular and Discrete Variables”, *Journal on Optimization*, vol. 29, no. 2, pp. 1164–1189, Apr. 2019, ISSN: 10526234. DOI: 10.1137/18M1175872.
- [7] C. Audet, S. Le Digabel, V. Rochon Montplaisir, and C. Tribes, “Nomad version 4: Nonlinear optimization with the mads algorithm”, *Les cahiers du GERAD*, Tech. Rep., 2021, G–2021–23.
- [8] M. Abadi, A. Agarwal, P. Barham, et al., *TensorFlow: Large-Scale Machine Learning on Heterogeneous Systems*, 2015. [Online]. Available: <https://www.tensorflow.org/>.
- [9] M. Sielemann, T. Giese, B. Oehler, and M. Gräber, “Optimization of an Unconventional Environmental Control System Architecture”, *SAE International Journal of Aerospace*, vol. 4, no. 2, pp. 1263–1275, Oct. 2011, ISSN: 1946-3855. DOI: 10.4271/2011-01-2691.
- [10] G. Schweiger, H. Nilsson, J. Schoeggel, W. Birk, and A. Posch, “Modeling and simulation of large-scale systems: A systematic comparison of modeling paradigms”, *Applied Mathematics and Computation*, vol. 365, Jan. 2020, ISSN: 0096-3003. DOI: 10.1016/J.AMC.2019.124713.
- [11] J. Blank and K. Deb, “Pymoo: Multi-Objective Optimization in Python”, *IEEE Access*, vol. 8, pp. 89 497–89 509, 2020. DOI: 10.1109/ACCESS.2020.2990567.
- [12] K. Deb, A. Pratap, S. Agarwal, and T. Meyarivan, “A fast and elitist multiobjective genetic algorithm: NSGA-II”, *IEEE Transactions on Evolutionary Computation*, vol. 6, no. 2, pp. 182–197, Apr. 2002. DOI: 10.1109/4235.996017.
- [13] D. Kraft, “A software package for sequential quadratic programming”, DLR German Aerospace Center – Institute for Flight Mechanics, Koln, Germany, Tech. Rep., 1988.
- [14] SAE, *Aircraft fuel weight penalty due to air conditioning*, Jun. 2004. DOI: 10.4271/AIR1168/8.

7

CONCLUSION

The optimal design of a complex energy conversion system, such as the Environmental Control System (ECS) of passenger aircraft, is a challenging problem whereby the characteristics of the thermodynamic cycle and the preliminary sizing of the main components are very interdependent and must be concurrently optimized. Moreover, in case of energy conversion systems for aerospace applications, the optimal design results from the trade-off between the minimization of the power consumption, system weight, and drag penalty. Furthermore, differently from stationary refrigeration systems, the ECS must guarantee safe and reliable operation over a much wider operating envelope depending on variable flight phases and environmental conditions. As a result, from a mathematical standpoint, evaluating novel ECS concepts implies solving a multi-objective, multi-point, integrated design optimization problem.

This dissertation documents research work on integrated design optimization methods tailored to the ECS of next-generation aircraft. The objective is the evaluation of a new ECS technology, namely an electrically-driven Vapor Compression Cycle (VCC) system powered by an oil-free high-speed centrifugal compressor, and the comparison of its performance with respect to those of the traditional Air Cycle Machine (ACM). This work is part of a larger research program involving both academic and industrial partners aiming to mature the airborne VCC technology and to bring it to the market of large passenger aircraft and helicopters. To fulfill this purpose, two main research areas have been identified and addressed in this dissertation:

- the advancement of the state-of-the-art regarding high-speed oil-free centrifugal compressors, i.e., the most critical components of airborne VCC systems;
- the development of an automated integrated design framework for aircraft ECS, suitable for both ACM and VCC-based configurations, embedding a multi-point and multi-objective optimization strategy.

Based on the results of this work, the following main conclusions can be drawn.

High-speed centrifugal compressors

1. Novel design guidelines for single-stage and twin-stage centrifugal compressors have been devised based on the results computed with an in-house compressor model validated with experimental data and CFD simulations. The results of multiple design optimization case studies corroborate the validity of the proposed design guidelines.
2. High-speed compressor stages operating with working fluids made of heavy and complex molecules are less efficient if compared to compressor stages for fluids made of simpler molecules. However, compressor stages operating with complex-molecule fluids produce lower axial thrust if compared to their simple-molecule counterparts, thus making them particularly suitable for the use of oil-free gas bearings.
3. High-speed compressors featuring small size are characterized by lower efficiency, as a result of manufacturing constraints, leading to higher relative tip clearance and higher relative surface roughness. This effect is partly mitigated when using working fluids characterized by lower density, thus leading to the design of larger flow passages. Moreover, the efficiency penalty is more sensitive to variations of clearance gap than to surface finishing.
4. According to the developed design guidelines, twin-stage centrifugal compressors, featuring two impellers mounted in back-to-back configuration on the same shaft, and running on oil-free gas bearings, can achieve pressure ratios higher than 10 with overall efficiency values exceeding 65%. The higher efficiency, combined with the wide operating range and lower weight, as compared to volumetric machines of equivalent power rating, are deemed key enablers for the adoption of VCC systems for airborne applications.
5. The optimal conceptual design of twin-stage compressors is such that the first stage features a higher pressure ratio and a value of swallowing capacity which can be more than double that of the second stage. This combination of the non-dimensional parameters enhances the efficiency of the entire compression process, without penalizing the operating range.

Integrated design optimization of novel ECS configurations

1. A dynamic thermal model of the air distribution system and the pressurized compartments of a passenger aircraft has been developed and validated with proprietary data provided by one of the industrial partners, i.e., Airbus. The model can be applied to characterize the operating envelope of the ECS, given limited information about the aircraft type and the flight mission. This information can be used to define the design specifications for the optimization of the ECS. The model will be released open-source upon publication of Chapter 4 of this dissertation.
2. A novel design methodology for energy conversion systems, integrating the optimization of the thermodynamic cycle and the preliminary sizing of its main components, has been developed and applied for the evaluation of a new technology for

the ECS of passenger aircraft. The optimal design framework has been successfully utilized to compare the performance of an ECS based on a bleedless ACM and an electrically-driven VCC system for an Airbus A320. The main novelty lies in the implementation of a multi-point and multi-objective strategy, which simultaneously optimizes the design variables related to the system, heat exchangers, and turbomachinery components.

3. For the prescribed aircraft configuration, the ECS based on the electrically-driven VCC system equipped with a high-speed twin stage radial compressor can be both lighter and more energy-efficient than the state-of-the-art bleedless ACM architecture. However, if compared to the most compact ACM designs, the VCC system is characterized by a higher average drag penalty. Overall, the fuel weight penalty associated with the optimal VCC system configuration is approximately 20% lower than the one of the bleedless ACM. In the light of these results, the electrically-driven VCC system is envisaged to become the state-of-the-art ECS technology in next-generation aircraft, pending experimental verification and validation.
4. The VCC system design leading to the minimum fuel weight penalty corresponds to the design point associated with the minimum electric power consumption and drag penalty. This result is obtained by maximizing the frontal area of the evaporator and the condenser. Conversely, the minimization of the fuel weight penalty related to the bleedless ACM is primarily driven by the minimization of the system weight.
5. A data-driven model for single-stage centrifugal compressors has been successfully trained on a synthetic dataset of about 165k compressor designs. The data-driven model has been integrated within the design optimization framework to improve the robustness of the VCC system model and reduce the computational cost associated with the optimization. A benchmark performed on a simple VCC system configuration shows that the number of function evaluations needed to identify the Pareto front of optimal solutions reduces from 13050 to 4500 when adopting the data-driven model. A similar approach could be adopted to replace also the models of the compact heat exchangers, or any other complex component model.

7.1. LIMITATIONS AND RECOMMENDATIONS

The main limitations of this work are outlined in the following, together with recommendations to address them in future research projects.

1. The model for single-stage and twin-stage centrifugal compressors documented in Chapters 2-3 does not account for the rotor-dynamic analysis of the impeller-shaft assembly supported by gas bearings. However, the absence of rotor-dynamic calculations in the preliminary design phase may lead to the detection of unfeasible designs during the detailed design phase, and thus to additional time-consuming design iterations. This risk can be significantly mitigated by including a rotor-dynamic model based on first principles in the compressor conceptual design tool.
2. The integrated design optimization of the ACM and VCC system includes only the main turbomachinery devices, i.e., the cabin air compressor and the refrigerant

compressor. However, to further refine the analysis, also the design variables of the ACM compressor and turbine, as well as those related to the cabin air turbine of the VCC system, should be integrated into the optimization. Additionally, all the turbomachinery components, together with the condenser and re-heater of the bleedless ACM, should be accounted for in the weight estimation of the system.

3. The design optimization of the VCC system presented in Chapter 5 has been performed by assuming that refrigerant R134a is the working fluid. However, with the present implementation, replacing the working fluid requires a manual modification of the VCC system model and a restart of the optimization procedure. The next version of the design optimization framework should allow for the input and the optimization of the thermo-physical properties of the working fluid with minimal user interaction.
4. The design optimization of the VCC system presented in Chapter 5 includes only the design variables describing the main dimensions of the condenser and the evaporator. Conversely, the design variables controlling the shape of the fins and tubes have been set to fixed values, to reduce the computational cost. However, they might have a non-negligible influence on the optimization results. Therefore, in future studies, it is recommended to perform a sensitivity analysis before selecting the list of active design variables and performing the optimization.
5. The dataset used to train the data-driven compressor model in Chapter 6 includes only one operating point for each of the prescribed working fluids, with the exception of refrigerants R134a and R1233zd(E), which feature two operating points. However, to further reduce bias in the dataset and increase the range of applicability of the data-driven model, the dataset should be extended by including multiple operating conditions for each working fluid.

7.2. OUTLOOK

Based on the experience gained during this research project, the author envisages the following possibilities to further extend this work.

1. The methodology developed for the fluid dynamic design of centrifugal compressors can be further extended by resorting to CFD-based shape optimization. The outcome of the second design iteration of the IRIS compressor can be used as a baseline to quantify the performance gain achievable by means of more advanced design methods.
2. The performance benchmark presented in Chapter 5 demonstrates the potential fuel savings achievable by adopting a VCC system in place of the bleedless ACM for the ECS of an Airbus A320. However, only one VCC system configuration and one working fluid have been analyzed. Future studies could make use of the integrated design method developed in this work to evaluate the performance of more advanced VCC system architectures, e.g., featuring multiple pressure levels, and hybrid ACM-VCC system configurations, while treating the working fluid as an additional design variable.

3. The models of the most critical components of the VCC system, i.e., condenser, evaporator, and centrifugal compressor, have been validated individually with experimental data available in the literature. However, after the commissioning of the IRIS test rig with the centrifugal compressor, the model of the entire VCC system should be validated with experimental data retrieved from the novel facility. The direct validation of the VCC system model would augment the confidence in the results documented in this work.
4. The problem of the computational cost associated with optimization studies featuring a large number of design variables and non-linear constraints is discussed in Chapter 6. As documented, a possible solution to mitigate this issue is to model the most complex components of the system by resorting to a data-driven approach. An alternative solution consists in improving the convergence rate of the optimization algorithm, i.e., by using a surrogate-based approach. Future studies could apply an online data-driven approach to create and progressively refine surrogate models used to speed up the optimization.
5. The data-driven model developed in this study and documented in Chapter 6 is only valid for single-stage centrifugal compressors. However, as discussed in Chapter 5, the temperature lift, thus the pressure ratio, characterizing VCC systems used for aircraft ECS applications requires the use of multi-stage compressors. Therefore, future research efforts should be focused on extending the validity of the data-driven model to twin-stage compressors and applying it to test cases of industrial interest.

A

SOLAR RADIATION

A.1. CLEAR-SKY SOLAR RADIATION

The solar constant E_{sc} is defined as the intensity of solar radiation on a surface normal to the sun's rays, just beyond the atmosphere, at the average earth-sun distance. The value of the solar constant used in this work is the one proposed by the World Meteorological Organization in 1981, i.e., $E_{sc} = 1367 \text{ W m}^{-2}$ [1]. The extraterrestrial radiant flux E_0 varies throughout the year since the earth's orbit is slightly elliptical. Its value can be approximated as

$$E_0 = E_{sc} \left(1 + 0.033 \cos \left(2\pi \frac{n-3}{365} \right) \right), \quad (\text{A.1})$$

where n is the day of the year.

The earth's orbital velocity also varies throughout the year, so the apparent solar time (AST) varies from the time measured by a clock running at a uniform rate. This variation is quantified by the equation of time (ET), which reads

$$\text{ET} = 2.2918(0.0075 + 0.1868 \cos \Gamma - 3.2077 \sin \Gamma - 1.4615 \cos 2\Gamma - 4.089 \sin 2\Gamma), \quad (\text{A.2})$$

where ET is expressed in minutes and

$$\Gamma = 360^\circ \frac{n-1}{365}. \quad (\text{A.3})$$

The conversion between Local Standard Time (LST) and apparent solar time involves also a longitude correction. This corresponds to four minutes per degree difference between the local site longitude and the longitude of the Local Standard Meridian (LSM) for the prescribed time zone. Hence the AST can be computed as

$$\text{AST} = \text{LST} + \frac{\text{ET}}{60} + \frac{\text{LON} - \text{LSM}}{15}. \quad (\text{A.4})$$

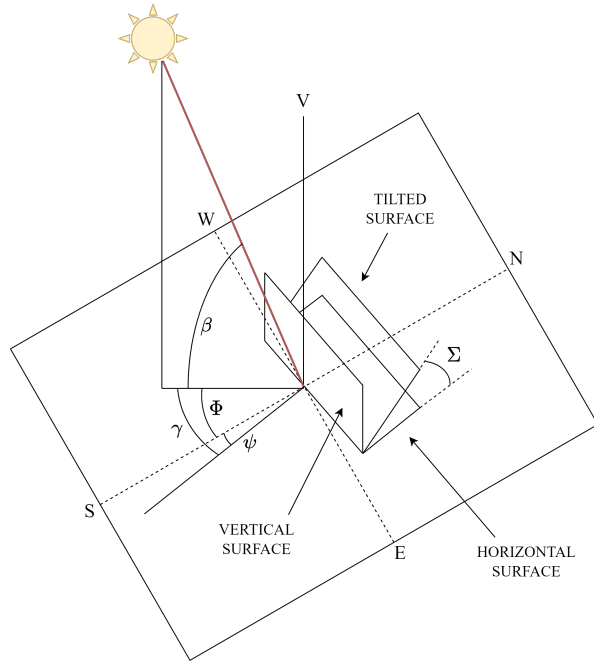


Figure A.1: Angles formed by solar radiation incident on a tilted surface.

The angle between the earth/sun line and the equatorial plane, called solar declination δ , varies throughout the year since the earth's equatorial plane is tilted with respect to the orbital plane. This variation causes the changing seasons with their unequal periods of daylight and darkness. For most engineering applications, the following equation provides sufficient accuracy

$$\delta = 23.45^\circ \sin \left(360^\circ \frac{n + 284}{365} \right). \quad (\text{A.5})$$

The sun's position in the sky can be conveniently expressed in terms of solar altitude and azimuth. With reference to Fig. A.1, the solar altitude angle β is defined as the angle between the horizontal plane and a line emanating from the sun. Its value ranges from 0° when the sun is on the horizon, to 90° if the sun is directly overhead. The solar azimuth angle Φ is defined as the angular displacement from the south of the horizontal projection of the earth/sun line. In turn, solar altitude and azimuth angles depend on the local latitude LAT , the solar declination δ , and the hour angle H , expressed as

$$H = 15(AST - 12). \quad (\text{A.6})$$

The azimuth angle is uniquely determined by its sine and cosine, given by

$$\begin{aligned}\sin \Phi &= \frac{\cos \delta \sin H}{\cos \beta}, \\ \cos \Phi &= \frac{\cos \delta \cos H \sin \text{LAT} - \sin \delta \cos \text{LAT}}{\cos \beta}.\end{aligned}\tag{A.7}$$

Solar radiation on a clear day is defined by its direct and diffuse components. The former represents the solar radiation emanating directly from the solar disc, whereas the diffuse component accounts for radiation emanating from the rest of the sky. These two components are calculated as

$$\begin{aligned}E_b &= E_0 e^{-\tau_b m^{ab}}, \\ E_d &= E_0 e^{-\tau_d m^{ad}}.\end{aligned}\tag{A.8}$$

Values of τ_b and τ_d are location-specific, and vary during the year. They embody the dependence of clear-sky solar radiation on local conditions, such as elevation, precipitable water content, and aerosols. Their average values have been determined at prescribed locations through ASHRAE research projects RP-1453 [2] and RP-1613 [3]. Air mass exponents ab and ad are correlated to τ_b and τ_d through the following empirical relationships

$$\begin{aligned}ab &= 1.454 - 0.406\tau_b - 0.268\tau_d + 0.021\tau_b\tau_d, \\ ad &= 0.507 + 0.205\tau_b - 0.080\tau_d - 0.190\tau_b\tau_d.\end{aligned}\tag{A.9}$$

The relative air mass m corresponds to the ratio between the mass of the air column in the actual earth/sun path and the one computed assuming that the sun is directly overhead. It can be computed according to [4]

$$m_0 = \frac{1}{\sin \beta + 0.50572(6.07995 + \beta)^{-1.6364}},\tag{A.10}$$

where the subscript 0 indicates that the receiving object is at ground level. Conversely, if the receiver is flying at high altitude, the relative air mass must be corrected as follows [5]

$$m = m_0 \left(\frac{T_{\text{amb}} - 0.0065z}{T_{\text{amb}}} \right)^{5.2561}.\tag{A.11}$$

A.2. SOLAR RADIATION ON A RECEIVING SURFACE

The orientation of a receiving surface is characterized by the tilt angle and azimuth. The tilt angle Σ is the angle between the surface and the horizontal plane. A value of 0° corresponds to a horizontal plane, whereas a value of 90° represents a vertical surface. The surface azimuth ψ is defined in the same fashion as for the sun's position. Surfaces that face west have a positive surface azimuth; those that face east have a negative surface azimuth. The surface-solar azimuth angle γ is defined as the angular difference between

the solar azimuth and the surface azimuth: $\gamma = \Phi - \psi$. Values of γ greater than 90° or lower than -90° indicate that the surface is in the shade. Finally, the angle between the earth-sun line and the normal to the irradiated surface is called the incidence angle and is computed as

$$\cos \theta = \cos \beta \cos \gamma \sin \Sigma + \sin \beta \cos \Sigma. \quad (\text{A.12})$$

The total clear-sky irradiance reaching the receiving surface can be expressed as the sum of three components: the beam component $E_{t,b}$ originating from the solar disc, the diffuse component $E_{t,d}$, originating from the sky dome, and the ground-reflected component $E_{t,r}$ originating from the ground in front of the receiving surface

$$E_t = E_{t,b} + E_{t,d} + E_{t,r}. \quad (\text{A.13})$$

Once the incidence angle is known, the beam component can be simply computed as

$$E_{t,b} = E_b \cos \theta. \quad (\text{A.14})$$

If $\cos \theta \leq 0$, the beam component is null. The diffuse component is more difficult to estimate because of the non-isotropic nature of the diffuse radiation. For vertical surfaces, it can be approximated according to [6]

$$E_{t,d} = E_d Y, \quad (\text{A.15})$$

where

$$Y = \max(0.45, 0.55 + 0.437 \cos \theta + 0.313 \cos^2 \theta). \quad (\text{A.16})$$

For a non-vertical surface, the diffuse component can be approximated with the following simplified relationships

$$\begin{aligned} E_{t,d} &= E_d (Y \sin \Sigma + \cos \Sigma) & \text{if } \Sigma \leq 90^\circ, \\ E_{t,d} &= E_d Y \sin \Sigma & \text{if } \Sigma > 90^\circ, \end{aligned} \quad (\text{A.17})$$

where Y is calculated for a vertical surface having the same azimuth as the prescribed receiving surface. Finally, the ground-reflected irradiance for surfaces of all orientations is given by

$$E_{t,r} = \rho_g (E_b \sin \beta + E_d) \frac{1 - \cos \Sigma}{2}, \quad (\text{A.18})$$

where ρ_g is the ground reflectance, and is often assumed to be equal to 0.2 for a typical mixture of ground surfaces.

NOMENCLATURE

Roman symbols

A	Surface area [m^2]
E	Irradiance [W m^{-2}]
E_0	Extraterrestrial radiant flux [W m^{-2}]
E_{sc}	Solar constant [W m^{-2}]
H	Hour angle [deg]
m	Relative air mass [-]
m_0	Relative air mass on ground [-]
n	Day of the year [-]
	Refractive index [-]
\dot{Q}	Heat flow rate [W]
r	Reflection coefficient [-]
T	Temperature [K]
t	Transmittance [-]
z	Altitude [m]

Greek symbols

β	Solar altitude angle [deg]
Γ	Day correction [-]
γ	Surface-solar azimuth angle [deg]
δ	Solar declination [deg]
θ	Incidence angle [deg]
ρ	Ground reflectance [-]

Σ	Tilt angle [deg]
τ	Location-specific irradiance coefficients [-]
Φ	Solar azimuth angle [deg]
ψ	Receiving surface azimuth angle [deg]

Subscripts

a	Absorbed component
b	Direct beam component
d	Diffuse component
p	P-polarized light
r	Reflected component
s	S-polarized light
t	Component acting on the receiver surface
tr	Transmitted component

Abbreviations

AST	Apparent solar time
ET	Equation of time
LAT	Site latitude
LSM	Local standard meridian
LST	Local standard time
LON	Site longitude

BIBLIOGRAPHY

- [1] M. Iqbal, "Chapter 3 - the solar constant and its spectral distribution", in *An Introduction to Solar Radiation*, Academic Press, 1983, pp. 43–58, ISBN: 978-0-12-373750-2. DOI: 10.1016/B978-0-12-373750-2.50008-2.
- [2] D. Thevenard, "Updating the ashrae climatic data for design and standards (rp-1453)", ASHRAE, Tech. Rep., 2009.
- [3] D. Thevenard and C. A. Gueymard, "Updating climatic design data in the 2013 ashrae handbook—fundamentals (rp-1613)", ASHRAE, Tech. Rep., 2009.
- [4] F. Kasten and A. T. Young, "Revised optical air mass tables and approximation formula", *Applied Optics*, vol. 28, no. 22, pp. 4735–4738, Nov. 1989. DOI: 10.1364/AO.28.004735.
- [5] G. S. Aglietti, S. Redi, A. R. Tatnall, and T. Markvart, "Harnessing high-altitude solar power", *IEEE Transactions on Energy Conversion*, vol. 24, no. 2, pp. 442–451, 2009. DOI: 10.1109/TEC.2009.2016026.
- [6] D. Stephenson, "Equations for solar heat gain through windows", *Solar Energy*, vol. 9, no. 2, pp. 81–86, 1965, ISSN: 0038-092X. DOI: 10.1016/0038-092X(65)90207-0.

B

AIRBUS A320 TECHNICAL SPECIFICATIONS

The technical data used in Chapter 4 and related to the Airbus A320 is reported here for the sake of reproducibility of results. However, the data has not been disclosed by the industrial partner Airbus due to confidentiality, but rather collected from different sources available in the scientific literature and in technical manuals. Therefore, the data reported in this appendix may be inaccurate or outdated.

Table B.1: General dimensions of Airbus A320 [1]–[4].

Cockpit		Cabin		Underfloor	
R_{cpt} [m]	2.07	R_{cab} [m]	2.07	$L_{\text{cargo,fwd}}$ [m]	4.95
L_{cpt} [m]	3.5	L_{cab} [m]	26.9	$L_{\text{cargo,aft}}$ [m]	9.8
V_{cpt} [m ³]	9	V_{cab} [m ³]	139	L_{EEbay} [m]	4
$A_{\text{cpt,int}}$ [m ²]	8	$A_{\text{cab,int}}$ [m ²]	360	$V_{\text{cargo,fwd}}$ [m ³]	15.56
$m_{\text{cpt,int}}$ [kg]	80	$m_{\text{cab,int}}$ [kg]	3600	$V_{\text{cargo,aft}}$ [m ³]	20.77
$c_{\text{cpt,int}}$ [J/kg]	1000	$c_{\text{cab,int}}$ [J/kg]	1000	V_{EEbay} [m ³]	9
$L_{\text{pipe,cpt}}$ [m]	13.45	$L_{\text{pipe,cab}}$ [m]	13.45	H_{floor} [m]	1.3
$D_{\text{pipe,cpt}}$ [m]	0.08	$D_{\text{pipe,cab}}$ [m]	0.18		
$L_{\text{wshield,f}}$ [m]	2.08	L_{wind} [m]	0.23		
$L_{\text{wshield,l}}$ [m]	1.32	H_{wind} [m]	0.33		
$H_{\text{wshield,f}}$ [m]	0.5	N_{wind} [-]	60		
$H_{\text{wshield,l}}$ [m]	0.5				

Table B.2: Dimensions and material properties of the fuselage composite structure of Airbus A320 [5], [6].

Parameter	Skin	Skin core	Insulation	Int. panel	Int. panel core
Material	Carbon phenolic	Hexcel HRH-10-1/8-6.0	Glass fibre	Glass phenolic	Fibrelam 1100 HRH-10-1/8-4.0
t [mm]	1.36	12.0	80.28	0.5	4.0
ρ [kg m^{-3}]	1800	93	9.6	2550	64
k_t [$\text{W m}^{-1} \text{K}^{-1}$]	1.0	0.068	0.036	0.24	0.0675
c [$\text{J kg}^{-1} \text{K}^{-1}$]	600	1300	1005	1110	1300

Table B.3: Dimensions and material properties of the floor and cabin wall composite structures of Airbus A320 [5], [6].

Parameter	Panel	Core
Material	Carbon phenolic	Fibrelam 6100 HRH-10-1/8-9.0
t [mm]	0.762	23.88
ρ [kg m^{-3}]	1800	139
k_t [$\text{W m}^{-1} \text{K}^{-1}$]	1.0	0.0675
c [$\text{J kg}^{-1} \text{K}^{-1}$]	600	1300

Table B.4: Dimensions and material properties of the flight deck windshield of Airbus A320.

Parameter	Glass shield	Outer panel	Inner panel
Material	Tempered glass	Opticor	Opticor
t [mm]	5.0	20.0	25.0
ρ [kg m^{-3}]	2500	1130	1130
k_t [$\text{W m}^{-1} \text{K}^{-1}$]	0.8	0.21	0.21
c [$\text{J kg}^{-1} \text{K}^{-1}$]	800	840	840
n [-]	1.47	1.52	1.52
τ [-]	0.918	0.9	0.9

Table B.5: Dimensions and material properties of the cabin windows of Airbus A320.

Parameter	Outer panel	Air cavity	Inner panel
Material	Opticor	Air	Opticor
t [mm]	10.0	7.0	5.0
ρ [kg m^{-3}]	1130	-	1130
k_t [$\text{W m}^{-1} \text{K}^{-1}$]	0.21	-	0.21
c [$\text{J kg}^{-1} \text{K}^{-1}$]	840	-	840
n [-]	1.52	-	1.52
τ [-]	0.9	-	0.9

B

NOMENCLATURE

Roman symbols

A	Surface area [m^2]
c	Specific heat capacity [$\text{J kg}^{-1} \text{K}^{-1}$]
D	Diameter [m]
H	Height [m]
k_t	Thermal conductivity [$\text{W m}^{-1} \text{K}^{-1}$]
L	Length [m]
N	Number of elements [-]
n	Refractive index [-]
R	Radius [m]
t	Thickness [m]
V	Volume [m^3]

Greek symbols

ρ	Density [kg m^{-3}]
τ	Transmittance [-]

Subscripts

cab	Cabin
cpt	Cockpit
f	Frontal
fwd	Forward
int	Interior
l	Lateral
wind	Window
wshield	Windshield

BIBLIOGRAPHY

- [1] C. Müller, D. Scholz, and T. Giese, “Dynamic simulation of innovative aircraft air conditioning”, in *1st CEAS European Air and Space Conference*, 2007.
- [2] “A319/a320/a321 flight deck and systems briefing for pilots”, Airbus, Tech. Rep., 1998.
- [3] “A320: Aircraft characteristics airport and maintenance planning”, Airbus, Tech. Rep., 2020.
- [4] “Airbus a320/a321 ground operations manual: Aircraft data, limitation and description”, LTU International Airways, Tech. Rep., 2015.
- [5] L. Krakkers, “Parametric fuselage design: Integration of mechanics and acoustic and thermal insulation”, Ph.D. dissertation, Delft University of Technology, 2009, ISBN: 9789085595601.
- [6] D. Petersen, R. Rolfes, and R. Zimmermann, “Thermo-mechanical design aspects for primary composite structures of large transport aircraft”, *Aerospace Science and Technology*, vol. 5, no. 2, pp. 135–146, 2001, ISSN: 1270-9638. DOI: 10.1016/S1270-9638(00)01089-0.

C

SOFTWARE

The following software has been developed or extended as part of the research work documented in this dissertation:

- TurboSim: Python suite for the design of turbomachinery based on scaling principles, including centrifugal compressors, axial turbines, and radial inflow turbines
- DeSimECS: Modelica library for the Design and Simulation of Energy Conversion Systems
- DesOptECS: integrated multi-point and multi-objective Design Optimization framework for novel Environmental Control Systems
- DynTherM: Modelica library for the Dynamic Simulation of Thermal Management systems
- NiceProp: Python program for teaching and research in the field of Non-Ideal Compressible Fluid Dynamics (NICFD)
- DEEP: Data-driven Embedded Ecosystem for Propulsion and Power applications

ABOUT THE AUTHOR



Andrea Giuffré was born in Carate Brianza, Italy, on April 28th, 1994. He obtained both his Bachelor's degree and his Master's degree cum laude in Mechanical Engineering at Politecnico di Milano. During his academic studies, he became passionate about turbomachinery, energy conversion systems, and propulsion systems. His curiosity for these topics encouraged him to pursue a Master's thesis in the group of Propulsion & Power at Delft University of Technology in 2018. This experience exposed him to the world of scientific research and led to his first presentation at an international conference and subsequently to his first publication in a top-tier scientific journal. His enthusiasm for the vibrant scientific community and his ambition to contribute to the transition to a low-carbon global economy motivated him to move to the Netherlands in 2019 and pursue his Ph.D. in Aerospace Engineering at Delft University of Technology. During his Ph.D. program, Andrea performed scientific research about environmental control systems for next-generation aircraft in tight collaboration with numerous industrial partners within the framework of the NEDEFA project. Moreover, he supervised four M.Sc. thesis students and three interns, and he taught lectures about the design of centrifugal compressors in the turbomachinery course of the M.Sc. program. Andrea is currently a post-doctoral researcher in the group of Propulsion & Power, where he performs research on thermal management systems for battery-powered aircraft. In his free time, Andrea enjoys cooking, traveling, and playing sports - in particular, the ones that keep him in contact with nature, e.g., skiing, diving, and mountain biking.

LIST OF PUBLICATIONS

JOURNAL ARTICLES

A. Giuffre', P. Colonna, and C. De Servi, "Dynamic Thermal Model of Passenger Aircraft for the Estimation of the Cabin Cooling and Heating Requirements", *Applied Thermal Engineering*, 2023. (Submitted)

A. Giuffre', F. Ascione, P. Colonna, and C. De Servi, "Electrically-Driven Vapor Compression Cycle Systems for the ECS of Next-Generation Aircraft: an Integrated Design Optimization Study", *Aerospace Science and Technology*, 2023. (Submitted)

F. Ascione, **A. Giuffre'**, P. Colonna, and C. De Servi, "Effect of Low-GWP Refrigerants on a Novel Electrically-Driven Helicopter ECS Optimal Design", *International Journal of Refrigeration*, 2023. (Submitted)

A. Giuffre', F. Ascione, C. De Servi, and M. Pini, "Data-Driven Modeling of High-Speed Centrifugal Compressors for Aircraft Environmental Control Systems", *International Journal of Refrigeration*, vol. 151, pp. 354-369, 2023, ISSN: 0140-7007. DOI: 10.1016/j.ijrefrig.2023.03.019.

A. Giuffre', P. Colonna, and M. Pini, "Design Optimization of a High-Speed Twin-Stage Compressor for Next-Gen Aircraft Environmental Control System", *Journal of Engineering for Gas Turbines and Power*, vol. 145, no. 3, 2023, ISSN: 0742-4795. DOI: 10.1115/1.4056022.

A. Giuffre', P. Colonna, and M. Pini, "The Effect of Size and Working Fluid on the Multi-Objective Design of High-Speed Centrifugal Compressors", *International Journal of Refrigeration*, vol. 143, pp. 43-56, 2022, ISSN: 0140-7007. DOI: 10.1016/j.ijrefrig.2022.06.023.

F. Tosto, **A. Giuffre'**, P. Colonna, and M. Pini, "Flow Deviation and Critical Choking in Transonic Turbine Cascades Operating with Non-Ideal Compressible Flows", *Journal of the Global Power and Propulsion Society*, vol. 6, pp. 181-199, 2022. DOI: 10.33737/jgpps/151659.

A. Giuffre', and M. Pini, "NiceProp: An Interactive Python-Based Educational Tool for Non-Ideal Compressible Fluid Dynamics", *SoftwareX*, vol. 17, 2022, ISSN: 2352-7110. DOI: 10.1016/j.softx.2021.100897.

A. Giuffre', and M. Pini, "Design Guidelines for Axial Turbines Operating with Non-Ideal Compressible Flows", *Journal of Engineering for Gas Turbines and Power*, vol. 143, no. 1, 2020, ISSN: 0742-4795. DOI: 10.1115/1.4049137.

CONFERENCE PROCEEDINGS

M. Pini, **A. Giuffre'**, A. Cappiello, M. Majer, and E. Bunschoten, "Data-Driven Regression of Thermodynamic Models in Entropic Form", *Proceedings of the 4th International Seminar on Non-Ideal Compressible Fluid Dynamics for Propulsion and Power*, vol. 29, pp. 22-32, 2023. DOI: 10.1007/978-3-031-30936-6_3.

A. Giuffre', F. Ascione, C. De Servi, and M. Pini, "Data-Driven Modeling of High-Speed Centrifugal Compressors for Aircraft Environmental Control Systems", *Proceedings of the Global Propulsion and Power Society*, 2022.

A. Giuffre', P. Colonna, and M. Pini, "Design Optimization of a High-Speed Twin-Stage Compressor for Next-Gen Aircraft Environmental Control System", *Proceedings of the ASME Turbo Expo*, vol. 10C, 2022. DOI: 10.1115/GT2022-81690.

F. Tosto, **A. Giuffre'**, P. Colonna, and M. Pini, "Non-ideal Effects in Compressible Swirling Flows", *Proceedings of the 3rd International Seminar on Non-Ideal Compressible Fluid Dynamics for Propulsion and Power*, vol. 28, pp. 36-43, 2021. DOI: 10.1007/978-3-030-69306-0_5.

A. Giuffre', and M. Pini, "Design Guidelines for Axial Turbines Operating with Non-Ideal Compressible Flows", *Proceedings of the ASME Turbo Expo*, vol. 2C, 2020. DOI: 10.1115/GT2020-14209.